2015

INTEGRATED NANOSCALE IMAGING AND SPATIAL RECOGNITION OF BIOMOLECULES ON SURFACES

Congzhou Wang
Virginia Commonwealth University

COPYRIGHT PAGE

Integrated Nanoscale Imaging and Spatial Recognition of Biomolecules on Surfaces

A dissertation submitted in partial fulfillment of the requirements for the degree of Doctor of
Philosophy at Virginia Commonwealth University

by

Congzhou Wang

Master of Medicine in Pharmacy – Chongqing University, China, 2012

Bachelor of Engineering in Pharmaceutical Engineering – Huaqiao University, China, 2009

Advisor: Vamsi K. Yadavalli, Ph.D.

Associate Professor of Chemical and Life Science Engineering

Virginia Commonwealth University

Richmond, Virginia

December 2015

Acknowledgements

It is my pleasure to acknowledge several mentors and colleagues who provided strong support for completion of this dissertation.

First of all, I would like to express my deep gratitude to my research advisor, Dr. Vamsi Yadavalli, who encouraged, inspired and helped me to pursue various interdisciplinary interesting projects. He taught me innumerous things at every stage of my research through his academic expertise, allowing me to improve my critical thinking, scientific writing skill and problem solving ability. He has set the best standard for my academic career. I am truly enjoying and proud to work with him and in such a productive lab.

The completion of this dissertation would not have been possible without the support of a number of collaborators that contributed many discussions and provided experimental assistance. I am very grateful to Dr. Christopher Ehrhardt and Cristina Stanciu (Department of Forensic Science, Virginia Commonwealth University, Richmond, Virginia) for the immense assistance with experiment design, paper writing and endless cell culture work. Later stages of this work would not have been possible without Dr. Kenneth Wynne and Dr. Olga Zolotarskaya (Department of Chemical and Life Science Engineering, Virginia Commonwealth University, Richmond, Virginia), for synthesizing antimicrobial polymer and interpreting data with an elegant model. Dr. Umesh Desai and Dr. Yingzi Jin (Department of Medicinal Chemistry, Virginia Commonwealth University, Richmond, Virginia), thanks for the assistance with the heparin project. I would also like to thank my committee members Dr. Stephen Fong

(Department of Chemical and Life Science Engineering, Virginia Commonwealth University, Richmond, Virginia) and Dr. Christopher Lemmon (Department of Biomedical Engineering, Virginia Commonwealth University, Richmond, Virginia) for insightful suggestions throughout this work.

I am grateful to all of my friendly and collaborative labmates. Nick, thank you for teaching me experimental skills and providing nice ideas throughout my first year of work. Ramendra, thank you for immense help with my experiments and constantly exchanging inspiring ideas. Mahmoud, thank you for the assistance with my experiments.

Finally, to my family and friends, I am extremely appreciative of the constant support throughout the duration of my graduate work at VCU. This dissertation is dedicated to my mum, dad and fiancée, Jie.

Table of Contents

Abstract vii

CHAPTER 1 1

INTRODUCTION 1

- 1.1 Introduction 1
- 1.2 Specific Aims 6
- 1.3 Background and Significance 9

CHAPTER 2 18

INVESTIGATION OF BIOMOLECULAR INTERACTIONS BY AFM-BASED FORCE SPECTROSCOPY 18

- 2.1 Introduction 18
- 2.2 Experimental Section 22
- 2.3 Results and Discussion 25
- 2.4 Conclusions 45

CHAPTER 3 47

FORCE RECOGNITION MAPPING OF PROTEINS ON MIXED SELF-ASSEMBLED MONOLAYER SURFACES 47

- 3.1 Introduction 47
- 3.2 Experimental section 51
- 3.3 Results and Discussion 54
- 3.4 Conclusions 71

CHAPTER 4 73

SPATIAL MAPPING OF CELL-SURFACE TARGETS AND ASSESSMENT OF THEIR CHANGES AT THE SINGLE CELL LEVEL 73

- 4.1 Introduction 73
- 4.2 Experimental Section 77
- 4.3 Results and discussion 81
- 4.4 Conclusions 106

CHAPTER 5 108

THE EFFECT OF INACTIVATION AND GROWTH TEMPERATURE ON THE SURFACE PROPERTIES OF *YERSINIA PESTIS* 108

- 5.1 Introduction 108
- 5.2 Experimental section 112
- 5.3 Results and Discussion 116
- 5.4 Conclusions 130

CHAPTER 6 132

REAL TIME OBSERVATION OF THE EFFECT OF ANTIMICROBIAL COPOLYOXETANES ON *ESCHERICHIA COLI* SURFACES 132

- 6.1 Introduction 132
- 6.2 Experimental section 135
- 6.3 Results and Discussion 138
- 6.4 Conclusions 147

CHAPTER 7 149

REAL TIME OBSERVATION OF THE ANTIMICROBIAL EFFECT OF COPPER ON BACTERIAL SURFACES 149

- 7.1 Introduction 149
- 7.2 Experimental section 152
- 7.3 Results and discussion 154
- 7.5 Conclusions 163

CHAPTER 8 165

HYDROPHOBICITY PROFILES OF *BACILLUS CEREUS* AT THE SINGLE SPORE LEVEL 165

- 8.1 Introduction 165
- 8.2 Experimental section 168
- 8.3 Results and discussion 170
- 8.4 Conclusions 179

CHAPTER 9 181

DNA MAPPING ON SINGLE HUMAN EPITHELIAL CELL SURFACES 181

- 9.1 Introduction 181
- 9.2 Experimental Section 182

9.3 Results and discussion......185
9.4 Conclusions and future work......189
CHAPTER 10......190
CONCLUSIONS, CHALLENGES AND FUTURE WORK......190
10.1 Conclusions......190
10.2 Challenges and Future Work......193
References......204
Vita......241

Abstract

INTEGRATED NANOSCALE IMAGING AND SPATIAL RECOGNITION OF BIOMOLECULES ON SURFACES

By Congzhou Wang, Ph. D

A dissertation submitted in partial fulfillment of the requirements of the degree of Doctor of Philosophy at Virginia Commonwealth University.

Virginia Commonwealth University, 2015

Major Director: Vamsi K. Yadavalli, Ph.D., Associate Professor of Chemical and Life Science Engineering

Biomolecules on cell surfaces play critical roles in diverse biological and physiological processes. However, conventional bulk scale techniques are unable to clarify the density and distribution of specific biomolecules *in situ* on single, living cell surfaces at the micro or nanoscale. In this work, a single cell analysis technique based on Atomic Force Microscopy (AFM) is developed to spatially identify biomolecules and characterize nanomechanical properties on single cell surfaces. The unique advantage of these AFM-based techniques lies in

the ability to operate *in situ* (in a non-destructive fashion) and in real time, under physiological conditions or controlled micro-environments.

First, AFM-based force spectroscopy was developed to study the fundamental biophysics of the heparin/thrombin interaction at the molecular level. Based on force spectroscopy, a force recognition mapping strategy was developed and optimized to spatially detect single protein targets on non-biological surfaces. This platform was then translated to the study of complex living cell surfaces. Specific carbohydrate compositions and changes in their distribution, as well as elasticity change were obtained by monitoring *Bacillus* cells sporulation process.

The AFM-based force mapping technique was applied to different cellular systems to develop a cell surface biomolecule library. Nanoscale imaging combined with carbohydrate mapping was used to evaluate inactivation methods and growth temperatures effects on *Yersinia pestis* surface. A strategy to image cells in real time was coupled with hydrophobicity mapping technique to monitor the effect of antimicrobials (antimicrobial polymer and copper) on *Escherichia coli* and study their killing mechanisms. The single spore hydrophobicity mapping was used to localize the exosporium structure and potentially reconstruct culture media. The descriptions of cell surface DNA on single human epithelial cells potentially form a novel tool for forensic identification.

Overall, these nanoscale tools to detect and assess changes in cell behavior and function over time, either as a result of natural state changes or when perturbed, will further our understanding of fundamental biological processes and lead to novel, robust methods for the analysis of individual cells. Real time analysis of cells can be used for the development of lab-on-chip type assays for drug design and testing or to test the efficacy of antimicrobials.

CHAPTER 1

INTRODUCTION

1.1 Introduction

Biomolecular interactions on cell surfaces play critical roles in diverse biological and physiological processes [1]. Typical cell surface biomolecules include membrane proteins, lipids, glycans and nucleic acids. As important cell surface biomarkers, understanding how they interact with their specific ligands, their presentation on different types and strains of cell surfaces, and changes in their distribution on cell surfaces during cellular activities or in response to various environments therefore provides a means to identify different cell types and strains, monitor specific cellular processes, as well as to reconstruct culture and environmental conditions. These studies also have broader implications in unraveling the molecular basis of relevant biological and pathological processes, and developing new tools for disease diagnosis/detection, study of mechanisms of drug action/drug screening, and forensic identification at a molecular and single cell level [2, 3].While cell surface biomolecular interactions are also typically studied using affinity chromatography, fluorescence, and surface plasmon resonance (SPR) [4-6], these bulk scale techniques are unable to clarify the density and distribution of specific biomolecules *in situ* on single, living cell surfaces at the micro or nanoscale.

Atomic force microscopy (AFM), as an important tool widely used over the last couple of decades in biological research, has the ability to not only characterize cell surfaces with nanoscale resolution and three dimensional images, but also measure inter- and intra-molecular interaction forces with piconewton sensitivity ("AFM-based force spectroscopy", AFM-FS) [7-9]. Using a modified AFM tip as a probe, interaction forces between tip-bound ligands and surface-bound cognate receptors (or vice-versa) can be determined from force curves, which show the cantilever deflection (Δx) due to adhesion forces between the tip and sample [10]. The modification of the AFM tip is achieved by covalently bonding a molecule to it (e.g. antibody, aptamer, lectin etc.). To collect a force curve, the cantilever with the modified tip moves vertically (z-axis) toward the surface, contacts the surface, and then retracts. The interaction forceis then obtained by applying Hooke's law ($F=-k\Delta x$), where F is the force and k is the spring constant of the cantilever. Analysis of these force curves can be used to uncover biophysical and biochemical properties, and thereby provides a strategy for single cell analysis (Figure 1.1).

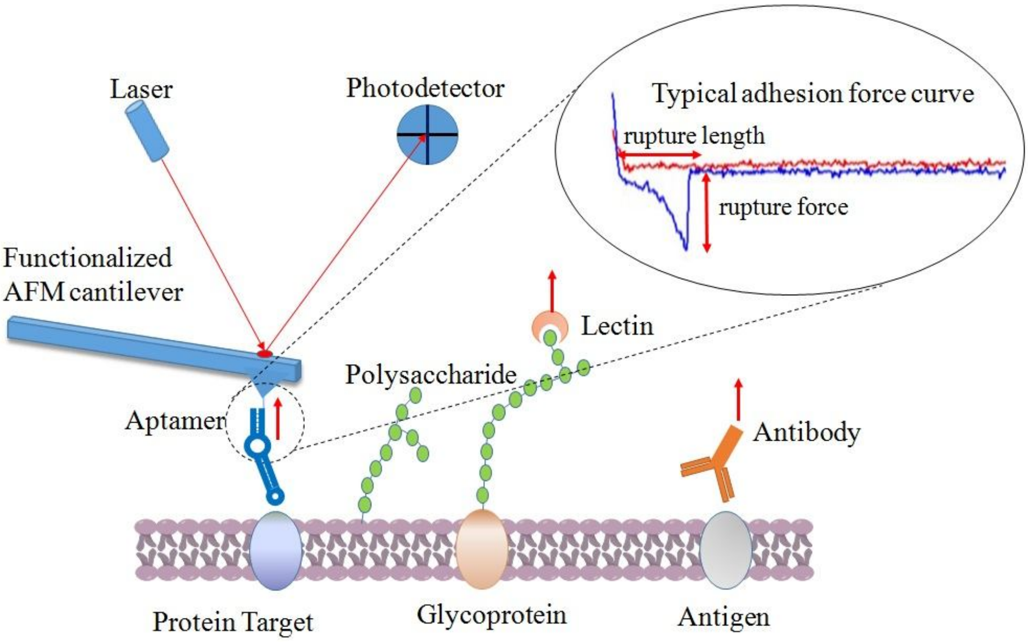

Figure 1.1. Probing cell surfaces using AFM based force spectroscopy.

In recent years, the process of collecting such force curves has been expanded with the advent of automated scanning modes that allow us to rapidly obtain spatial distributions of interaction forces in a process called "AFM-based force recognition mapping" [11-13]. Briefly, an array of force curves on an area is collected with a biofunctionalized AFM tip. The adhesion forces of all force curves can then be combined with their corresponding surface coordinates, allowing display in the form of a "map", simultaneously showing the position of specific biomolecules and their adhesion. Using the force interaction data, it is then possible to spatially recognize specific molecules on surfaces. The unique advantage of this technique is its ability to spatially identify the specific targets *in situ* and at the single cell level without extra sample preparation such as cell wall lysis. Using different bio-functionalized probes, we can localize various specific targets on the cell surface *via* simultaneous topographic and force information. Additionally, the AFM tip can be used as an indenter to determine the mechanical nature of the cell surface at the nanoscale *via* nanoindentation coupled with a technique of "elasticity mapping" [14]. Similar to the force map, the mechanical elasticity map can be overlaid on the topography of the cell to show the variation of properties across the entire cell (Figure 1.2). Importantly, AFM can be performed in real-time, under physiological conditions, as well as under controlled environments varying pH, salt, inhibitors or other effectors. This enables observation of force map and elasticity map changes in real-time, monitoring cellular activities, retracing different growth environments and cell states, as well as evaluating the effects of exogenous substances on cell surfaces (for instance, the effects of drugs, antibiotics or antimicrobials on pathogens).

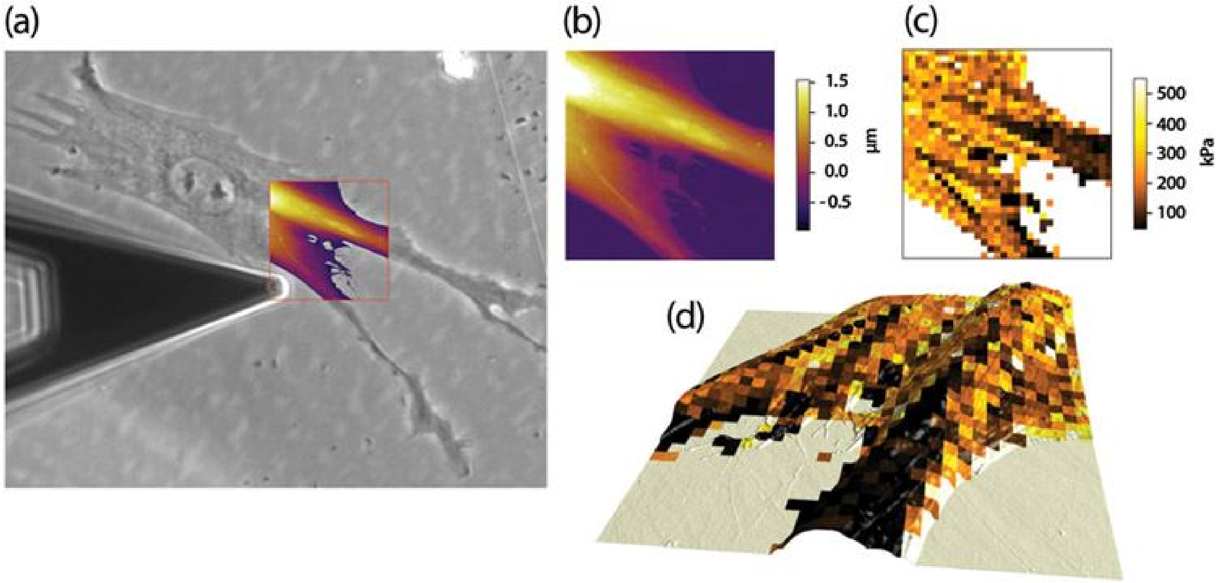

Figure 1.2. AFM based elasticity mapping on cell. The optical phase contrast image of a cell with the cantilever hovering over it, and with an optically defined region of interest (red box) for elasticity mapping is shown in (a). After the AFM topography scan (b), the elasticity map was obtained, and analyzed using the Hertz model (see explanation below).The modulus values were plotted and displayed as a 2D image (c). The modulus map was overlaid onto the AFM topography image and rendered in 3D (d).[1]

1.1.1 Research Objective

The objective of this research was to develop and enhance the strategy of integrated imaging and spatial recognition of cell surface biomolecules to further our understanding of fundamental biological processes at the nanoscale. This can lead to novel, robust methods for the analysis of individual cells, as well as detecting and assessing changes in cell behavior and function over time, either as a result of natural state changes or when perturbed.

As discussed below, this research followed various steps leading to the goal of probing complex

---

[1] *(Image adapted from: http://www.asylumresearch.com/Gallery/Nanomechanics/ForceMapping/ForceMapping2.shtml)*

cellular surfaces. Initially, AFM-FS was used to investigate the specific biomolecular interaction between heparin and thrombin in order to uncover key kinetic parameters. This study also enabled the development of broader techniques to study both non-biological surfaces and living cell surfaces, combining force recognition with spatial localization. To translate the biophysical "mapping" technique to complex, living cell surfaces, the research focused on expanding applications towards the single-cell detection of pathogens. *Bacillus cereus* and *Yersinia pestis* cell surfaces were used as models due to their importance as related to food-safety and bioterrorism, and necessity for rapid analysis of types and virulence. For instance, the descriptions of their cell wall carbohydrates could be useful for type/strain classification, monitoring cellular processes such as sporulation, and evaluating the effect of inactivation methods and growth temperatures on cell surface biochemical nature. *Escherichia coli* and *Bacillus cereus* spore surfaces were used as targets wherein the descriptions of cell surface hydrophobicity (which originate from lipids and hydrophobic proteins), could be useful for studying antimicrobial mechanisms and culture media effect. Finally, human epithelial cells including buccal and palm cells were selected as targets wherein the descriptions of cell surface DNA form a novel tool for forensic identification. Together, these studies enable visualization of the spatial distributions of target biomolecules and assessment of their changes on cell surfaces *in situ*, which could lead to the development of robust strategies for the analysis of cells at the individual level. The spatial localization of specific cell surface targets (sugars, lipids, DNA etc.) offers a new avenue to classify various cell types/strains, monitor diverse cellular processes, study mechanisms of drug action, and reconstruct different culture conditions and cell states from a nanoscale and single cell perspective.

1.2 Specific Aims

This research focused on the following aims:

(1) Development of techniques to spatially recognize target biomolecules on (model) surfaces using single-pair biomolecular interactions.

(2) Translation of these techniques for the spatial localization of specific targets on complex living cell surfaces.

(3) Investigation of specific cell related questions from a nanoscale perspective using bacteria as model organisms. These include observations on how the distribution of specific biomolecules changes among different cell types and strains, during specific cellular processes or under different micro-environments.

(4) Determination of whether such spatial distributions and changes can be used for broader applications in single cell analyses: classification of various cell types, strains or states, reconstruction of culture conditions (such as medium and temperature), and monitoring of cell activities with external effectors (e.g. antimicrobials) to elucidate mechanism of action.

1.2.1 Biomolecular interactions and spatial recognition of single biomolecules on controlled model surfaces.

In order to measure pairwise interaction forces using AFM-FS, proper immobilization methods need to be first developed to covalently attach biomolecules on AFM probes and substrates at the molecular level (preferably at the single molecule level). Concurrently, strategies are necessary to improve the accuracy of force measurement, such as minimizing nonspecific tip-surface adhesion forces, and measuring interaction forces at the molecular level. The target molecules need to be attached to surfaces in a well-separated fashion in order to evaluate the ability of identification and localization. Two important factors, which may determine the accuracy and efficiency of the "force recognition" technique – the selection of proper bio-probe and spatial resolution, will be optimized. Based on the force spectroscopy research, an "AFM-based force recognition mapping" technique will be developed for spatial recognition of specific biomolecules on controlled (model) surfaces. These tasks will enable studies on more complex surfaces in subsequent aims.

1.2.2 Force spectroscopy on living cell surfaces.

The translation of "force recognition" techniques from Aim 1 to complex, living cell surfaces offers the opportunity to obtain spatial distribution of cell surface biomolecules *in situ*. The cell separates its cytoplasm from the extracellular environment *via* a cell membrane consisting of a phospholipid bilayer with embedded proteins and carbohydrates located on the extracellular surface of the membrane. It is extremely challenging to detect a specific biomolecule embedded in the complex cell membrane from topography imaging alone. Therefore, in order to investigate cell surfaces in physiological environments, proper strategies will be developed for immobilizing cells in their native state. Optimization of the "force recognition" techniques involving the resolution and data collection time is necessary to adapt to complex cell surfaces. These tasks will facilitate a versatile platform and provide a nanoscale perspective to quantitatively detect and spatially localize the cell surface biomarkers at the single cell level.

1.2.3 Single cell analysis *via* spatial mapping of cell surface targets and assessment of their changes.

Using the techniques developed in the above tasks, spatial distribution of specific cell surface biomolecules will be used to address specific cellular questions from a single cell and nanoscale perspective. *B. cereus* will be selected as a model system to study the spatial distribution of cell surface carbohydrates and quantitatively assess the changes among different cell types and strains, during a specific cellular process (sporulation) or under different micro-environments. As the AFM can be performed in real-time and controllable micro-environments, it is possible to observe the biomolecular distribution change in real-time and various micro-environments. Overall, this will lead to visualization of targets of interest and their changes on cell surfaces and the development of robust strategies for the analysis of cells at the individual level.

Following Aim 3, the spatial distribution of cell surface biomolecules and their changes will be used to classify various cell types, strains or states, reconstruct culture media, as well as monitor cell activities with external effectors to elucidate their mechanisms of action. Specifically, hydrophobic contents and the changes will be detected on various bacteria for cell type classification (such as *B.cereus* and *B. subtilis*), culture media reconstruction and monitoring cell activities with external effectors to elucidate their mechanisms of action (antimicrobials). Surface carbohydrates on *Y. pestis* inactivated by different methods and grown in different temperatures will be studied to determine the best inactivation method to preserve its surface biochemical nature, and its surface adaption to different environments. These tasks will demonstrate whether the spatial distribution of specific cell surface biomolecules and the changes can be used as a reliable, rapid and versatile analysis tool for single-cell level study.

1.3 Background and Significance

This section will define the background and significance of this research, first introducing the advantages, development and enhancement of the technique, and translating this technique on complex cell surfaces for addressing pratical cellular related questions.

1.3.1 Atomic Force Microscopy as an integrated biophysical tool

Primarily devised for high resolution imaging, the AFM is a powerful and widely used tool for investigating molecular scale processes under physiological environment. AFM-FS allows the measurement of inter- and intra-molecular interaction forces with piconewton resolution [10, 15, 16]. Using a biomolecule modified AFM tip as a probe, interaction forces between tip-bound ligands and cognate surface-bound receptors (or vice-versa) can be measured. As the interaction forces closely depend on the loading rates exerted on the molecular complex [17, 18], Dynamic Force Spectroscopy (DFS), a subset of AFM-FS which allows collection of force data over variable loading rates, has emerged as a valuable technique for the characterization of dissociation kinetics and energy profile of the interacting molecules under varying conditions [19, 20]. The first step of this research is to build an AFM-FS based platform for studying biomolecular interactions at the molecular scale. This is also intended to provide a facile means for attaching biomolecules on non-biological surfaces in a well-separated fashion and measuring their interaction forces.

1.3.2 Molecular interactions in biological processes

Pair-wise biomolecular interactions involving different proteins, proteins and polysaccharides, or proteins and DNA, play crucial roles in diverse biological processes [1, 21]. For example, the interactions between polysaccharides and proteins are pivotal to a range of physiological and pathological processes, including blood coagulation, inflammation and tumor metastasis [22-25]. A fundamental understanding of the biophysical nature of these events, such as adhesion force, binding affinity and stability in different kinds of environments, has major applied importance [26, 27]. Here, the heparin-thrombin interaction is used as a model biophysical system.

Heparin, a highly sulfated glycosaminoglycan (GAG), is widely used as an injectable anticoagulant as well as in the form of anticoagulant coatings on various biomedical devices. Heparin is known to accelerate the inactivation of blood coagulation proteinase (thrombin) by its inhibitor antithrombin(AT) [28, 29]. The mechanism of this reaction reveals a classic interplay of site-specific and site-nonspecific interactions. The first step involves AT binding to a specific five residue sequence on the polymeric chain of heparin. Thrombin binds to a remote site on the same heparin chain and then “walks” toward AT to form the ternary ‘locked’ complex, which results in thrombin inhibition [30-33]. Thus, thrombin regulation is of paramount importance and understanding the fundamentals of the heparin–thrombin interaction is critical. In this research, heparin–thrombin interaction is selected as a model system to build an AFM-FS based platform for studying biomolecular interaction at the molecular scale.

1.3.3 Recognition and mapping of single proteins

One of the important challenges in surface characterization using the AFM and other microscopes is that it is generally unable to distinguish between different or similarly shaped objects of disparate chemical nature based on the topographical image alone. For instance, it is extremely challenging to detect a transmembrane protein embedded in the cell membrane from topography imaging alone. Consequently, there is a clear need to develop methods to spatially probe and identify biomolecules on biosurfaces, possibly based on their bioactivity or their interactions. A recent enhancement to the AFM toolkit called AFM-based force recognition mapping, involves the integration of imaging and force spectroscopy to facilitate multidimensional data collection about a system. It is now possible to record the adhesion force between the AFM tip and a surface during scanning. Thus, information on topography may be obtained in conjunction with mechanical stiffness or elasticity, or coupled with adhesive forces and other measures of interaction. This powerful enhancement has been adapted for applications including the detection and localization of specific molecular recognition events, as well as for simultaneous topography and force recognition imaging of specific receptors on complex surfaces [34, 35].

In order to improve the spatial accuracy of this technique however, two important criteria need to be met: First, single proteins need to be attached to surfaces in a well-separated fashion. This is to ensure that the interactions are molecular and not multivalent. Early research indicated that mixed self-assembled monolayers (SAMs) synthesized *via* co-adsorption from solutions containing mixtures of thiols provided a useful platform for the study of single molecules by incorporating properties from different thiol molecular species [36]. Second, proper bio-probes with specificity to various protein targets need to be selected, and covalently attached to AFM tips [37-40]. In this research, different bio-probes ranging from short synthetic DNA/RNA oligonucleotides called aptamers [41, 42] to sugar binding lectins are used. Mapping isolated proteins on non-biological surfaces may be expanded to be a versatile platform for detection of specific biomarkers on living cell surfaces, which is more complex than non-biological surface.

1.3.4 Detecting specific biomarkers on living cell surfaces

The AFM can directly investigate live cells under near physiological environments in a non-destructive fashion. More practicably, the AFM-based force recognition mapping technique that combines AFM-FS with the high spatial resolution of the AFM, offers the opportunity to map living cell surface recognition sites or biomarkers that would not be otherwise found by traditional, macroscale techniques. Specifically, the AFM is used to study bacterial surfaces at the single cell level and to monitor cellular activities by observing specific biomolecular targets at the cell surface [43, 44]. *B. cereus* is chosen as a model bacterium owing to its importance in the food industry, and due to genetic and structural similarity with the more virulent *B. anthracis.* The characterization and profiling carbohydrate compositions of these bacilli has great fundamental and applied importance, especially for identification of different genera, strains and physiological states of bacteria.

1.3.5 Multi-parametric tracking on living cell surfaces during biological process

AFM-based force recognition mapping also provides a means for tracking the change of these cell surface biomarkers during various biological processes and under different conditions. Specifically in this research, *B. cereus*, as a typical spore-forming cell, is able to metabolically transform into oval, dormant spores in response to unfavorable environmental conditions. It has been shown that vegetative *B. cereus* cells have different carbohydrate compositions in comparison to spores. These compositional biomarkers switches could be used to discriminate the vegetative or spore stage of *Bacillus* and track the sporulation process. Therefore, the carbohydrate compositions obtained by AFM-based force mapping can also be used as important parameters for tracking bacterial related activities. Here, both the morphology and carbohydrate compositions changes on cell surfaces can be monitored during the sporulation process at the nanoscale.

Additionally, morphological changes during sporulation are accompanied by variations in the mechanical properties of the cell surface as multilayers of protein coats and peptidoglycan layers encase cellular contents and genetic information into the newly formed spore [45]. Similar as the force mapping, AFM based elasticity mapping allowed us to rapidly obtain spatial distribution of elasticity [46, 47]. Using the AFM tip as an indenter, quantitative information on the elasticity of the sample can be obtained spatially [48]. Therefore, AFM imaging combined force and elasticity mapping will provide a multi-parametric platform for tracking cell related biological processes.

1.3.6 Applications of spatial mapping of cell surface targets

Evaluation of the effect of inactivation and growth temperature

Y. pestis, the causative agent of plague, has been responsible for several recurrent, lethal pandemics in history [49, 50]. Currently, it remains an important pathogen to study owing to its virulence, adaptation to different environments during transmission, and potential use in bioterrorism [51, 52]. Manipulation of viable *Yersinia* organisms in the laboratory usually necessitates elevated biosafety and biocontainment procedures, even with avirulent or vaccine strains. However, to facilitate downstream biochemical or physical analyses in a Biosafety Level 1 laboratory environment, effective inactivation without affecting its intrinsic properties is critical. Furthermore, the effect of growth temperature may be relevant to the *natural* ecology of *Y. pestis*. Temperatures in nature typically vary from 0^{o}C to 42°C, involving transmission from the cold-blooded flea vector (20-25°C) to the warm-blooded mammal host (37°C), and infected animals during winter hibernation (6°C) [53]. Adaptations to different growth temperatures have been associated with transformations on *Y. pestis* surfaces [54-56].

In this research, a functionalized AFM probe and force recognition mapping strategy is developed to analyze how the biochemical nature of the single cell surface is affected by different inactivation methods and growth temperatures [57, 58]. The lectin wheat germ agglutinin (WGA) is used to spatially detect and quantify the surface lipopolysaccharides (LPS) via the carbohydrate N-acetylglucosamine (GlcNAc) with outermost localization on the cell surface as one of the terminal residues of the core LPS oligosaccharide. These results provide tools for studying virulent pathogens using equipment that may not have elevated biocontainment capabilities - inactivation followed by nanoscale evaluation of the effects on cell morphology and surface bioactivity. Understanding how external microenvironments (temperature, irradiation), including those designed to inactivate the *Y. pestis*, affect the structure and biochemical behavior of the cell surface, can help us not only design better inactivation protocols, but also shed light on the *in situ* characteristics of pathogens.

Differentiation of Bacillus spore types and growth conditions

Members of the *Bacillus* ACT group (*anthracis, cereus and thuringiensis*) are able to transform into metabolically dormant states called spores. It is now well known that these spores possess unique hydrophobic surface property and the spore surface hydrophobicity is closely related to their adhesion to inanimate surface and phagocytic cells [59, 60], escape from macrophages [61], pathogenicity [62], and germination [63]. Furthermore, prior reports have shown that the *bacilli* spore surface hydrophobicity differs widely among species and strains [64-66]. Thus, the characterization and understanding of *Bacillus* spore surface hydrophobicity has great fundamental and applied importance. To date, surface hydrophobicity of various species and strains of bacilli has been well studied using several methods including microbial adhesion to hydrocarbons (MATH) [67], hydrophobic interaction chromatography (HIC) [68], salt precipitation [69], and contact angle measurements [70]. However, one of the primary disadvantages of these approaches is that they need large populations of spores for the bulk scale analysis. In the case of a bioterrorist attack, each hour of detection delay could increase infections and spread.

AFM based chemical force microscopy (CFM) has rapidly emerged as an important tool in microbiology [71, 72]. Specifically, using functional AFM tips as probes, adhesion forces between tip-bound groups ($-CH_3$) and surface hydrophobic groups on bacteria can be measured. This technique enables researchers to map out spatial distributions of hydrophobic groups such as lipids and hydrophobic proteins [9, 73]. The unique advantage of CFM is the ability to rapidly investigate single spore (or limited amount of spores) under near physiological environments in a non-destructive fashion. The nanoscale hydrophobic profiling on single spores offers a new way for differentiation of Bacillus spore types. The evaluation of culture medium effect on single spore surface hydrophobicity provides more useful information for forensic investigation purpose such as retracing spore culture processes and sources.

Monitoring antimicrobial mechanism of action in real time

A better understanding of killing mechanisms of antimicrobial compounds is critical to the development of new broad-spectrum agents. Among the different kinds of antimicrobials, synthetic amphiphilic polycations structurally mimic the naturally occurring antimicrobial peptides [74-76]. Similar to antimicrobial peptides, net positively charged polycations are able to electrostatically bind to the anionic bacterial surface, while the amphipathic structure facilitates their insertion into the hydrophobic core of the cell membrane [77, 78]. So far, different models for the interaction of antimicrobial peptides with the bacterial membrane have been proposed based on *antimicrobial peptides interacting with model membrane systems*. However, the killing mechanism of synthetic amphiphilic polycations and their effect on *natural membrane system* (live bacterial surface) still need to be clarified.

Among different metals, copper (Cu) and its compounds have been widely utilized as cheap and effective antimicrobial materials. In recent years, micro- and nano-particles of metals have attracted considerable interest owing to their potency, high specific surface area, chemical stability, heat resistance and long shelf-life [79]. Most of the studies have hypothesized that bacteria are killed by a copper ion release mechanism instead of nanoparticle penetration into bacteria [80]. However, compared to copper nanoparticles, *copper microparticles and their antimicrobial mechanism have been poorly studied*.

As AFM imaging can be performed in real-time and controllable micro-environments, it is possible to monitor the changes in cells in real-time and various micro-environments including the presence of drugs, antibiotics or antimicrobials. Here, observation of the effect of antimicrobials (polycationic and metallic ions) on live bacterial cells (from morphology and surface hydrophobicity perspectives) under physiological conditions *in situ* and real time were used to provide models for killing mechanisms at the single cell level.

[This chapter contains results that have been previously published in:

Wang C, Yadavalli VK, "Investigating biomolecular recognition at the cell surface using atomic force microscopy," Micron, 60, 5-17, May 2014.

CHAPTER 2

INVESTIGATION OF BIOMOLECULAR INTERACTIONS BY AFM-BASED FORCE SPECTROSCOPY

2.1 Introduction

Pair-wise biomolecular interactions involving different proteins, proteins and polysaccharides, or proteins and DNA, play crucial roles in diverse biological processes [1, 21]. The interactions between polysaccharides and proteins are key to a range of physiological and pathological processes, including blood coagulation, inflammation and tumor metastasis [22-25]. A fundamental understanding of the biophysical nature of these events, such as adhesion force, binding affinity and stability in different kinds of environments, has major applied importance [26, 27]. Heparin, a highly sulfated glycosaminoglycan (GAG), is widely used as an injectable anticoagulant as well as in the form of anticoagulant coatings on various biomedical devices. Heparin is known to accelerate the inactivation of blood coagulation proteinase(thrombin) by its inhibitor antithrombin(AT) [28, 29]. The mechanism of this reaction reveals a classic interplay of site-specific and site-nonspecific interactions. The first step involves AT binding to a specific five residue sequence on the polymeric chain of heparin. Thrombin binds to a remote site on the same heparin chain and then “walks” toward AT to form the ternary ‘locked’ complex, which results in thrombin inhibition [30-33]. For optimal operation, nature has designed heparin-thrombin interaction to be a site-nonspecific interaction [81], which enables “walking” of thrombin on the sulfated polysaccharide chain [14]. This is expected to be characterized by fast ‘on’ and ‘off’ reactions. Interestingly, the formation of the ternary complex is to be achieved under rapid blood conditions, which enhances the probability of thrombin dissociation and raises the possibility of inadvertent clot formation. Thus, thrombin regulation is of paramount importance and understanding the fundamentals of the heparin–thrombin interaction is critical (Figure 2.1).

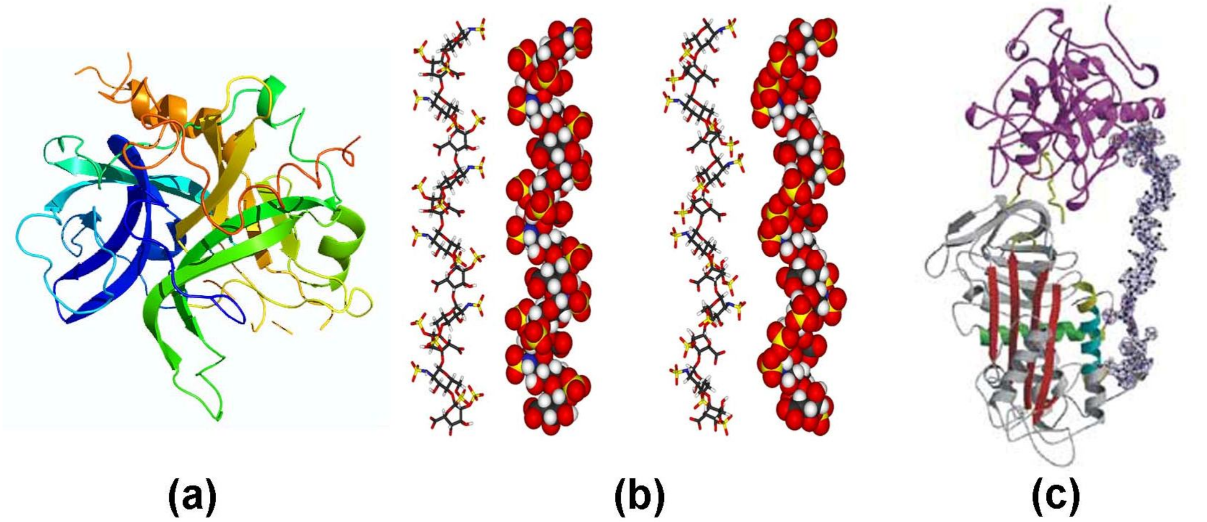

Figure 2.1. (a) Secondary structure of thrombin. (b) Two different structures of heparin. (c) Stereo representation of the crystal structure of the ternary complex between antithrombin (bottom), thrombin (top) and heparin (right side) [2] [31].

---

[2] *(Image adapted from: http://fineartamerica.com/featured/thrombin-protein-secondary-structure-dr-tim-evans.html and https://en.wikipedia.org/wiki/Heparin)*

To date, the binding interactions between heparin and thrombin have been studied primarily at the bulk level, using approaches such as fluorescence, affinity chromatography and surface plasmon resonance (SPR). Oshima et al. [82] showed that the interaction of thrombin with fluorescein-labeled heparin is affected by NaCl, implying that electrostatic force is the dominating factor of the interaction. Using quantitative affinity chromatography, Olson et al. [81] also demonstrated that the strong dependence of the binding on NaCl concentration was best accounted for by the electrostatic interactions of thrombin and heparin. In a study conducted via SPR, a heparin-coated surface was able to bind much more thrombin than AT III, indicating that the heparin–thrombin interaction is less specific compared to the heparin–AT III interactions [83]. However, these methods require large amounts of heparin/thrombin, and are principally applied to study the bulk scale interactions at their steady states. They are also unable to evaluate these weak forces in varying media directly at the molecular level. On the other hand, most biological processes generally occur under non-equilibrium conditions at the molecular scale [84]. Given that the binding of thrombin and heparin might be primarily due to weak, non-covalent forces, there is a need to unravel the molecular mechanism of heparin–thrombin interaction at a fundamental level from a mechanical and dynamic perspective.

In this chapter, we discuss the use of Atomic Force Microscopy (AFM)-based Force Spectroscopy (AFM-FS) to study the fundamental biophysics of the interactions between heparin and thrombin at the molecular level. Primarily devised for high resolution imaging, the AFM is a powerful and widely used tool for investigating molecular scale processes. AFM-FS allows the measurement of inter- and intra-molecular interaction forces with piconewton resolution [10, 15, 85]. As the interaction forces closely depend on the loading rates exerted on the molecular complex [17, 18], Dynamic Force Spectroscopy (DFS), a subset of AFM-FS which allows collection of force data over variable loading rates, has emerged as a valuable technique for the characterization of dissociation kinetics and energy profile of the interacting molecules under varying conditions [19, 20].

For force measurements using AFM-FS and DFS, the first step is to covalently immobilize each biomolecule of the pair-wise interaction on an AFM tip and a substrate, respectively. Together with different immobilization strategies, the rupture forces between the tip-bound and surface-bound molecules can then be measured in real-time, under physiological conditions, as well as under controlled microenvironments [86]. To attach the protein (thrombin) molecules to a surface and to minimize non-specific tip-surface adhesion forces, a well characterized mixed self-assembled monolayer (SAM) platform is used, wherein lysine residues on the protein surface are conjugated to NHS groups on a gold surface. However, for heparin, an additional challenge in its study lies in the development of suitable tethers for the covalent attachment of the carbohydrate. The synthesis of a versatile heparin-PEG-thiol allows facile immobilization to gold surfaces via an Au-S linkage. As shown below, heparin molecules can be modified with a poly(ethylene glycol) (PEG) containing mercapto-terminal group to enable immobilization on a gold substrate and create a functionalized surface.

The morphology of the GAG-functionalized surface is characterized via non-contact mode AFM imaging. The interaction forces of single pairs of heparin and thrombin molecules are determined in PBS buffer using AFM-FS. Control experiments are performed to measure the interaction forces between the heparin surface and bare (no attached thrombin) cantilever. The specificity of the binding interactions is confirmed via the blocking of binding sites on the thrombin molecule with free heparin. Finally, using DFS, the effect of NaCl concentration on the binding kinetics and energy landscape of the heparin and thrombin are studied. The results reveal that the heparin–thrombin complex becomes less stable with the increase of NaCl concentration. AFM-FS coupled with the heparin and thrombin surface functionalization therefore provides a versatile platform for studying the sugar-protein interactions at the molecular scale under different environmental conditions. Indeed, to date, very little is known by way of force interactions of most anticoagulation proteins (thrombin, factor Xa, factor XIa, antithrombin etc.). These findings may therefore offer a new insight into the molecular mechanism of blood (anti)coagulation under applied force or flow conditions, useful in the design and screening of cardiovascular drug candidates. Also, this chapter builds an AFM platform to study the single pair molecular interactions and facilitates AFM-based single molecules detection and mapping on various surfaces.

2.2 Experimental Section

2.2.1 Materials and instrumentation

(1-Mercaptoundec-11-yl) hexaethylene glycol (Oligoethylene glycol (OEG) terminated thiol), $HS-C_{11}-(EG)_6OH$, and (1-mercaptohexadecanoic acid)-N-succinimidyl ester (NHS terminated thiol), $HS-C_{15}COO-NHS$, were purchased from Assemblon Inc. (Redmond, WA) and Nanoscience Instruments Inc. (Phoenix, AZ) respectively. Human α-thrombin was purchased from Hematologic Technologies (Essex Junction, VT). Heterofunctional polyethylene glycol (PEG): $HS-PEG-NH_2$ (MW 1,000) was purchased from Laysan Bio (Arab, AL). Heparin sodium salt (H3393, 17000-19000 Da) was purchased from Sigma-Aldrich (St. Louis, MO). Phosphate-buffered saline (PBS pH 7.4) (11.9 mM phosphates, 137 mM sodium chloride and 2.7 mM potassium chloride), Sodium chloride (biological, certified crystalline) and Ethanol (200-proof) were purchased from Fisher Scientific. Ultrapure water (resistivity 18.2 MΩ•cm) was obtained from a MilliQ water purification system (Millipore Scientific, MA). Gold surfaces were purchased from Agilent Technologies, Inc. (Foster City, CA). Gold coated PPP-CONTCSAu cantilevers from Nanosensors (Neuchatel, Switzerland) and AC240TS cantilevers from Asylum Research (Santa Barbara, CA) were used for force measurement and imaging respectively.

In all experiments described in this thesis, AFM cantilevers were cleaned using an UV/Ozone Procleaner (BioForce Nanosciences Inc. Ames, IA) before use. All AFM imaging and force spectroscopy experiments were performed using an Asylum MFP-3D atomic force microscope (Asylum Research, Santa Barbara, CA). NMR experiments were carried out on a Bruker 400MHz NMR spectrometer (Bruker BioSpin, Woodlands, TX).

2.2.2 Synthesis of heparin-PEG-thiol

10mg heparin sodium was dissolved in 1ml formamide. 12 mg HS-PEG-NH_2 was then added and the reaction was maintained at 50°C for 6 hours. 5 mg aqueous sodium cyanoborohydride was added and incubated at 50 °C for an additional 24 hours. The reaction mixture was diluted with 1 mL of water and dialyzed against 1 L of water for 48 hours using a 3500 Da molecular weight cutoff dialysis membrane. The retentate was recovered and lyophilized. The freshly prepared sample was dissolved in D_2O, and further characterized by ^1H NMR at 400 MHz to verify the formation of the heparin-PEG-thiol. Signals, in part per million (ppm), are relative to the residual peak of the solvent (D_2O, $\delta = 4.79$ ppm).

2.2.3 Functionalized substrate and cantilever preparation

Gold surfaces were rinsed with ethanol several times prior to formation of the mixed thiol SAMs. Functionalized heparin substrates were prepared by a two-step method: (i) incubating the freshly cleaned gold surface in a 1 μM heparin-PEG-thiol aqueous solution for 2 hours at ambient temperature, followed by rinsing with water; (ii) immersing the surface in a HS-C$_{11}$-(EG)$_6$OH ethanol solution overnight (16 hours) followed by rinsing with ethanol. Gold coated cantilevers were cleaned in UV/ozone for 15 minutes. Cantilevers were functionalized by an approach as described earlier [87] - immersion in mixed thiol solution (HS-C$_{11}$-(EG)$_6$OH and HS-C$_{15}$COO-NHS) in ethanol for 16 hours. Cantilevers were then rinsed with ethanol, and incubated in a 100 nM solution of thrombin in PBS buffer for 1 hour at ambient temperature.

2.2.4 AFM imaging of surfaces and dynamic force spectroscopy

Cantilevers were cleaned using high-intensity UV light. Spring constants of functionalized cantilevers were measured prior to each experiment using the thermal fluctuation method [88]. AC240TS cantilevers (k=~2 N/m, resonance frequency f=70 kHz) were used for initially characterizing the heparin attached surfaces in non-contact mode. Regions containing heparin molecules were identified prior to force measurements by non-contact imaging. Subsequently, PPP-CONTCSAu cantilevers (k=~0.2 N/m, f=24 kHz) functionalized with thrombin were used for measurement of interaction forces. Force-distance curves were collected in a liquid environment by moving the tip to different locations, holding on surface for 5 seconds and then retracting it in a repeated, cyclic manner. Several hundred curves were collected for each experiment at different points on the surface. The force of contact was kept <300 pN to avoid damaging the surface heparin and to preserve the functionalized AFM tip. Force curves that showed binding events at rupture lengths between 10-50 nm were selected and analyzed in IgorPro (Wavemetrics, OR). A binding probability was estimated as the ratio of the number of analyzed curves showing binding events to the total number of curves collected in each experiment. Control experiments were conducted to measure the interaction forces using bare cantilevers (PEG thiol/no attached protein) on heparin surface. Blocking experiments were performed by measuring the interaction forces in the presence of free heparin (5µg/ml) in PBS.

By varying the loading rates of the heparin-thrombin interaction, Dynamic Force Spectroscopy (DFS) measurements were conducted from ~10 to ~300 nN/s. The loading rate was accurately determined by estimating the speed of the cantilever at the instant of contact. At each loading rate, several hundred force-distance curves were collected and analyzed to obtain the rupture force histogram. The effect of NaCl on the binding and stability of the heparin/thrombin complex was further investigated using buffers made at varying concentrations of NaCl.

2.3 Results and Discussion

2.3.1 Synthesis and characterization of heparin-PEG-thiol

To measure pair-wise interaction forces, the first step is to covalently immobilize each biomolecule on an AFM probe (cantilever) and a carefully prepared substrate [89]. The receptor and ligand are repeatedly brought in contact with one another and the molecular interaction monitored. Typically, gold-coated substrates present a wealth of possible conjugation chemistries and are widely used. In the case of thrombin, several strategies are available for covalently immobilizing the protein [90]. Here, surface lysines on thrombin were utilized to attach it to a gold cantilever via an NHS linkage. On the other hand, heparin possesses unique challenges in this regard. While heparin is a negatively charged polysaccharide and could hypothetically be electrostatically immobilized to a positively charged substrate, this bond is not strong enough to prevent the molecules being picked up by the probe during retraction [91]. It is therefore necessary to modify the heparin to enable covalent attachment, while preserving its chemical nature. Some reports have discussed the biotinylation of heparin through its un-substituted groups [92]. Here, the heparin was modified using a hetero-bifunctionalpoly(ethylene glycol) (PEG) linker with thiol and amine end group (HS-PEG-NH_2). This creates a versatile heparin conjugate that enables to covalently bind to a gold surface via an Au-S bond (Figure 2.2).

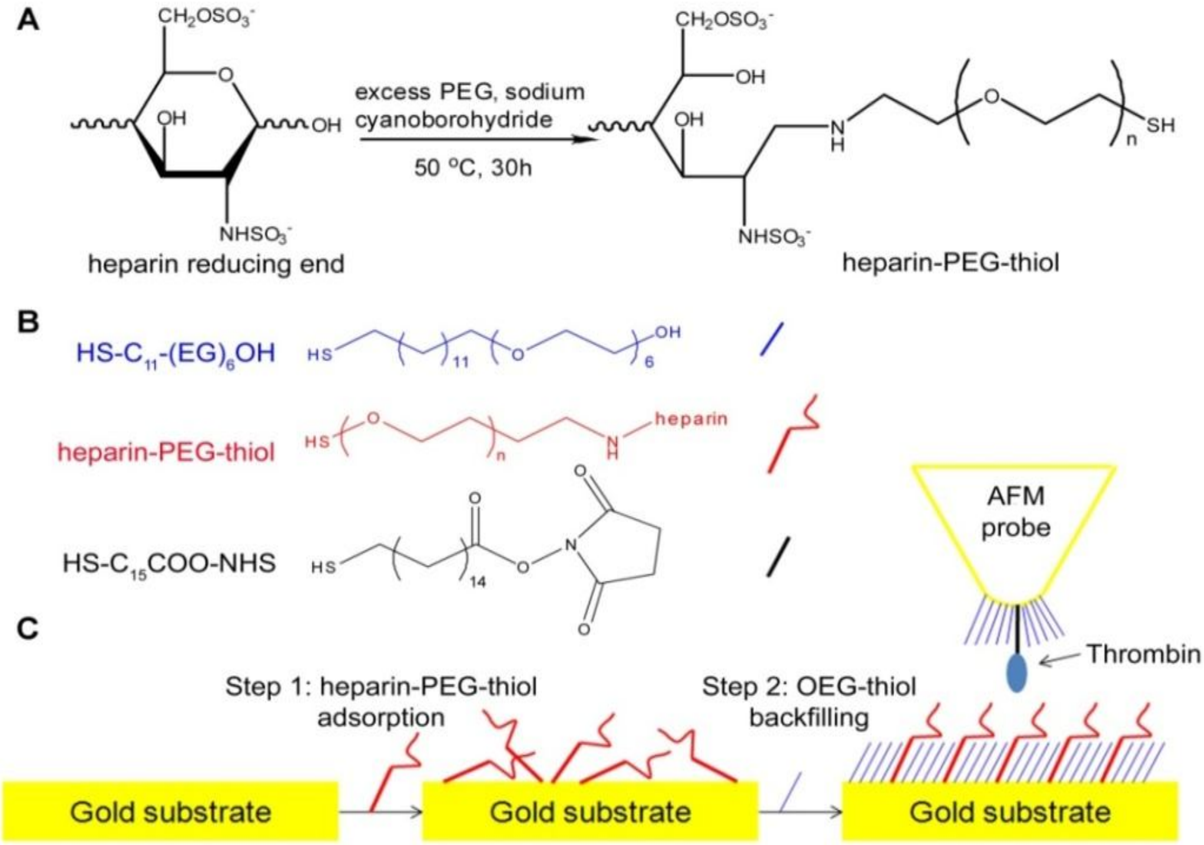

Figure 2.2. (A) Schematic and structure of thiolation of heparin to form heparin-PEG-thiol. (B) Molecular structure of thiols used to form the self-assembled monolayers: $HS-C_{11}-(EG)_6OH$, heparin-PEG-thiol and $HS-C_{15}COO-NHS$. (C) Self-assembled monolayers formed on the gold surface and AFM probe with corresponding adsorption of heparin-PEG-thiol and thrombin on the functionalized substrates.

The sole reducing end of heparin was reacted with the amine group of $HS-PEG-NH_2$ in anhydrous formamide and the imine formed was reduced using sodium cyanoborohydride [93]. This also allows the heparin to retain its core biochemical properties after functionalization. The heterofunctional PEG was selected for its physical and chemical inertness as well as the availability of different terminal functional groups. The PEG further acted as a spacer of controllable length between the biomolecule and the underlying substrate, allowing to enhance bioactivity relative to direct immobilization [94]. This modification method is advantageous because of covalent attachment to the Au-substrate which makes them stable during the force measurement, and also exposes the maximum amount of binding sites on the heparin chain [95]. The selection of the reducing end preserves the chemical nature of the heparin. To verify this and the modification of the heparin with HS-PEG-NH_2, ^1H NMR was conducted. Unmodified heparin, HS-PEG-NH_2 and the product were characterized by comparison of ^1H NMR data:

Heparin (400 MHz, D_2O): δ 2.05 $NHCOC\underline{H}_3$,δ 5.08 IdoA2S, H-1.

HS-PEG-NH_2 (400 MHz, D_2O): δ 2.7 $SHC\underline{H}_2$, δ 3.19 $NH_2C\underline{H}_2CH_2O$, δ 3.7 $OC\underline{H}_2C\underline{H}_2O$.

PEG-labeled heparin (400 MHz, D_2O): δ 2.05 $NHCOC\underline{H}_3$, δ 2.7 $SHC\underline{H}_2$, δ 2.95 $NHC\underline{H}_2CH_2O$, δ 3.42 $NHC\underline{H}_2CH$, δ 3.7 $OC\underline{H}_2C\underline{H}_2O$, δ 5.08 IdoA2S, H-1

Heparin contains a major IdoA2S-GlcNS6S repeating disaccharide unit and minor amounts of GlcA, IdoA, GlcNAc, and GlcNS residues. ^1H NMR of PEG-labeled heparin shows characteristic peaks for heparin (anomeric proton of IdoA2S, and methyl of acetyl in GlcNAc), as well as the signals for PEG (2.7 ppm corresponding to -$C\underline{H}_2$-SH group and 3.7 ppm corresponding to the PEG backbone). The newly formed linkage leads to the reduction of $NH_2C\underline{H}_2CH_2O$ signal at 3.19 ppm, and the increase of $NHC\underline{H}_2CH_2O$ signal at 2.95 ppm. Attachment to amine introduces a new peak at 3.42 ppm, representing the hydrogen on the former anomeric carbon at the heparin reducing end. The NMR spectrum therefore indicates the success of heparin-PEG conjugation (Figure 2.3).

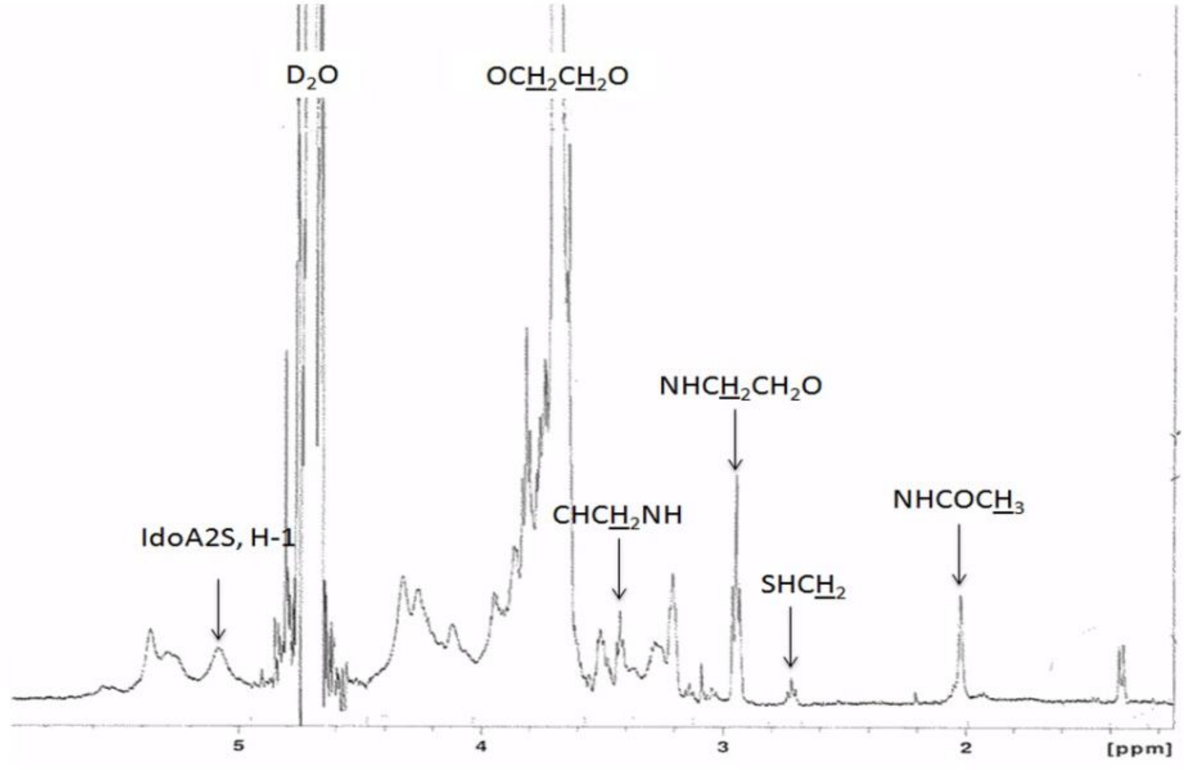

Figure 2.3. ^{1}H NMR analysis of PEG-labeled heparin showed characteristic peaks of heparin (anomeric proton of IdoA2S, and methyl of acetyl in GlcNAc), as well as the signals for PEG (SHC$\underline{H}_2$, and OC$\underline{H}_2$C$\underline{H}_2$O). The newly formed linkage leads to the increase of NHC$\underline{H}_2$CH$_2$O signal at 2.95 ppm and a new peak at 3.42 ppm represents the hydrogen on the former anomeric carbon at the heparin reducing end.

2.3.2 Surface modification and heparin/thrombin immobilization

For biophysical analyses between the heparin and thrombin, a well-characterized mixed self-assembled monolayer (SAM) strategy was used. This platform has been demonstrated to provide an ideal surface to attach well-separated single molecules and study single-pair interactions without the interference of non-specific adhesion [96]. Here, a two-step approach was used to form a surface with covalently immobilized heparin molecules. The heparin-PEG-thiol was first immobilized on a gold surface. This was followed by backfilling of the bare gold area with an OEG thiol (HS-C_{11}-$(EG)_6$OH) (Figure 2.2B and 2.2C). The OEG thiol resists protein adhesion and nonspecific tip-surface interaction, while the sparsely distributed heparins act as reactive sites for thrombin on AFM tips. By carefully regulating the ratio of heparin-thiol to OEG thiol, the heparin density on the substrate is easily controllable.

Figure 2.4A shows a non-contact AFM image of a surface with a typical concentration of immobilized heparin. The morphology of the heparin surface was homogeneous and stable after repeated AFM imaging. The 80 nm line profile across the heparin immobilized surface shows height values for the surface features that correspond well with the cross-section diameter obtained from Small-angle X-ray Scattering (0.9 nm) and the maximum transversal dimensions (1 nm) in the three-dimensional NMR structure of a heparin fragment [97, 98]. It may be noted that the well-separated single heparins demonstrate that the “backfilling” method provided the heparin with appropriate distribution and orientation. Analyzing length of the features shows that most of the heparin molecules have length of 25 nm-35 nm (Figure 2.5), which is consistent with the length estimated from the X-ray scattering data (32 nm contour length for a heparin with 17800 Da and 22 nm for a flexible and mildly bent heparin with 19000 Da) [97, 99]. The different size of the features may result from the heterogeneous length of heparin [100]. As a control, imaging an OEG thiol surface without the heparin-thiol expectedly did not show similar features.

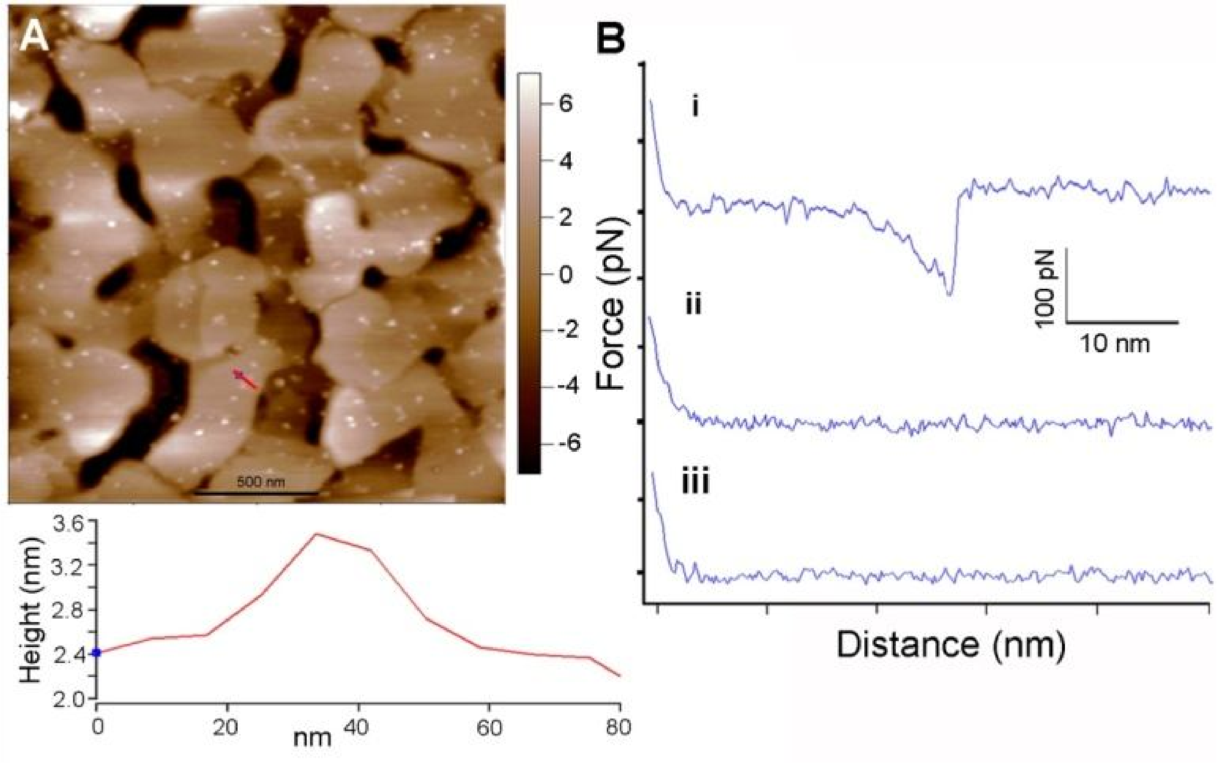

Figure 2.4. (A) AFM topography images recorded in PBS of mixed SAM consisting of heparin-PEG-thiol and OH-PEG-thiol; (B) Typical AFM force–distance curves obtained in the experiments: (i) typical selected retract trace indicating a specific molecular recognition event; (ii) no tip-surface sticking when using the bare AFM tip (no thrombin attached); (iii) in the presence of free heparin in the PBS solution, the force drops to zero.

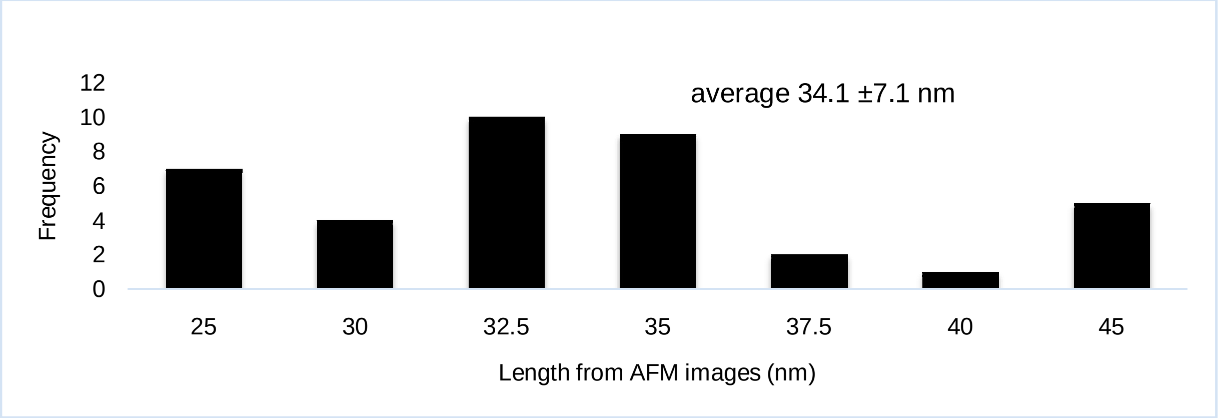

Figure 2.5. Distribution of lengths of heparin molecules as obtained from AFM imaging.

2.3.3 Measurement of heparin and thrombin interaction forces

Subsequent to the imaging, force measurements were conducted with AFM tips functionalized with thrombin on the heparin-attached surface at a loading rate of ~50 nN/s in PBS buffer. Several hundreds of force curves were collected: two sets of experiments (~300 force curves per set) were conducted on two different samples using two different tips. Of these, 19.7 ± 2.0% force curves showing a specific binding event were analyzed to construct the force distribution histogram. These curves classified as specific binding events are manifested in a cantilever deflection observed as a non-linear delayed retraction curve with a different slope as that of the contact region. The typical force-distance curve is shown in Figure 2.4B. In contrast, the force curves with non-specific adhesion show a linear retraction curve with invariable slope [101]. As our group has previously demonstrated, some force curves showing a small tip-surface adhesion were also analyzed because of a clearly discernible interaction event [102]. Approximately 20% of force curves with large non-specific adhesion peaks (>200 pN) were discarded. Overall, the low binding probability and percentage of non-specific adhesion events indicate that the mixed SAM platform is successfully able to modulate the orientation and density of heparin on the substrate, as well as decrease the nonspecific tip-surface interactions, critical for the accurate determination of rupture forces of individual heparin-thrombin binding pairs.

The force distribution histogram for heparin and thrombin rupture force at a loading rate of ~50 nN/s is shown in Figure 2.6B. The distribution of the rupture force between the heparin and thrombin shows a clear, single peak at 102.3±1.3 pN. A few force curves (<4%) shows higher rupture forces, indicating that multiple molecules may be interacting. However, due to the low concentration of heparin and thrombin coupled with the mixed SAM strategy used, we can infer that most of the binding events are due to the single pair of heparin and thrombin. On increasing the concentration of heparin-PEG-thiol, the force distribution histograms show multiple force peaks at ~100 pN, 200 pN and 300 pN, implying that multiple pair interactions are likely to dominate with the increase of heparin density because each thrombin functionalized tip could interact with multiple heparin molecules simultaneously. Previous studies have shown that thrombin binds to heparin chains at least six saccharide units in length (at least 3~4 nm) [31, 99, 103]. Interestingly, by tabulating the rupture distances of all collected force curves and conducting an autocorrelation analysis (Figure 2.7), a periodicity of 5.7 nm is observed which roughly corresponds to the size of the binding pocket of the heparin chain for thrombin. This implies the mechanism that thrombin binds to a remote site on the same heparin chain and then "walks" toward AT to form the ternary 'locked' complex.

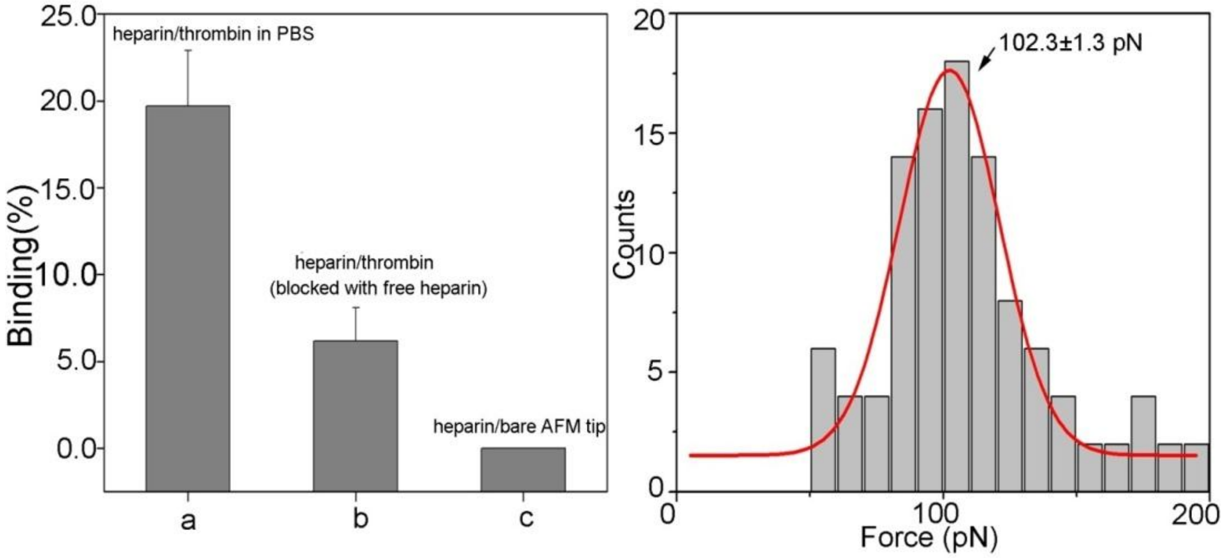

Figure 2.6. (A, left) Comparison of binding percentages for heparin/thrombin interactions with different control experiments: a: heparin on substrate and thrombin on AFM tip; b: heparin on substrate and thrombin on AFM tip in the presence of free heparin; c: heparin on substrate and bare AFM tip (no thrombin attached). (B, right) Histogram showing unbinding force distributions of heparin interaction with thrombin with a Gaussian fit of the data (solid line).

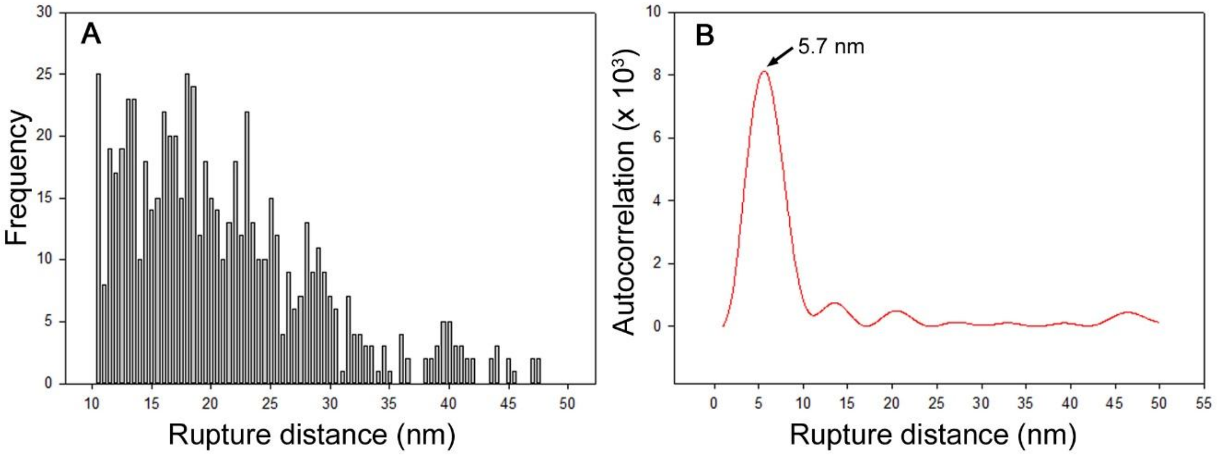

Figure 2.7. (A) Histogram of rupture distances for heparin-thrombin pair. The y-axis represents number of events. Total number of force curves in this analysis = 650. (B) Periodicity was determined from an autocorrelation program written in Matlab. A clear period of ~5.7 nm is observed for the data.

Two different control experiments were carried out to verify that the measured forces were indeed those of the heparin/thrombin interaction. First, a bare Au-cantilever (without attached thrombin) was used to detect the heparin-attached surface. In this experiment, most of the force curves showed zero interaction (Figure 2.4B) with no specific binding events detected. Second, blocking experiments were conducted by measuring the interaction forces in the presence of free heparin. The thrombin-attached tip was first incubated in heparin PBS solution for 30 minutes. Then force curves were collected on heparin-attached surface in the same medium. The binding probability dropped to 6.2 ± 1.9 % as shown in Figure 2.6A.Thus it can be postulated that the binding sites on the tip-attached thrombin are blocked by the free heparin in liquid. The significant decrease of binding probability of these two control experiments compared with heparin/thrombin system in PBS solution demonstrates that the observed interactions between the functionalized cantilever and the surface are likely caused by specific binding between the heparin and thrombin.

2.3.4 Dynamic force spectroscopy (DFS) of heparin and thrombin in PBS

It is widely acknowledged that the specific unbinding forces rely on the intrinsic interactions of molecules as well as on the loading rates. Using DFS, it is therefore possible to transform the AFM to determine useful thermodynamic and kinetic parameters [104]. By evaluating the most probable rupture forces at different loading rates, details of the dissociation dynamics of the heparin–thrombin interaction as well as the energy barriers through dissociation can be calculated. Here, three cases were considered – a single energy barrier, a double energy barrier model with a potential well trough between two interaction barriers, and the recently developed model by Friddle et al. that interpolates between kinetic and equilibrium regimes [104, 105]. The double barrier Bell-Evans model is optimal at high loading rates and is therefore not rightly applicable to the lower loading rate regime, which contains the most interesting information in this study. Many biological systems that show "double-barriers" can be described by a single energy barrier, and the presumed "outer barrier" region simply represents near-equilibrium unbinding regime where the force does not depend on the loading rate. In our experiments as well, the rupture forces were found to linearly dependent on the logarithm of loading rates (Figure 2.8A) over the range investigated implying a single energy barrier. It is important to note that small range of loading rates was chosen keeping in mind physiologically relevant fluid environments, such as during hemodialysis that are relevant to the clotting cascade [106]. For the loading rate range investigated in this study, a simple linear dependence therefore precluded the need to use the model proposed by Friddle et al. [105]. However, as an internal reference, higher loading rates to 400 nN/s were investigated, wherein the force-loading rate dependence is no longer linear. Over this larger range, this model fits the data well (complete analysis shown in Figure 2.9). For this heparin-thrombin system however, it is assumed that a single barrier approach can describe the relevant interactions.

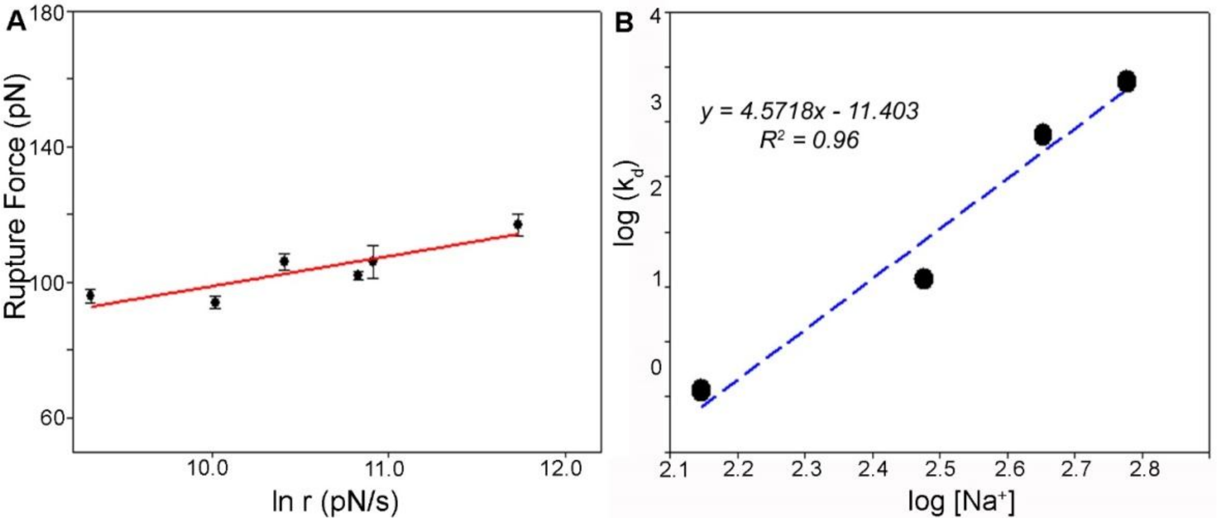

Figure 2.8. Dynamic force spectra of heparin and thrombin interactions at different loading rates in PBS. (A) Fitting the data with the Bell-Evans model yields a simple linear fit. The rupture forces of the complex measured reveal the width of the energy barrier in PBS (x_B) to be 4.6Å, while the off-rate (k_{off}) is 0.04 s^{-1}. (B) log dependence of the k_{off} with the Na^+ concentration shows a linear fit with a slope of 4.57, which corresponds very well with the earlier reported fit of 4.8 [81].

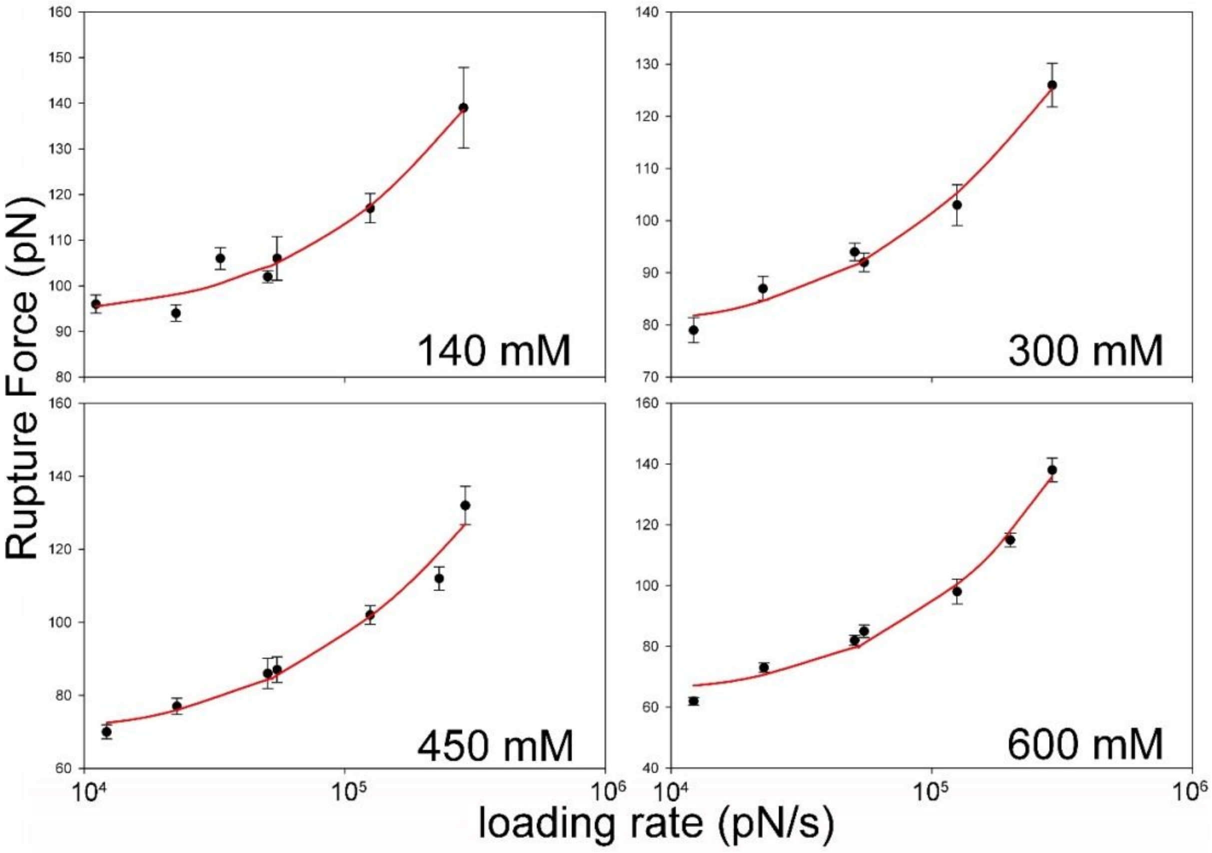

Figure 2.9. Dynamic force spectroscopy at different salt concentrations over a larger loading rate range (to 10^6 pN/s). Data was fit using the model proposed by Friddle et al. (PNAS, 2012). Notice that at lower loading rate regimes, the model approximates the linear fit shown in Figure S2 above, showing that for our experiments, the single barrier model is valid. x-axis is presented in $\log_{10}$.

Based on this fit, kinetic parameters can be extracted using the following Bell-Evans equations described earlier [107]:

$$F = \frac{k_B T}{x_B} \, ln\left(\frac{r x_B}{k_B T k_{off}}\right) \qquad (1)$$

$$f_B = \frac{k_B T}{x_B}\,(\text{slope}) \qquad (2)$$

$$k_{off} = \frac{r_0}{f_B} \qquad (3)$$

where F is the most probable rupture force, k_B is the Boltzmann constant, T is the absolute temperature, r is the loading rate, r_0 is loading rate at zero force, x_B is the distance between bound state and unbound state for the transition state, which can be calculated from the slope of fitting curve. k_{off} is the dissociation rate of bond at zero applied force, which can be calculated as the intercept of the fit. In the case of heparin and thrombin, both k_{off} and x_B are important for evaluating the susceptibility of the bond dissociation to applied force or under flow conditions [108]. Once k_{off} has been determined, the height of the energy barrier, ΔG can be deduced using the following equation according to the transition state theory [109, 110]:

$$\Delta G = -k_B T \ln \frac{k_{off} h}{k_B T} \qquad (4)$$

where h is Planck's constant and $k_B T$ is the thermal energy. The linear fit to the data points in Figure 2.8A indicates that the heparin-thrombin complex overcomes one energy barrier during its dissociation under applied force with a height of 32.80 $k_B T$. The corresponding k_{off} for the heparin-thrombin interaction in PBS was found to be 0.04 s^{-1}. The low k_{off} indicates the formation of a highly stable complex between heparin and thrombin.

2.3.5 Binding as a function of NaCl concentration

Finally, the binding kinetics of the heparin–thrombin interaction were investigated in the presence of salt. This served two purposes – observe the heparin–thrombin energy landscape, and provide an internal reference for this system. Previous study has shown that NaCl has a strong influence on the interactions of heparin–thrombin and the binding of heparin and thrombin can be described by the relationship [81]:

$$\log K_{d,\,obs} = \log K_{d(non\text{-}ionic)} + \alpha \log [Na^+], \qquad (5)$$

where α is related to the number of Na^+ ions released upon charge-neutralization reaction between heparin and thrombin. The negatively charged sulfo/carboxyl groups on the heparin chains can form ion pairs with positively charged residues on thrombin. Initially, the repulsive energy of multiple negatively charged groups in heparin promotes the binding of Na^+ to minimize these forces. When heparin binds thrombin, the positively charged residues interact at the anionic sites to result in the entropically favorable release of Na^+ ions. However, there can also be a significant influence to the binding via H-bonding [111]. The energy of interaction therefore has contributions from the polyelectrolyte effect, H-bonding and hydrophobic interactions. To uncover the specific effect of NaCl on heparin–thrombin interaction at the molecular scale, DFS was applied to study the dissociation kinetics and energy profile under different NaCl concentrations (300 mM, 450 mM and 600 mM). The high salt concentration is used to demonstrate this polyelectrolyte effect. As previously shown in PBS (137 mM NaCl), rupture forces were acquired over a range of loading rates between ~10 nN/s and ~200 nN/s at different NaCl concentrations and plotted as a function of loading rates (Figure 2.10). It can be seen that increasing the NaCl concentration resulted in decreased rupture forces (raw data shown in Table 2.1). The strength of the heparin/thrombin complex therefore becomes *weaker* with an increase of salt concentration. Fitting the forces vs. loading rates reveals that the interactions are compatible with the single energy barrier model (Figure 2.10). The fitted dissociation kinetic parameters of the model are tabulated in Table 2.2 and the sketch of energy profile at different NaCl concentrations are shown in Figure 2.11.

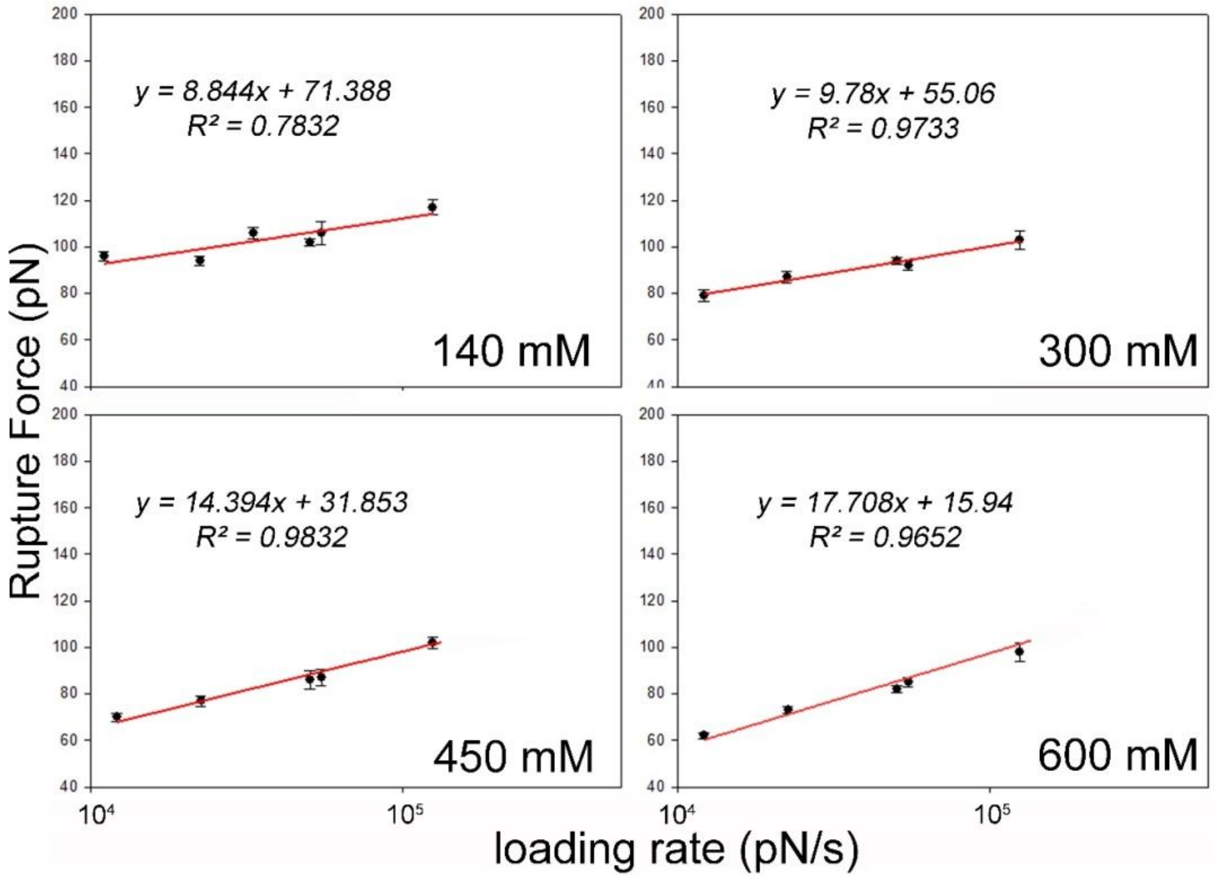

Figure 2.10. Dynamic force spectroscopy at different salt concentrations. Loading rates were varied up to 10^5 pN/s at each salt concentration and a linear fit could be estimated that allowed calculation of k_{off}, x_B and ΔG. x-axis is presented in $\log_{10}$.

Table 2.1. Rupture forces under different loading rates and solutions.

Salt concentration	Loading rates (nN/s)	Mean rupture force (pN)
PBS (137 mM)	11.1	96 ± 2
	22.5	94 ± 1.8

PBS (137 mM)	33.3	106 ± 2.4
	50.6	102 ± 1.3
	55	106 ± 4.8
	125	117 ± 3.2
	285	139 ± 8.8
300 mM NaCl	12.2	79 ± 2.4
	22.5	87 ± 2.3
	50.6	94 ± 1.7
	55	92 ± 1.8
	125	103 ± 3.9
	290	106 ± 4.2
450 mM NaCl	12.2	70 ± 1.9
	22.7	77 ± 2.2
	50.6	86 ± 4.1
	55	87 ± 3.5
	125	102 ± 2.6
	230	112 ± 3.2
	290	132 ± 5.2
600 mM NaCl	12.2	62 ± 1.2
	22.7	73 ± 1.5
	50.6	82 ± 1.6
	55	85 ± 2.1
	125	98 ± 4.1
	200	115 ± 2.3
	290	138 ± 3.9

Table 2.2. Dissociation kinetic parameters and energy profile of heparin/thrombin complex under different conditions.

NaCl concentration	k_{off} (s^{-1})	x_B (nm)	ΔG (k_BT)
PBS (137 mM)	0.04	0.46	32.8
300 mM	0.37	0.42	30.45
450 mM	7.6	0.28	27.42
600 mM	22.96	0.23	26.32

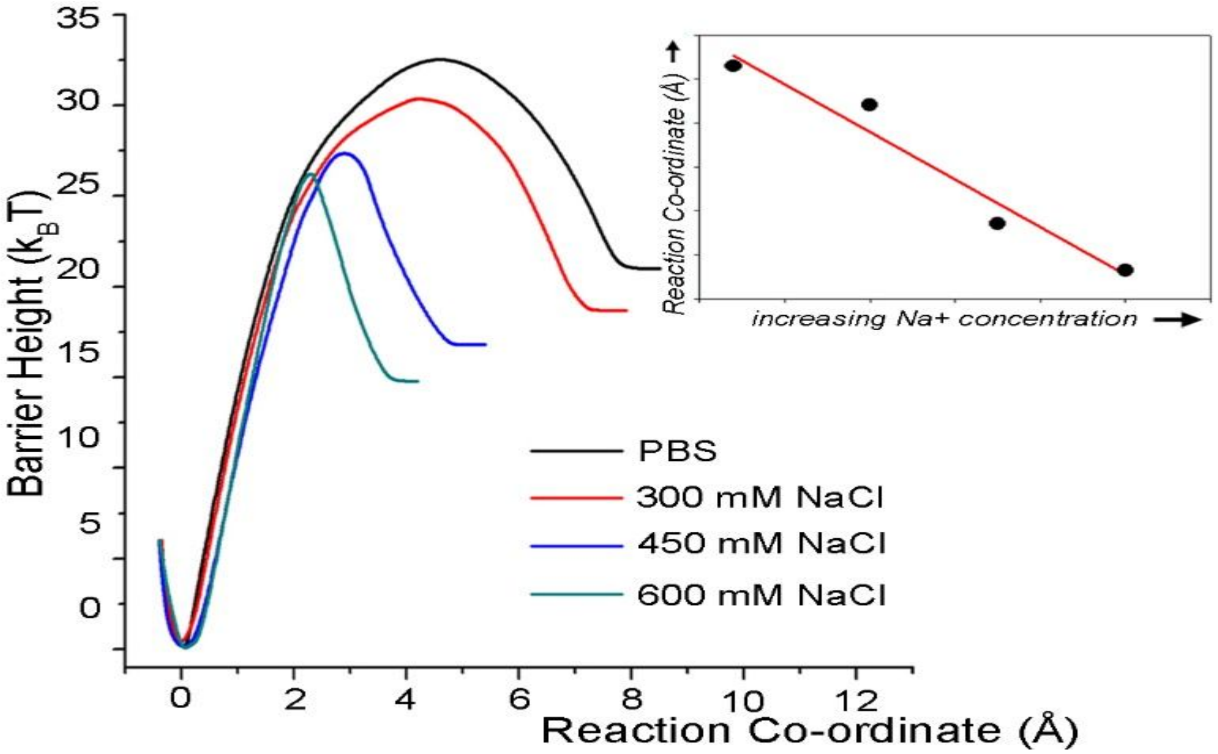

Figure 2.11. Sketches of energy landscapes show intermolecular potential of the heparin/thrombin interactions in PBS with increasing NaCl concentration. The positions of energy barrier together with the height of thermal energies are derived from the linear fit of the dynamic force spectroscopy data. For example, in PBS (black), the x_B and the ΔG are calculated to be 4.6Å and $32.8k_BT$. These parameters characterizing energy landscapes under different conditions are also summarized in Table 2.2. The energy landscapes showed that both the position (Inset) and the height of the interaction energy barrier shifted toward lower values with the increase in NaCl concentration.

The force-spectroscopy results show the predicted (Eq. 5) linear log-dependence in the off-rates vs. [Na$^+$]. The logarithm of the observed k_{off} for the heparin–thrombin interaction is directly proportional to log [Na$^+$] in buffer (Figure 2.8B). Remarkably, the linear fit of the data reveals a slope of 4.6, which is very close to the earlier reported regression fit of 4.8 obtained via fluorescence titrations [81]. This implies that 4-5 ionic interactions are involved in the heparin-thrombin interaction. It can be seen that as the [Na$^+$] increases, the contribution of the polyelectrolyte decreases. Extrapolating this dependence indicates that the binding reflects complete contribution of the non-polyelectrolyte binding at 1.1M salts, which is close to the ideal value of 1 M according to Eq. 1. Indeed, as observed from the energy barrier, an increase in salt concentration is manifested by a shift in the energy landscape(decrease in x_t and ΔG, Figure 2.11). As the double log k_{off} – [Na$^+$] profile is linear, it must imply that the k_{on} is invariant across the range of [Na$^+$]. This result is similar to an earlier DFS study of integrin/ fibronectin interactions [112]. As shown, the energy barrier operates at lower, physiologically relevant forces, which make them more sensitive to the molecular structure or environmental changes.

The energy barrier ΔG decreases as expected with an increase in [Na$^+$], implying that, at a sufficiently high salt concentration, the off-rate is driven by non-ionic interaction. The energy barrier of the heparin – thrombin reaction is kinetically invisible but mechanistically significant. From a loading rate perspective, a shift to lower x_t and ΔG is also observed at faster loading rates. These results therefore show that at higher loading, the nonionic forces between heparin and thrombin, which are highly directional in comparison to ionic forces, can be expected to "*orient*" the thrombin molecule on the heparin chain. Once initiated and established at higher flows, electrostatic forces facilitate the movement of thrombin toward antithrombin along the heparin chain. One can predict that the initial "*orientation*" is such that it favors the formation of the (eventual) productive antithrombin – thrombin complex. A recent computational analysis predicts the occurrence of weak nonionic forces in heparin-thrombin interaction supporting the above conclusion [113].

This analysis revealed that the stability of the heparin/thrombin complex is suppressed by higher salt concentration. This conclusion is consistent with the theory of protein–polyelectrolyte interactions, in which the binding of the complex is reduced with increase ionic strength, due to the screening of electrostatic attractions [114]. Within this framework, the binding of thrombin to heparin in the presence of monovalent cation can be regarded as an ion exchange-type process involving the stoichiometric release of bound counter-ions from negatively charged groups on the heparin polyelectrolyte chain. The binding of thrombin to heparin is therefore not favored when the Na^+ concentration is elevated due to the unfavorable release of Na^+ ions from the polysaccharide into a salt solution [115]. Earlier molecular simulations of heparin–FX06 interaction showed that the electrostatic interaction between heparin and the positively charged FX06 residues was the main contributor for lowering the Gibbs free energy and stabilizing the complex [116]. FX06 is a peptide fragment from fibrin, and its interaction with heparin is closely related to endothelial cell adhesion, spreading and proliferation [117]. Such detailed information can typically not be extracted from bulk kinetic measurements. The single-molecule force spectroscopy study therefore uncovers the nature of the biophysical interactions and helps explains the operation of this fundamental biochemical process.

2.4 Conclusions

In this chapter, a molecular approach was shown to investigate the nature of the heparin-thrombin interaction using AFM-based force spectroscopy and uncover the contributions of the electrostatic and non-ionic contributors to this interaction. As critical components of the blood coagulation cascade, it is important to elucidate these interactions. Here, the focuses are developing a protein-resistant and GAG-functionalized surface for measuring interactions in different liquid environments using dynamic force spectroscopy. The versatile heparin conjugate synthesized here is key to covalent immobilization to Au surfaces, and can be widely applied to several types of interaction analyses and investigations. By changing the NaCl concentration, it was shown that the heparin–thrombin complexes are less stable with increase of NaCl concentration, implying that electrostatic components are the primary contributor to the energy landscape of the heparin/thrombin interaction. In AFM-FS, the dependence of binding on the interaction time (time of thrombin-attached tip contacting with a heparin functionalized-surface) can be used to roughly estimate the association rate constant k_{on}, whereby the dissociation constant K_{off} (k_{off}/k_{on})could be determined [46]. The platform developed in this study coupled with heparin-modified tip (heparin-PEG-SH on gold coated cantilever) also shows the potential to detect interactions with multiple coagulation related proteins (including factor Xa, factor XIa and antithrombin) and elucidate molecular mechanism of blood (anti) coagulation. These insights into the heparin-thrombin interaction from a force and energy viewpoint at the single molecule scale can provide better understanding of the mechanisms of blood (anti)coagulation under applied force or flow conditions. Furthermore, this chapter builds an AFM platform to study the single pair molecular interactions and facilitates subsequent AFM-based single molecules detection and mapping on various surfaces.

[This chapter contains results that have been previously published in:

Wang C, Jin Y, Desai UR, Yadavalli VK, "Investigation of the heparin-thrombin interaction by dynamic force spectroscopy," Biochimica et Biophysica Acta, 1850, 1099-1106, June 2015.]

CHAPTER 3

FORCE RECOGNITION MAPPING OF PROTEINS ON MIXED SELF-ASSEMBLED MONOLAYER SURFACES

3.1 Introduction

As discussed in the previous chapters, AFM is a powerful tool for high precision imaging and sophisticated biophysical investigations [85, 86]. More importantly, due to simple and rapid sample preparation and the ability to manipulate individual molecules, AFM-FS has been used to study various biomolecular systems, including antigen/antibody [118], glycoproteins/carbohydrates [119], integrin/fibronectin [120] and DNA/peptides [121]. These investigations have revealed insights into fundamental biological and biochemical processes, and enabled the development of tools including biosensors and bio-analytical devices [122]. In this chapter, based on the AFM-FS and single molecular approaches, development of techniques to spatially recognize target biomolecules (specific proteins) on model surfaces using single-pair biomolecular interactions are reported.

One of the important challenges in using the AFM is that it is generally unable to distinguish between different or similarly shaped objects of disparate chemical nature based on the topographical image alone. For instance, it is extremely challenging to detect a transmembrane protein embedded in the cell membrane from topography imaging alone. Consequently, there is a clear need to develop methods to spatially probe and identify biomolecules on biosurfaces based on their bioactivity or even their interactions. A recent enhancement to the AFM toolkit has been the integration of imaging and force spectroscopy to facilitate multidimensional data collection about a system. It is now possible to record the adhesion force between the AFM tip and a surface during scanning. Thus, information on topography may be obtained in conjunction with mechanical stiffness or elasticity, or coupled with adhesive forces and other measures of interaction. This powerful enhancement has been adapted for applications including the detection and localization of specific molecular recognition events, as well as for simultaneous topography and force recognition imaging of specific receptors on complex surfaces [34, 35]. Several studies have shown that both structure and function even on soft cell surfaces can be successfully characterized, and that specific proteins on the cell membrane can be localized [123, 124].

Two strategies are adopted in this integrated imaging and force spectroscopy modality. The first collects the maximum adhesion in addition to *z*-height at each point *during* the retraction of the force scan. While this mode of data collection leads to faster analysis, it often requires the use of special hardware [125]. A second technique called “adhesion force recognition mapping” (AFRM) using biomolecular interaction forces, has been developed from AFM-FS. This allows the detection of targets or recognition sites on biosurfaces with piconewton force sensitivity and nanometer spatial resolution without the use of supplementary hardware [12, 126, 127]. An array of force curves on an area is collected with a biofunctionalized AFM tip. The unbinding forces of all force-distance traces can then be combined with their corresponding surface coordinates, allowing display in the form of a “map”, simultaneously showing the position of specific biomolecules and their adhesion. Using the force interaction data, it is then possible to pinpoint specific molecules on surfaces [12, 128].

Typically, antibodies have been the commonly used biomolecules for functionalizing AFM tips owing to their specificity to various targets [37-40]. However, there are two primary disadvantages of using antibodies as bio-probes, especially for combination imaging and force spectroscopy. First, antibodies are relatively large and their structures tend to expand the AFM tip, compromising spatial resolution. Second, controlling the orientation of the antibody attached to the tip is difficult owing to the number of available surface lysines [129]. There is therefore a great need to find other biomolecules capable of functioning as bio-probes for AFRM. An attractive alternative is presented by the use of aptamers: small, stem-loop single-stranded synthetic DNA/RNA oligonucleotides, whose affinity and specificity is comparable to those of antibodies towards their targets. Aptamers are selected by an evolutionary selection process, which allows the synthetic creation of sequences with exquisite recognition to a wide variety of targets including proteins and small molecules [41, 42]. In contrast to antibodies, aptamers are small and chemically stable. Moreover, commercially customized aptamers can be modified with functional groups at their ends, facilitating easy attachment to AFM tips. For instance, a thiol functionalized aptamer can attach to a gold-coated tip via Au-S covalent bonds with a controllable orientation. Various groups including our group have previously demonstrated the usefulness of aptamers for single molecule biophysical studies [130-132].

To date however, only a few studies have focused on spatial localization or surface mapping using aptamers as the bio-probes. Lin et al. [133] performed AFM-based “dynamic recognition imaging” of IgE molecules attached to a mica substrate using its DNA aptamer. However, this recognition mapping required specialized hardware. Boyd et al. [134] mapped the placement of oligonucleotides on a surface using complementary oligonucleotides. However, the ability of aptamers to be used as bio-probes applied in the adhesion force recognition mapping strategy for the detection of single molecules on surfaces with demonstrated *specificity* and *selectivity* remains unanswered. Here, aptamers as ultrasensitive molecular recognition elements is demonstrated, and how surfaces may be mapped using AFRM to locate and identify target molecules is shown. Specifically, DNA aptamers are used as versatile bio-probes to enable adhesion force mapping of proteins at the molecular level. Two different pairwise systems are demonstrated in this mapping system - human α-thrombin with its DNA aptamer, and vascular endothelial growth factor ($VEGF_{165}$) and its DNA aptamer. The choice of these two structurally distinct proteins is dictated by their importance in glycan chemistry and the coagulation process. Heparin binds to the anion-binding exosite on human α-thrombin [135, 136], and $VEGF_{165}$ also contains a heparin binding domain [137]. This allows to simultaneously investigate their response to external heparin in solution.

The capability of spatially and temporally localizing specific binding sites on the surface *via* simultaneous topographic and force information provides unique advantages. The consistency between the spatial and force map shows that aptamers are valuable potential tools for the detection of specific target molecules on biosurfaces at an ultrasensitive level. In addition, it is possible to visualize real-time changes in interactions as external environmental conditions are altered. Combined with different immobilization strategies or nanografting lithography, different interactions can be detected in specific regions with high lateral resolution at the nanoscale, thereby providing a high-throughput technique to study aptamer or protein arrays or for screening molecules of interest on complex (cell) surfaces.

3.2 Experimental section

3.2.1. Materials and instrumentation

(1-Mercaptoundec-11-yl) hexaethylene glycol (Oligoethylene glycol (OEG) terminated thiol), HS-C_{11}-$(EG)_6$OH, and (1-mercaptohexadecanoic acid)-N-succinimidyl ester (NHS terminated thiol), HS-C_{15}COO-NHS, were purchased from Asemblon Inc. (Redmond, WA) and Nanoscience Instruments Inc (Phoenix, AZ) respectively. Phosphate-buffered saline (PBS pH 7.4) (11.9 mM phosphates, 137 mM sodium chloride and 2.7 mM potassium chloride) and Ethanol (200-proof) were purchased from Fisher Scientific. Molecular Biology Grade DNase free water (Fisher Scientific, Pittsburgh, PA) was used for all experiments. Gold surfaces were purchased from Agilent Technologies, Inc. (Foster City, CA). Gold coated PPP-CONTCSAu cantilevers from Nanosensors (Neuchatel, Switzerland) and AC240TS cantilevers from Asylum Research (Santa Barbara, CA) were used for force measurement and imaging respectively. DNA aptamers with a 5′-dithiol S-S modifier and a $(CH_2)_6$ spacer with RNase free HPLC purification (Table 3.1) were custom synthesized by Integrated DNA Technologies Inc (Coralville, IA). Human α-thrombin was purchased from Hematologic Technologies Inc (Essex Junction, VT). $VEGF_{165}$ was purchased from BioVision Inc (San Francisco, CA). Heparin sodium salt was purchased from Sigma-Aldrich Inc (St. Louis, MO).

Table 3.1. Sequences of the aptamers used in this study.

Identification	Sequence
thrombin aptamer [138]	5′ - TTTTGGTTGGTGTGGTTGG -3′
$VEGF_{165}$ aptamer [139]	5′ - CCGTCTTCCAGACAAGAGTGCAGGG-3′

3.2.2. Functionalized substrate and probe preparation

Gold surfaces were rinsed with ethanol several times prior to formation of the mixed self-assembled monolayers (SAMs). Functionalized SAMs were prepared as described earlier [87]. Freshly cleaned gold surfaces were incubated in a 1mM mixed thiol solution in ethanol for 20 hours at room temperature. The molar ratio of the NHS thiol to the OEG thiol was kept at 1:10000 to obtain sparse distribution of binding sites for protein immobilization. After formation of the mixed SAM, the surfaces were washed with ethanol, and incubated in a 5.5 nM solution of human α-thrombin or13 nM solution of $VEGF_{165}$ in PBS buffer for 1 hour at room temperature. Following incubation, the surfaces were washed with PBS buffer to remove any unattached protein, and placed in a fluid cell containing 500 µl of PBS for AFM imaging and force mapping. Gold coated cantilevers (PPP-CONTCSAu) were incubated with 5 µM 5´-thiol modified human α-thrombin DNA aptamer or the $VEGF_{165}$ aptamer in PBS buffer for 1 hour to obtain aptamer-functionalized AFM tips.

3.2.3. AFM imaging of surfaces and force mapping

Spring constants of functionalized cantilevers were measured using the thermal fluctuation method [88]. AC240TS cantilever (spring constant ~2 N/m, resonance frequency 70 kHz) were cleaned using high-intensity UV light to remove organic contamination and used for imaging and characterization of the surfaces in non contact mode. Subsequently, Au-coated cantilevers (spring constant ~0.2 N/m, resonance frequency 24 kHz) functionalized with the DNA aptamers were used to map the surfaces with attached protein and obtain adhesion data. Each experiment was repeated at least 3 times to demonstrate reproducibility. For instance, three different aptamer-functionalized tips were used to map three different thrombin surfaces. The surface traces shown are representative results from one experiment. In contrast to conventional force-distance collection, a strategy of force mapping was used for these experiments. Regions containing protein molecules were identified prior to force mapping by non-contact imaging. Force-distance curves were obtained by moving the tip to these locations and collecting a series of sequential force curves in an $m \times n$ grid. Each force curve was obtained at the same loading rate (200 nN/s) by pressing the cantilever to a low trigger point (300 pN), allowing binding to occur, and then retracting.

All force maps were obtained by collecting 50×50 force curves over a defined area (500 nm×500 nm), estimating the unbinding force values, and displaying these values by scale of color. The height maps of the same area were generated simultaneously as the force mapping occurred. Blocking experiments were performed by a buffer exchange of PBS containing 5µg/ml heparin in the fluid cell followed by force mapping. As control experiments, a thrombin DNA aptamer-modified tip was used to map the $VEGF_{165}$ attached surface. Inversely, a $VEGF_{165}$ DNA aptamer-modified tip was used to map a surface with attached thrombin. All procedures including the overlays of height map and force map were performed using custom routines in Igor Pro 6.22 A (Wavemetrics Inc, OR). Force curves were analyzed automatically using a custom written “Pulloff Program” which allowed for very fast processing of data.

3.3 Results and Discussion

The key requirement of force spectroscopy lies in the immobilization of biomolecules on surfaces with appropriate distribution and orientation [130, 140]. A direct approach to confirm immobilization is to image the surfaces before and after the process at high spatial resolution and under physiological conditions [141]. However, often, the topography is not enough to verify the biomolecules themselves, their bioactivity or their interactions. Here, the exquisite molecular recognition of aptamer “chemical antibodies” against protein targets via attachment to AFM cantilevers are utilized to spatially identify specific targets. While the use of aptamers to “recognize” surface proteins was shown earlier [133], here a more facile technique is reported. This method allows mapping of a surface coupling the chemical sensitivity of the aptamer with a high spatial resolution and does not require specialized hardware. This strategy follows the force recognition mapping strategy discussed above, wherein the surface is scanned with a specific aptamer. The binding of the aptamer to its target is indicated by small changes in the pattern of oscillation as the probe is scanned over the surface [133, 142]. A large number of force-distance curves can be rapidly collected over a specified area, and a map of these adhesion/rupture forces (a force volume map), superimposed on the topographic image indicates where the targets are located. In these experiments, the interactions of aptamers against surfaces populated with their targets as well as surfaces populated with different targets are studied to demonstrate their specificity. Also, how binding events attenuated by blocking for instance, result in different force maps, clearly show how real-time processes can be tracked on biosurfaces.

3.3.1 Mixed self-assembled monolayers on gold surface and immobilization of human α-thrombin and $VEGF_{165}$

Mixed self-assembled monolayers (SAMs) synthesized *via* co-adsorption from solutions containing mixtures of thiols have been demonstrated as a useful platform for the study of single proteins by incorporating properties from different thiol molecular species [36]. In this study, a mixed thiol system consisting of two thiols- OEG-terminated thiol, along with an NHS-terminated thiol was used to covalently immobilize single proteins on gold. The OEG-terminated thiols resist protein adsorption, while the sparsely distributed NHS-terminated thiol act as reactive sites for lysine residues on proteins. The surface prior to protein immobilization did not show any particles or clusters, thereby verifying the flatness and uniformity of the mixed SAM (Figure 3.2a). Figure 3.1a shows a non-contact AFM image of the mixed SAM surface after incubating in human α-thrombin. The particle features indicate that the proteins are immobilized on the mixed SAM successfully. A control experiment was conducted to verify that the proteins were immobilized by the NHS-terminated thiol. Figure 3.2b shows AFM image of a gold surface with only OEG-terminated thiol after incubation with thrombin as a representative protein. In contrast to the mixed thiol surface, the OEG-terminated thiol surface did not show any particles after protein incubation, implying the proteins on mixed thiol surface were immobilized by NHS end groups of thiol. The well separated single proteins also show that the OEG-terminated thiols further provide an inert background to decrease nonspecific protein adhesion, making the surface amenable to biophysical analyses.

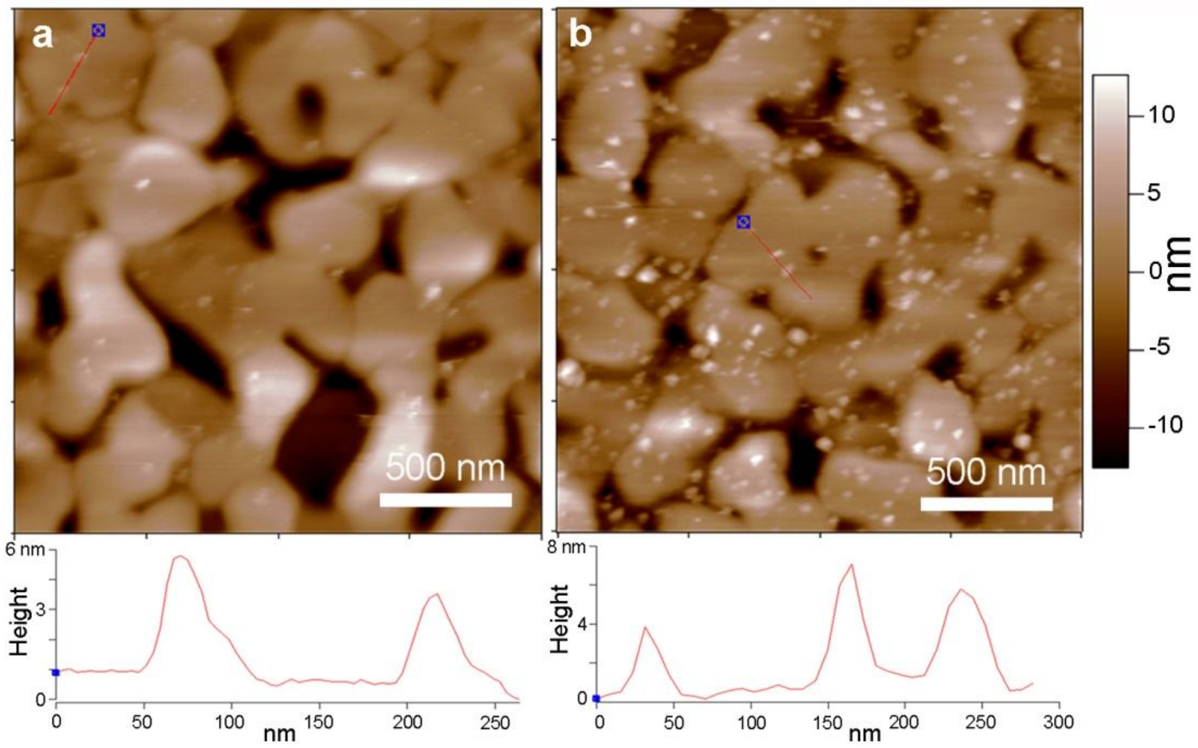

Figure 3.1. AFM images of the two surfaces investigated in this study. Both proteins are chemically attached to a mixed self-assembled monolayer. (a) Surface with immobilized thrombin molecules. (b) Surface with immobilized VEGF$_{165}$ molecules. The image is shown at a higher concentration than (a) to demonstrate the ability to control distribution of surface proteins. Height profiles below show single protein molecules on the gold terraces.

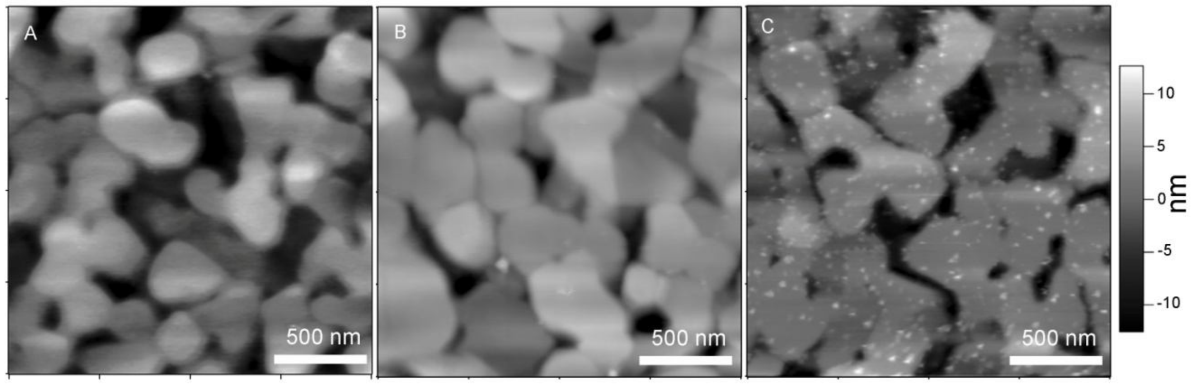

Figure 3.2. AFM images of the three surfaces investigated in this study. (a) Surface of mixed thiol self-assembled monolayer (OGE-terminated thiol and NHS-terminated thiol) prior to protein incubation . (b) Surface of OEG-terminated thiol after protein incubation and washing. (c) Mixed thiol self-assembled monolayer surface with immobilized thrombin molecules (thrombin concentration 18 nM).

Figure 3.1b shows a non-contact AFM image of mixed-SAM surface modified with attached $VEGF_{165}$. As expected, the morphology of the $VEGF_{165}$ surface is homogeneous and stable during repeated AFM scanning. The protein concentration is a critical parameter for protein immobilization and is controllable. In initial experiments, higher protein concentration were observed to lead to higher protein densities on mixed SAM surface (Figure 3.2 c). As reported, a higher particle density observed is due to a higher starting concentration of $VEGF_{165}$. The distribution of height values observed, results from the different lysine binding sites on proteins resulting in different configurations of immobilized proteins. From an analysis of their structure, $VEGF_{165}$ (pdb: 2VPF) and human α-thrombin (pdb: 1HAP) monomer contain 12 and 21 lysine residues respectively, which are almost evenly distributed on each surface [143]. Therefore, the proteins may be immobilized by their lysine residues at different locations in a variety of configurations. The height values shown in the $VEGF_{165}$ line profile, ranging from 4-8 nm are further consistent with dimensions obtained using X-ray crystallography (4.5×6.8×8.6 nm) [144]. Similarly, line profiles for thrombin surfaces show feature heights around 4 nm, corresponding well with X-ray crystallography data (4.5×4.5×5.0 nm) [145]. For both proteins, the width and length dimensions are slightly larger owing to the expected tip-broadening effect, whereby the convolution of the AFM tip tends to give an overestimation of particle size [146]. In these experiments, the use of sharp tips reduces this disparity. It is noted that while different approaches can orient proteins, many of them involve several modification steps [12, 147]. Here, use of a facile and established mixed SAM linking strategy results in a low background and well-separated molecules of thrombin and $VEGF_{165}$. Further, by using flexible spacers attached to aptamers and conducting statistical analysis of several hundred force curves, the effect of inhomogeneous protein orientation is minimized in our experiments [84].

3.3.2 Force mapping on protein-attached surfaces by aptamers

Subsequent to imaging, force mapping was conducted with the cantilever functionalized with thiol modified DNA aptamers. Figure 3.3 shows a surface with VEGF$_{165}$ probed using a VEGF$_{165}$ DNA aptamer. It is important to note that the height map and force recognition map are obtained simultaneously on the same area allowing overlay as shown. Excellent correspondence can be observed between the molecules in the height map and a simultaneous increase of the adhesion force at the same positions. The low adhesion background forces indicates that OEG-terminated SAM is able to decrease the nonspecific tip-surface interactions, critical for the accuracy of force recognition mapping. To verify the applicability of force recognition mapping strategy used as a general tool, a second system involving human α-thrombin and its specific DNA aptamer was studied by the same approach. Figure 3.4 shows a uniform distribution of the thrombin, wherein, features observable in the height map also reveal a correspondingly strong adhesion. The good correlation between the force map and height map provides a clear evidence that the force recognition mapping could be a valuable tool to detect single proteins on surfaces *via* the specific interactions of proteins and their pairwise DNA aptamers. The low adhesion force background on other areas further demonstrates mixed-SAMs as a reliable platform to reduce the nonspecific adsorption of proteins and study them individually.

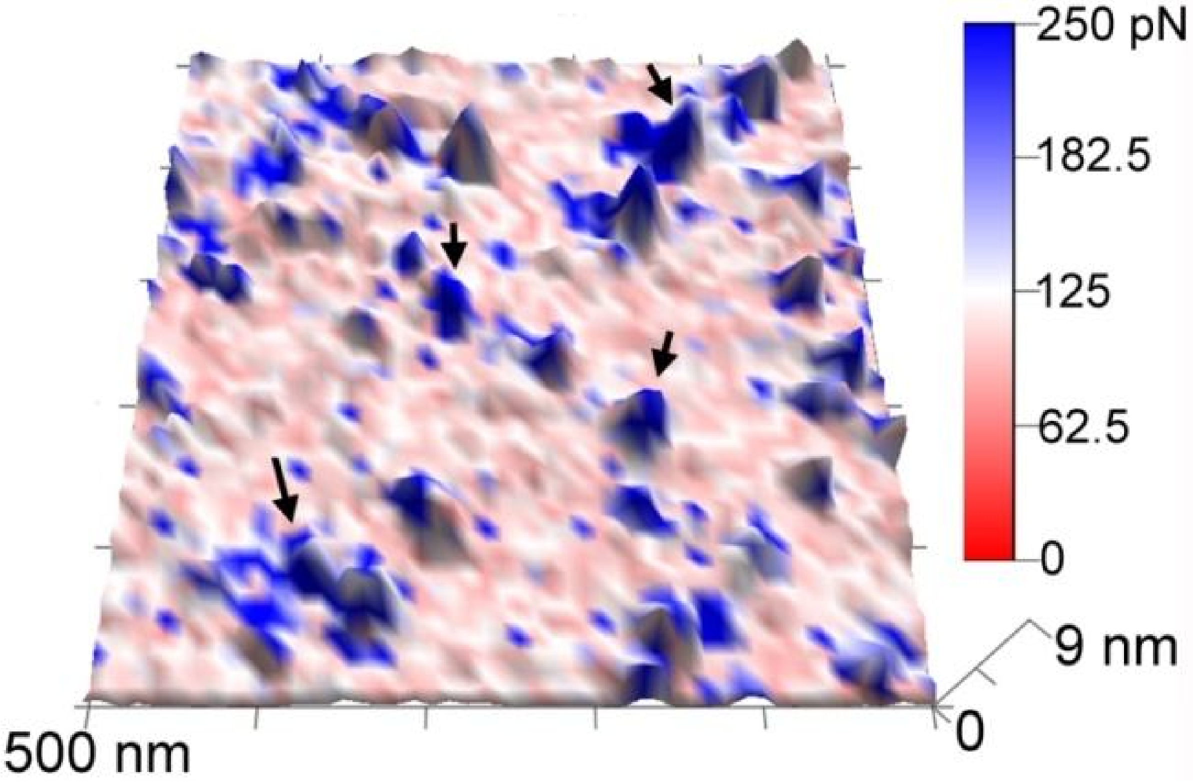

Figure 3.3. Surface maps showing simultaneous height and interaction. VEGF$_{165}$ is immobilized on a surface probed with a VEGF$_{165}$ aptamer. Overlay of the adhesion force on the height indicates the proteins correlate well with higher adhesion force areas (marked by black arrows). Some blue spots reflecting non-specific adhesion are seen on the surface.

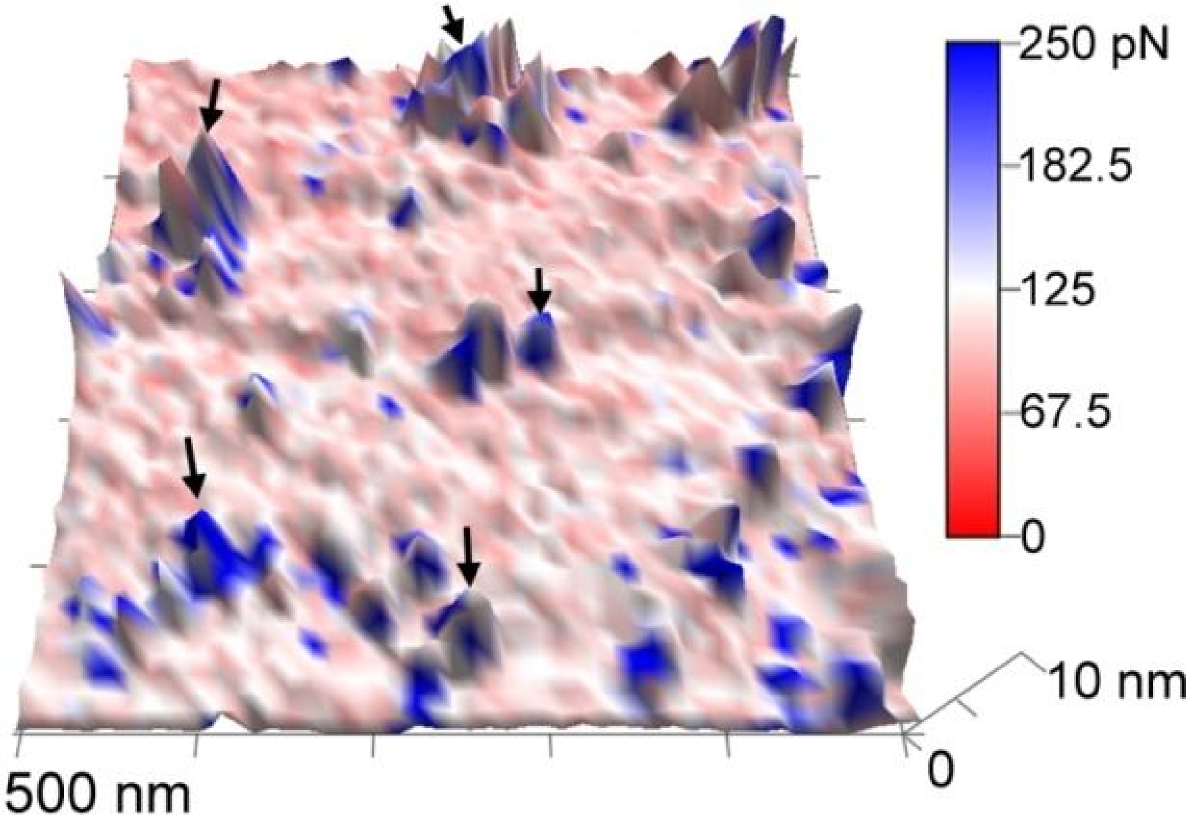

Figure 3.4 Surface maps showing simultaneous height and interaction. Thrombin is immobilized on a surface probed with a thrombin aptamer. Overlay of the adhesion force on the height indicates the proteins correlate well with higher adhesion force areas (marked by black arrows). Some blue spots reflecting non-specific adhesion are seen on the surface.

Some earlier works have also shown the potential of adhesion force mapping for detecting specific recognition sites on biosurfaces. For instance, Andre et al. [148] performed adhesion force mapping on living *Lactococcus lactis* cells to detect specific peptidoglycans. The force maps combined with topographic images demonstrated the peptidoglycans were arranged as lines running parallel to the short cell axis. However, the height map and force map are obtained separately, which tends to be time-consuming and makes it difficult to evaluate the accuracy of the force mapping. One of significant advantages of the force recognition mapping strategy described here is the simultaneous collection of both force and height data. This imaging modality allows overlay of the force map on the height map which clearly shows the locations of the proteins correlate well with areas showing higher adhesion forces (red areas). Consequently, it is easy to test the recognition accuracy from the overlay of height map and force map. As a quantitative measure of this accuracy, a “false hits” parameter is calculated, which is defined as the ratio of spots showing a high adhesion force with no corresponding topographic feature. The $VEGF_{165}$-$VEGF_{165}$ aptamer system (Figure 3.3) and the thrombin-thrombin aptamer system (Figure 3.4) showed 9% and 8% respectively of false hits. Overall, the different areas detected by the two aptamer functionalized probes showed <10% of false hits and >90% accuracy in finding correlations between adhesion and topographic features showing the high accuracy of force mapping approach used.

Two control experiments were carried out to confirm the specificity of the pairwise aptamer-protein interaction. This was checked by investigating each aptamer with the other protein. First, a cantilever with an attached thrombin DNA aptamer was used to probe a surface with attached $VEGF_{165}$. While topographic features were captured, most of the high features in height map do not show corresponding high adhesion force in force map. Second, a cantilever with an attached $VEGF_{165}$ DNA aptamer was used to probe a surface with attached thrombin. Similarly, most molecules do not give rise to corresponding adhesion areas on the same positions. In these control experiments, the accuracy of the surface probing was quantified by looking at the number of adhesion events that do not correspond to height features (false hit). The values of false hit for the $VEGF_{165}$/thrombin DNA aptamer (Figure 3.5c and 3.5d) and thrombin/$VEGF_{165}$ DNA aptamer (Figure 3.6c and 3.6d) systems are 15% and 25% respectively. These numbers are somewhat higher because the adhesion forces here may be caused by some degree of non-specific charge interactions between negatively charged aptamers and the proteins, which are not due to the sequence-specific interactions, consistent with earlier reports [149]. However, overall across our experiments and the controls, the excellent correlations between height and force map show a high degree of sequence-specific interactions between the proteins and its pairwise aptamers. Given the availability of specific DNA aptamers for a variety of targets, this increases the versatility of this technique for high efficiency and high accuracy force recognition mapping.

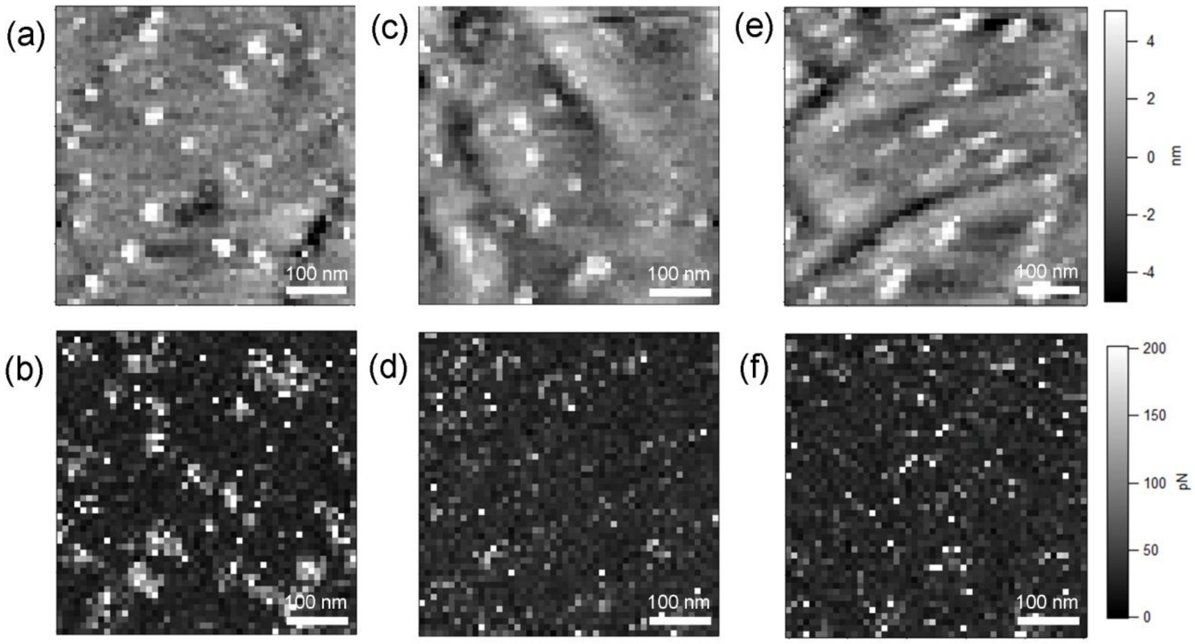

Figure 3.5. Simultaneous height (a,c and e) and adhesion maps (b, d and f) for the $VEGF_{165}$ studied with its corresponding DNA aptamer. (a)(b) Height map and adhesion force map of $VEGF_{165}$ probed with $VEGF_{165}$ DNA aptamer. (c)(d) Control experiment: Height map and adhesion force map of $VEGF_{165}$ probed with thrombin DNA aptamer. (e)(f) Blocking experiment: height map and adhesion force map of $VEGF_{165}$ probed with $VEGF_{165}$ DNA aptamer in the presence of free heparin that blocks DNA binding sites.

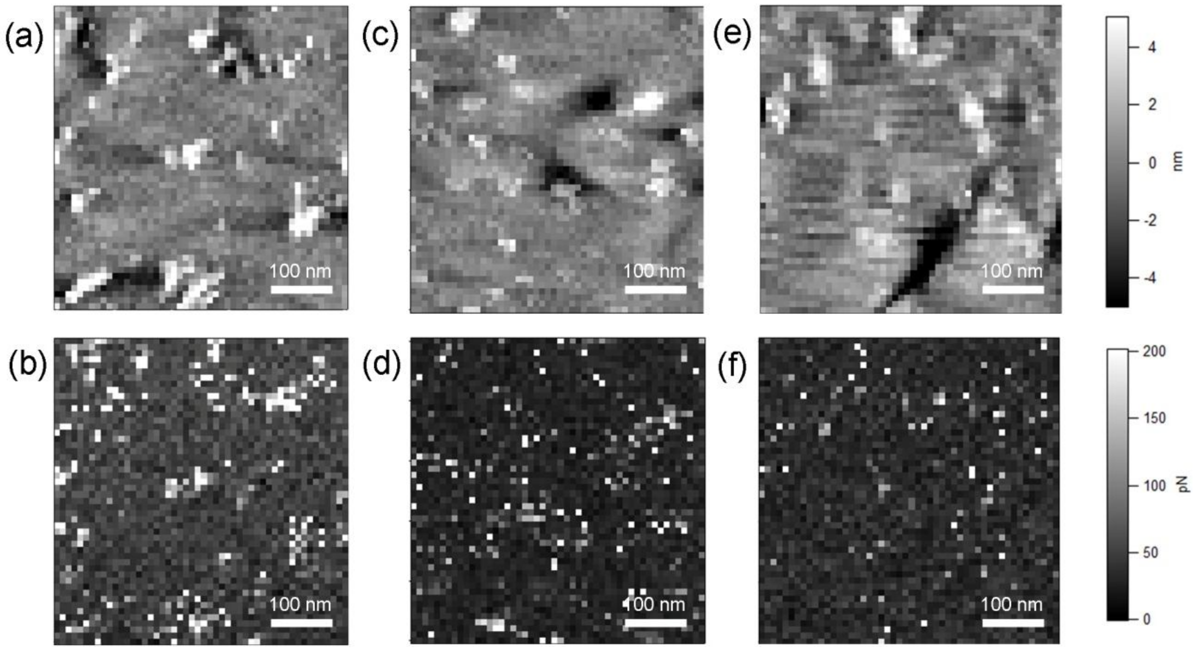

Figire 3.6. Simultaneous height (a,c and e) and adhesion maps (b, d and f) for the thrombin on a surface studied with its corresponding DNA aptamer. (a)(b) Height map and adhesion force map of thrombin probed with thrombin DNA aptamer. (c)(d) Control experiment: Height map and adhesion force map of thrombin probed with VEGF$_{165}$ DNA aptamer. (e)(f) Blocking experiment: height map and adhesion force map of thrombin probed with thrombin DNA aptamer in the presence of free heparin that blocks DNA binding sites.

3.3.3 Force analysis in force recognition mapping

The AFRM approach not only provides a visual representation of the spatial location of interactions but also a quantitative picture of the pairwise interactions. In these experiments, 2500 curves were collected over a 500 nm^2 surface area. Force curves were analyzed automatically using a custom algorithm that can rapidly process data to differentiate the specific binding and non-specific interaction and determine the values of binding forces. Typical AFM force–distance curves (retraction traces) obtained in the experiments are shown in Figure 3.7. As expected, no adhesion forces are observed when the tip encounters the OEG SAM (background) surface. Curves classified as specific binding events are manifested in a cantilever deflection observed as a non-linear delayed retraction curve with a different slope as that of the contact region [102].

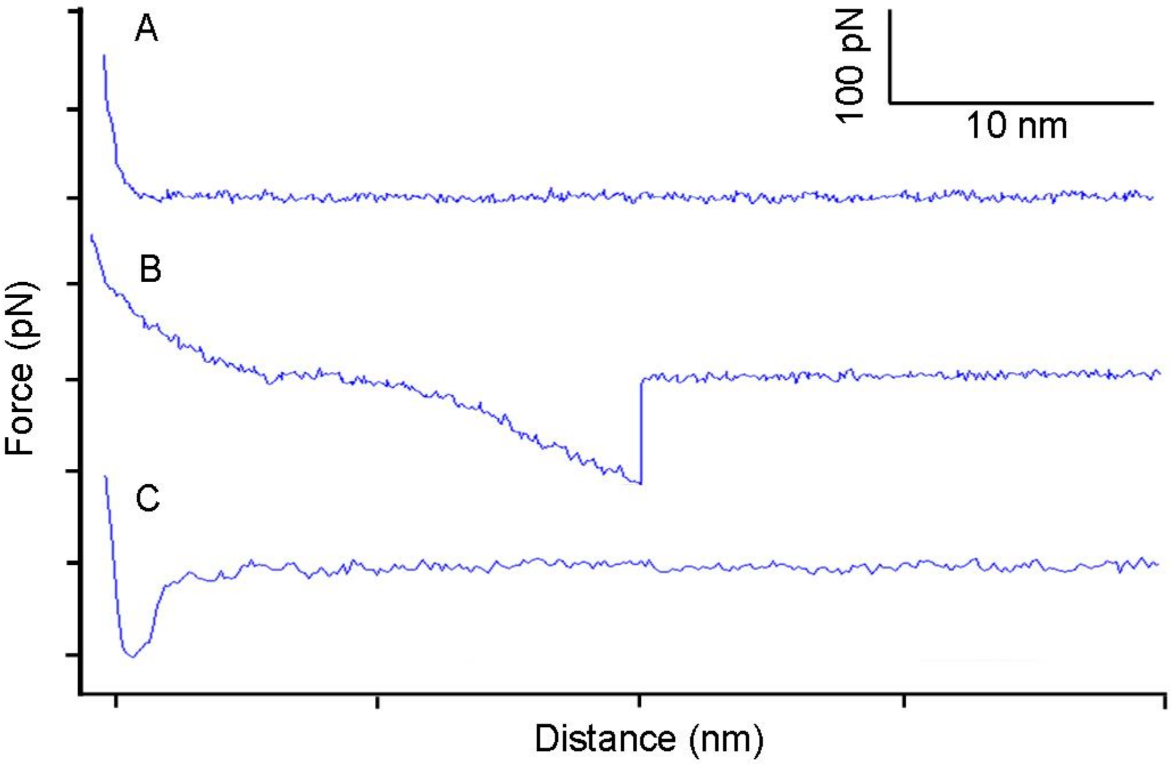

Figure 3.7. Typical AFM force–distance curves (retraction traces) obtained in the experiments: (A) No tip surface adhesion when the tip encounters the OEG SAM on the surface (B) typical selected traces indicating a molecular recognition event and (C) few traces showed a non-specific adhesion force in control experiments (thrombin/VEGF aptamer or VEGF/thrombin aptamer).

The force distribution histogram for VEGF$_{165}$ and its aptamer at a loading rate of 200 nN/s is shown in Figure 3.8A. The distribution of the rupture force between the VEGF$_{165}$ and its aptamer shows a clear single peak at 99.0±4.3 pN. The absence of higher force peaks further confirms a single pair recognition between VEGF$_{165}$ and its aptamer. Similarly, the distribution of the rupture force between the thrombin and its aptamer shows a single peak at 82.5±2.5 pN (Figure 3.9). The typical rupture force values of both systems are 90.0±10 pN at a loading rate of 200 nN/s, consistent with our previously reported values [84]. The rupture force between $VEGF_{165}$ and its RNA aptamer is around 100 pN at the loading rate from 25 nN/s to 270 nN/s. Jiang et al. [150] measured the adhesion force between IgE and its aptamer using AFM-based force spectrocopy. The rupture force of 160±29 pN at the loading rate range from 80-210 nN/s is at a comparable order of magnitude with our results. This level of specific adhesion force is also well within the range of 35-165 pN that has been reported as the estimated range of force required to rupture a single antigen-antibody complex [118], which implies that the DNA aptamer has a great potential to be a bioprobe with high selectivity and binding affinity. In a recent study, the rupture force between a protein (protein tyrosine kinase 7) and both its aptamer and its antibody was measured using AFM-based force spectroscopy on cell surface [151]. The similar force values indicates that DNA aptamer interactions with proteins can be as robust as those of antibodies. However, the range of targets for aptamers, their chemical stability and small size offer distinct advantages. Overall, ~9% and 13% of the curves on thrombin and $VEGF_{165}$ attached surfaces showed binding events (Figure 3.8B). These low binding percentages, which result from the low protein concentration and mixed SAM strategy for separated protein immobilization, imply that the dominant events represent single protein-aptamer binding.

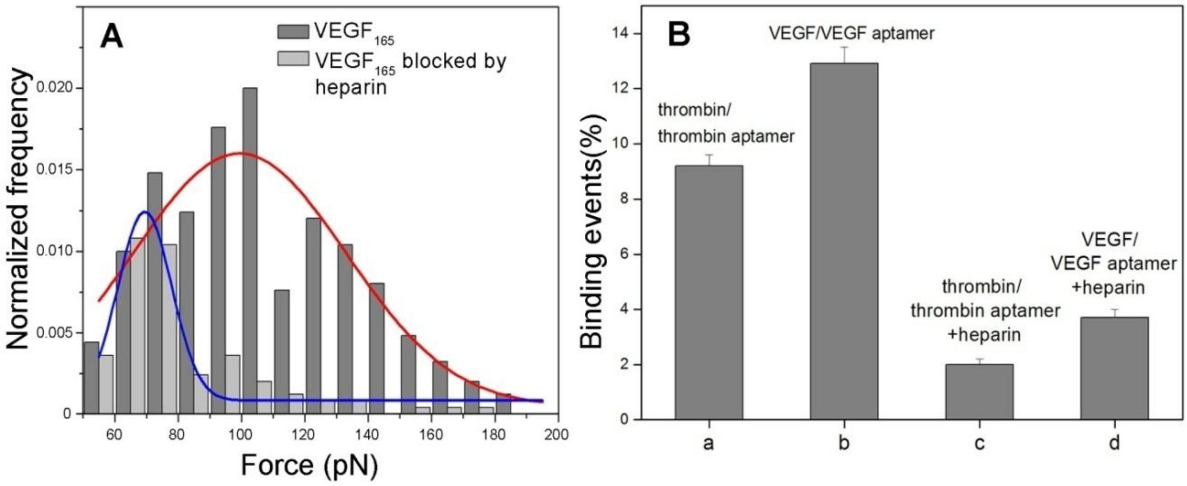

Figure 3.8. **A**: Histogram showing rupture force distributions for VEGF$_{165}$ DNA aptamer interaction with VEGF$_{165}$, and with heparin-blocked VEGF$_{165}$ (n = 2500). The solid lines are the Gaussian fits for VEGF$_{165}$ aptamer with VEGF$_{165}$ (red) and VEGF$_{165}$ aptamer withVEGF$_{165}$ blocked with heparin (blue). The loading rate was maintained at 200 nN/s. **B**: Analysis of the rupture forces showing binding percentages for experiments with aptamers and target proteins: **a**: Thrombin aptamer on AFM tip/ thrombin on surface; **b**: VEGF$_{165}$ aptamer on AFM tip/ VEGF$_{165}$ on surface; **c**: Thrombin aptamer on AFM tip/ thrombin on surface blocked by heparin; **d**: VEGF$_{165}$ aptamer on AFM tip/ VEGF$_{165}$ on surface blocked with heparin. Blocking experiments showing the decrease of binding percentage in the presence of heparin. Binding percentage is defined as percentage of force curves showing binding events among 2500 force curves over a 500 nm^2 area.

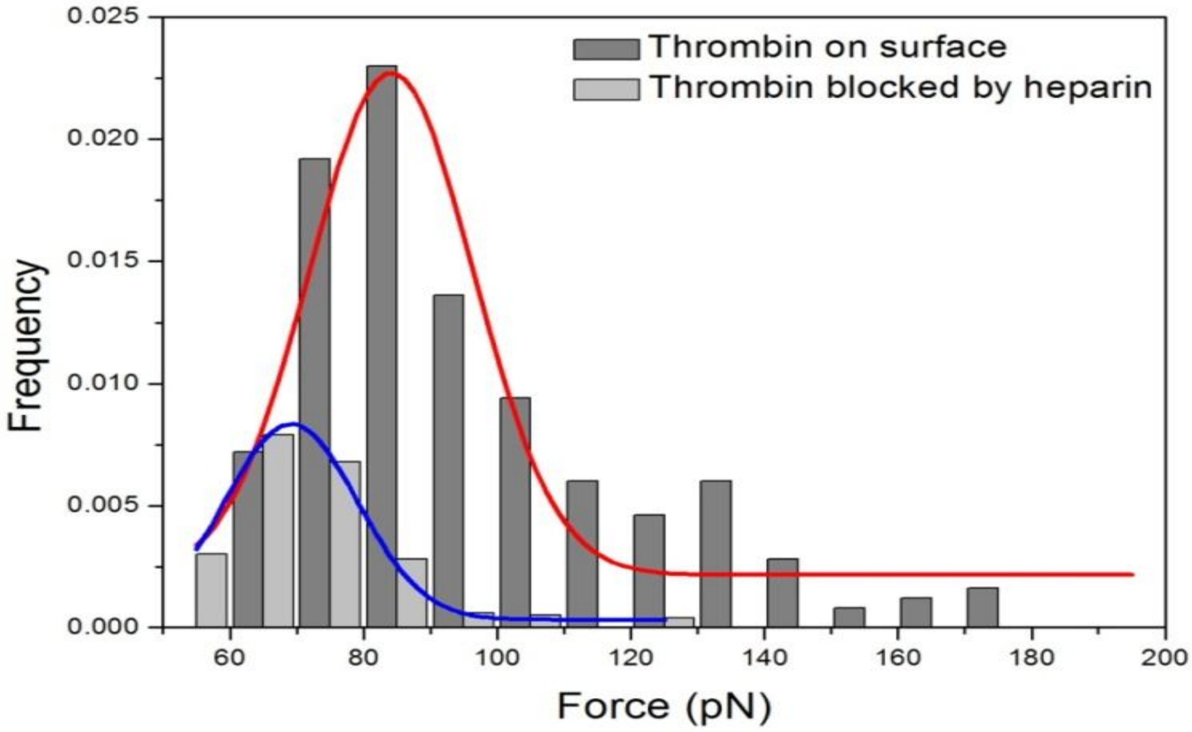

Figure 3.9. Histogram showing rupture force distributions for thrombin DNA aptamer interaction with thrombin, and experiment with heparin-blocked thrombin. The solid lines are the Gaussian fits for thrombin aptamer with thrombin (red) (n=2500) and thrombin aptamer with thrombin blocked with heparin (blue) (n=2500). The loading rate was maintained at 200 nN/s.

It may be noted that, in addition to the adhesion mode described above, an AFM-based force mapping method termed "dynamic recognition imaging" has also emerged to identify recognition sites on bio-surfaces. Using a ligand functionalized AFM cantilever oscillating on a sample surface, receptors are detected due to a reduction in the oscillation amplitude when specific binding events occur [128, 152, 153]. The force maps generated by this approach tend to have higher spatial and time resolution compared to adhesion force mapping described in this manuscript. However, unlike the AFRM approach, quantitative force values cannot be obtained directly using dynamic recognition. There have been some studies utilizing techniques such as fluorescence microscopy in conjunction with dynamic recognition, to detect the location of recognition sites on cell surface. However, this has to be followed by conventional AFM-based force spectroscopy to obtain quantitative force information [40, 154-157]. In contrast, our approach enables us to obtain the adhesion force values during the force mapping process. This has further implications when it comes to investigating complex surfaces or even studying real-time changes in the microenvironment.

3.3.4 Blocking with free heparin

Both heparin and the human α-thrombin DNA aptamer bind to the anion-binding exosite on human α-thrombin [135, 136]. VEGF_{165} also contains a heparin binding domain crucial for its DNA aptamer to bind [137]. To confirm the specificity between proteins and their corresponding DNA aptamers, and to demonstrate the ability to visualize the real-time effect of changes in the system, blocking experiments were conducted by adding free heparin to the aqueous microenvironment. In both the human α-thrombin and VEGF_{165} systems, surfaces were mapped pior to and after the addition of heparin. Figure 3.10 shows the force recognition mapping of VEGF_{165} attached surface by VEGF_{165} DNA aptamer in the presence of heparin. The height map shows well separated high features, while a significant decrease of high adhesion areas can be observed. Force analysis showed that both the binding percentages as well as magnitude of the rupture forces dropped significantly (Figure 3.8B**)**. Similar changes in the force map could also be observed in the system of thrombin-thrombin DNA aptamer in the presence of heparin.Thus we can postulate that the presence of heparin binding to human α-thrombin and VEGF_{165} covered the available binding sites for their relevant DNA aptamers. A few high adhesion areas may be observed due to nonspecific binding events between the tip and surface.

However, these are much lower in comparison to the recognition map in the absence of blocking, further verifying the specificity and versatility of the aptamer probe technique. These experiments show the potential of the force recognition mapping working in a complex medium in real time by adding exogenous substances to the microenvironments, which provides a better understanding of dynamic biological processes. As applications of such processes, we consider adhesion force maps showing that VEGF receptors on cell surfaces tend to concentrate toward cell boundaries and cluster rapidly after the addition of VEGF or the antibody of VEGFR [35]. Similarly, a recent report showed the binding kinetics between glyceraldehyde-3-phosphate dehydrogenase (GAPDH) and glyceraldehyde-3-phosphate (Gly-3-P) [158]. Adhesion force maps were obtained on the GAPDH-attached surface using an AFM cantilever functionalized with a Ras homologue. At various concentrations, the density of GAPDH decreased with the concentration of Gly-3-P, further allowing calculation of the thermodynamic association constant of GAPDH and Gly-3-P.

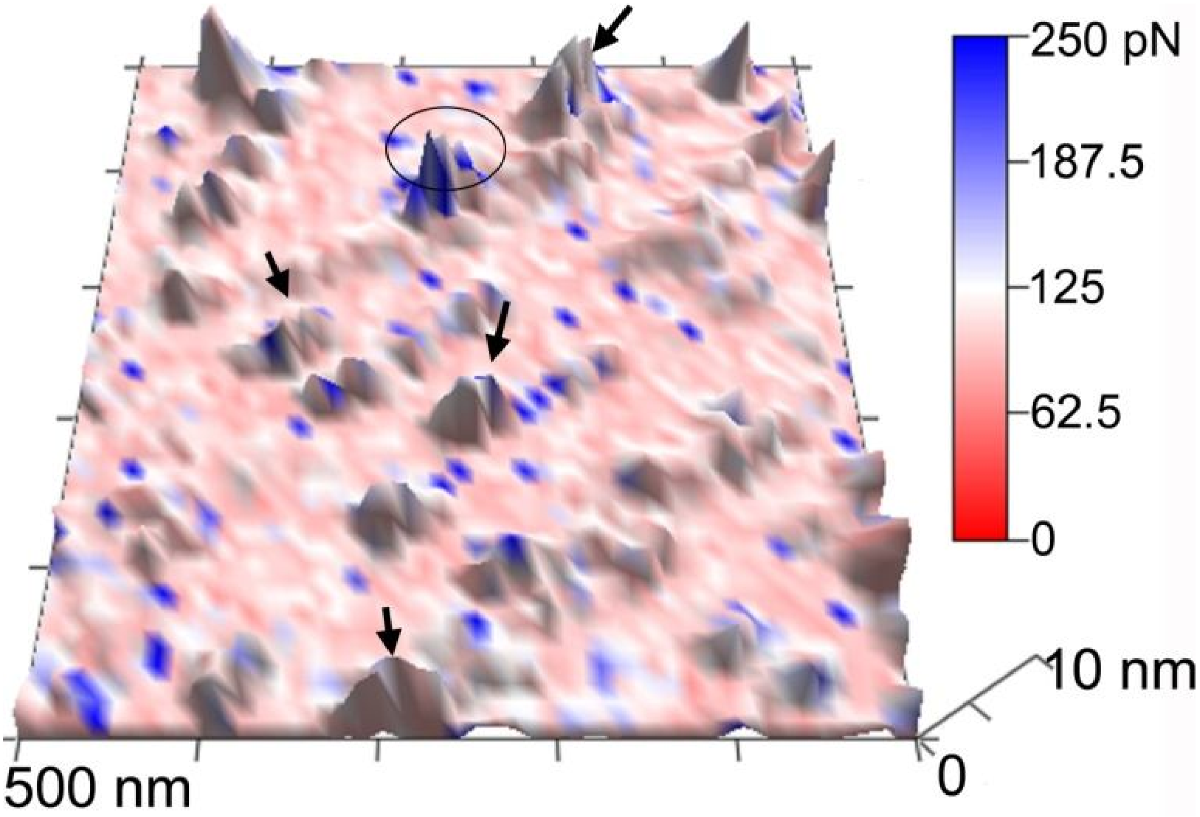

Figure 3.10. Control experiment showing attenuation in detection on blocking. Simultaneous height and adhesion maps for the $VEGF_{165}$ protein probed with its corresponding DNA aptamer. However, here the surface was incubated with free heparin that blocks DNA binding sites. Protein features no longer show interactions (marked by black arrows). Infrequent non-specific interaction events with the protein may be observed (black circle).

3.3.5 Resolution of force recognition mapping

In addition to accuracy and specificity, the spatial resolution is another pivotal parameter of force mapping. Spatially smaller than antibodies, aptamer-functionalized cantilevers enable a higher spartial resolution. The spatial resolution of the force maps we obtained are accurate to 10 nm (2500 force curves collected over an area of 500 nm×500 nm). Previous studies have indicated that this resolution is sufficient to detect specific biomolecules on static or cell surface using a biofunctionalized AFM tip [128, 148, 159, 160]. In this modality, the spatial resolution must be balanced by the time of data collection. For instance, many biological processes may occur faster than the time required by AFM to collect force curves. Further, repeated force curves collections may damage the integrity and biofunctionality of a biofunctional tip. Thermal drift of the instrument in liquid environment may occur after a long period of time. As such, in our experiments, the robustness of the DNA aptamers enabled easy collection of several thousand force curves in a repeatable fashion. One complete force map could be obained in 40 minutes without any significant drift. While 10 nm is a reasonable lower limit to study single proteins by adhesion force mapping, certain systems may be studied at higher or lower resolutions as demanded by the implicated biology.

3.4 Conclusions

In this chapter, it is demonstrated that the location and distribution of proteins can be mapped using aptamer-based force recognition mapping. Aptamers are highly stable and versatile against different targets such as the ones shown - human α-thrombin and $VEGF_{165}$ on mixed SAM surfaces. The non-contact mode images by AFM showed well-separated proteins on the surface, and the unbinding force values correlate well with single-pairwise interactions between the DNA aptamer and protein. The overlay of height and force data on the same areas showed strong adhesion forces on high features at a resolution down to 10 nm. The specificity of DNA aptamers to their targets was confirmed by heparin blocking and control experiments. These results demonstrate that DNA aptamers as bioprobes coupled with the force recognition mapping have the capability to localize specific proteins at a single molecule level, as well as detect changes in binding due to environmental changes. Similarly, the interactions of diverse protein/ligands such as receptor/ligand [13], antigen/antibody [161] and carbohydrate/lectin [159] can also be used to detect target biomolecules on biosurfaces including cells. This technique provides applications in the area of screening biomolecules on arrays or directly observing the changes on complex cell surfaces due to external stimuli.

[This chapter contains results that have been previously published in:

Wang C, Yadavalli VK, "Spatial recognition and mapping of proteins using DNA aptamers," Nanotechnology, 25, 455101, Oct 2014.]

CHAPTER 4

SPATIAL MAPPING OF CELL-SURFACE TARGETS AND ASSESSMENT OF THEIR CHANGES AT THE SINGLE CELL LEVEL

4.1 Introduction

The research conducted in the previous chapters developed a powerful technique to spatially recognize target biomolecules on non-biological surfaces using single-pair biomolecular interactions. Translation of the “force recognition” techniques from non-biological surfaces to complex, living cell surfaces offers the opportunity to obtain spatial distribution of cell surface biomolecules *in situ*. Compared to model surfaces in previous chapters, soft cell surface is more complex since it is extremely challenging to detect a biomolecule embedded in the complex cell membrane from topography imaging alone. In this chapter, in order to investigate cell surfaces in physiological environments, proper strategies are developed for immobilizing cells in their native state. Optimization of the “force recognition” techniques involving the resolution and data collection time is necessary to adapt to complex cell surfaces. Here, *B. cereus* is selected as a model system to study the spatial distribution of cell surface carbohydrates and quantitatively assess the changes among different cell types and strains, during a specific cellular process (sporulation) or under different micro-environments. This leads to visualization of targets of interest and their changes on cell surfaces and the development of robust strategies for addressing specific cellular questions from nanoscale and single cell level.

Carbohydrates are important components of bacterial cell surfaces, with their compositions displaying heterogeneity across strains [162]. Cell surface carbohydrates play important roles in various bacterial activities and functions, including adhesion on surfaces, molecular recognition, and providing defense mechanisms to guard against unfavorable environmental conditions [163-165]. The examination of carbohydrate compositions of bacteria has been used for taxonomic differentiation, identification of different genera and types and strains of bacteria [166, 167], as well as reconstruction of culturing conditions [168]. The species and strain-specific compositions and related bacterial functions make carbohydrates excellent biomarkers to identify potential vaccine antigens, for diagnostics, as well as for elucidation of the molecular basis for bacterial virulence and pathogenicity. However, the knowledge of the organization of these cell surface polysaccharides is still limited.

Members of the *Bacillus cereus* group including *B. cereus*, *B. anthracis*, and *B. thuringiensis* are genetically related species [169]. The characterization and profiling of these bacilli has great fundamental and applied importance. For instance, *B. anthracis*, the causative agent of anthrax, and *B. cereus*, a food-poisoning organism are two major pathogenic bacilli [170, 171]. Owing to their ability to form spores in response to nutrient deprivation conditions, the profiles of both vegetative cells and spores for these bacilli have been of great interest [172]. For instance, changes in the surface carbohydrate compositions on *B. anthracis* and *B. cereus* were investigated as surface biochemical markers for tracking the spore-forming process [173]. To date, several techniques have been applied to analyze the bacterial surface carbohydrate compositions, primarily involving the use of gas chromatography-mass spectrometry (GC-MS), ion-exchange chromatography, gel chromatography and high-performance liquid chromatography (HPLC) [4, 174, 175]. However, these approaches require large populations of cells for analysis and extensive sample preparation using biochemical methods. For example, prior to GC-MS analysis, two steps are necessary: chemical extraction and release of carbohydrates from the cell walls, followed by various derivatization methods [166, 172, 176, 177]. While some chromatography techniques are able to separate the native carbohydrates without requiring derivatization, additional mass spectral information is required for compound identification [178, 179].

Critically, however, these techniques as bulk scale tools are unable to *directly* clarify the density and distribution of specific carbohydrates on single, living cell *surfaces* at the micro or nanoscale. The high sampling requirement for conventional carbohydrate analyses has limited utility on many types of environmental samples or *in situ* applications with a low target cell population. In particular, a prevailing challenge is in the area of determining the spatial location of carbohydrates on the cell wall [172]. Descriptions of cell wall carbohydrates can be useful for strain classification and development of diagnostic and vaccine applications. This emphasizes the real need to develop a facile, fast and versatile platform to quantify the bacterial cell surface carbohydrate compositions at the single cell level, which can in turn, provide new insights into the biochemical properties of these bacteria.

Atomic force microscopy (AFM) has rapidly emerged as an important tool widely used over the last couple of decades in bacterial research [71, 72, 180]. The unique advantage of the AFM is the ability not only to characterize cellular surfaces with nanoscale resolution and three dimensional imaging, but also measure inter- and intra-molecular interaction forces with piconewton sensitivity [7-9]. Using biomolecule modified AFM tips as probes, interaction forces between tip-bound ligands and cognate surface-bound receptors (or vice-versa) can be measured [10]. In recent years, the process of collecting such force data has been further expanded with the advent of automated scanning modes that allow us to rapidly obtain spatial distributions of interaction forces and elasticity [11-13]. Importantly, bacterial samples for AFM can directly investigate live cells under near physiological environments in a non-destructive fashion. Elegant work from the Dufrêne laboratory has shown the versatility of this technique for detecting specific biomarkers on different kinds of cell surfaces [148, 181, 182]. An excellent review by the same group summarized the application of AFM based multiparametric mapping technique in cellular systems [57]. However, to date, most studies have observed localized areas on cell surfaces (typically below 0.5 μm ×0.5 μm) rather than the entire cell surfaces.

In this chapter, in order to demonstrate a whole cell profiling strategy, *B. cereus* (T-strain) is used as a model bacterium to investigate bacterial cell surfaces and spatially map specific carbohydrate profiles using AFM-based recognition mapping. *B. cereus* is an important concern in the food industry and it also shares a genetic and structural similarity with the more virulent *B. anthracis*, the causative agent for anthrax [10]. Using two specific carbohydrate binding lectins, wheat germ agglutinin (WGA) and concanavalin A (ConA) as probes, it is shown that the carbohydrates - N-acetylglucosamine (GlcNAc) and glucose/mannose (Glu/Man) can be detected, mapped, and quantified on single entire bacterial cell surfaces at the nanoscale. The choice of these targets was dictated by several studies showing the heterogeneity and changes in aminosugar and simple sugars across different strains and species, making them critical targets for profiling [162, 168, 172, 173]. It is shown that these carbohydrates can be measured in both vegetative and spore states in liquid environments. The cell profiles in height maps show good consistency with high adhesion force signals in force maps and vitally, show a change from the vegetative to the spore state. Additionally, the morphological and mechanical (elasticity) changes of *Bacillus cereus* bacteria during sporulation demonstrates the power of AFM applied in microbiology for multi-parametrically probing important biological processes at the single cell scale. Directly probing the cell surfaces can result in real time analysis and the ability to observe the effect of external microenvironments at a single cell level. This work demonstrates AFM-based "recognition force mapping" as a versatile platform to quantitatively detect and map the bacterial surface biomarkers (such as carbohydrate compositions) and monitor the changes of surface biochemical properties during bacterial related activities at the single cell level.

4.2 Experimental Section

4.2.1 Materials and instrumentation

(1-Mercaptoundec-11-yl) hexaethylene glycol (Oligoethylene glycol (OEG) terminated thiol), $HS-C_{11}-(EG)_6OH$, and (1-mercaptohexadecanoic acid)-N-succinimidyl ester (NHS terminated thiol), $HS-C_{15}COO-NHS$, were purchased from Nanocs Inc (Boston, MA). Wheat germ agglutinin (WGA), concanavalin A (ConA), 3 aminopropyltriethoxysilane (APTES) and glutaraldehyde were purchased from Sigma-Aldrich (St. Louis, MO). Phosphate-buffered saline (PBS pH 7.4) (11.9 mM phosphates, 137 mM sodium chloride and 2.7 mM potassium chloride) and ethanol (200-proof) were purchased from Fisher Scientific. Mica was purchased from Ted Pella (Redding, CA). Ultrapure water (resistivity 18.2 MΩ•cm) was obtained from a MilliQ water purification system (Millipore Scientific, MA). AC240TS cantilevers (Olympus) were used for non-contact mode imaging, while gold coated TR800PB cantilevers (Olympus) were used for force mapping.

4.2.2 Cell culture and sporulation conditions

Cultures of vegetative *B. cereus* (T-strain) were maintained at 30°C on Trypticase Soy Agar (TSA) (30 g Trypticase soy broth, (211768, Becton Dickinson, Franklin Lakes, NJ) and 15 g agar (AB1185, American BioAnalytical, Natick, MA)). Starter cultures were grown by inoculating single colonies of *B. cereus* into 125 mL of Trypticase soy broth and incubating for 24 hours at 30°C and 225 rpm. G Medium was used as the base sporulation formulation [183], and supplemented with peptone (BP9725, Fisher Scientific, Pittsburgh, PA) and tryptone (61184, Acros Organics, Waltham, MA)) (both at 8 g/L). Sporulation was performed by adding 1 mL of starter culture into 250 mL of sporulation medium and incubating at 30°C and 275 rpm in an orbital shaker. Six different time points during sporulation were selected to make samples: 0 hour, 8 hours, 12 hours, 16 hours, 24 hours and 42 hours. “0 hour” represents the *B. cereus* in starter culture before triggering sporulation. The others represent the cells in sporulation conditions (culture in G medium).

4.2.3 Sample preparation for AFM

Aminopropyl-mica (AP-mica) coupled with glutaraldehyde was used to immobilize cell samples. Freshly cleaved mica was incubated in APTES vapor in a vacuum desiccator for 12 hours. The AP-mica was immersed in 1 mL 2% (v/v) glutaraldehyde water solution for 1 hour and rinsed with deionized water. A 20 µL cell suspension was spotted and incubated for 30 minutes. The sample was immersed in 1 mL 1% (v/v) ethanolamine PBS solution for 30 minutes to block the glutaraldehyde on the areas without cells. Finally, the mica was rinsed with PBS to remove the loosely-immobilized cells and unreacted ethanolamine.

For making cell suspensions, 1 mL cell suspension was taken from the culture medium and placed into a sterile 2 mL Eppendorf tube. Cells were collected by low speed centrifugation (1 min, 4°C, 4000 rpm). Each pellet was re-suspended and washed two times with 2 mL sterile distilled water. Finally, the pellet was resuspended in 2 mL PBS buffer and kept in refrigerator (4°C) before use.

4.2.4 AFM probe functionalization and recognition force mapping

AC240TS cantilever (spring constant ~2 N/m, resonance frequency 70 kHz) were cleaned using high-intensity UV light to remove organic contamination and used for imaging and characterization of the surfaces in non contact mode. Gold coated cantilevers were cleaned in UV/ozone for 15 minutes. Cantilevers were functionalized as described earlier [87] - immersion in mixed thiol solution ($HS-C_{11}-(EG)_6OH$ and $HS-C_{15}COO-NHS$) in ethanol for 16 hours. Cantilevers were rinsed with ethanol, and incubated in a 100 nM solution of lectin (WGA or ConA) in PBS buffer for 1 hour at ambient temperature. Our group has earlier shown that this functionalization strategy limits the number of lectins on the surface to 1-3 [102]. Spring constants of the functionalized cantilevers were measured using the thermal fluctuation method.

Subsequently, lectin-functionalized cantilevers (spring constant ~0.15 N/m, resonance frequency 15 kHz) were used to obtain force data on cells. Each experiment was repeated on at least 5 different *B.cereus* cell surfaces to demonstrate reproducibility. Force-distance curves were obtained by collecting a series of sequential force curves in an $m \times n$ grid. Each force curve was obtained at the same loading rate (135 nN/s, at a ramp velocity of 900 nm/s) by pressing the cantilever to a low trigger point (200 pN), allowing binding to occur (contact time 0.1 second), and then retracting. All force maps were obtained by collecting ~80×80 force curves over a defined area (~3 μm×3μm), estimating the unbinding force values, and displaying these values by scale of color. The height maps of the same area were generated simultaneously as the force mapping occurred. Blocking experiments were performed by a buffer exchange of PBS containing 5μg/ml lectin in the fluid cell followed by force mapping. As a control experiment, a tip without lectin attached (only $HS\text{-}C_{11}\text{-}(EG)_6OH$) was used to map the cell surface. All images including height and force maps were performed using custom routines in Igor Pro 6.32 A (Wavemetrics Inc, OR) for fast processing of data.

4.2.5 Atomic force microscopy imaging and measurement of mechanical properties via nanoindentation during sporulation

Super sharp silicon cantilevers (AC240TS, spring constant ~2 N/m, resonance frequency 70 kHz) from Olympus (Tokyo, Japan) with nominal radii of curvature 9±2 nm were used for imaging samples at a high resolution. The morphology of the samples including height profile and cell size were analyzed using custom routines in Igor Pro 6.32 (Wavemetrics Inc, OR). AFM-based nanoindentation experiments were carried out using different probes (k ~ 20 N/m) compared to those used for imaging (PPP-ZEIHR, Nanosensors, Neuchatel, Switzerland). Spring constants of cantilevers were measured prior to each experiment using the thermal fluctuation method [88]. Stiffer cantilevers were used owing to the nature of the cells probed in air, with well-known high rigidity of bacterial spores [184]. In contrast to conventional point-by-point load-indentation reported earlier, a strategy of elasticity mapping was used for these experiments to observe the entire cell area. Indent curves were obtained by collecting a series of sequential indent curves in an $m \times n$ grid. Each indent curve was obtained at the same loading rate (300 nN/s) by indenting the cantilever to the samples until a constant load force (150 nN) was reached. All the procedures including analysis of the indent curves using the Hertz model [185, 186], generating elasticity maps as well as the overlays of height maps andelasticity maps were carried out with Igor Pro 6.32 software. Elasticity maps were obtained by collecting 50×50 indent curves over a defined area (~3×3 μm) and estimating the Young's moduli.

4.3 Results and discussion

The intersection of atomic force microscopy, with its capabilities of high resolution imaging and force spectroscopy, with microbiology, has provided an exciting strategy to study organisms both biophysically and biochemically [72, 187]. The application of force spectroscopy for detecting specific recognition sites on cell surfaces and spatially mapping them has been an important step in this regard. For instance, Francius et al. [159] used two lectin modified probes, Con A (glucose/mannose) and *Pseudomonas aeruginosa* lectin (galactose) to detect carbohydrates on *Lactobacillus rhamnosus* strain GG (LGG) surfaces. The force maps showed the Glu/Man and Gal distribution of the LGG wild-type are markedly different from those of the mutant strains. Andre et al. [148] performed recognition force mapping on *Lactococcus lactis* (LL) cells to detect specific peptidoglycans. The force maps combined with topographic images demonstrated that the peptidoglycans were arranged linearly and parallel to the short cell axis. However, these studies focused on small areas of the cells (400 nm×400 nm on LGG [159] and 500 nm ×500 nm on LL cells [148]) with height and force channels obtained separately. These approaches zooming in smaller area are accurate for specific target detection and distribution mapping. However, for quantitative analysis surface composition on single cells, mapping larger areas including entire cells, can provide an efficient strategy for spatial localization and real time analysis. For instance, consider that bacterial vegetative cells and spores are ~2 orders of magnitude larger in terms of surface area. (3.4±0.3 μm^2 and 2.2±0.3 μm^2 for the *B. cereus* cells in this work). As shown below, observation of the entire cell morphology provides a unique opportunity to profile single, live cells for a range of targets.

4.3.1 Nanoscale imaging and probing of *Bacillus*

To observe the morphology and spatially locate carbohydrate markers using AFM, the first step involves proper sample preparation. Two requirements are needed: i) Cells should be firmly fixed on substrate to avoid dragging by an AFM tip, especially in liquid, and ii) Cells should be maintained in the native state to preserve lectin-reactive sites on the surface. Here, a simple chemical fixation method was used to immobilize the cell samples on substrate: Amine-functionalized mica (AP-mica) was modified with glutaraldehyde to form an aldehyde-terminated surface. Following aldehyde functionalization, the substrate was gently rinsed with sterile water to remove unreacted glutaraldehyde, which might damage the bioactivity of carbohydrates on cell surfaces. For morphology observation, both *B. cereus* vegetative cells and spores were initially imaged in air to show their high resolution surface topography, including surface nanostructures (Figure 4.1) [188]. Figure 4.1a and 4.1b shows *B. cereus* vegetative cells are rod-shaped and form vegetative cell chains. A quantitative analysis was performed on several cell samples from different areas and images (n=20). The dimensions of these vegetative cells were 2.8±0.5 µm in length and 1.2±0.2 µm in width, consistent with previously reported dimensions [184, 189]. Compared to the rod-shaped vegetative cells, the *B. cereus* spore shows a characteristic ovoid shape (Figure 4.1c and 4.1d). In addition to prior verification using phase contrast microscopy, several morphological characteristics typical of spores are observed by AFM imaging - i. surface ridges extending along the entire spore length, a characteristic surface feature owing to the folding of the spore coat in the dehydrated state [190, 191]. ii) An ultrathin capsule (~20 nm) surrounding the spores, presumably the exosporium, another characteristic feature of *B. cereus* spores and, iii) a significant length decrease following spore formation.

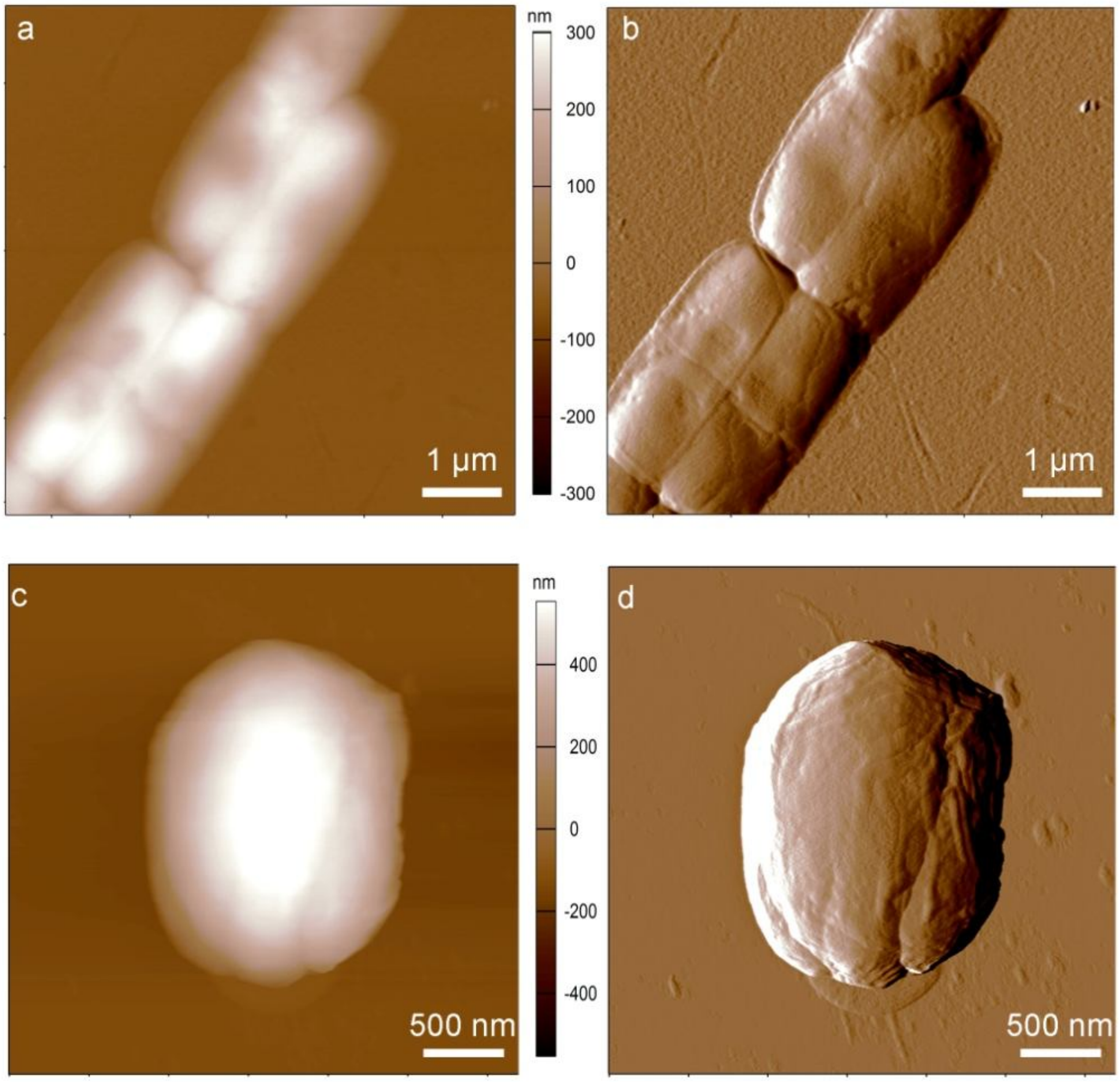

Figure 4.1. *B. cereus* vegetative cells and spores in air. (a) and (c) are height maps of vegetative cells and spore, respectively. (b) and (d) are the corresponding amplitude images.

4.3.2 Spatial recognition of surface carbohydrates on vegetative cells

To spatially recognize and map carbohydrates on *B. cereus,* force spectroscopy experiments were conducted in a liquid microenvironment using cantilevers functionalized with different lectins –

concanavalin A (which displays specificity to Glu/Man) and wheat germ agglutinin (WGA, specific to the amino sugar GlcNAc). Figure 4.2 shows the height and force (interaction) maps of the cell surfaces for each lectin. For clarity, these images have been overlaid. Force curves were analyzed automatically using a custom algorithm in IgorPro that can rapidly differentiate between specific binding and non-specific interactions and also determine binding forces. Curves classified as specific binding events are manifested in a cantilever deflection observed as a non-linear delayed retraction curve with a different slope as that of the contact region. Examples of the raw data of individual layers and representative force traces are shown in Figure 4.3. An excellent correspondence can be observed between the cell profiles in the height map and a simultaneous increase of the recognition events at the same areas. In comparison, there was very low adhesion on the background. For WGA as the probe, Figure 4.2b shows the cell profiles revealing correspondingly higher recognition events compared to cells probed with Con A (Figure 4.2a). Histogram analysis of force curves (Figure 4.4) show that the forces in the Con A-Glu system are higher than for the WGA-GlcNAc system, consistent with previous reports [192]. It can be seen that in ConA-Glu system, the main adhesion forces are around 120 pN and some are around 60 pN. This may be because at a pH> 7, ConA exists as a tetramer, in which four binding sites that can act independently. In addition, the elasticity on single cell surface is not homogenous, which will result in different contact area between tip and surface at different locations. Thus, there are possibilities of single interaction and multivalent interactions. The overall distribution is observed to be uniform across the surface and not concentrated at edges. The three-dimensional data obtained allows a rendering of the entire cell as shown in Figure 4.5a. A further advantage of mapping the entire cell surface rather than zooming in on a smaller area on single cell surface is that the carbohydrate compositions of the cell surface can be quantitatively estimated (Figure 4.5b). As a quantitative measure, the binding was calculated as a % of interaction traces to the total number of traces collected on the cell surface. This binding % is analogous to a molar concentration since each interaction event represents the binding of a single (or double) molecule pair. The density of Glu/Man (9.8±3.9 %) is calculated to be much lower than that of GlcNAc (40.2±7.2 %) on *B.cereus* cell surfaces, where the data are from five independent experiments on different cells. To verify these results, earlier studies which analyzed vegetative *B. cereus* cell walls were referenced. Comparison of surface carbohydrate compositions among several strains is summarized in Table 4.1. Although different strains show the variation of carbohydrate compositions, it can be easily seen that the amount of GlcNAc is higher than that of Glu/Man in each strain with a variation from ~2:1 to ~10:1. The calculated value of 4:1 on *B. cereus* strain T vegetative cells in this work falls within this expected range. Among these different strains, the strain 03BB102 and G9241 show similar molar ratio (~4:1) with *B. cereus* strain T in this study. Interestingly, these results are in excellent consistency with the reported values on *B. cereus* AHU 1356 strain, wherein the lysozyme digests of the cell wall showed that the polysaccharide component was composed of GlcNAc, ManNAc, GalNAc, and Glc in ratios of 4:1:1:1 [193].

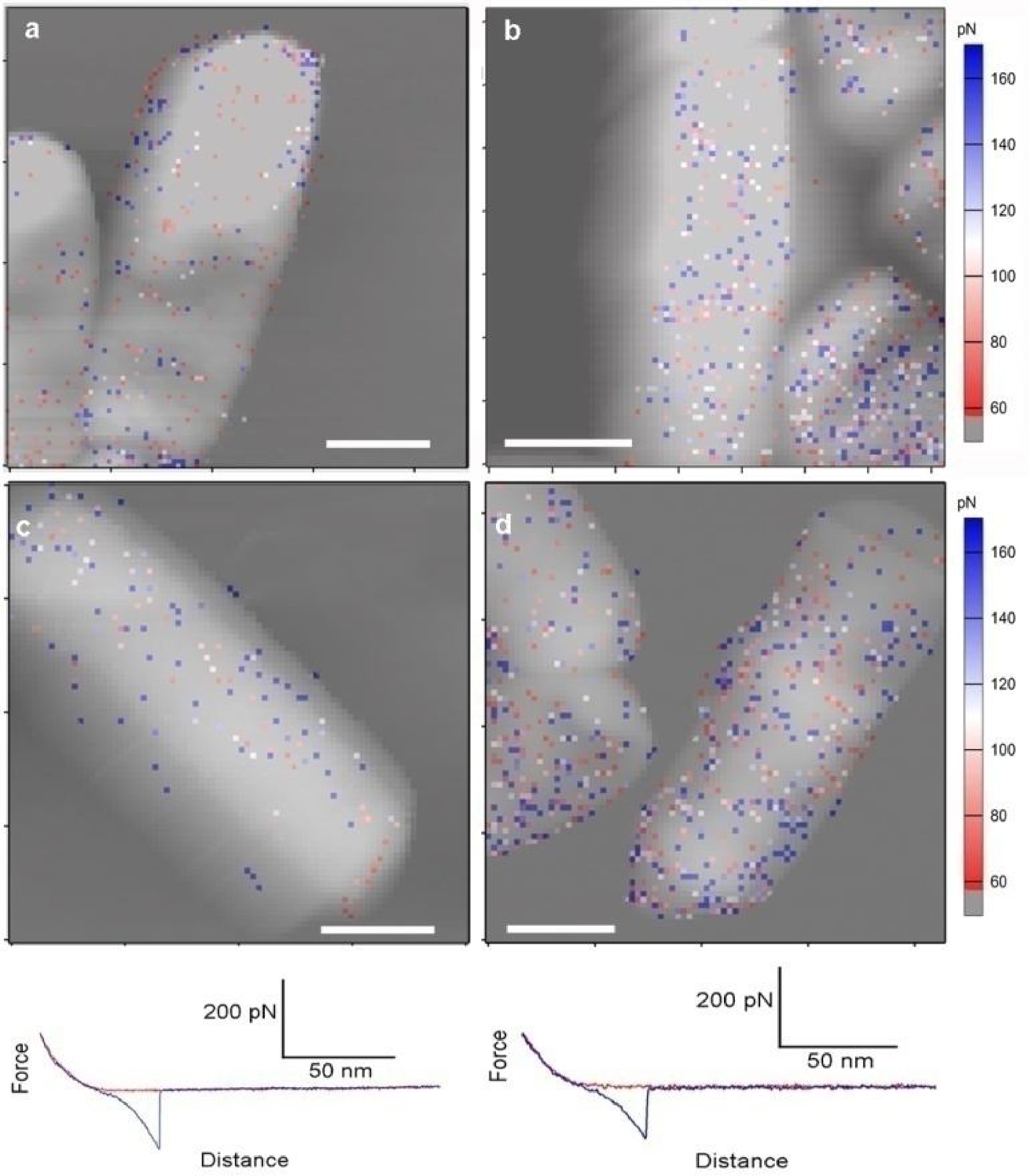

Figure 4.2. Overlay of force and height profiles for the carbohydrates on *B. cereus* vegetative cell surfaces studied with their corresponding lectins. Two sets of experiments are presented. (a) and (c) Glu/Man probed with Con A. (b) and (d) GlcNAc probed with WGA. Typical force curves are also shown at the bottom of figure. (Scale bars = 1 µm).

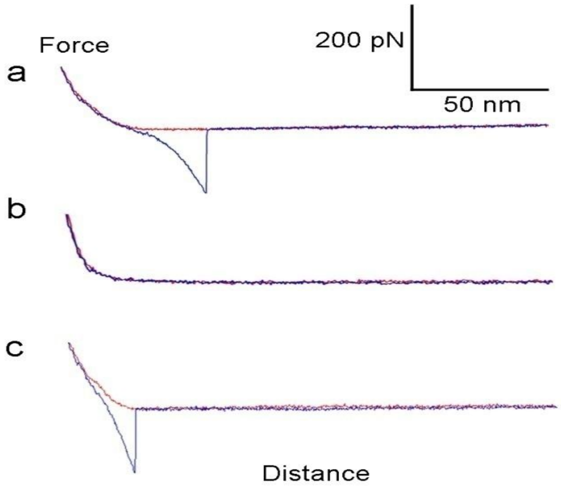

Figure 4.3. Typical AFM force–distance curves (retraction traces) obtained in the experiments: (A) typical selected traces indicating a molecular recognition event (B) No tip surface adhesion when the tip encounters the background and (C) few traces showed a non-specific adhesion force were excluded from force maps.

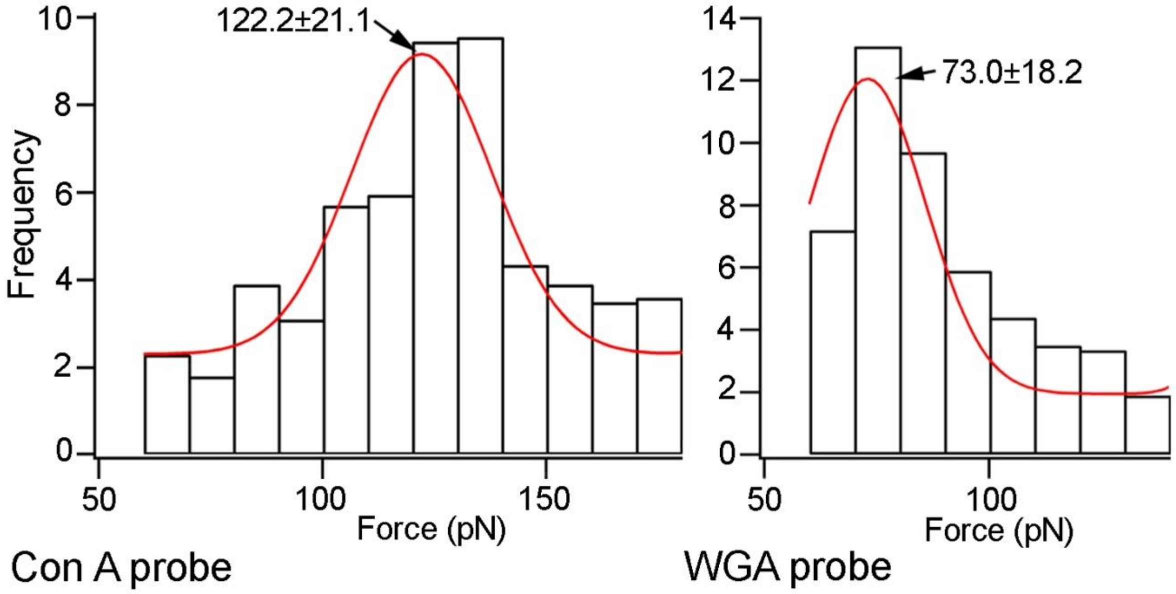

Figure 4.4. Histogram analysis of force curves with the lectins Con A and WGA immobilized on the AFM tip for detecting glucose/mannose and GlcNAc respectively. The data are from five independent experiments for each system conducted in PBS. The forces in the Con A-Glu system are higher than for the WGA-GlcNAc system, consistent with previous reports.

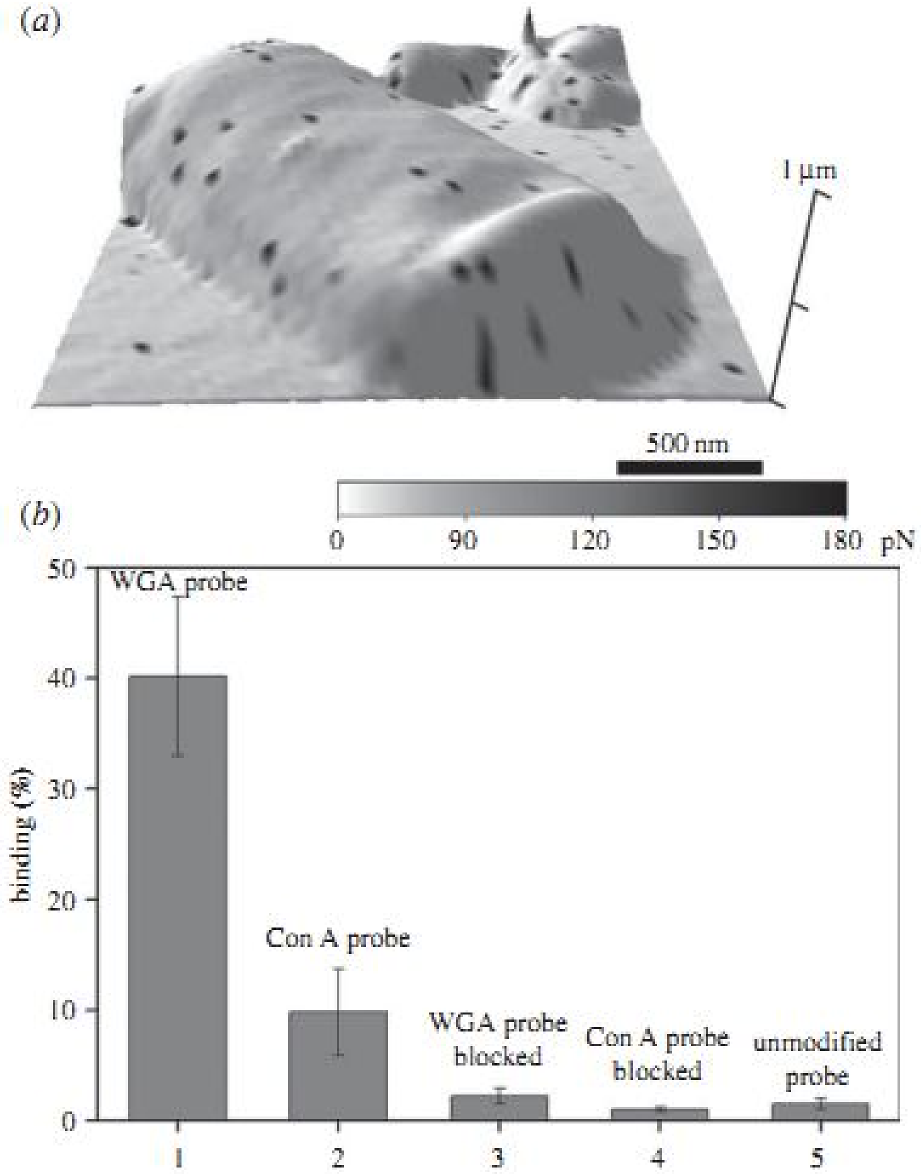

Figure 4.5. (a) 3D rendering of a *B. cereus* vegetative cell showing Con A binding sites to Glu/Man. (b) Analysis of the rupture forces showing binding of lectins and target carbohydrates on *B. cereus* vegetative cells: **1**: WGA on AFM tip/ GlcNAc on cell surface; **2**: Con A on AFM tip/ Glu/Man on cell surface; **3**: WGA on AFM tip/ GlcNAc on cell surface blocked by WGA in buffer; **4**: Con A on AFM tip/ Glu/Man on cell surface blocked with Con A in buffer. **5**: Unmodified AFM tip (without lectin attached) on cell surface. Blocking and bare tip experiments show a decrease in binding (calculated as the ratio of the number of points showing recognition events to the total number of points collected on the cell surface). The data are from five independent experiments for each system.

Table 4.1. Comparison of surface carbohydrate compositions on vegetative cells among several *B. cereus* strains (Glu- glucose, Man- mannose, GlcNAc- N-Acetylglucosamine, ND - none detected) (*data adapted from* [172]).

Strain	Carbohydrate composition (%±SD)			Molar ratio Glu/Man:GlcNAc
	Glc	Man	GlcNAc	
ATCC 14579	27.7±2.2	ND	45.2±2.5	0.75
F666	24.5±7.9	ND	32.3±6.5	0.93
ATCC 10987	2.6±1.3	ND	25.7±3.0	0.12
03BB102	5.1±0.8	0.9±0.5	22.9±2.7	0.27
G9241	5.2±0.7	ND	21.7±1.0	0.29
03BB87	2.5±0.9	ND	28.0±3.2	0.11

Several control experiments were carried out to confirm the specificity of the pair-wise lectin-carbohydrate interactions. First, an unmodified (“bare”) Au-cantilever (functionalized in a similar manner with only OH-PEG-thiol modified but without attached lectin) was used to probe the cell surface. Minimal specific recognition events can be observed on the cell surfaces (Figure 4.6a), implying that the observed recognition between the lectin functionalized cantilever and the cell surfaces are specific in nature. Second, cell surfaces were mapped using lectin probes following the addition of relevant (free) lectins in buffer. This blocks the surface carbohydrates making them unlikely to show up when probed by the corresponding lectin. Figure 4.6b and c show the force mapping of *B.cereus* cell surface by Con A and WGA-modified AFM probes respectively. A significant decrease of high adhesion force areas is observed (quantitatively shown in Figure 4.5), with a few non-specific high adhesion spots, confirming that the interactions observed are specific in nature and not the result of the lectin-modified tips binding non-specifically to the cell surface. These experiments further demonstrate the potential of this strategy to work in a complex medium in real time, by observing changes in the cell surface on adding exogenous substances to the microenvironment.

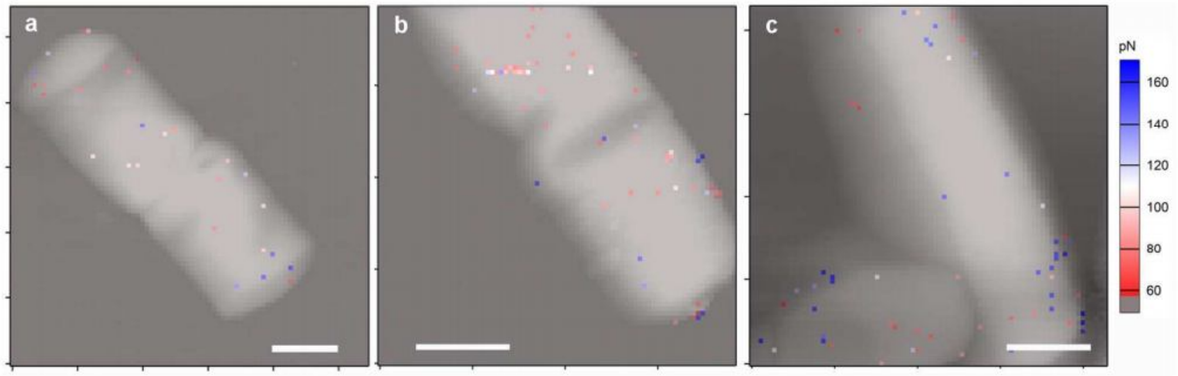

Figure 4.6. Control experiments on *B. cereus* cell surfaces: (a) Bare tip: Overlaid height and force map of cell surface probed with a bare tip (without lectin attached). (b) Blocking experiment: height and force map of cell surface probed with ConA lectin in the presence of free Con A that blocks Glu/Man binding sites. (c) Blocking experiment: height and force map of cell surface probed with WGA lectin in the presence of free WGA that blocks GlcNAc binding sites. (Scale bars = 1 µm).

4.3.3 Spatial recognition of surface carbohydrates on spores

Following the study of vegetative cells, *B. cereus* spore surfaces were investigated. As a typical spore-forming cell, *B. cereus* is able to metabolically transform into oval, dormant cells in response to unfavorable environmental conditions [194]. It has been shown that vegetative *B. cereus* cells have different carbohydrate compositions in comparison to spores. These compositional biomarkers switches are important to potentially discriminate between vegetative or spore stages of *Bacillus* as well as to detect single cells [195]. Using recognition force mapping, GlcNAc and Glu/Man were spatially mapped on *B. cereus* spore surfaces**.** Figure 4.7 shows the spatial distribution of the carbohydrates on *B. cereus* spore surfaces. Rare projection spots on the height images may result from biopolymers that could have been pulled out by the AFM tip. The carbohydrate compositions of the spore surface can again be quantitatively estimated (Figure 4.8). Similar control experiments including unmodified probes and blocking experiments were conducted. As expected, the binding probability decreased significantly, which further confirms the specificity of lectin-carbohydrate interactions on the spore surface as well (Figure 4.8).

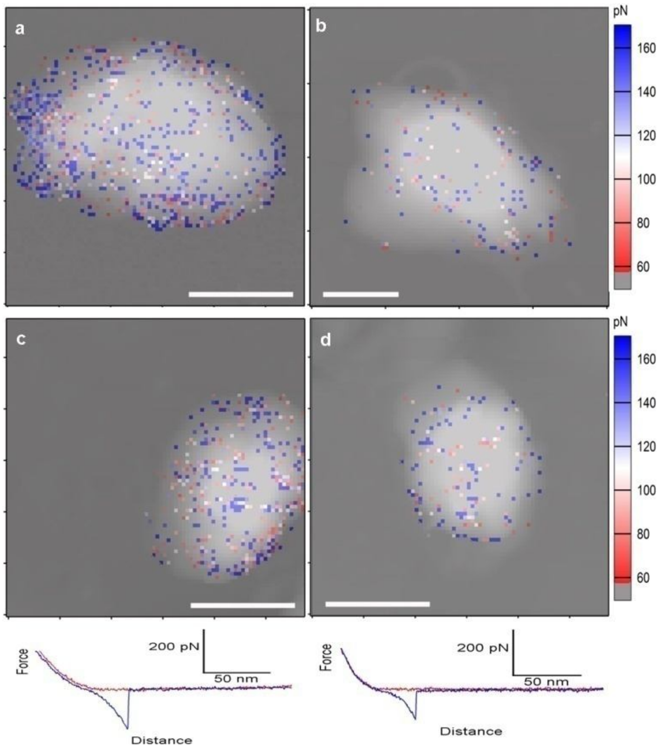

Figure 4.7 Overlay of force and height profiles for the carbohydrates on *B. cereus* spore surfaces studied with their corresponding lectins. Two sets of experiments are presented. (a) and (c) Glu/Man probed with Con A. (b) and (d) GlcNAc probed with WGA. Typical force curves are also shown at the bottom of figure. (Scale bars = 1 µm).

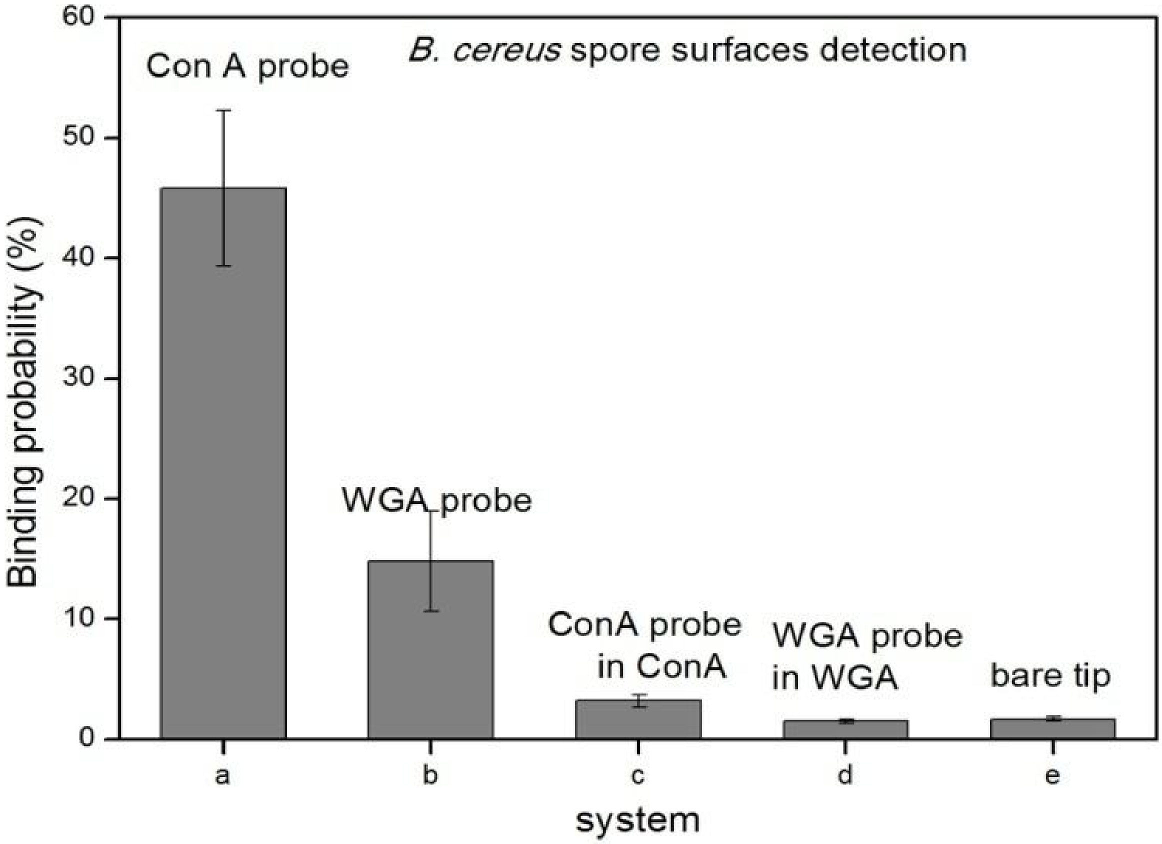

Figure 4.8. Analysis of the rupture forces showing binding of lectins and target carbohydrates on *B. cereus* spores: **a**: WGA on AFM tip/ GlcNAc on spore surface; **b**: Con A on AFM tip/ Glu/Man on spore surface; **c**: WGA on AFM tip/ GlcNAc on spore surface blocked by WGA in buffer; **d**: Con A on AFM tip/ Glu/Man on spore surface blocked with Con A in buffer. **e**: Unmodified AFM tip (without lectin attached) on spore surface. Blocking and bare tip experiments show a significant decrease in binding.

From Figure 4.7, the density of Glu/Man (45.8±6.5 %) is observed to be much higher than that of GlcNAc (14.8±4.2 %) on the spore surfaces. This trend which is opposite to the vegetative surface studied above is intriguing. Previous studies of spore carbohydrate compositions on different strains have shown that GlcNAc < Glu/Man for most strains although some variations can be observed from the vegetative cell to spore form [173, 195]. Compared to the vegetative cells, the change of carbohydrate compositions in spores may be due to the lectin probe primarily interacting with the surface of the exosporium, known to envelop spores of *B. cereus*. Surface interactions on vegetative cells would also likely involve peptidoglycan components of the cell wall. We also do not rule out the interaction of the lectin Con A with teichoic acid, a significant component of gram positive bacilli cell walls. While this interaction is cross-reactive to Glu/Man, earlier works have shown that the ratio of teichoic acid and other components remains roughly the same in both vegetative cells and spores [196]. The exosporium is a complex mixture of carbohydrates, lipids, and proteins with an overall composition that is distinct from the cell wall of vegetative cells [174]. In previous studies, the carbohydrates were released from whole spores using hydrolysis, such that carbohydrates both on the surface and *inside* the spore would be analyzed. In contrast, AFM force mapping primarily probes the surface of spores. Compared to the vegetative cells, the new synthetic protective layers on spore surfaces during sporulation may lead to the change of carbohydrate compositions when detecting surface carbohydrates using AFM force mapping. Among these newly formed surface structures of spore, the outermost exosporium, a transparent loose-fitting membrane which is mainly composed of highly glycosylated glycoprotein BclA, known to envelop spores of *B. cereus* [197, 198]. In this work, the estimated carbohydrate composition value (GlcNAc: Glu/Man) is in excellent agreement with a previously reported value of 1:3 (molar ratio) measured from the *B. cereus* T-strain spore (same strain as this study) exosporium [174], in which only the outer exosporium was extracted and analyzed.

Carbohydrate compositions obtained by recognition force mapping can therefore be used as significant parameters for tracking bacterial related activities. An important consideration in whole cell analysis is the curvature of the cell which can result in artifacts at the cell-substrate interface. In these experiments, the aspect ratio (height/width) for a number of cells and spores was calculated (n=10). For vegetative cells aspect ratio is 0.30±0.05 and for spores 0.66±0.08. On areas such as the top of the cell, this problem is minimized. In the case of vegetative cells, there were also few issues at the cell substrate interface owing to the flatness of these cells. Here, several cells in different orientations have been investigated to consider these concerns. Probing the whole cell provides quantitative spatial distributions beyond yes/no answers. It should be noted that both GlcNAc and Glu/Man can be found on vegetative cells and spores, which implies that they are not necessarily *stand-alone* carbohydrate markers for all cell types. An interesting extension would be to detect spore-specific biomarkers and figure out presence/absence. An example would be rhamnose, the main sugar component of BclA which is spore-specific [199]. However, the rhamnose binding lectin and antibody of BclA are currently not commercially available. The ability of this technique is therefore limited to targets that can be directly probed by specific binding ligands. However, several advantages including the uncovering of spatial, high-resolution and potential real time information on whole, live cells under physiological environments is a powerful tool in the development of bacterial profiling strategies.

4.3.4 Resolution of recognition force mapping

In recent years, there has been rapid progress in developing new modes in AFM-based imaging starting with topography and recognition imaging. Among these, Quantitative Imaging and Peak Force Tapping methods are able to image cell surface morphology and biophysical properties (e.g., elasticity and adhesion) simultaneously at high speed and high resolution [200, 201]. The higher lateral resolution provided by Peak Force Tapping has been found to be attractive when imaging smaller areas, including single proteins [201]. While these are extremely promising strategies, we note that there are advantages of the technique presented here: For instance, there is no requirement of any specialized equipment. The experiments presented were conducted on a standard, widely used AFM capable of performing force spectroscopy using regular, functionalized cantilevers.

In addition to accuracy and specificity, spatial resolution of this technique is a key parameter of recognition force mapping. For complex surfaces over whole cell areas, it is important to balance demands of spatial resolution and accuracy [202]. For example, increasing the spatial resolution can provide a better look at cell surfaces. However, force spectroscopy at two points too close to each other may not be optimal as surface targets such as carbohydrates are flexible polymers that may display multiple interactions. Moreover, an increase in data collection time causes further challenges including possible damage to the integrity and functionality of a bio-functionalized tip owing to repeated force curves, or thermal drift over long periods of time. The high level of control of scan size, scan speed and loading as reported in this paper results in an accurate estimation of surface composition. In these experiments, a ramp velocity of 0.9 µm/s was used, which reduces time of experiment while minimizing the effect of hydrodynamic drag force and hysteresis [203, 204]. One complete force map on an area of ~4×4 µm with a resolution of 80×80 (6400 force curves) can be easily obtained in less than one hour without drift, tip damage or multiple interactions. It can be envisioned that in conjunction with the biophysical tools and strategies discussed here, new instrumental tools can further add to the repertoire of ways to probe bacterial cells at the single cell level and in real time.

4.3.5 Multi-parametric tracking cell surface during biological process at the single cell level

Morphological change during sporulation

Besides surface biomarkers tracking, the morphological and mechanical changes of *B.cereus* bacteria during sporulation were studied using a strategy of AFM imaging and elasticity mapping. The morphogenesis of the endospore and released mature endospore can be observed clearly by time-resolved AFM imaging (Figure 4.9 and 4.10). As a starting point, the vegetative cells prior to addition to G medium ("0 hour") were observed to be rod-shaped and forming vegetative cell chains (Figure 4.9a). A quantitative morphology analysis was performed on several cell samples from different areas and images ($n=20$). The dimensions of these vegetative cells were 2.8±0.5 μm in length, 1.2±0.2 μm in width, consistent with previously reported dimensions [184, 189]. Height profiles were measured along the "long-axis" of single cells as the cell surface was observed to change in flatness over time, especially as the endospores develop. Three morphology parameters were analyzed from height images: H_{max}, the maximal height of single cells, ΔH, the maximal height difference on single cell surfaces, wherein the height of the endospore could be estimated as the difference in the heights between the top and the flat region of the cell, and the root mean square (RMS) roughness on single cell surfaces. At the "0 hour" stage, the maximal height of single cells is 366.5±12.2 nm, consistent with reported values also measured by AFM [184]. No obvious bumps are observed on the height and amplitude images coupled with 34.3±3.5 nm of the maximal height difference and 22.2±5.6nm of RMS roughness on single cell implies that the cell surfaces are flat and no endospores formed before the sporulation was triggered. Following an 8 hour period, cell imaging showed no obvious differences compared to the 0 hour vegetative cells (Figure 4.9b),indicating that the endospore formation had not begun.

Figure 4.9c represents the onset of sporulation after 12 hours in culture, wherein the cells were observed to have a raised structure at one end (red arrows).This is observed by visual examination as well as an increase in the maximal height of single cells and height differences from AFM imaging (Table 4.2). This morphology change shown at this time point may be caused by the asymmetric division of the protoplasm, which is the first morphological characteristic of sporulation process [205]. Figure 4.10 shows a rapid progression of the sporulation process till the lysis of the cell and subsequent release. In Figure 4.10a at 18 hours, the endospore-like bumps are more pronounced and observable. Expectedly, the height profile analysis shows the maximal height of single cells, height difference and RMS roughness on cell surfaces increase significantly, implying that the endospores were building their thick and multilayered spore walls (Figure 4.11a) [206, 207].At these intermediate points, it is worth noting that the height difference on cell surfaces increased is due to two reasons including the increase of maximal height in certain areas of the spores with a simultaneous decrease in surrounding areas. This also can be observed from the very thin and flat (~40 nm) edges of the mother cells (Figure 4.10b). In contrast, vegetative cells are largely homogeneous in height with a very small difference between the highest and lowest points of the cells. Finally, after 42 hours, the isolated mature endospores are formed and released (Figure 4.10c). Besides the characteristic ovoid shape of the spores [208], several morphological characteristics confirm the spore formation - i. surface ridges extending along the entire spore length, a characteristic surface feature owing to the folding of the spore coat in the dehydrated state[190, 191]. ii)An ultrathin membrane (~20 nm of height) surrounding the spores (red arrows in Figure 4.10c). This exosporium is another characteristic feature of *B. cereus* spores [64]. iii) Debris on the substrate indicating lysis of mother cell after the mature spore is released [209]. (green arrows in Figure

4.10c) and, iv) A significant length decrease of cells. The spores with 1.8±0.2 µm in length are shorter than that of initial vegetative cells (2.8±0.5 µm).

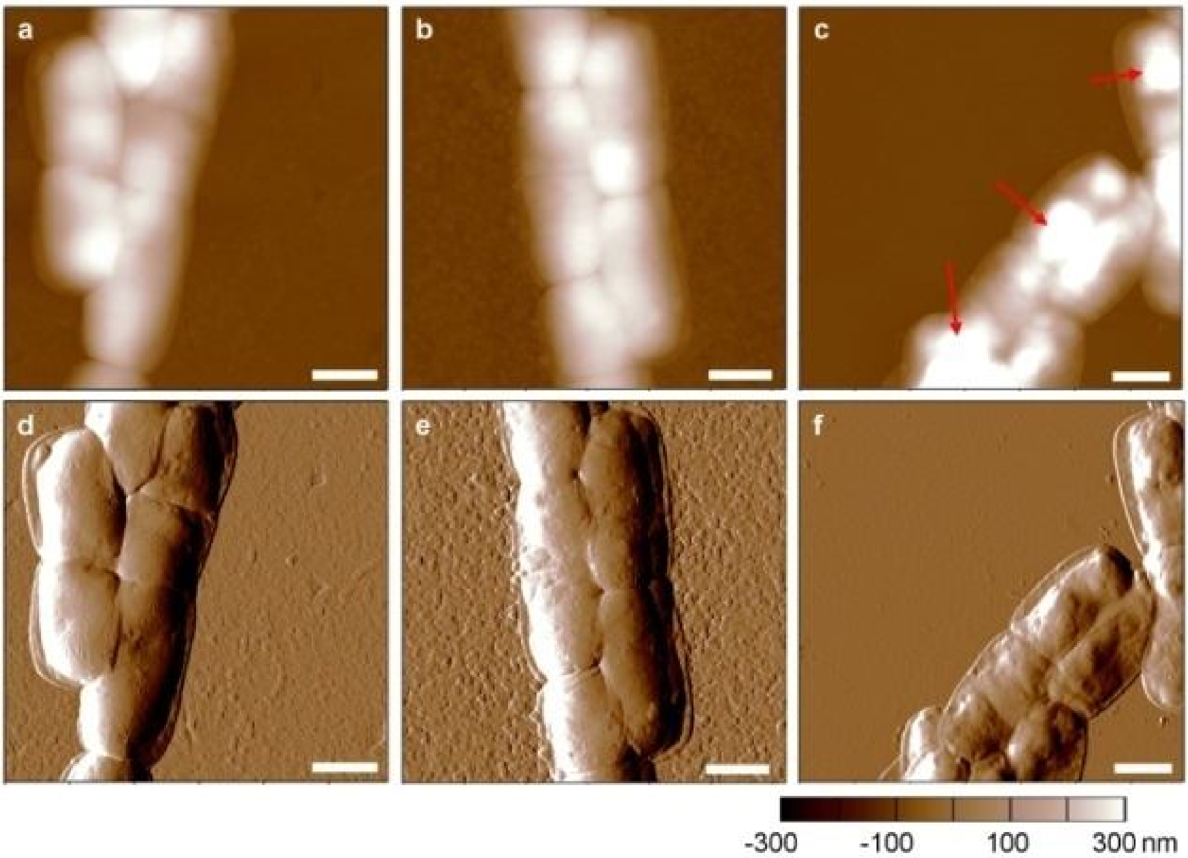

Figure 4.9. Topography (top row) and AFM amplitude (bottom row) images of *Bacillus cereus* before and at the onset of sporulation trigger. (a, d) Height image before cells were added to G medium. (b, e) Following an 8 hour culture. (c) Following 12 hours. The red arrows show the onset of sporulation. Scale bars = 1 µm.

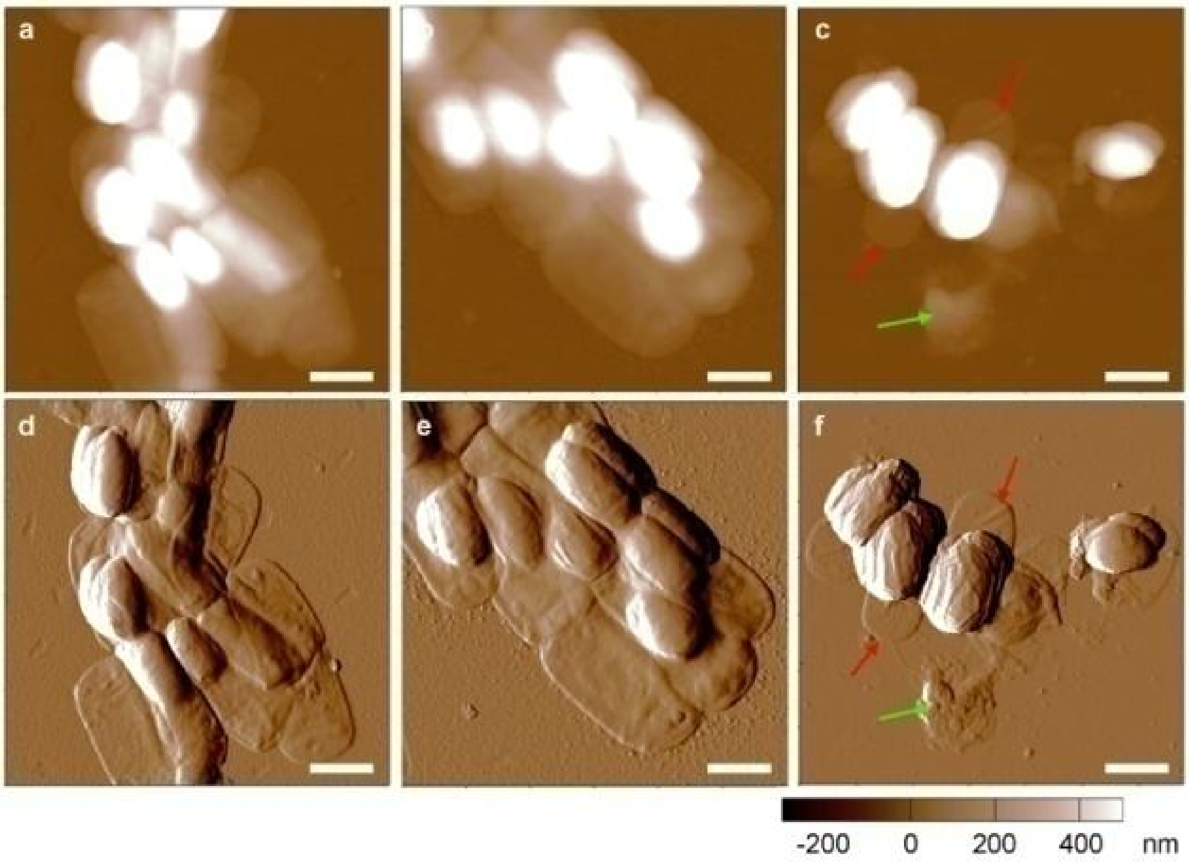

Figure 4.10: Topography (top row) and AFM amplitude (bottom row) images of *Bacillus cereus* after sporulation was triggered. (a, d) 18 hours. (b, e) 24 hours. (c, f) 42 hours. At this point, the cells lyse and spores are released. Red arrows show the exosporium of the released endospores. Green arrows show the surrounding cell debris. Scale bars = 1 μm.

Table 4.2. Morphology analysis of *Bacillus cereus* at different time points during sporulation. The height profile measurements were performed on several images on different areas (n=20). A: Maximal height of single cells (nm). B: Maximal height difference on single cell surfaces (nm).

	0 hour	8 hours	12 hours	18 hours	24 hours	42 hours
A	366.5±12.2	370.3±12.7	442.0±50.9	667.5±27.0	703.9±22.8	789.6±17.4
B	34.3±3.5	37.0±5.2	183.4±36.9	418.5±41.5	585.2±41.40	740.8±35.2

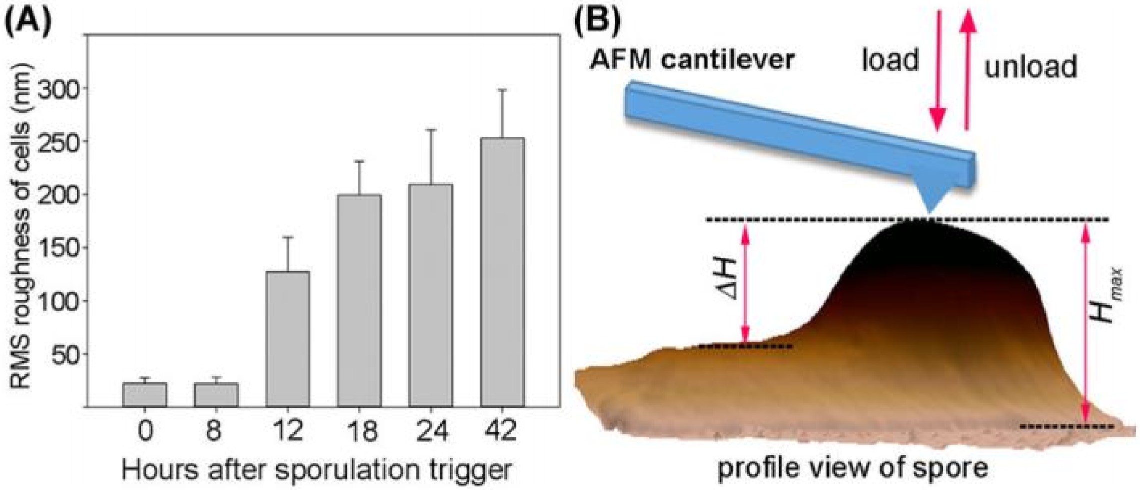

Figure 4.11. (a) RMS roughness values obtained from cell surfaces via AFM imaging (n~10 cells). As spores form, the roughness of the cells increase till the cells are lysed at t=42 hrs. (b) Schematic representation of morphology analysis associated with of a nanoindentation experiment on a "24 hours" sample. "H_{max}" represents the "maximal height of single cell (nm)". "ΔH" represents the "maximal height difference on single cell surface".

Mechanical change during sporulation

In addition to morphology variation, measuring the mechanical properties of cellular systems is an important parameter to characterize various cellular processes including adhesion, division, sporulation and carcinogenesis [210, 211].There have been a few reports on measuring mechanical changes during cellular processes using AFM based nanoindentation. These have included changes in *Escherichia coli* before and after thermal treatment [212], changes in stiffness of neurons during neurite outgrowth and upon disruption of microtubules[213], and the elasticity variation of *Pseudomonas aeruginosa* prior to and after antibiotic treatment [214]. However, the transition of mechanical properties from the vegetative cell to the spore has not been reported. In general, the nanomechanical characterization of *B. cereus* is largely unknown. During the sporulation process, the *B. cereus* mother cells synthesize multiple protein layers (inner coat and outer coat) and a thick peptidoglycan layer (cortex) for building the endospore. This implies that endospore formation would be accompanied by a change in the elasticity of the cell surfaces. Also, it is postulated that if the observed bump at either end of these cells is a real, incipient endospore, the elasticity of these structures should be close to that of a mature endospore and different from the rest of the cell. The AFM allows us to determine this progression *via* nanoindentation coupled with a technique of "elasticity mapping" to determine the mechanical nature of the entire cell surface at the nanoscale (Figure 4.11b). Three representative samples at 0 hour, 24 hours, 42 hours and a mature spore were studied. The indent curves fit well to a Hertzian mechanical model, allowing us to obtain spatially resolved Young's moduli. In each case, the mechanical elasticity map could be overlaid on the topography of the cell to show the variation of properties across the entire cell (Figure 4.12).

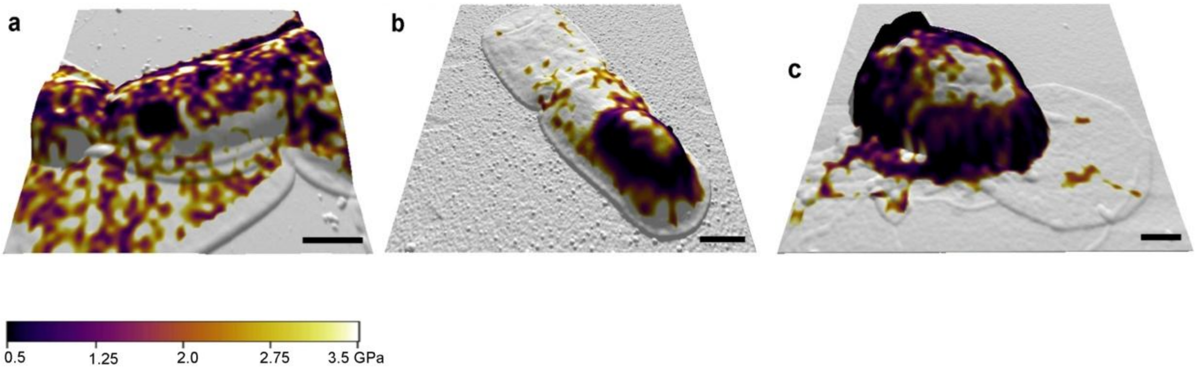

Figure 4.12. Change of nanoscale mechanical property before and after sporulation was triggered. (a) Elasticity map of vegetative cells.(b) Elasticity map after cells were cultured in G medium for 24 hours. (c) Elasticity map after cells were cultured in G medium for 42 hours. The scale bar in each image represents 250 nm. Scan sizes were varied to capture entire cells.

Initially, vegetative cells were probed as shown in Figure 4.12a. The overlay of elasticity map and height map shows good correspondence between the elasticity and morphology (softer on vegetative cell surface and stiffer on glass). The average Young's modulus across the vegetative cell surface is 0.72±0.29 GPa, which is in excellent agreement with the recently reported value of 0.83±0.48 GPa measured at a few points on a *B. cereus* cell surface [184]. Following sporulation and the development of the nascent endospore, three characteristic regions of elasticity can be observed on the cell surface (Figure 4.12b, sample after "24 hours" sporulation): i. An area on the flat surface of mother cell with an average modulus (2.52±0.59 GPa) that is higher than that of a vegetative cell. This is hypothesized to be because the protoplasm of mother cell has been used to build endospore multilayers causing an increase in stiffness. Another explanation is that that the indentation may "feel" more of the stiff substrate since the sample is very thin at this area [185]. However, this only happens when the radius of contact area is comparable to the sample thickness [215]. The AFM height images show that the thickness of this area is around 120 nm, while the radius of tip (close to contact area) is only around 10 nm. Thus, the "finite thickness effect" is negligible for the whole process study. ii. A softer "ring-like" area at the edge of endospore that may be caused by the curvature/edge effects, and iii. A stiffer area in the center of endospore. This is hypothesized to be because of endospore multilayers causing an increase in stiffness [216]. The underlying endospore can be clearly detected at this stage. A high resolution elasticity map obtained over the entire endospore area (Figure 4.13) further delineates the clear characteristic elasticity distributions. Here, measurements of elasticity over 2500 points (50 x 50 grid) over a smaller area of the cell surface are shown. As expected, elasticity map on the 42 hour sample (released spore, Figure 4.12c) reveals a similar elasticity distribution and Young's modulus with the 24 hour sample, implying the bump on the topographical image at this time period is indeed an underlying endospore. Taken together, the nanoindentation data further confirm the formation of endospore from the spatially observed progression of this process.

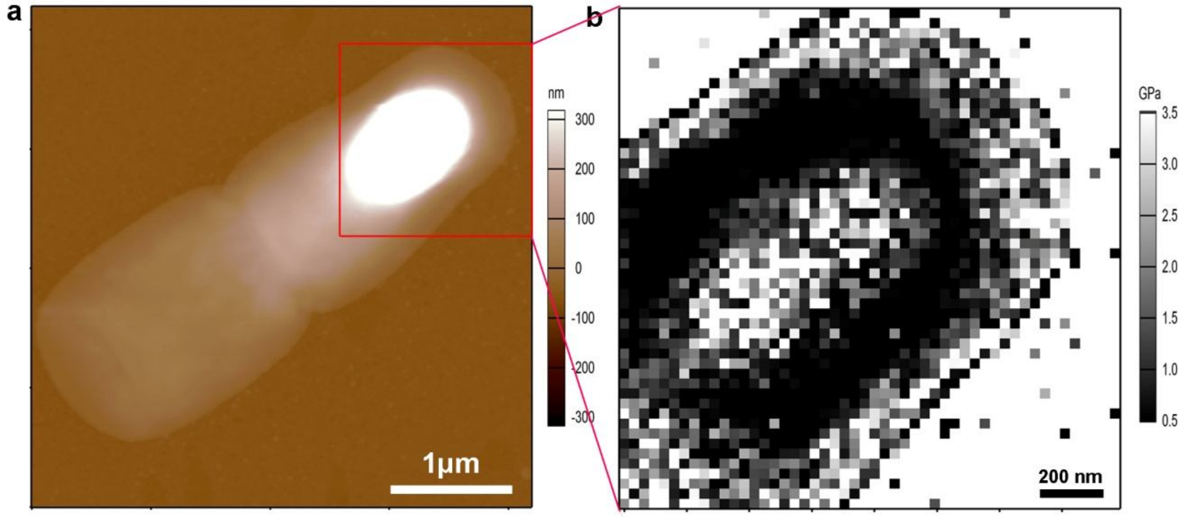

Figure 4.13. Nanomechanical map of a *Bacillus cereus* cell after 24 hours of initiation of sporulation. The underlying spore is clearly visible from the topography and elasticity maps. (b) The elasticity map (50x50, higher resolution on smaller area) corresponds to the area (marked by red box) in the height map.

Finally, mature spores harvested from sporulation medium and after air dried were investigated. The high resolution map of the entire spore is shown in Figure 4.14a in the form of an overlay of mechanical data on the surface topography. This image is obtained by the simultaneous capture of both mechanical and topographical data in a single scan that is completed under 30 minutes. While the spatial resolution is therefore somewhat limited in comparison to previous images, it demonstrates this technique as a fast method to extract information from the cell/spore. Surface ridges on *B. cereus* as observed through nanoscale imaging in earlier reported works are clearly seen in the topographical images [194, 217]. Interestingly, these areas are also clearly observed as softer regions of the spore surface. This is consistent with earlier hypotheses that in an air-dried state, the decreased spore core and cortex dimensions result in ridges formed due to the folding of the spore coat [194].The nanoindentation therefore reveals this configuration on the raised folds. The progression of the average modulus across this area (~200 data points) during the process of spore formation is shown in Figure 4.14b. The moduli at the 24 hour and newly released spore are very similar, while that of the air dried spore is around 50% higher. This is expected owing to the process of dehydration that results in mechanically robust spores. The average modulus of 5.1±0.3 GPa is consistent with reported values of 6.6±0.4 GPa on mature *Aspergillus nidulans* spores [218].Overall, the resultant increase in mechanical strength of the spores contributes to their mechanical robustness and resiliency. It must be noted here that *Bacillus* (endo) spores, as indeed several cellular systems, have a high curvature. Therefore, an accurate determination of the exact elasticity values across the entire cell, especially at the edges is challenging. In our results, a softer ring-like area surrounds the stiffer center area of endospore. This may be due to the curvature/edge effects of nanoindentation as well as the collapsed exosporium of the sample during air drying. However, the flat center area of endospore provides reliable elasticity values to confirm the observations.

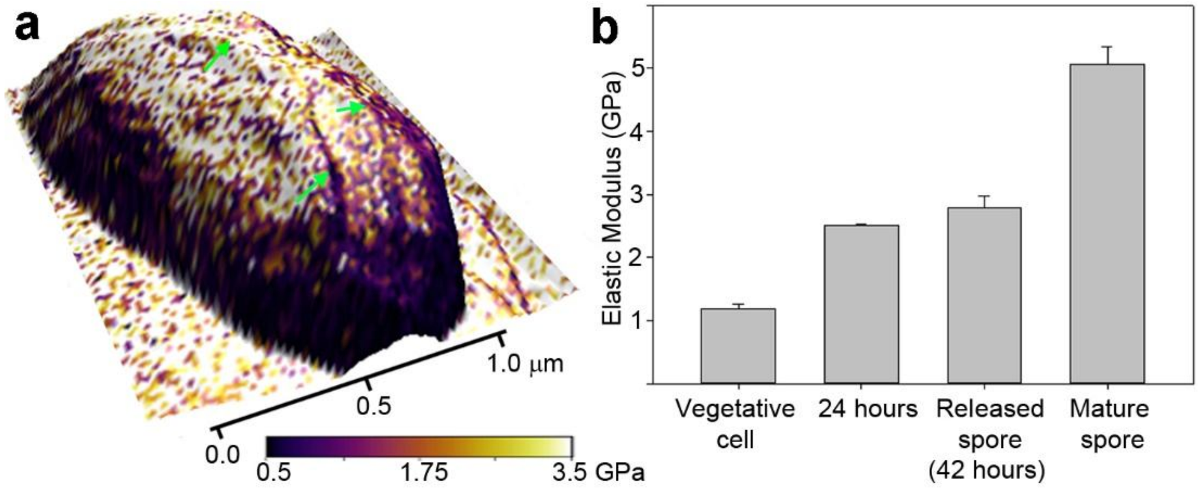

Figure 4.14 (a) Nanomechanical map formed by overlay of elasticity data on the topography of a *Bacillus cereus* spore. The green arrows show the position of ridges on the surface of the spore. (b) Change in elastic modulus across the center region of the cells during the process of sporulation (~200 points measured across several samples). The elastic modulus increases nearly 300% from the vegetative cell to the mature spore.

4.4 Conclusions

In summary, in this chapter, the AFM recognition force mapping strategy is demonstrated to quantitatively detect and spatially map surface carbohydrates on vegetative and spore cells of *B. cereus* at the single cell level. The correlations between the force and height maps clearly show that recognition force mapping can spatially locate specific targets on entire cell surfaces. By calculating the binding using different lectin probes, WGA and ConA, it is shown that surface molar ratios of Glu/Man:GlcNAc range ~1:4 on a vegetative cell but switch to ~3:1 on a spore. These values are in excellent quantitative agreement with previously reported bulk analyses using GC-MS, while providing clear spatial distributions on the cell surface. Control experiments were used to confirm the specificity of the lectin-carbohydrate interactions. One of the significant advantages of the recognition force mapping strategy described here is the simultaneous collection of both forces and height data which renders the analysis of the single spore quickly (each image can be obtained and analyzed < 1 hour). Furthermore, time-lapsed AFM imaging and elasticity mapping demonstrate the power of AFM applied in microbiology for multi-parametrically probing important biological processes at the single cell scale. Overall, AFM-based "recognition force mapping" is shown to be a versatile platform to quantitatively detect and map bacterial surface biomarkers, specifically carbohydrate compositions but easily extendable to a host of cell-surface targets, while monitoring changes in surface biochemical properties during cellular processes at the single cell level.

[This chapter contains results that have been previously published in:

Wang C, Ehrhardt CJ, Yadavalli VK, "Single cell profiling of surface carbohydrates on Bacillus cereus," Journal of the Royal Society Interface, 12, 20141109, Feb 2015.

Wang C, Stanciu C, Ehrhardt CJ, Yadavalli VK, "Morphological and mechanical imaging of Bacillus cereus spore formation at the nanoscale." Journal of Microscopy, 258, 49-58, Jan 2015.]

CHAPTER 5

THE EFFECT OF INACTIVATION AND GROWTH TEMPERATURE ON THE SURFACE PROPERTIES OF *YERSINIA PESTIS*

5.1 Introduction

Previous chapters have shown the spatial mapping of specific cell surface biomolecules is a powerful tool for monitoring changes in cell surface biochemical properties during cellular processes or when microenvironment is disturbed at the single cell level. In this chapter, the applications of this technique for addressing practical cellular related questions are shown in a different cell system.

Yersinia pestis is a facultative, anaerobic bacterium that induces a systemic, infectious plague with high mortality and morbidity. It has been the causative agent of at least two historical pandemics: the Justinian plague and the Black Death [49, 50]. The present number of human plague incidents in the world is relatively stable (~ 2000 reported cases per year) [219]. Nevertheless, as a virulent bacterial pathogen with strains resistant to multiple antibiotics, and potential use in bioterrorism, *Y. pestis* remains a threat to human health and the subject of active inquiry [51]. Research using wild-type *Y. pestis* involves strains classified at Biosafety Level 3 (BSL3). However, a number of avirulent or vaccine strains are widely utilized and manipulations and analyses are conducted with appropriate Biosafety Level 2 (BSL2 or BSL2+) bio-containment procedures and equipment. For example, *Y.pestis* KIM strain is often used as an avirulent surrogate [52]. Avirulent strains of *Yersinia pseudotuberculosis* have been proposed as live vaccines against bubonic plague and can be studied in a BSL2 environment [220]. Attenuated strains of pathogenic bacteria have also been used as models to provide guidelines evaluating the effectiveness of techniques to inactivate bacteria in different settings [221, 222].

While many laboratories can handle and perform routine microbiological assays at BSL2 using such avirulent strains, there are numerous situations that may necessitate transport of intact organisms *outside* this environment. Downstream analyses including flow cytometry, mass spectrometry, high resolution microscopy - scanning electron microscopy (SEM), transmission electron microscopy (TEM) and atomic force microscopy (AFM) tend to involve specialized instrumentation with a large footprint in the lab. Similarly, samples may need to be shipped externally to a different laboratory with complementary expertise. Proper approaches are needed to inactivate such pathogens (reduce to a non-viable and non-infectious state) prior to removal from a BSL2 setting and ensure safety of researchers and compliance with regulatory standards. It is often vital that the process of inactivation preserves the cellular integrity, surface morphology, and biochemical properties of the bacteria to enable further study.

Several protocols have been reported for the inactivation of pathogenic microorganisms prior to characterization/analysis [223]. Chemical fixation methods such as cross-linking with aldehydes and precipitation with alcohols can be used [224], and are common front end steps for a variety of staining procedures prior to light microscopy [225]. Physical methods such as irradiation or heating at high temperature have also been employed [226-228]. However, the question of how the inactivation process affects *subsequent biochemical analysis* of the cell has received lesser attention [229]. A recent study concluded that inactivation procedures had minimal effect on the protein expression and spectral data quality for liquid chromatography-tandem mass spectrometry (LC-MS/MS), but recommended inactivation with ethanol with a secondary preference to irradiation [230].

Furthermore, the effect of growth temperatures may be relevant to the *natural* ecology of *Y. pestis*. Temperatures in nature typically vary from 0°C to 42°C, involving transmission from the cold-blooded flea vector (20-25°C) to the warm-blooded mammal host (37°C), and infected animals during winter hibernation (6°C) [53]. Adaptations to different growth temperatures have been associated with transformations on *Y. pestis* surfaces [54-56]. In this work, using AFM based nanoscale imaging and force recognition mapping, the surface properties of the avirulent strain KIM D2 are investigated. Though the KIM D2 strain is attenuated for virulence (lacks plasmid pCD1) and is classified as BSL 2, it still contains virulence-associated genes, and other two critical pathogenicity-related plasmids which provide it with specialized mechanisms for infiltrating mammalian hosts [231]. Considering that it has been used in the lab as a model for *Y.pestis* studies [232], and given a historical precedent of accidental infection [52], characterization of this strain has great applied importance.

Initially, changes in the morphology of *Y. pestis* following different treatments (methanol, formaldehyde, heat, UV radiation) are presented. To analyze how the biochemical nature of the cell surface is affected, the force recognition mapping strategy is used to study the properties of single cells [57, 58]. The lectin wheat germ agglutinin (WGA) is used to spatially detect and quantify the surface lipopolysaccharides (LPS) via the carbohydrate N-acetylglucosamine (GlcNAc) with outermost localization on the cell surface as one of the terminal residues of the core LPS oligosaccharide. LPS has been long investigated as an important factor in the virulence of Gram-negative *Y. pestis* owing to its heterogeneity and variation in response to temperature changes during transmission [233, 234]. Structurally, *Y. pestis* LPS is composed of lipid A embedded into the outer membrane, and a core oligosaccharide anchored to the lipid A [235]. Both domains can change their structures under different environments, and are hypothesized to help *Y. pestis* avoid host innate immune responses and enhance its pathogenicity [236]. Temperature-dependent variations in the domain structures have been reported, making surface LPS an important and accessible target [54, 237, 238]. Here, whether ecologically significant transitions could be observed in methanol-fixed cells is examined. Specifically, whether the well-documented shifts in structural and chemical features of the cell surface could be captured in cells grown at three different temperatures is examined.

Although the methods investigated here are not indicative of the full range of inactivation protocols for bacteria, they represent fundamentally different and common strategies, and have been used for the direct examination of *Yersinia* [239, 240]. These results provide insight into the tools for studying virulent pathogens with equipment that may not have elevated biocontainment capabilities - inactivation followed by nanoscale evaluation of the effects on cell morphology and surface bioactivity. Understanding how external microenvironments (temperature, irradiation), including those designed to inactivate the *Y. pestis*, affect the structure and biochemical behavior of the cell surface, can help us not only design better inactivation protocols, but also shed light on the *in situ* characteristics of pathogens.

5.2 Experimental section

5.2.1 Chemicals and instruments

(1-Mercaptoundec-11-yl) hexaethylene glycol (Oligoethylene glycol (OEG) terminated thiol), HS-C_{11}-$(EG)_6$-OH, and (1-mercaptohexadecanoic acid)-N-succinimidyl ester (NHS terminated thiol), HS-C_{15}COO-NHS, were purchased from NanocsInc. (Boston, MA). Wheat germ agglutinin (WGA), 3-aminopropyltriethoxysilane (APTES) and glutaraldehyde were purchased from Sigma-Aldrich (St. Louis, MO). Phosphate-buffered saline (PBS pH 7.4) (11.9 mM phosphates, 137 mM sodium chloride and 2.7 mM potassium chloride) and ethanol (200-proof) were purchased from Fisher Scientific (Waltham, MA). Mica was purchased from Ted Pella (Redding, CA). Ultrapure water (resistivity 18.2 MΩ.cm) was obtained from a MilliQ water purification system (Millipore Scientific, MA). AC240TS cantilevers (Olympus) were used for non-contact mode imaging in air, while gold coated TR800PB cantilevers (Olympus) were used for force measurements.

5.2.2 Cell culture and fixation/inactivation protocols

Y. pestis KIM strain (NR-4682, Derivative 2, BEI resources, Manassas, VA) was maintained on trypticase soy broth (TSB, EMD Chemicals Inc., Gibbstown, NJ) at 25°C. For samples grown at different temperatures, single colonies of *Y. pestis* were inoculated into 125 ml of lysogeny broth (Lennox, BD, Franklin Lakes, NJ) and incubated for 24 hours at 25°C or 37 °C and 225 rpm. In addition, a small aliquot (~10mL) of a 37°C culture was incubated at 6°C for ~9 months. For methanol and formaldehyde fixation, 1 ml cell suspension was taken from the culture medium and placed into a sterile 1.5 ml microcentrifuge tube. Cells were collected by low-speed centrifugation (1 minute, 4°C, 3220 x g). The pellet was re-suspended and washed with 1 ml sterile ultrapure water to remove the culture media. The pellet was then re-suspended in 500µl of 100% methanol (Pharmco Inc.) and incubated at 4°C for 10 minutes, or in 500 µl of formaldehyde (4%) (Fisher Scientific) and incubated at 4°C overnight. Following incubation, the cells in methanol or formaldehyde were collected by centrifugation. Each pellet was re-suspended and washed two times with 1 ml ultrapure water. Finally, the pellet was re-suspended in 1 ml PBS buffer before use. 10 µl of cell suspension was then plated onto eight trypticase soy agar plates and placed into a stationary incubator at 25°C for 48 hours to verify sterility. For heat inactivation, 1 ml of cell suspension in a microcentrifuge tube was placed in a water bath at 68°C for 10.5 hours. The cell suspension was cooled to room temperature and 10µl was plated on eight TSA plates and placed in a stationary incubator at 25°C for 48 hours to verify sterility. The suspension was washed following the same protocol used for methanol and formaldehyde inactivated samples. For UV inactivation, cells were collected by low-speed centrifugation (1 minute, 4°C, 3220 x g). The pellet was re-suspended and washed with 1 ml sterile ultrapure water to remove the culture media. Before transport from BSL2 to BSL1 laboratory for AFM analysis, 10 µl of cell suspension was plated onto glass slide and put into UV crosslinker (Fisher Scientific) at an exposure of ~4 mJ/cm^2.

5.2.3 Sample preparation for AFM

Aminopropyl-functionalized mica (AP-mica) coupled with glutaraldehyde was used to immobilize cell samples. Freshly cleaved mica was incubated in APTES vapor in a vacuum desiccator for 12 hours to form AP-mica. The mica was immersed in 1 ml 2% (v/v) glutaraldehyde water solution for 1 hour and rinsed with deionized water. A 20 µl cell suspension was spotted and incubated for 30 minutes. The sample was then immersed in 1 ml 1% (v/v) ethanolamine PBS solution for 30 minutes to block the glutaraldehyde on the areas without cells. Finally, the AP-mica surface was rinsed with distilled water three times to remove loosely-immobilized cells, remaining culture media, salts and unreacted ethanolamine.

5.2.4 AFM probe functionalization and force recognition mapping

AC240TS cantilever (spring constant ~2 N/m, resonance frequency 70 kHz) were cleaned using high-intensity UV light to remove organic contamination and used for imaging in air and characterization of the surfaces in non contact mode. Gold coated cantilevers were cleaned in UV/ozone for 15 minutes. The gold cantilevers were then functionalized by immersion in mixed thiol solution ($HS-C_{11}-(EG)_6-OH$ and $HS-C_{15}COO-NHS$) in ethanol for 16 hours[87]. Cantilevers were rinsed with ethanol, and incubated in a 100 nM lectin (WGA) in PBS buffer for 1 hour at ambient temperature. Our group has earlier shown that this functionalization strategy limits the number of lectins on the tip surface to 1-3 [102]. Lectin-functionalized cantilevers (spring constant ~0.15 Newton/meter (N/m), resonance frequency 15 kHz) were then used to obtain force data on cells in PBS. Each experiment was repeated on at least 5 different cells. Force curves were obtained by collecting a series of sequential force curves in an $m \times n$ grid (an array with m lines and n points per line). Each force curve was obtained at the same loading rate (135 nN/s, at a ramp velocity of 900 nm/s), allowing binding to occur (contact time 0.1 second), and then retracting. 80×80 force curves were collected over a defined area (~3µm×3µm) and unbinding forces were displayed on a scale of color. The height maps of the same area were generated simultaneously. As a control, blocking experiments were performed by a buffer exchange of PBS containing 5μg/ml lectin in the fluid cell. All images including height and force maps were analyzed using custom routines in Igor Pro 6.32 A (Wavemetrics Inc, OR).

5.2.5 Transmission Electron Microscopy (TEM) imaging

For TEM imaging, cells were pelleted and fixed in 2.5% glutaraldehyde in 0.1M cacodylate buffer, pH 7, with 500 ppm ruthenium red for 4 hours at 4°C followed by three washes in 0.1M cacodylate buffer (20-40 minutes each). Next, samples were fixed in 2% osmium tetroxide in 0.1M cacodylate buffer, pH 7.0, with 500 ppm ruthenium red for 1 hour and washed three times in 0.1M cacodylate buffer. Cells were then dehydrated through an ethanol series (50%, 70%, 80%, 95%, and three changes of 100% ethanol for 10-20 minutes each) and washed three more times in propylene oxide (30 minutes each). Samples were infiltrated with a 1:1 mixture of propylene oxide and resin overnight followed by two to three changes in fresh, pure resin for approximately eight hours each. Lastly cells were polymerized in the resin for two days at 55-50°C. A Leica EM UC6i Ultramicrotome (Leica Microsystems, Chicago IL) was used to make 600-700Å sections onto grids which were then stained with 5% uranyl acetate and Reynold's Lead Citrate. Imaging was performed with a JEOL JEM-1230 TEM (Jeol USA, Inc., Peabody MA) with a GatanOrius SC1000 digital camera (Gatan, Pleasanton, CA).

5.3 Results and Discussion

Understanding the effect of different inactivation strategies on the surface properties provides a means to gauge the suitability of the bacterial cell for further study. This is critical when transporting bacteria outside a BSL-2 environment for downstream analyses. Investigation of the nanoscale morphology and surface biochemical property of *Y. pestis* at different temperatures can also provide a way to elucidate the mechanisms of survival and persistence in the environment. However, to date, such studies on strains of pathogenic and non-pathogenic bacteria have been limited. Chen et.al. first showed SEM images of *Y. pestis* at different growth temperatures, with capsular antigens as a granular layer on the surface [241]. Images observing the surface morphology with or without glucose in growth media [55], and with or without the hemin storage gene were also shown using SEM [242]. Chao et.al. compared the effect of different fixation methods including aldehyde and alcohol fixation on bacterial morphology using AFM imaging [96]. Both fixation methods could effectively preserve cell morphology, whereas aldehyde fixation was preferable to alcohol, since the latter tended to detach the surface filaments (i.e., flagella and pili). Xing et. al. revealed the significant changes of morphological and nanomechanical properties of *Bacillus anthracis* spore before and after heat inactivation [243]. Here, both the morphology (ultrastructure) of *Y. pestis* as well as changes in the biochemical properties of the cell surface under different conditions are shown. These analyses at a single cell level demonstrate how the external microenvironment plays roles in modulating both the morphology and key components of the bacterial surface.

5.3.1 The effect of fixation/inactivation methods on the surface morphology of *Y. pestis*.

Initially, the treated cells were plated onto agar plates and placed in a stationary incubator at 25°C for 48 hours to verify sterility. No bacterial growth was observed on all agar plates, indicating that the treatments were effective. Treated *Y. pestis* cells were imaged at the nanoscale in air using non-contact AFM imaging to show high resolution topography, including the presence of surface nanostructures. Figure 5.1a and 5.1d show *Y. pestis* inactivated by methanol treatment. It can be seen that the rod-shaped cell has a smooth surface, which is topographically similar to cells grown at the same temperature (~25°C) previously reported, albeit using SEM [55, 241]. Figure 5.1b and 5.1e show formaldehyde inactivated *Y. pestis*. Two morphological characteristics can be observed - i) cells aggregation and ii) uneven surfaces with stacked layer structures at the cell edges. Similar patterns of aggregation and surface changes are also observed with TEM imaging (Figure 5.2). AFM images show uneven surfaces and buckling of membrane boundaries are prevalent in formaldehyde-fixed cells. Figure 5.1c and 5.1f show that the morphology of heat-inactivated *Y. pestis* changes significantly and the size of the cell is altered with respect to methanol-treated cells. It is apparent that the surface topography is irregular, compared to methanol-treated cells. A quantitative analysis was performed on several cell samples from different AFM images ($n=20$). The area of the cell decreases by 35 and 40% for formaldehyde and heat treatment respectively, in comparison to the methanol-treated cells (Table 5.1). Compared to methanol inactivation, the roughness of *Y.pestis* surface increases significantly when using formaldehyde and heat treatments (Table 5.1).

Based on AFM and TEM results (Figure 1 and 2), it is hypothesized that the observed aggregation and uneven surfaces of the cells may result from formaldehyde induced cross-linking. Formaldehyde is a reactive electrophilic species that reacts readily with various biological macromolecules on cell surfaces, such as proteins, glycoproteins, and polysaccharides [244]. The intra-and intermolecular cross-linking of macromolecules on the cell surface may therefore considerably alter their morphology and make them irregular. Cellular debris or residual medium components that bind to the cell surface during batch culturing maybe cross-linked to *Y. pestis* surface further affecting its intrinsic morphology [245]. In contrast, methanol has minimal cross-linking effects. The resulting morphology is consistent with images of non-fixed organisms, [55, 241] and the edges do not show the same uneven appearance observed in formaldehyde-treated samples (Figure 1 and 2). It should be noted that some methanol treated cells showed significant shrinkage (Figure 2a), likely an artifact of one step fixation with 100% methanol which may rapidly dehydrate the cell and cause a reduction in the overall cell volume. Although a majority cells are unaffected, fixing cells using a methanol gradient (e.g., 50%, 80%, and 100% methanol sequentially) would likely minimize this effect. The relative absence of cell aggregation suggests that methanol treatment may therefore be advantageous when analyzing samples with high cell concentrations as may be expected in some batch culture specimens. In the three inactivation methods, heat inactivation shows the greatest effect on cell morphology including the decrease of cell size and increase of surface roughness. This may be caused by a loss of cell surface integrity and the debris of denatured cell surface material. In addition, the ultrathin layer surrounding the cell body indicates this damaged outer membrane.

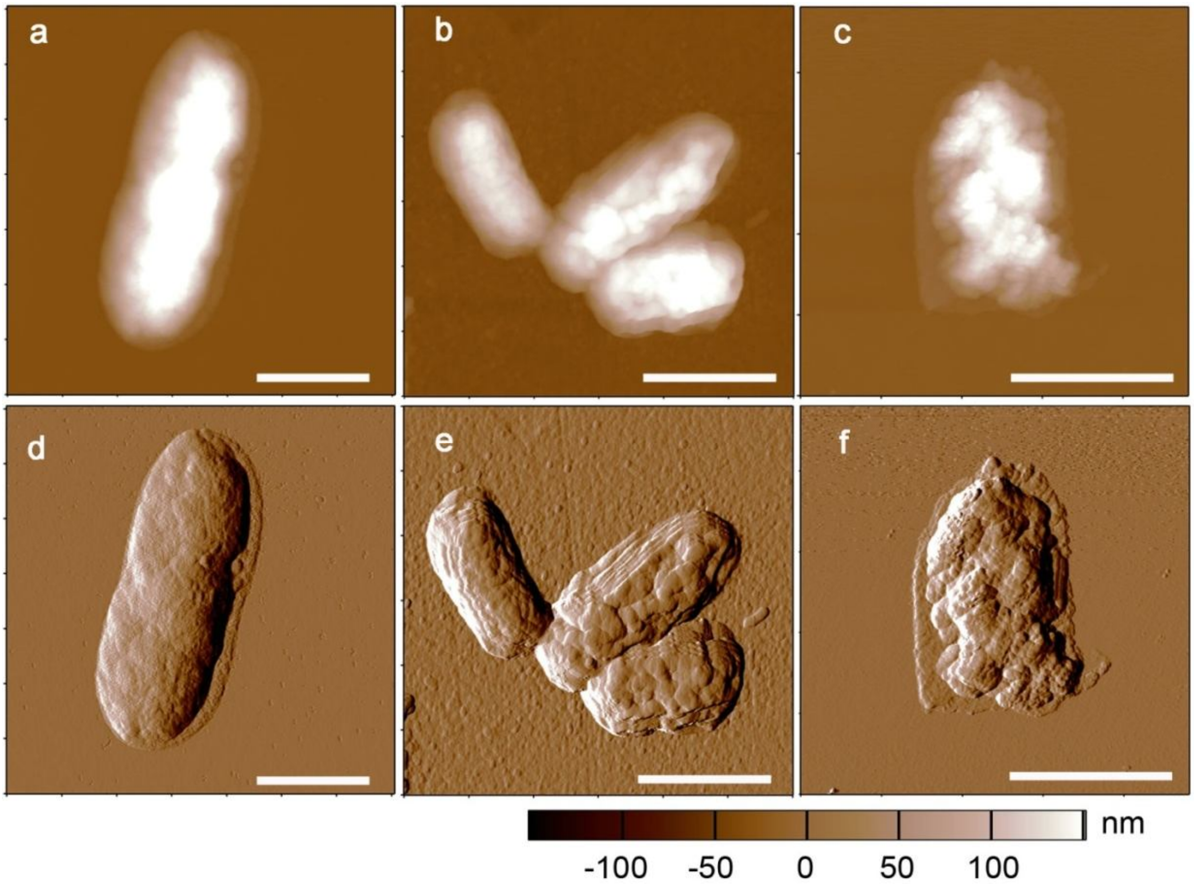

Figure 5.1. AFM images of *Y. pestis* cells after methanol (a and d), formaldehyde (b and e) and heat inactivation (c and f). Panels (a), (b) and (c) are height maps. Panels (b), (e) and (f) are the corresponding amplitude images. Scale bars = 1 µm.

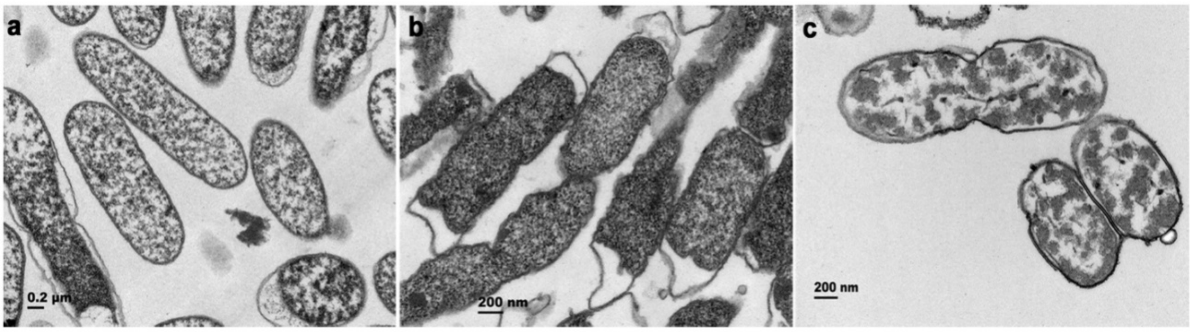

Figure 5.2. TEM images of *Y. pestis* cells (a) after methanol (b) formaldehyde and (c) heat inactivation. Scale bars = 0.2 µm.

Table 5.1. Quantitative analysis of *Y. pestis* surfaces grown at different temperatures and after different treatments (*n*=20).

Conditions (Culture temperature, inactivation)	RMS Roughness (nm)	Cell area (μm^2)	Cell height(nm)
25°C, methanol	17.31±5.08	2.24±0.72	185.67±6.38
25°C, formaldehyde	32.45±7.46	1.44±0.44	180.92±7.93
25°C,heating	31.03±4.38	1.33±0.19	125.75±6.49
37°C,methanol	25.79±7.15	2.00±0.37	195.50±15.94
6°C,methanol	22.50±5.68	1.85±0.36	171.75±8.99
37 °C, UV-C	16.40±3.79	2.68±0.24	224.00±14.51

5.3.2 The effect of inactivation methods on the biochemical nature of *Y. pestis* surfaces

Surface biochemical properties under different inactivation methods were investigated. One of the structural differences in LPS at different growth temperatures lies in the type and amount of the terminal monosaccharides [237]. To evaluate the effect of inactivation methods on *Y. pestis* surfaces, AFM-based “force recognition mapping” using cantilevers functionalized with wheat-germ agglutinin (WGA) (lectin specific to the amino sugar GlcNAc) was used to reveal a spatial map of the distribution of monosaccharides on the cell surface [9, 58]. Figure 5.3 shows the overlaid height and force (recognition) maps of *Y. pestis* surfaces treated by each of the inactivation methods. Force curves were analyzed automatically using a custom algorithm to rapidly differentiate between specific binding and non-specific interactions and determine binding forces. Figure 5.3a shows the spatial distribution of GlcNAc on a methanol inactivated cell. The overall distribution is observed to be homogeneous across the entire cell surface. It is important to note that the cell profiles show a simultaneous increase of recognition events, while the background without cells does not show any recognition events. In contrast, the density of GlcNAc on formaldehyde (Figure 5.3b) and heat inactivated (Figure 5.3c) cell surfaces drops significantly. Binding was calculated as a percentage of specific recognition events to the total number of force curves collected on the cell surface. The density of GlcNAc (10.8±0.9%) on methanol inactivated cells is ~5x higher than that of GlcNAc on formaldehyde (2.0±0.4%) and ~8x higher than heat (1.2±0.3%) inactivated cells, where the data are from five independent experiments on different cells (Figure 5.4). These results indicate that the morphological changes in *Y. pestis* inactivated by formaldehyde and heat also correlate with variation in GlcNAc content. This analysis confirms that formaldehyde and heat inactivation tend to damage the surface bioactivity of *Y. pestis*, compared to methanol fixed cells.

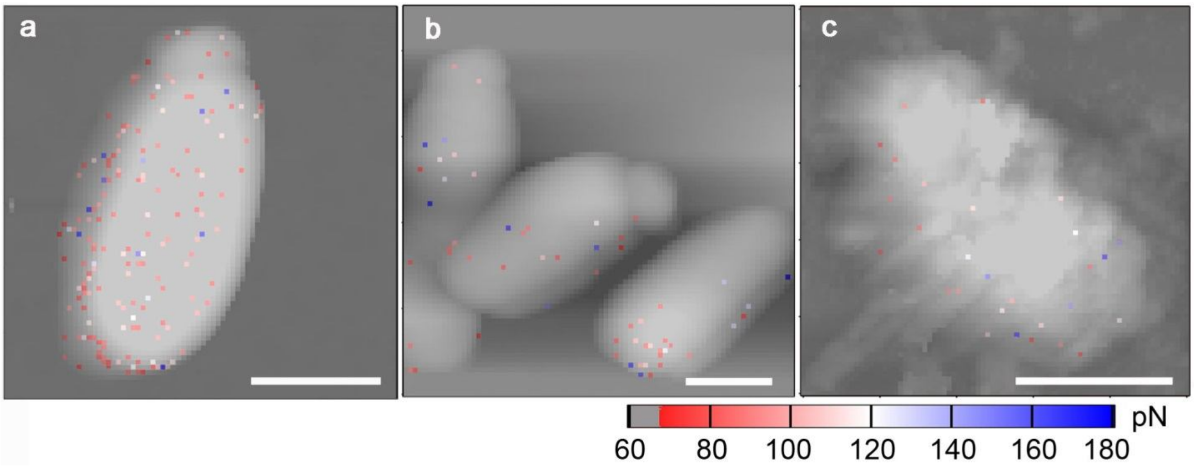

Figure 5.3. Overlay of force and height profiles for the carbohydrate GlcNAc on *Y. pestis* cell surfaces probed with its corresponding lectin WGA after methanol (a), formaldehyde (b) and heat inactivation (c). Scale bars = 1 μm. Pixel color indicates the magnitude of force (red represents low force and blue indicates high interaction force).

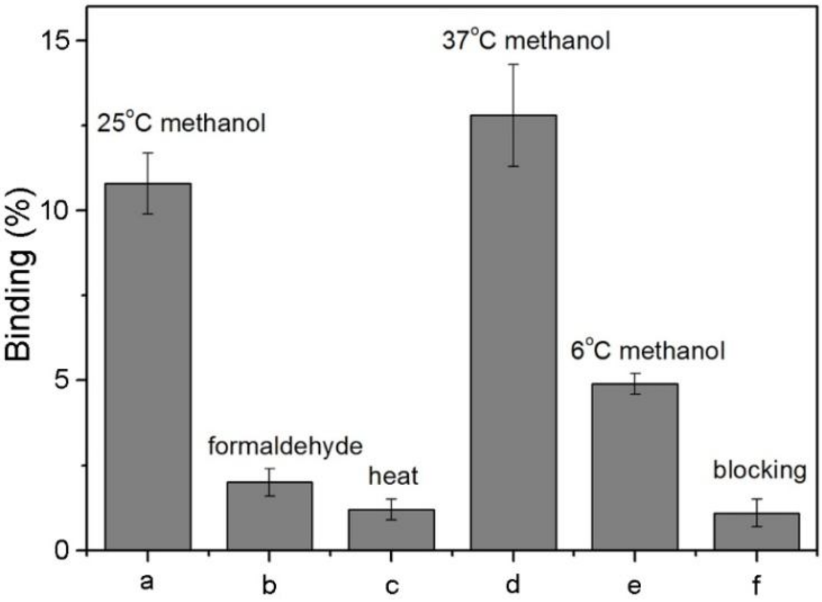

Figure 5.4. Analysis of the rupture forces showing the binding of WGA and the target carbohydrate GlcNAc on *Y. pestis* cells (calculated as the ratio of the number of points showing recognition events to the total number of points collected on the cell surface): (a) grown at 25°C inactivated using methanol; (b) grown at 25°C inactivated using formaldehyde; (c) grown at 25°C inactivated using heating; (d) grown at 37°C inactivated using methanol; (e) grown at 6 °C inactivated using methanol; (f) blocking experiment: cell surface of *Y. pestis* grown at 37°C probed with WGA lectin in the presence of free WGA that blocks GlcNAc binding sites showing a decrease in binding. The data are from five independent experiments for each system (n=5, error bar: standard deviation).

By observing the density and spatial distribution of specific carbohydrate target (GlcNAc) on cell surfaces, it can be concluded that methanol inactivation leads to minimal changes to the surface biochemistry of *Y. pestis*, whereas formaldehyde and heat treatments have significant effects on the cell surface. This is consistent with expected results wherein methanol treatment shave been demonstrated to preserve cell biochemical properties in comparison to other techniques. Earlier work showed a reduction in yeast cell aggregation in aqueous suspensions, facilitating sampling reproducibility of mass spectrometry (MS). Moreover, the MS signature quality improved when using methanol treatment, which implied the preservation of biomacromolecules on cell surfaces [246]. In a related study of the three common inactivation methods (heat, formaldehyde, alcohol) on the confocal resonance Raman spectra of purple non-sulfur bacteria, ethanol performed better than formaldehyde, whereas heat treatment had a strong, adverse effect on the resonant Raman spectrum [227]. Overall, compared to formaldehyde, there are several advantages of using methanol: i) lower toxicity and easy handling, ii) limited crosslinking, while formaldehyde crosslinking masks available specific binding sites of antigens hampering immunohistochemistry or bioactivity, iii) superior ultrastructure in comparison to formaldehyde treated cells [247-249], iv) permit immunological staining for most antibodies if needed downstream [247].

Although the elevated biosafety levels of the KIM D2 strain prevented us from analyzing live, untreated *Y. pestis* cells with the AFM, we assessed how each of the inactivation protocols may affect the 'natural' or in situ surface phenotype by analyzing cells that were sterilized via 254 nm ultraviolet light (UV-C) which penetrates the cell and damages genomic DNA. Both AFM imaging and biochemical force mapping were conducted on UV-C treated *Y. pestis*. Quantitative analysis based on AFM imaging shows that methanol treated cell size (including cell area and height) is similar to that of UV-C inactivated cells (Table 5.1). The density of GlcNAc indicates that methanol treated cell has similar surface biochemical nature with UV-C treated cell (Figure 5.5), further confirming the consistency of nanoscale surface features in methanol-treated cells.

Here, because of the infeasibility of analyzing untreated/wild-type *Y. pestis* directly with the AFM, UV-C inactivation was used as a reference to evaluate our chemical and thermal inactivation methods. UV-C induces the formation of DNA adducts inside the cell including cyclobutane pyrimidine dimers and pyrimidine pyrimidone photoproducts causing cells to be unable to reproduce, but preserves the surface morphology and biochemical nature [250]. Indeed, quantitative and qualitative analysis showed that UV-C inactivated cells were similar to methanol treated cells morphologically and biochemically serving as a control for the observed nanoscale surface features in methanol-treated cells. However, it is important to note that UV-C is itself not used as an inactivation method due to the possibility for photo-reactivation or dark repair of UV-damaged pathogens, leading to the re-growth of the pathogen under favorable environmental conditions [251]. Additionally, UV irradiation (254 nm) is potentially ineffective for liquid samples or samples with a large amount of cellular material due to its low penetration depth. From an application perspective, UV treated samples therefore typically require further treatments, minimizing its effectiveness in comparison to methanol [252].

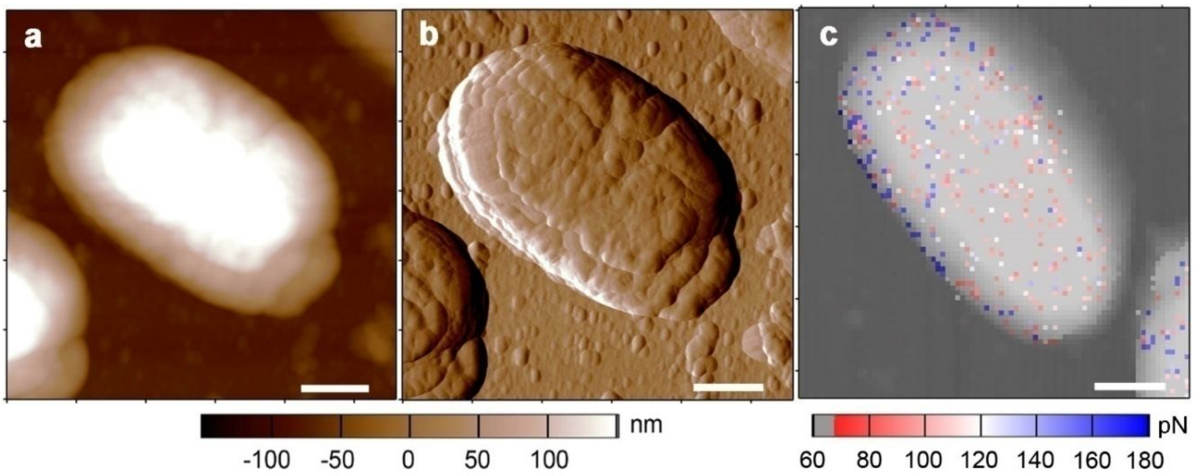

Figure 5.5. AFM images of *Y. pestis* cell after UV-C treatment. (a) Height image. (b) Corresponding amplitude image. (c) Overlay of force and height profiles for the carbohydrate GlcNAc on the cell surface after UV-C treatment. Scale bars = 0.5 μm. The color of pixels indicates the magnitude of force (red represents low force and blue indicates high interaction force).

5.3.3 The effect of growth temperature on *Y. pestis*

An important virulence factor for plague in mammals involves induction by a temperature shift from <26°C to 37°C, which mimics the transition from a flea to a warm-blooded mammalian host. Transmission from a flea or poikilothermic insects (20-25°C) to animals during winter hibernation (6°C) is a further prospect that cannot be ignored due to its important biological impact [53]. This adaptation to different growth temperatures has been associated with the transformation and modification of *Y. pestis* cell surface morphology and concomitant biochemical properties, especially surface lipopolysaccharides (LPS) [54-56]. The choice of a suitable inactivation method facilitates investigation of pathogenically relevant transitions in the surface polysaccharide composition induced by temperature variation. Here we tested whether ecologically significant transitions could be observed in methanol-fixed cells. Specifically, it was examined whether the well-documented shifts in structural and chemical features of the cell surface could be captured in cells grown at three different temperatures after each sample had been fixed with 100% methanol.

Figure 5.6 shows the morphology of *Y. pestis* grown at different temperatures at the single cell level. A morphological characteristic can be observed on *Y. pestis* grown at 6°C (Figure 5.6a), which is not observed on *Y. pestis* grown at 25 and 37°C - the ultrathin capsule surrounding the cell. This feature may be due to the loss of water. To survive at low temperatures, *Y. pestis* tends to reduce the fractional volume of cellular water [253]. Interestingly, this observation is similar to the morphology of "viable but non-culturable" *Y. pestis* in cold (~4°C) tap water. SEM and TEM images showed that the periplasmic space was greatly increased in the *Y. pestis* in cold (~4 °C) tap water and the cytoplasm of these cells had condensed into a small rounded cytosol, related to the low metabolic activity at this state [254]. Further work is needed to confirm that cells observed with AFM are truly in a dormant metabolic state. Figure 5.6b and 5.6c show *Y. pestis* grown at 25°C and 37°C, respectively. Cells grown at 37°C shows a rough surface compared to the smooth surface of those grown at 25°C (High resolution images on smaller areas (250 nm) are shown in Figure 5.7a, b). This result is consistent with previous studies, in which *Y. pestis* grown at 37°C shows an uneven and rough surface, while *Y. pestis* grown at 25 °C has a relatively smooth surface [55, 241]. Quantitative analysis of surface roughness further indicates that roughness at 37°C (25.79±7.15 nm) is ~50% higher than that at 25°C (17.31±5.08 nm) (Table 5.1). In Figure 5.6c, scattered particles and aggregates, as well as particulate strands (marked by green arrows) can be observed in the extracellular space of cells grown at 37°C. It is hypothesized that these features may represent the Fraction 1 (F1) capsular antigen [241], which has been observed to assemble into thin fibrils and denser aggregates on the bacterial surface.

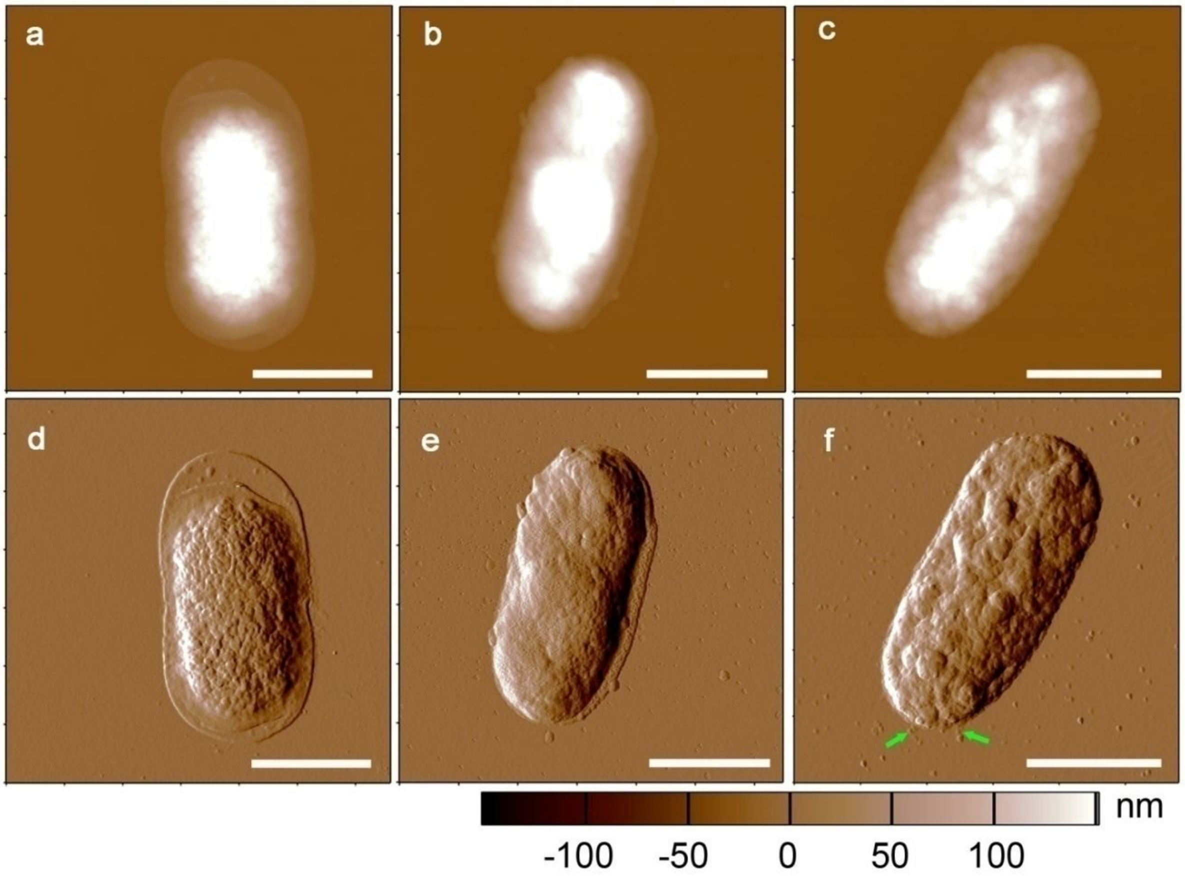

Figure 5.6. AFM images of *Y. pestis* cells grown at different temperatures: 6°C (a and d), 25°C (b and e) and 37°C (c and f). Panels (a), (b) and (c) are height maps. Panels (b), (e) and (f) are the corresponding amplitude images. Scale bars = 1 μm. Green arrows mark the particulate strands.

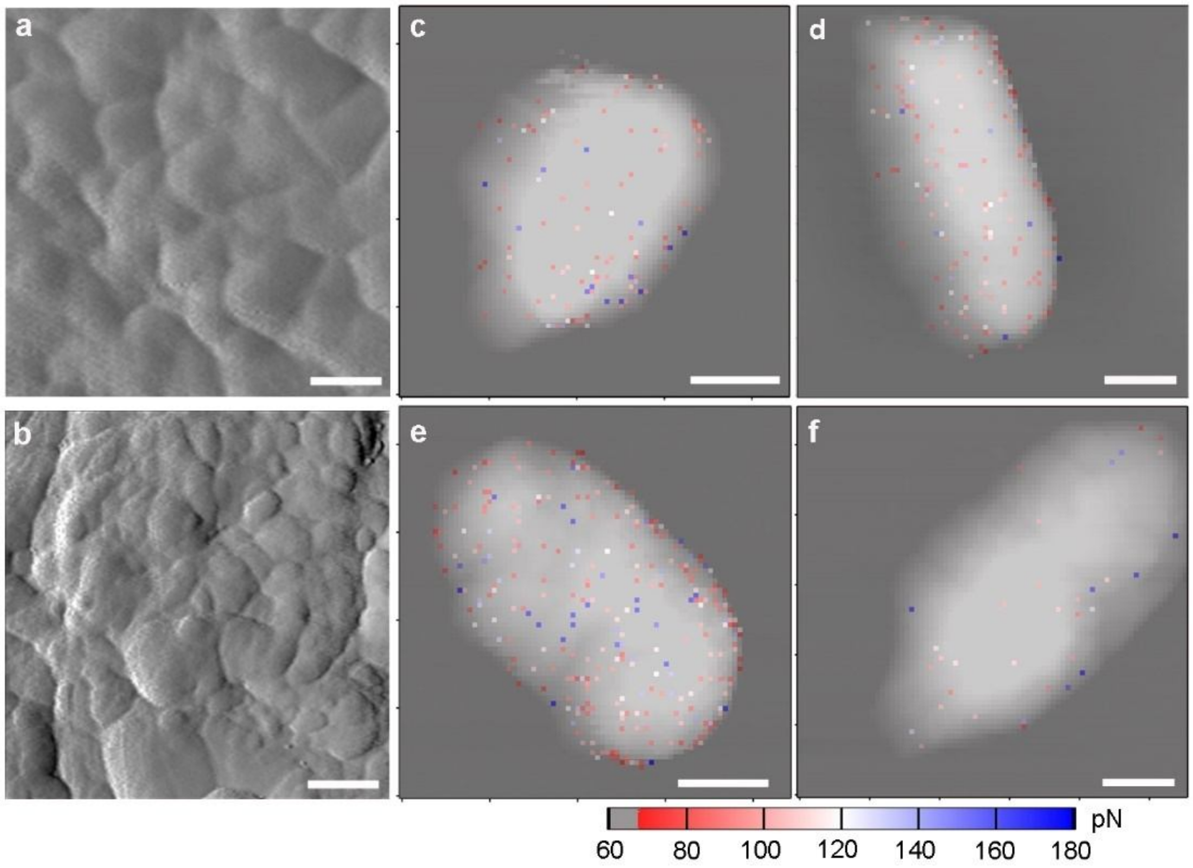

Figure 5.7. High resolution surface morphology of *Y. pestis* grown at (a)25°C and (b) 37°C (Scale bar = 50 nm). Carbohydrate mappingof *Y. pestis* surfaces grown at (c) 6°C. (d) 25°C. (e) 37°C. (f) Blocking experiment: the cell surface of *Y. pestis* grown at37°C probed with WGA lectin in the presence of free WGA that blocks GlcNAc binding sites. (Scale bars = 0.5 μm.) The color of pixels indicates the magnitude of force (red to blue indicating an increase in interaction force).

Surface LPS on cells cultivated at different temperatures were investigated by detecting the terminal carbohydrate residue-GlcNAc using AFM-based force recognition mapping. The LPS of Gram-negative bacteria plays multiple important roles in pathogenesis, epidemiology and disease control [237]. The examination of surface carbohydrate compositions of bacteria has been used for taxonomic differentiation, identification of different genera and types and strains of bacteria [166, 167], as well as reconstruction of growth conditions [168]. The oligosaccharide moiety of LPS primarily plays a protective role such as preventing host immunity system attacks, or camouflaging with common host carbohydrate residues [255]. Thus, understanding the structure of LPS on *Y. pestis* surface can provide significant insight into the virulence of the pathogen in different environments. GlcNAc is chosen as the indirect target biomarker for LPS due to the following reasons: a) GlcNAc is present on most strains of *Y. pestis*, b) since all strains of *Y. pestis* have been found to lack the O-antigen, GlcNAc is located at the terminal end of the LPS core oligosaccharide, making its binding sites readily exposed to functionalized AFM cantilevers and, c) lectin-probes specific to GlcNAc are readily available.

Figure 5.7c, 5.7d and 5.7e show the spatial distribution of the GlcNAc on *Y. pestis* grown at 6°C, 25°Cand 37°C, respectively. The distribution of GlcNAc is dense on cells grown at 37°C but sparse on cells grown at 6°C. The relative surface concentrations of GlcNAc can be quantitatively estimated (Figure 5.4). The density of GlcNAc on *Y. pestis* grown at 37°C (12.8±1.5%) is slightly higher than that of cells grown at 25°C (10.8±0.9%), but~2.5x higher than that of GlcNAc on the cells grown at 6°C (4.9±0.3 %). A control experiment was carried out to confirm the specificity of the pair-wise WGA-GlcNAc interactions. Surfaces of cells grown at 37°C were probed using WGA-modified AFM probes following the addition of free WGA in buffer to block the available binding sites of cell surface GlcNAc and make them unlikely to show up as recognition events. Figure 5.7f shows the force map of the cell surface in the presence of free WGA. A significant decrease of high adhesion force areas is observed (from 12.8±1.5% to 1.1±0.4%, Figure 5.4), with only a few non-specific high adhesion spots. This confirms that the interactions observed are specific in nature and not the result of the WGA-modified probes binding non-specifically to the cell surface.

Force recognition mapping offers a way to quantify and compare the density of GlcNAc on single cells grown at different temperatures (Figure 5.4 and Figure 5.7). These results are consistent with earlier reports on two types of *Y. pestis* strains including KIM218 and *caucasica* 1146 [237]. The amount of GlcNAc on 37°C cells is slightly higher than those at 25°C. Interestingly, the ratio of GlcNAc (25°C/37°C) on the KIMD2 strain (~0.84) is close to the ratio on KIM218 (~0.75) but different from the ratio on *caucasica* 1146 (~0.5) strain, which implies biochemical similarity and variation between closely and distantly-related strains, respectively. The decrease of GlcNAc amount on the *Y. pestis* grown at 6°C is intriguing. Using the combination of bulk scale analytical approaches including mass spectroscopy and nuclear magnetic resonance, the GlcNAc level on *Y. pestis* grown at 25 and 37°C is higher than that of cells grown at 6°C with a variation from ~1.8:1 to ~6:1 [53], suggesting that cold temperatures may alter LPS production in *Y. pestis*, and decrease the GlcNAc amount at the LPS terminal end. Overall, these results suggest that ecologically relevant modifications to the LPS structure, can be preserved using methanol fixation and subsequently analyzed with the AFM. Finally, control experiments further demonstrate the potential of this strategy to work in a complex, but controllable medium in real time, by observing morphological and biochemical changes on the cell surface after adding exogenous substances (for instance, antimicrobials) to the external microenvironment.

5.4 Conclusions

In this chapter, the effects of different inactivation methods (methanol, formaldehyde and heat) and growth temperature on *Y. pestis* are investigated using AFM based nanoscale imaging and force recognition mapping at the single cell level. Both imaging and spatial mapping of surface carbohydrate (GlcNAc) distributions show that methanol treatment is able to preserve the bacterial morphology and surface bioactivity. Different morphological characteristics and surface GlcNAc distributions could be observed via images and force maps of *Y. pestis* grown at different temperatures. The density of GlcNAc on *Y. pestis* grown at 37°C is slightly higher than cells grown at 25°C but nearly 3 times higher than cells grown at 6°C. Overall, this research provides a crucial first step to study virulent pathogens in the regular lab- inactivation followed by a nanoscale evaluation of the effects on cell morphology and surface biochemical behavior. Variations in the morphology and surface carbohydrates at different culture temperatures indicate adaptation of *Y. pestis* to different environments that can be measured and visualized at the single cell level.

[This chapter contains results that have been submitted for publication in:

Wang C, Stanciu C, Ehrhardt C, Yadavalli VK, "The effect of growth temperature on the nanoscale surface properties of Yersinia pestis" in Colloid and Surface B, October 2015]

CHAPTER 6

REAL TIME OBSERVATION OF THE EFFECT OF ANTIMICROBIAL COPOLYOXETANES ON *ESCHERICHIA COLI* SURFACES

6.1 Introduction

The research conducted in the previous chapters demonstrated that spatial mapping of biomolecules and changes on cell surfaces can be used to monitor cellular activities (such as sporulation) and retrace environmental conditions (such as inactivation methods and growth temperatures). However, none of these changes were monitored in real time. This increases the uncertainty of the observation. In the following two chapters, the real time AFM (including imaging and force mapping) is applied to study antimicrobial effect on single cell surfaces and their action of mechanisms in real time.

Bacterial resistance to conventional antibiotics has been an increasing threat worldwide owing to the misuse/overuse of drugs [256]. For example, resistant strains against β-lactam antibiotics have evolved rapidly, with a nearly 1000 fold increased resistance over just the past three decades [257]. Simultaneous development of resistance to several classes of antibiotics has created multidrug-resistant bacterial strains, the so-called "superbugs" [258]. Due to the relatively low numbers of new antibiotics approved the US Food and Drug Administration [259], developing and studying new classes of antimicrobial compounds to combat bacterial infections have great fundamental and applied importance. Previous studies in our group have shown the promising application of a novel class of copolyoxetanes, with quaternary ammonium and PEG-like side chains, as therapeutic agents against Gram positive and negative bacteria, owing to their effective antimicrobial behavior, water solubility, compositional tunability, as well as low cytotoxicity for human red blood cells, dermal fibroblasts, and foreskin fibroblasts. Copolyoxetanes offer an efficient alternative to conventional antibiotics for the treatment of resistant pathogens [260, 261]. As a polymer surface modifier, only 2 wt. % copolyoxetane added to a conventional polyurethane resulted in a coating that caused 100% kill in 30 minutes of *E. coli*(~10^7 CFU/mL) or *P. aeruginosa*, and 98.7% kill for *S. aureus* [262]. A better understanding of their killing mechanisms is critical to the development of these polymers as a new class of broad-spectrum antimicrobial agents.

Since synthetic amphiphilic polycations structurally mimic naturally occurring antimicrobial peptides [74-76], the killing mechanism of copolyoxetanes is thought to involve contact kill i.e. cell membrane disruption by ionic and hydrophobic interactions between the amphiphilic polycation molecules and the bacterial membrane [263, 264]. Their net positive charge allows the polycations to electrostatically bind anionic bacterial surfaces, while their amphipathic structure facilitates their insertion into the hydrophobic core of the cell membrane [77, 78]. Several models for the interaction of antimicrobial peptides with the bacterial membrane have been proposed, including the barrel stave [265, 266], toroidal pore [267, 268], and the carpet model [269-271]. These models describe the processes of an antimicrobial peptide attaching to, and inserting into membrane bilayers to form pores, and eventually kill the cell. However, these mechanisms have been based on antimicrobial peptides interacting with model membrane systems. The exact kill mechanism of copolyoxetanes (a synthetic amphiphilic polycation) and their effect on *natural membrane system* (live bacterial surface) still need to be clarified.

The AFM has rapidly emerged as an important tool widely used over the past couple of decades in microbiology [9, 71, 72, 272]. A unique advantage is the ability not only to visualize live cells under physiological conditions with nanoscale resolution and three-dimensional imaging, but also to measure cell surface biochemical properties (such as hydrophobicity or specific biomarkers) *via* functional AFM probes [58, 273, 274]. This makes it a powerful technique to the study of the effect and mechanisms of environmental effectors on cells. A series of AFM studies have been reported using bacterial cells to study mechanisms of action of antimicrobial peptides [275-280]. Typically, cells in these investigations are sampled out at selected time points and imaged in air to obtain high quality images. This approach requires drying of the cells, that can change the cell morphology, or create artifacts due to salts and small compounds in the culture medium [277]. To date, only few studies have observed changes in bacteria due to antimicrobial treatments in liquid environments [281-283].

A stronger insight into the effects of antimicrobial compounds on cells can be obtained by observations conducted *in situ* (liquid), in real time and preferably at the level of a single cell. Such studies at the cell surface can reveal the mechanisms of action and kill. Using high-speed AFM, Fantner et al. observed *E. coli* surfaces influenced by the antimicrobial peptide CM15 in real time and a short period of time [282]. Wu et al. described the single dividing mycobacterium JLS before and after the anti-mycobacterial drug (ethambutol) treatment in real time at the single cell level [283]. In this chapter, the real time AFM is used to monitor *E. coli* incubated with the antimicrobial copolyoxetane. Specifically, the *same* cell is observed over a period of time to observe in real time, the effect of addition of the antimicrobial to the external microenvironment.

In addition to observing the cell morphology, the change in the surface hydrophobicity due to the antimicrobial is quantified. The observed characteristic features on cell surfaces at different stages and concentrations are consistent with previously proposed carpet model for antimicrobial peptides. Using such a real time observation of cells can therefore provide critical insights into the mechanism of action of synthetic amphiphilic polycations.

6.2 Experimental section

6.2.1 Materials and instrumentation

Poly-L-lysine hydrobromide (P1524), Tris(hydroxymethyl)aminomethane and 1-undecanethiol were purchased from Sigma-Aldrich (St. Louis, MO). Phosphate-buffered saline (PBS pH 7.4) (11.9 mM phosphates, 137 mM sodium chloride and 2.7 mM potassium chloride) and ethanol (200-proof) were purchased from Fisher Scientific. Mica was purchased from Ted Pella (Redding, CA). Ultrapure water (resistivity 18.2 MΩ•cm) was obtained from a MilliQ water purification system (Millipore Scientific, MA). CSG30 cantilevers (NT-MDT) were used for non-contact mode imaging in liquid. Gold coated TR400PB cantilevers (Olympus) were used for chemical force mapping in liquid.

6.2.2 Polymer synthesis and characterization

The antimicrobial copolyoxetane polymer was provided by the laboratory of Dr. Kenneth Wynne at VCU. The synthesis and characterization of the polymer can be found in [261, 262].

6.2.3 Cell culture

E. coli (ATCC# 35218) was maintained on Trypticase Soy Agar (TSA) (30 g Trypticase soy broth (Becton Dickinson, Franklin Lakes, NJ), 15 g agar (American BioAnalytical, Natick, MA)). A freshly streaked plate was incubated overnight at 30 °C. A single colony was picked and inoculated into 125 mL of Trypticase Soy Broth (TSB) (30 g Trypticase soy broth (Becton Dickinson, Franklin Lakes, NJ). The culture was incubated for 20 hours at 30 °C and 225 rpm in an orbital shaker. The bacterial mass was harvested by centrifuging at 3220xg for 15 minutes, decanting the medium, and re-suspending the pellet in PBS. The fresh prepared *E. coli* was used for AFM imaging instantly.

6.2.4 Sample preparation and atomic force microscopy (AFM) imaging

Cells were immobilized using the poly-L-lysine fixation method described earlier [282]. Mica was coated with poly-L-lysine to increase the adherence of the bacteria. Freshly cleaved mica was immersed for 10 minutes in a solution of 0.05 mg/ml poly-L-lysine hydrobromide and 10 mM Tris (pH 8.0). The surface was then covered and dried vertically overnight at room temperature. The coated mica was stored at room temperature and was used within one week. Concentrated bacteria suspended in PBS were deposited on the coated mica and incubated for 30 minutes. The cells were kept hydrated at all times. Excess cells were rinsed off with three washes of 1 ml Millipore water. Images were taken in PBS with and without the antimicrobial copolyoxetane using non-contact mode imaging. A series of concentrations (~15 μg/mL, 30 μg/mL and 60 μg/mL) were used to study the concentration dependence of the action of copolyoxetane. To observe the cells *in situ* and in real time, the same cells (same areas on mica) were imaged at selected time intervals.

6.2.5 AFM probe functionalization and chemical force mapping

Gold coated cantilevers were cleaned in UV/ozone for 15 minutes. Cantilevers were functionalized *via* immersion in1-undecanethiol solution in ethanol for 16 hours to obtain CH_3 terminated group on probe surface. Then the cantilevers were rinsed with ethanol to remove unbound 1-undecanethiol. Subsequently, CH_3-functionalized cantilevers (spring constant ~0.09 N/m, resonance frequency 32 kHz) were used to obtain force data on cells in buffer. The same cells were force-imaged at selected time points (0 hour, 1.5 hours and 3 hours). At least 5 different *E. coli* cells were studied separately. Force-distance curves over the cell surface were obtained by collecting a series of sequential force curves in an $m \times n$ grid. Each force curve was obtained at the same loading rate (81 nN/s, at a ramp velocity of 900 nm/s) by pressing the cantilever to a low trigger point (200 pN), allowing binding to occur (contact time 0.1 second), and then retracting. All force maps were obtained by collecting ~32×32 force curves over a defined area (~2μm×2μm), estimating the adhesion force values, and displaying these values by scale of color. The height maps of the same area were generated simultaneously as the force mapping occurred. All images including height and force maps were performed using custom routines in Igor Pro 6.32 A (Wavemetrics Inc, OR) for fast processing of data.

6.3 Results and Discussion

6.3.1 AFM imaging copolyoxetane treated *E. coli* in real time

To observe the effect of copolyoxetane treatment on the Gram negative bacterial cell surface, AFM images of *E. coli* were acquired at selected time points including before (0 hour) and after adding the copolyoxetane (1 hour, 2 hours and 3hours) into the imaging buffer. Based on previous antimicrobial activity studies on *E. coli*, the minimal biocidal concentration (MBC), ~ 30 μg/mL, was used here to obtain the complete and rapid kill [260, 261]. Figure 6.1 shows the morphological change of *E. coli* under the action of copolyoxetane. Before adding copolyoxetane, the cell surfaces were smooth and there was no damage on the cell membranes (Figure 6.1a and 6.1e), indicating that the cell morphology was unaffected after poly-lysine fixation and imaging in PBS buffer. After 1 hour of incubation with copolyoxetane, minor indentation areas on cell surfaces were evident (marked by green arrows, Figure 6.1b and 6.1f), implying the partial removal of the LPS layer or outer membrane. After 2 hours of treatment, some protrusions formed on cell surfaces (marked by yellow arrows in Figure 6.1c and 6.1g). Interestingly, it seems that the biggest protrusion took place on the previous indentation area in Figure 6.1f, which implies that the copolyoxetane further interacted with the inner membrane after removal of the LPS layer or outer membrane and resulted in the formation of the vesicle-like structures on the cell surface. Furthermore, there was no obvious change on cell morphology from 2 hours to 3 hours (Figure 6.1d and 6.1h) probably due to the cell death after 2 hours' incubation in copolyoxetane. In addition, as a control experiment, the cells undergoing no copolyoxetane treatment were also monitored at the same time intervals using AFM imaging. It is obvious that the untreated *E. coli* cells experienced no morphological changes over the period of 3 hours (Figure 6.2).

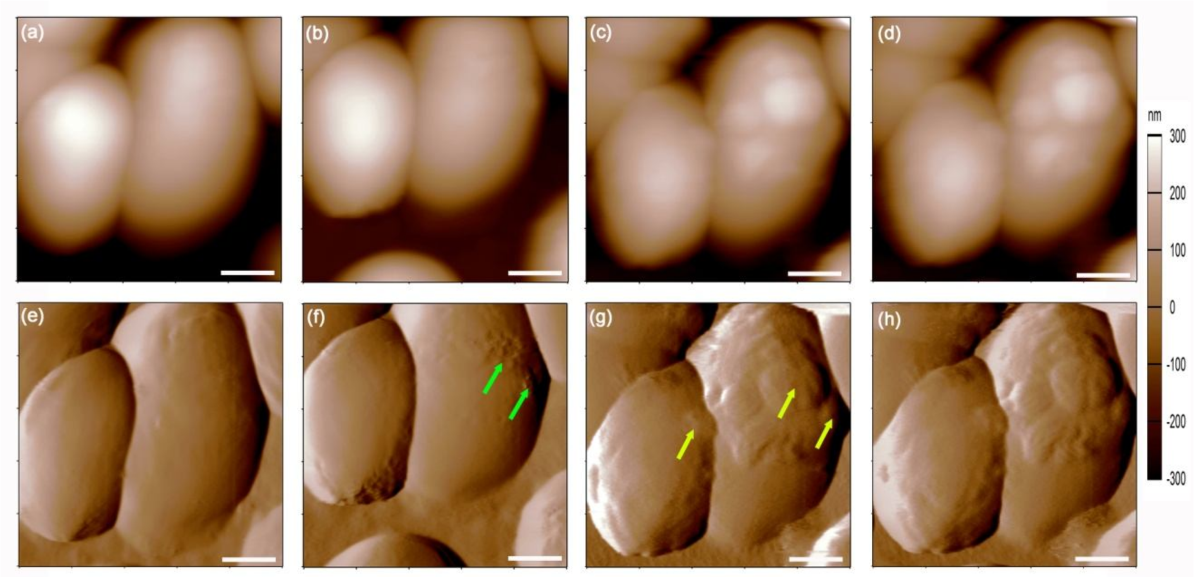

Figure 6.1. AFM imaging of copolyoxetane treated *E. coli* in real time. (a)-(d) are height images of *E. coli* at 0 hour (before adding copolyoxetane), 1 hour, 2 hours and 3 hours (after adding copolyoxetane), respectively. (e)-(h) are corresponding amplitude images. Green arrows mark the minor indentation area on cell surface. Yellow arrows indicate vesicle-like structures on cell surface. Scale bars: 500 nm.

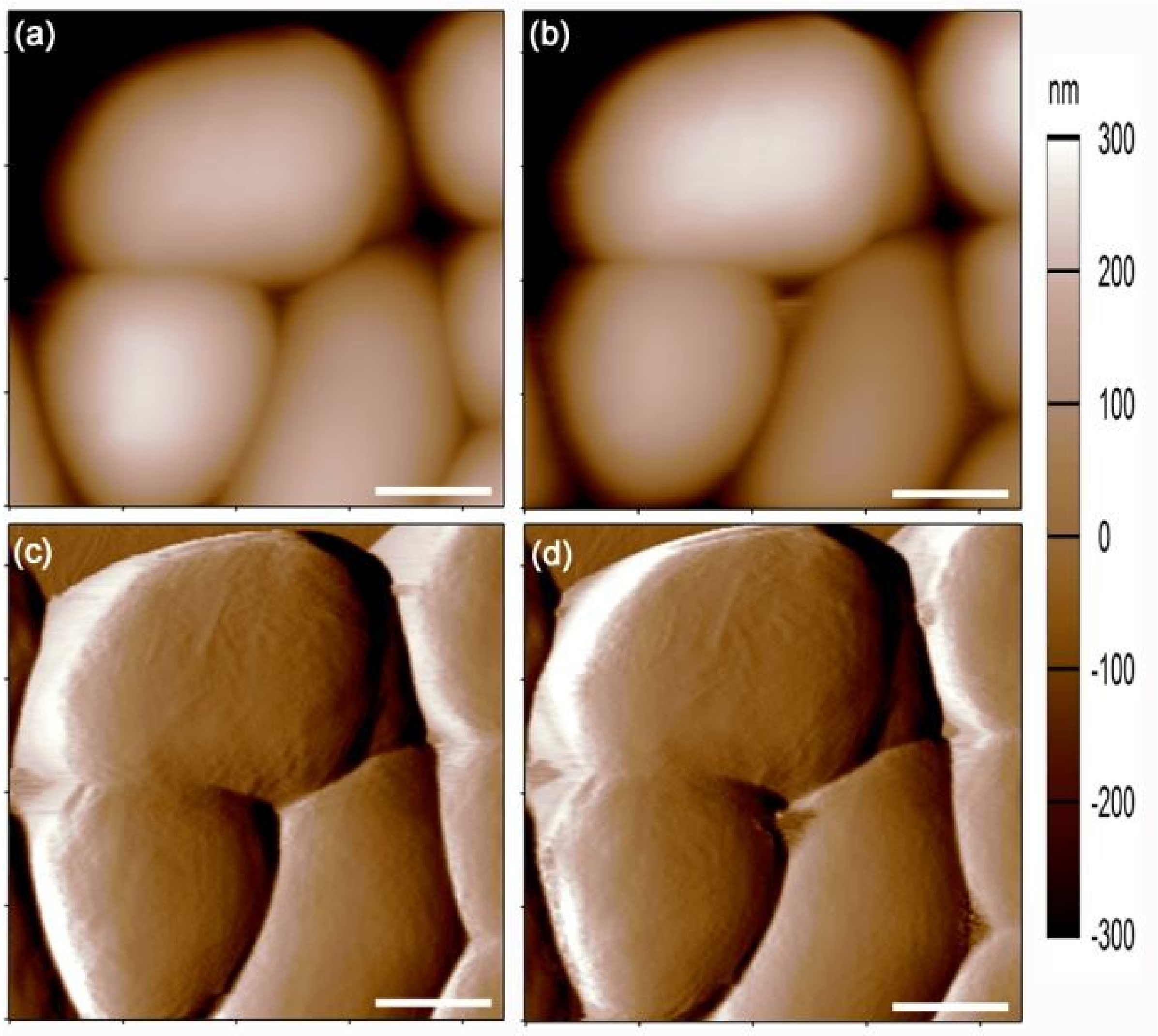

Figure 6.2 AFM imaging E coli in PBS in 3 hours. (a) and (b) are height images of E coli in PBS at 0 hour and 3 hours. (c)-(d) are corresponding amplitude images. Scale bars: 500 nm.

The AFM images in Figure 6.1 indicate that the activity of the copolyoxetane is time dependent. Two stages of morphological changes are shown. First, the copolyoxetane damages the LPS layer or outer membrane causing the formation of indentation on cell surfaces. Second, after the permeabilization of the outer membrane, the copolyoxetane further penetrates into and interacts with the inner membrane and form vesicle-like features. Similar phenomena (the outer membrane damage and formation of vesicle-like features) and the two-stage process were reported on previous studies on cationic antimicrobial peptides. For example, using AFM, Li et al. was able to observe the indentation on cell surfaces and micelle-like structures around the Sushi peptide treated cells [279]. However, since the AFM imaging was done in air, it is difficult to clarify the micelle-like structures around the cells are the real formed micelle or dried components from culture medium. In our AFM images, the protrusions formed on the previous indentation area on cell surface clearly show the dynamic two-stage process in situ. In addition, Hyldgaard et al. [284], Alves et al. [275], and da Silva et al. [276] also reported the indentation and vesicle-like features on Epsilon-poly-L-lysine, BP100, pepR and PGLa treated *E. coli* cells.

Based on the characteristic morphological alternations and two-stage process, the adoption of a carpet-like (or detergent-like) mechanism by the copolyoxetane seems to be reasonable [78]. The carpet mechanism was proposed to explain the activity of several antimicrobial peptides including dermaseptin S [270], melittin, magainin [277] and the antimicrobial peptides mentioned in last paragraph. Initially, the polycationic antimicrobials bind with negatively charged LPS (mainly with phosphate groups in the LPS inner core [284]) by electrostatic forces, which ultimately removes the LPS layer in a detergent-like fashion and disrupts integrity of the outer membrane. Here, the LPS layer in the outer membrane acts as the initial barrier for polycationic antimicrobials in their attempt to penetrate into their next target of action – the inner cell membrane [285]. After penetration of outer membrane and reaching a threshold concentration on the inner membrane, the polycationic antimicrobials induce the curvature of inner membrane and form vesicle-like features on cell surfaces. Finally, the release of vesicle or micelle will further result in the disruption of cell membrane structure and even the leakage of cytoplasm. In the real time AFM study (Figure 6.1), the MBC of copolyoxetane induced the appearance of indentation on cell surface, as well as the formation of vesicle-like features on indentation area. The lack of the third stage (the leakage of cytoplasm) may be because of the insufficient concentration and the rigid peptidoglycan layer beneath the outer membrane maintaining the cell structure.

6.3.2 AFM imaging *E. coli* treated with different concentration of copolyoxetane

The real time AFM imaging has demonstrated the time-dependent antimicrobial activity of copolyoxetane. To further investigate whether the activity is concentration-dependent, the *E. coli* morphology in 2× MBC and ½ ×MBC of copolyoxetane were observed in real time. Figure 6.3a, 6.3b, 6.3e and 6.3f show the morphological change of E.coli at 2× MBC of copolyoxetane. Similar as before, the *E. coli* cell had smooth surface without damage in PBS buffer (Figure 6.3a and 6.3e). After 1 hour of incubation with 2× MBC of copolyoxetane, both vesicle-like features (marked by yellow arrows) and leakage of cytoplasmic fluid (marked by red arrows) were clearly shown (Figure 6.3e and 6.3f), indicating the damage to the inner membrane [277]. There was no morphological change between 1 hour and 3 hours of incubation, indicating the cell death at 1 hour. The leaking soft and fluidic cytoplasmic content compromised the resolution of AFM images, which further reveals the dynamic process of antimicrobial activity at the single cell level. Here, it is interesting to see that the cytoplasmic content was leaking out from septal region of the cell, which may be explained by the cardiolipin, a negatively charged phospholipid, generally located at the septal region of the *E. coli* inner membrane [286], and the cationic copolyoxetane. In contrast, Figure 6.3c, 6.3d, 6.3g and 6.3h show the *E. coli* incubated in ½ ×MBC of copolyoxetane only displayed minor change (indentations marked by green arrows) on the cell surface in 3 hours. Therefore, Figure 6.3 reveals that the activity of the copolyoxetane is concentration dependent. At lower concentration of copolyoxetane (½ ×MBC), there was no vesicle-like feature and cytoplasm leakage, which implies that the copolyoxetane concentration has not reached threshold to disrupt the inner membrane and further initiate the cytoplasm leakage. At higher concentration (2×MBC), the three-stage morphological changes with the increase of time including surface indentation, vesicle-like feature and cytoplasm leakage are shown, which further demonstrates the carpet mechanisms of cationic copolyoxetane.

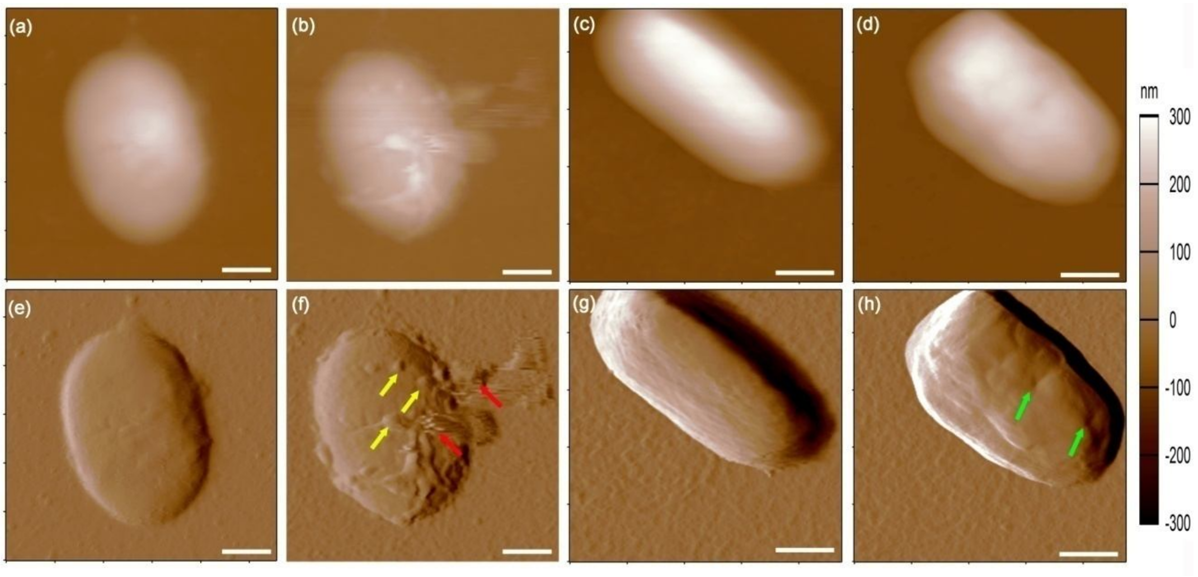

Figure 6.3. Concentration dependence of copolyoxetane effects on *E. coli* imaged by AFM. (a) and (b) are height images of *E. coli* in 2×MBC of copolyoxetane at 0 hour and 1 hour, respectively. (c) and (d) are height images of *E. coli* in ½ ×MBC of copolyoxetane at 0 hour and 3 hours. (e)-(h) are corresponding amplitude images. Yellow arrows: vesicle-like features. Red arrows: leaking cytoplasmic content. Green arrows: indentation. Scale bars: 500 nm.

As aforementioned, there are three typical models for the interaction of antimicrobial peptides with the bacterial membrane. In the barrel-stave model, peptide helices form a bundle and insert into the membrane, like a barrel composed of helical peptides as the staves. In the toroidal pore model, antimicrobial peptide helices insert into the membrane and induce the lipid monolayers to bend continuously and create the pore. In the carpet model, peptides accumulate on the membrane like a carpet and remain in a parallel or a surface state. At high concentrations, surface-oriented peptides are thought to disrupt the bilayer in a detergent-like manner, eventually leading to the formation of micelles/vesicles [78]. Model membrane studies have shown that most antimicrobial peptides follow the toroidal pore model or carpet model but not the barrel stave model. This is because the peptides in the barrel model need to insert into the membrane without deformation of the lipid bilayer whereas peptides in the toroidal pore and carpet model tend to induce the deformation (such as curvature) on cell membrane [277], which also can be observed in our AFM images. The difference between the toroidal pore and carpet model is the initial interaction process between polycations and cell membrane. In the toroidal pore model, polycations insert into the membrane individually then associate with lipid head groups, whereas polycations accumulate on the membrane like a carpet and remain in a parallel or a surface state in the carpet model [287].

6.3.3 The copolyoxetane effect on surface hydrophobicity of *E. coli*

To further study the antimicrobial mechanism of copolyoxetane especially its initial interaction mechanism with cell membrane and effect on cell surface biochemical nature, AFM based chemical force microscopy (CFM) was used to map the nanoscale hydrophobicity distribution on single *E. coli* surface. The surface hydrophobicity of *E. coli* has been an important biomarker relevant to its adhesion to inanimate surface and interaction with antimicrobial peptide [288, 289]. Specifically, using functional AFM tips as probes, adhesion forces between tip-bound groups (undecanethiol with -CH_3 terminal group in this study) and surface hydrophobic groups on bacteria can be measured. This technique enables researchers to map out spatial distributions of hydrophobic groups and their changes in real time [9, 73].

Figure 6.4 shows the overlaid height and adhesion force maps of the *E. coli* incubated with MBC of copolyoxetane at different time intervals. An excellent correspondence can be observed between the cell profiles in the height map and a simultaneous increase of the adhesion events at the same areas. Figure 6.4a indicates that the cell surface hydrophobicity was homogeneously distributed before the copolyoxetane was added. The hydrophobicity of *E. coli* surface is originated from the hydrophobic contents on cell surface, such as lipids and hydrophobic region of membrane proteins [290]. After adding the copolyoxetane, the adhesion events on cell surfaces significantly decreased at 1.5 hours and 3 hours (Figure 6.4b, 6.4c). As a quantitative measure, the hydrophobicity of the single cell was calculated as a percentage of adhesion events to the total number of traces collected on the cell surface. The hydrophobicity of the *E. coli* at 1.5 hours and 3 hours (~15%) is calculated to be much lower than *E. coli* at 0 hour (~ 91%) (Figure 6.5c). Furthermore, as a control experiment, adhesion force maps were collected on *E. coli* in PBS at different time points in 3 hours. Figure 6.5a and 6.5b shows that there is no obvious change in 3 hours in terms of cell surface hydrophobicity. Overall, the hydrophobicity mapping on single cells shows that the entire cell surface hydrophobicity decreased significantly with the action of copolyoxetane.

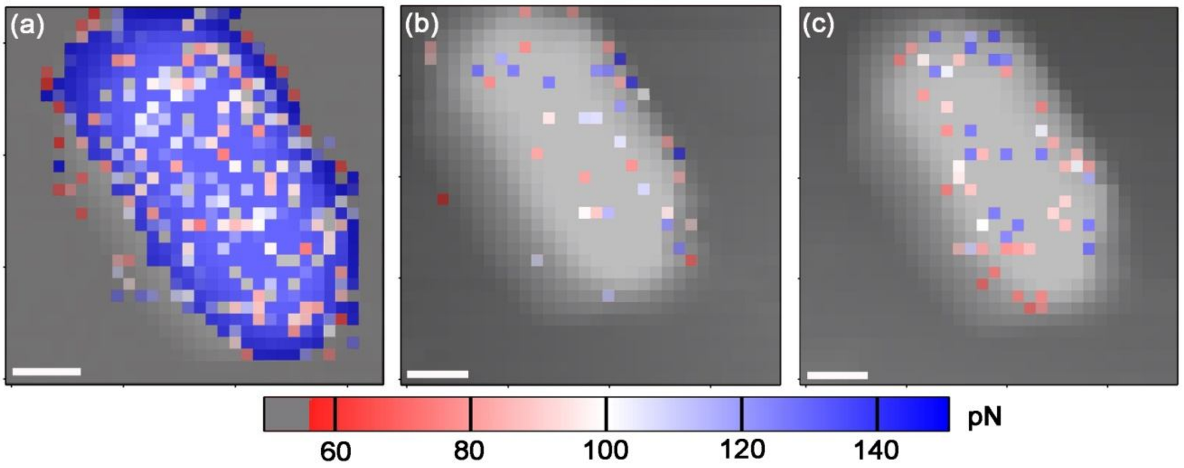

Figure 6.4. Overlay of force and height profiles for the hydrophobicity on *E. coli* cell surfaces before (a, 0 hour) and after adding MBC of copolyoxetane (b, 1.5 hours and c, 3 hours). Scale bars: 300 nm. The color of pixels indicates the magnitude of force value.

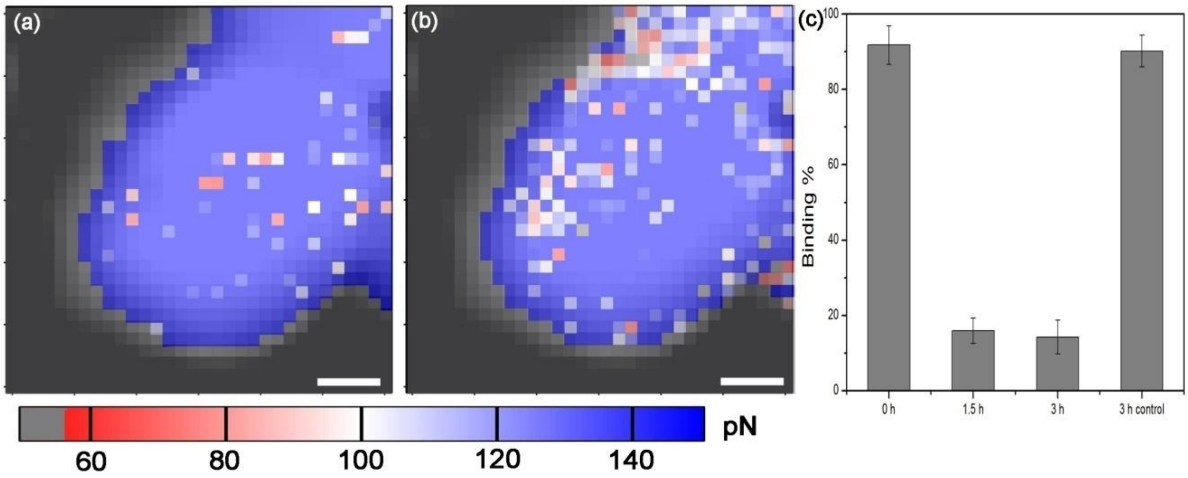

Figure 6.5. Control experiment: Overlay of force and height profiles for the hydrophobicity on *E. coli* cell surfaces in PBS in 3 hours. (a) 0 hour. (b) 3 hours. Scale bars: 200 nm. (c) Analysis of binding % shows the hydrophobicity of single *E. coli* cells decreased after adding copolyoxetane. Control experiment shows the hydrophobicity does not change in PBS in 3 hours. The data are from three independent experiments for each system.

AFM-based hydrophobicity mapping was able to further elucidate the exact mechanism from the perspective of surface biochemical nature. The decrease of hydrophobicity across the entire cell surface can be explained by that the copolyoxetane forms single or multiple layers on the cell surface by binding with the outer membrane LPS and the formed layers block the hydrophobic AFM probe to interact with hydrophobic contents on *E. coli* surface. Also, considering the structure of copolyoxetane, the positive charged ammonium and hydrophobic alkyl group tend to bind with negative charged groups and lipid A on LPS, respectively, leaving the PEG-like side chain (which is hydrophilic) facing the solution [288]. This study further demonstrates that the copolyoxetane initially binds to cell membrane in a carpet-like fashion (rather than insertion individually in the toroidal pore model), and this leads to the change of entire cell surface biochemical nature.

6.4 Conclusions

In this chapter, AFM is used for the analysis of the antimicrobial effect of copolyoxetane (a novel class of synthetic amphiphilic polycations) on model bacterium, live *E. coli* surfaces. The ability to image live cells in real time and liquid environment enables AFM to observe the time and concentration dependence of the copolyoxetane effects on live *E. coli*. The characteristic cell morphological change with the increase of time and copolyoxetane concentration including indentation area, vesicle-like features and cytoplasm leakage can be explained by the carpet model, in which the copolyoxetane interacts with *E. coli* membranes through a carpet-like mechanism leading to the removal of LPS layer, formation of membrane curvature and finally disruption of membrane structure. Furthermore, AFM-based CFM shows that incubating cells with copolyoxetane decreased the hydrophobicity across the entire cell surfaces at the early stage, confirming that the copolyoxetane molecules initially bind with cell membrane in a carpet-like fashion. Taken together, the real time AFM approach here clearly elucidates the antimicrobial mechanisms of copolyoxetane at the single cell level and this will provide important insights into mechanism of action of other synthetic amphiphilic polycations.

[This chapter contains results that have been submitted for publication in:

Wang C, Zolotarskaya OY, Ehrhardt C, Wynne KJ, Yadavalli VK, **"Real time observation of antimicrobial polycationeffects on *Escherichia coli*: adapting the carpet model for membrane disruption to quaternary copolyoxetanes"** ***submitted to Langmuir, November 2015]***

CHAPTER 7

REAL TIME OBSERVATION OF THE ANTIMICROBIAL EFFECT OF COPPER ON BACTERIAL SURFACES

7.1 Introduction

With a rise in the number of antibiotic-resistant pathogenic bacteria and a proliferation of nosocomial infections, there has been a strong need for researching new classes of antimicrobial agents [256]. Certain metals and their compounds have been found to have excellent antimicrobial properties against a variety of bacteria [291-293]. In recent years, the micro- and nano-particle forms of these metallic materials have attracted considerable interest owing to their high surface area, chemical stability, heat resistance and long shelf-life [79]. Frequently used metallic particles include Cu, Ag, Fe_2O_3, ZnO and Au [294-297]. Copper (Cu) and its compounds, in particular, have a long history as antimicrobial agents, and have been widely utilized as cheap and effective antimicrobial materials. For example, copper surfaces in hospital and institutional environments have been used because of their highly potent "contact killing" ability against various bacteria [80, 298]. Copper microparticles within a polymer matrix have been shown for potential applications in water treatment [299, 300]. Impregnating copper (particles) in materials ranging from textiles to non-porous solid surfaces have been proposed to minimize nosocomial infections [301, 302]. A better understanding of the antimicrobial mechanisms of copper is therefore critical to the development of this material as a new class of broad-spectrum antimicrobial agent.

The exact mechanisms of action of copper remain issues of debate [303]. Depending on material forms such as surfaces, particles (micro or nanoparticles) and salts, various mechanisms of the antimicrobial action have been proposed. For instance, copper surfaces (in both dry and wet condition) are postulated to kill bacteria via contact kill. This proceeds by steps of membrane damage, influx into the cells, oxidative damage, cell death, and DNA degradation, although the exact sequence of events is still unclear [291]. Copper particles may have two modes of action. The first involves penetration of particles into the cell wall, and inducing damage in the cellular membrane during the entry process [304, 305]. The second involves released Cu ions which produce reactive oxygen species (ROS) that can cause multiple toxic effects such as lipid peroxidation, protein oxidation and DNA degradation, finally killing the cells [306, 307]. The latter mechanism of action is generally considered more feasible in comparison to penetration into bacteria. For instance, it was shown that even large Cu microparticles embedded within an alginate matrix have a strong antimicrobial effect for water treatment [300]. However, questions related to the cellular interactions and mechanism of kill for Cu in the particulate form remain to be clarified.

In this chapter, real time atomic force microscopy (AFM) is used to visualize the antimicrobial mechanism of copper particles using live *Escherichia coli (E. coli)* as a model bacterium. AFM has been demonstrated to be a powerful platform for the study of the effect and mechanisms of antimicrobial peptides on cells [275, 278-280]. Compared to bulk scale analysis, AFM is able to visualize live cells under physiological conditions with nanoscale resolution. It is further possible to study cell surface biochemical properties in real time (such as hydrophobicity or specific biomarkers) *via* functional AFM probes with force recognition mapping technique [9, 58, 71]. In contrast to earlier reported studies using cell imaging via AFM, herein, for the first time we present studies in which the *same* cell is monitored both in terms of morphology and surface hydrophobicity change over time. To date, only few studies have observed morphological changes in bacteria due to metal nanoparticles treatments using AFM [293, 308, 309]. Typically in these investigations, different cells are sampled out at selected time points and imaged in air or liquid. Imaging in air requires drying of the cells that can change the cell morphology, or create artifacts due to salts or small compounds in the culture medium [277].

A clearer picture into the effects of the copper microparticles on cells can be obtained by observing same single cells *in situ* (liquid) and in real time. In this study, we use real time AFM to monitor *E. coli* incubated with antimicrobial copper microparticles. Specifically, we observe the *same* cell over a period of time, and the effect of addition of the antimicrobial to the external microenvironment. In addition to observing the cell morphology, we also quantify the change in the surface hydrophobicity due to the antimicrobial. Both the morphological and surface hydrophobicity changes on single cell surfaces are captured simultaneously during the antimicrobial treatment to provide a unique look at the antimicrobial mechanism of copper microparticles. Using such a real time observation of single cells can therefore provide critical insights into the mechanism of action of antimicrobial agents or external effectors.

7.2 Experimental section

7.2.1 Materials and instrumentation

Poly-L-lysine hydrobromide (P1524), Tris(hydroxymethyl)aminomethane and 1-undecanethiol were purchased from Sigma-Aldrich (St. Louis, MO). Phosphate-buffered saline (PBS pH 7.4) (11.9 mM phosphates, 137 mM sodium chloride and 2.7 mM potassium chloride) and ethanol (200-proof) were purchased from Fisher Scientific. Mica was purchased from Ted Pella (Redding, CA). Copper (I) particles (cuprous oxide) with a size range from 300 nm – 600 nm were used as antimicrobial agents. The particles were filtered using a 450 nm filter to obtain a dispersion in water at a bulk (solution) concentration of ~0.7 mM. Ultrapure water (resistivity 18.2 MΩ•cm) was obtained from a MilliQ water purification system (Millipore Scientific, MA). CSG30 cantilevers (NT-MDT) were used for non-contact mode imaging in liquid. Gold coated TR400PB cantilevers (Olympus) were used for chemical force mapping in liquid.

7.2.2 Cell culture

E. coli (ATCC# 35218) was maintained on Trypticase Soy Agar (TSA) (30 g Trypticase soy broth (Becton Dickinson, Franklin Lakes, NJ), 15 g agar (American BioAnalytical, Natick, MA)). A freshly streaked plate was incubated overnight at 30 °C. A single colony was picked and inoculated into 125 mL of Trypticase Soy Broth (TSB) (30 g Trypticase soy broth (Becton Dickinson, Franklin Lakes, NJ). The culture was incubated for 20 hours at 30 °C and 225 rpm in an orbital shaker. The bacterial mass was harvested by centrifuging at 3220xg for 15 minutes, decanting the medium, and re-suspending the pellet in PBS. The fresh prepared *E. coli* was used for AFM imaging instantly.

7.2.3 Sample preparation and atomic force microscopy (AFM) imaging

Cells were immobilized using the poly-L-lysine fixation method described earlier. Mica was coated with poly-L-lysine to increase the adherence of the bacteria. Freshly cleaved mica was immersed for 10 minutes in a solution of 0.05 mg/ml poly-L-lysine hydrobromide and 10 mM Tris (pH 8.0). The surface was then covered and dried vertically overnight at room temperature. The coated mica was stored at room temperature and was used within one week. Concentrated bacteria suspended in PBS were deposited on the coated mica and incubated for 30 minutes. The cells were kept hydrated at all times. Excess cells were rinsed off with three washes of 1 ml water. Images were taken in PBS with and without the copper dispersion (0.1 mg/ml) using non-contact mode imaging. To observe the cells *in situ* and in real time, the same cells (same areas on mica) were imaged at selected time intervals (0 hour, 1 hour, 2hours and 3hours). As a complementary experiment, cells incubated with copper particles were sampled out at selected time points (0 hour, 1 hour and 3 hours) and imaged in air to obtain high quality images.

7.2.4 AFM probe functionalization and chemical force mapping

Gold coated cantilevers were cleaned in UV/ozone for 15 minutes. Cantilevers were functionalized *via* immersion in1-undecanethiol solution in ethanol for 16 hours to obtain a CH_3 terminated group on probe surface. Cantilevers were rinsed with ethanol to remove any unbound

1-undecanethiol. Subsequently, CH_3-functionalized cantilevers (spring constant ~0.09 N/m, resonance frequency 32 kHz) were used to obtain force data on cells in buffer. The same cells were force-imaged at selected time points (0 hour, 1.5 hours and 3 hours). At least 5 different *E. coli* cells were studied separately. Force-distance curves over the cell surface were obtained by collecting a series of sequential force curves in an $m \times n$ grid. Each force curve was obtained at the same loading rate (81 nN/s, at a ramp velocity of 900 nm/s) by pressing the cantilever to a low trigger point (200 pN), allowing binding to occur (contact time 0.1 second), and then retracting. All force maps were obtained by collecting ~32×32 force curves over a defined area (~2μm×2μm), estimating the adhesion force values, and displaying these values by scale of color. The height maps of the same area were generated simultaneously as the force mapping occurred. All images including height and force maps were performed using custom routines in Igor Pro 6.32 A (Wavemetrics Inc, OR) for rapid data processing.

7.3 Results and discussion

7.3.1 The effect of Cu on *E. coli* cell morphology in real time

Initially, the real time AFM imaging was conducted in buffer to monitor the effect of Cu (I) particles on the Gram negative bacterium at the single cell level. AFM images of the same *E. coli* were acquired at selected time intervals including before (0 hour) and after adding the particles (1 hour, 2 hours and 3 hours) into the imaging buffer. Figure 7.1 shows the morphological change of the *E. coli* under the action of Cu. Prior to addition, the cell structure was intact, and no damage to the cell membrane was observed (Figure 7.1a and 7.1e). This also indicated that the cell morphology was unaffected after poly-lysine fixation and imaging in PBS buffer. After 1 hour of incubation with Cu, the cell structure collapsed from the peripheral area (Figure 7.1b and 7.1f), implying damage of the cell membrane and leakage of the soft and fluidic cytoplasmic contents. After 2 hours of treatment, the collapse and leakage of the cytoplasmic contents were more obvious (Figure 7.1c and 7.1g). After 3 hours of treatment, the cell lost most of the cytoplasmic contents and left the flat membrane debris on the substrate (Figure 7.1d and 7.1h). In these experiments, the concentration of Cu ions was estimated to be 0.7 mM considering the limited solubility of the particles in water. It may be noted that the bulk concentration and the surface concentration may be different. Quantitative analysis based on height images of the cell further show the significant morphological change during the process. Two parameters of the cell morphology are obtained via analyzing the height images: a) surface area (with cytoplasm) of the cell decreased from 3.2 μm^2 to 0.6 μm^2. b) Cell height at the central area decreased from 750 nm at 0 hour to 60 nm at 3 hours.

As a control experiment, cells without any Cu treatment were monitored at the same time intervals using AFM imaging. As expected, untreated *E. coli* cells in PBS did not show collapse and leakage of cytoplasm over a 3 hours period (Figure 7.2), implying that the changes in Figure 7.1 were indeed, induced by the Cu particles. Furthermore, a conventional approach was used to evaluate the effect of Cu on *E. coli* morphology by three individual steps including incubating cells with copper particles, sampling out small amount of cells at different time points and imaging the cells in air. As shown in Figure 7.3, the morphological changes on the cells with the increase of incubation time are similar to the single cell study. Before incubation with copper microparticles, the cell structures were intact. After 1 hour of incubation, some of the cells collapsed from the peripheral areas. After 3 hours of incubation, most of cells became flat, implying the collapse of cell and leakage of cytoplasm. It may be noted that some advantages of observing single cells versus ensembles come from being able to observe unique cells and precise cellular features that are typically averaged out over populations.

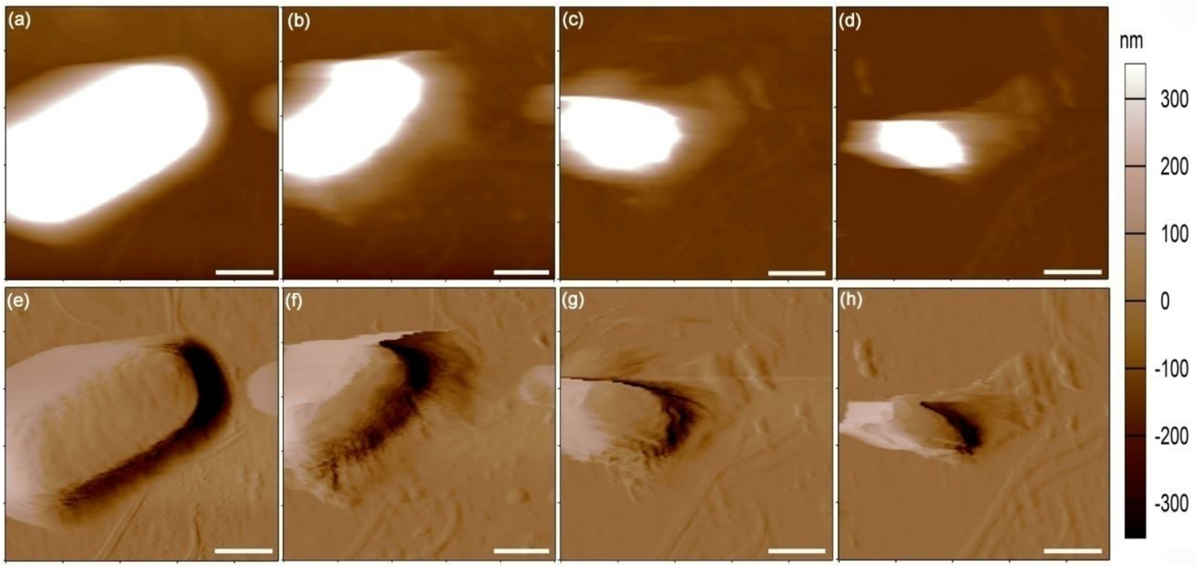

Figure 7.1. AFM imaging of Cu treated *E. coli* in real time and in aqueous environment. (a)-(d) are height images of cells at 0 hour (before addition), 1 hour, 2 hours and 3 hours (after addition), respectively. (e)-(h) are corresponding amplitude images. A steady decrease in cell size is clearly noted. Scale bars: 500 nm.

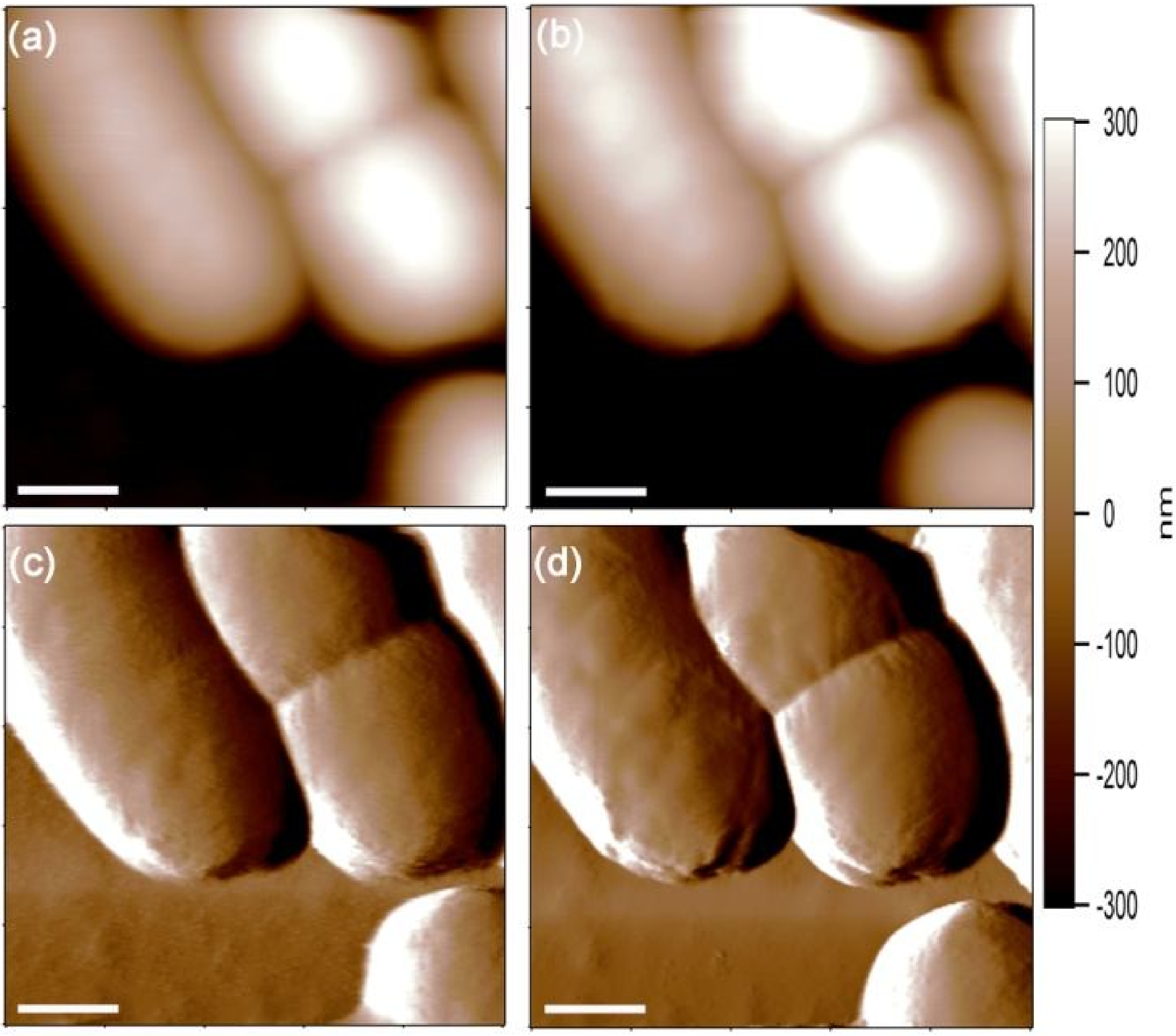

Figure 7.2. AFM imaging *E. coli* in PBS buffer over 3 hours. (a) and (b) are height images of cells at 0 hour and 3 hours. (c)-(d) are corresponding amplitude images. Scale bars: 500 nm.

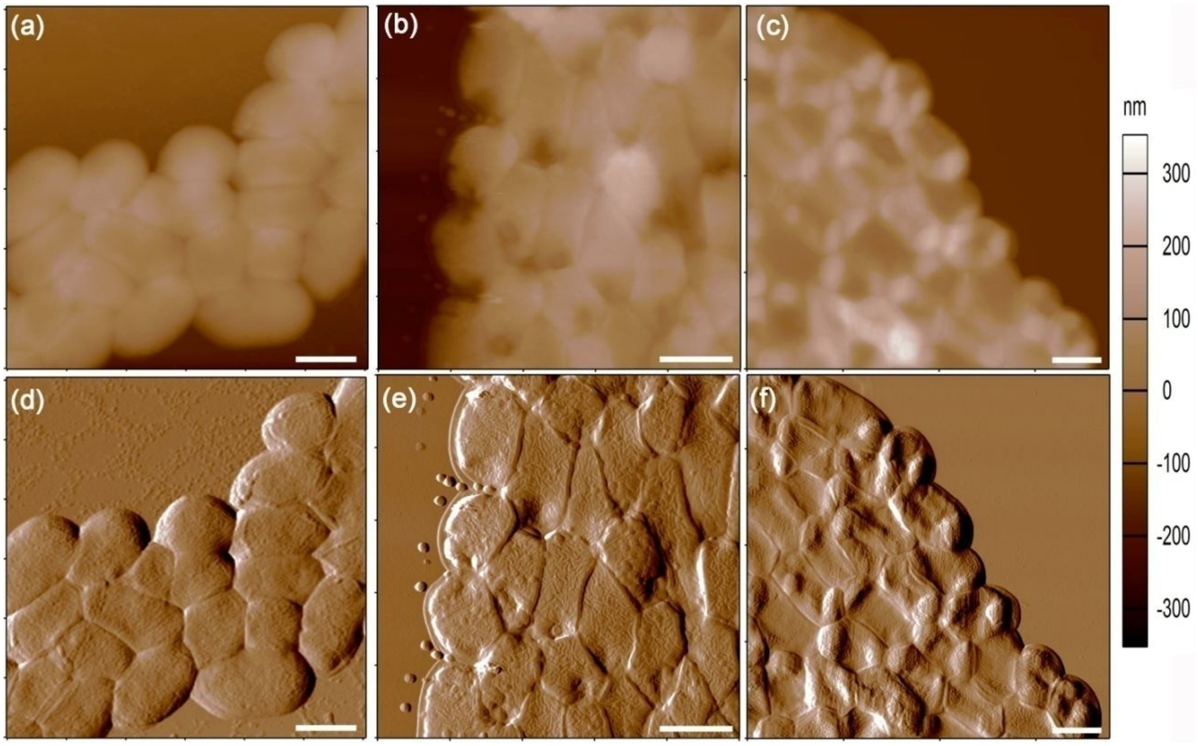

Figure 7.3. AFM imaging Cu treated *E. coli*. in air (a)-(c) are height images of cells at 0 hour (prior to addition), 1 hour and 3 hours (after addition), respectively. (e)-(h) are corresponding amplitude images. Scale bars: 1 μm.

7.3.2 The effect of Cu on *E. coli* cell surface hydrophobicity in real time

Nanoscale AFM imaging above showed that Cu induced cell membrane damage and cytoplasm leakage. This raises a deeper question in terms of precisely how the Cu affects and damages the cell membrane. To answer this question, we focused on the change of cell surface biochemical nature during the treatment. AFM based chemical force microscopy (CFM) was used to characterize cell surface biochemical nature by mapping the nanoscale hydrophobicity distribution on the *E. coli* surface. The surface hydrophobicity of *E. coli* originates from the hydrophobic contents on the cell surface, including lipids and hydrophobic membrane proteins [290]. These are typically relevant to its adhesion to inanimate surfaces as well as their interaction with antimicrobial peptides [288, 289]. Hydrophobicity can therefore be an important biomarker to evaluate the cell surface biochemical changes during Cu treatment. Specifically, using methyl (-CH_3) functionalized AFM tips as probes, interaction forces between the tip and surface hydrophobic groups on bacteria can be measured. This technique enables us to map out spatial distributions of hydrophobic groups as well as their changes in real time [9, 73].

Figure 7.4 shows the overlaid height and interaction force maps of the *E. coli* at different time intervals. An excellent correspondence can be observed between the cell profiles in the height map and a simultaneous increase of the adhesion events at the same areas. Figure 7.4a indicates that the cell surface hydrophobicity was homogeneously distributed prior to addition of Cu. After incubation with the Cu particles, both the interaction forces and adhesion events on cell surfaces decreased at 1.5 hours and 3 hours (Figure 7.4b, 7.4c). As a quantitative measure, two parameters can be used to estimate the magnitude of hydrophobicity on single cells: a) the average interaction force value on single cell surface, and b) the binding percentage which is calculated as a percentage of adhesion events to the total number of traces collected on the cell surface. The hydrophobicity of the *E. coli* at 1.5 hours (~92 pN and 81%) and 3 hours (~65 pN and 43%) is calculated to be much lower than *E. coli* at 0 hour (~132 pN and 91%) (Figure 7.5c). As a control experiment, adhesion force maps were collected on *E. coli* in PBS at different time points in 3 hours. Figure 7.5a and 7.5b indicates that cell surface hydrophobicity did not change in 3 hours. Overall, this hydrophobicity mapping on single cells provides a unique look at the spatial profile of the cell surface and its biochemical nature. It shows that the entire cell surface hydrophobicity decreases with the action of Cu.

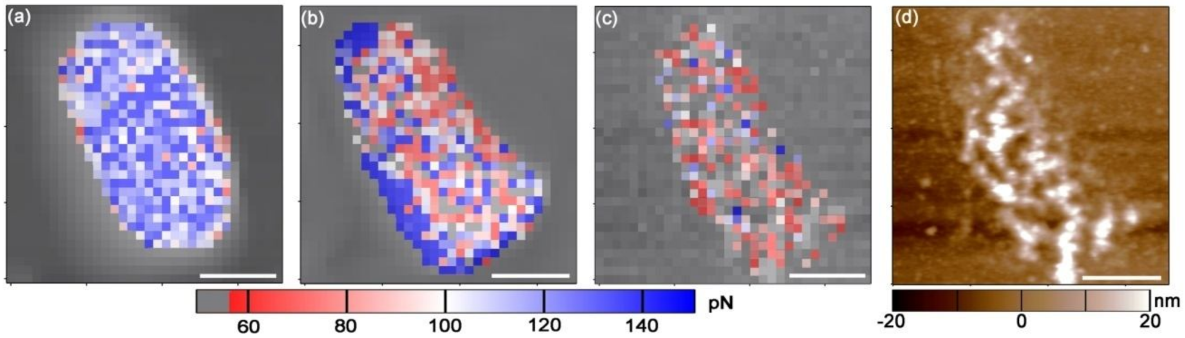

Figure 7.4. Overlay of force and height profiles for the hydrophobicity on *E. coli* cell surfaces before (a, 0 hour) and after adding 100 µg/ml of copper microparticles (b, 1.5 hours and c, 3 hours). (d) Height map of the E. coli at 3 hours. Scale bars: 500 nm. The color of pixels indicates the magnitude of force value.

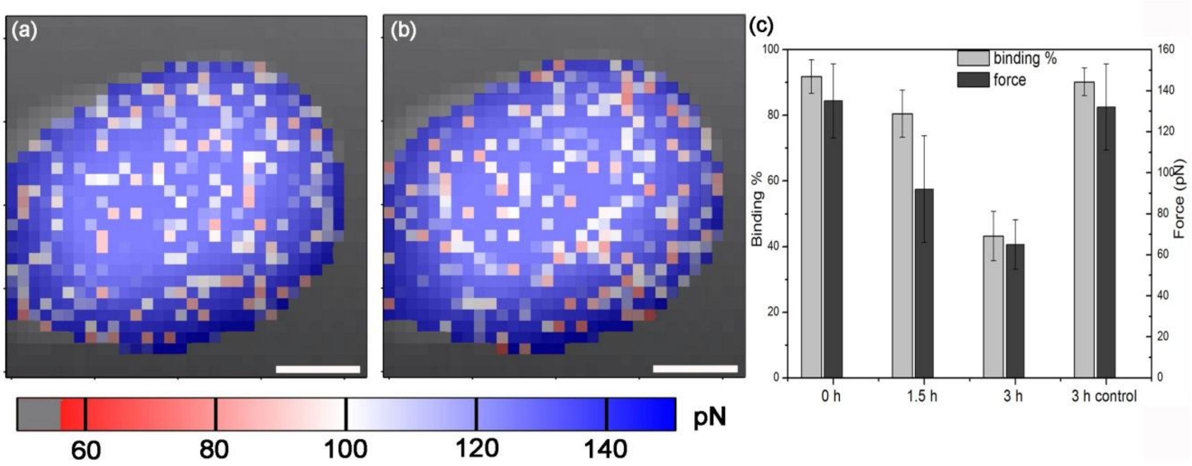

Figure 7.5. Control experiment: Overlay of force and height profiles for the hydrophobicity on *E. coli* cell surfaces in PBS in 3 hours. (a) 0 hour. (b) 3 hours. Scale bars: 500 nm. (c) Analysis of force values and binding % shows the hydrophobicity of single *E. coli* cells decreased after adding copper microparticles. Control experiment shows the hydrophobicity does not change in PBS in 3 hours. The data are from three independent experiments for each system.

7.3.3 Antimicrobial mechanism of Cu

Several models for the interaction of different antimicrobial agents such as peptides with bacterial membranes have been proposed, including barrel stave [265, 266], toroidal pore [268, 310] and carpet models [269-271]. For instance, these models describe the process of attachment to, and insertion into membrane bilayers to form pores that disrupt and kill the cell. In an earlier report, we showed how synthetic amphiphilic polycations structurally mimic naturally occurring antimicrobial peptides [74-76], and kill cells by a carpet mechanism, resulting in little observable cell damage. The mechanism of bacterial kill involved cell membrane disruption by ionic interactions between the polycations and the bacterial membrane [263, 264]. Significantly, the cells were killed without any changes to the surface morphology, but accompanied by a drastic reduction in surface hydrophobicity owing to carpeting of the surface by the polycation [311]. In contrast, here the morphological change of the *E. coli* shown in Figure 7.1 indicates the leakage of cytoplasm. Effectively, the cell is completely damaged (~80% loss of surface) with an increase of incubation time and the leakage of cytoplasm is observably due to damage to the cell membrane.

Similar morphological changes (membrane damage and cytoplasm leakage) induced by metallic particles were observed by AFM imaging in previous studies. For example, after copper iodide treatment, AFM imaging showed that both the Gram negative *DH5α* and positive *Bacillus subtilis* cells lost their cytoplasm and became flat because of cell membrane damage [308]. In another report, magnesium oxide resulted in the considerable change of *E. coli* cell membrane, and the leakage of cell content [293]. Grass et al. proposed that copper metal surfaces kill the bacteria by damaging cell membrane as the first critical step, and followed by successive events including Cu influx into the cells, oxidative damage, cell death, and DNA degradation [291]. Thus, cell membrane damage has often been postulated as the first possible killing mechanism of Cu particles.

As mentioned above, one of the most accepted mechanisms of the antimicrobial action of metallic particles is that the released metal ions penetrate into the cell membrane. It may be noted that here even though our particles were filtered to below 0.45 µm, the release of ions happens for both micro and nanosized particles. In our study, the concentration of Cu^+ was estimated to be 0.7 µmol/ml. The study of embedded microparticles in polymer matrices further confirmed that the antimicrobial effect of Cu tends to be related to metal ion release rather than the penetration of the cell membrane by the particle itself [300]. These raise the second possible kill mechanism of Cu, wherein released ions enter the cell and cause toxic effects such as generation of reactive oxygen species (ROS), and subsequent lipid peroxidation, protein oxidation and DNA degradation in cells [303, 306]. Specifically, Cu^+ and Cu^{2+} can act as catalysts in Fenton-like reactions to generate ROSs such as O_2• and OH•, that can participate in a number of reactions detrimental to cellular molecules, such as the oxidation of proteins and lipids [312]. Also, it was reported that the entered ions can bind with intracellular sulfur-containing amino acids, leading to denaturation of protein and bacterial death [313, 314].

It should be noted that previous studies on the antimicrobial mechanism of copper (particles and surfaces) considered membrane damage or ROS generation as independent events or successive events proceeding from cell membrane damage to ROS generation [291, 308]. The AFM-based hydrophobicity mapping in real time was able to further observe this mechanism from the perspective of cell surface biochemical nature. The decrease of hydrophobicity on cell membrane over the incubation time can be explained by considering the initial generation of ROS, followed by subsequent lipid peroxidation and protein oxidation. The biochemical changes of the lipids and proteins decreased the hydrophobicity of cell membrane, since the initial hydrophobicity of the cell membrane is known to arise from lipids and hydrophobic region of proteins. Membrane damage and ROS generation can therefore be considered to be integrated modes of copper antimicrobial activity. ROS generation caused by Cu ions affects the biochemical nature of membrane lipids and proteins, leading to the membrane damage and cytoplasm leakage. A reasonable sequence may therefore be hypothesized based on our results - ions penetrate into the cell membrane, generate ROS. This then causes a change in membrane permeability, leading to further ions entering the cell in a feedback loop. Finally, the cell membrane disintegrates completely, resulting in leakage of the cell cytoplasm.

7.5 Conclusions

In this chapter, *in situ* AFM was used for the analysis of the antimicrobial effect of copper particles on live *E. coli*. The ability to image live cells in real time and a liquid environment enabled observation of changes at the level of a single cell. Morphological changes to the membrane including damage and cytoplasm leakage were observed during Cu particle treatment, most significantly on the same cell over time. Further, chemical force microscopy showed that Cu decreased the hydrophobicity with the increase of incubation time, indicating a dramatic change in the cell surface biochemical nature. Based on these results, the antimicrobial mechanism of Cu was proposed to include the generation of reactive oxygen species caused by Cu ions that affect the biochemical nature of membrane lipid and protein, leading to the membrane damage and cytoplasm leakage. Taken together, the real time AFM approach here clearly elucidates the antimicrobial mechanisms of Cu particles at the single cell level and will provide important insights into the mechanisms of action and design of metallic antimicrobial agents.

[This chapter contains results that have been submitted for publication in:

Wang C, Ehrhardt C,Yadavalli VK, "Nanoscale observation of the antimicrobial effect of copper on bacterial surfaces" in Applied Microbiology and Biotechnology, November 2015]

CHAPTER 8

HYDROPHOBICITY PROFILES OF *BACILLUS CEREUS* AT THE SINGLE SPORE LEVEL

8.1 Introduction

Members of the *Bacillus* ACT group (*anthracis, cereus and thuringiensis*) are able to transform into metabolically dormant states called spores. Spores are particularly important from a public health perspective owing to their relevance in foodborne illnesses and bioterrorism [171, 315, 316]. These constructs have a common structure consisting of several concentric layers: an inner core surrounded by a cortex and a coat with an additional loose balloon-like outer layer called the exosporium. This durable architecture makes them resistant to many harsh conditions such as heat treatment and disinfection procedures [66]. It is now well known that these spores possess unique hydrophobic surface property, making them tend to adhere to the hydrocarbon phase of hexadecane-aqueous partition system [67]. The spore surface hydrophobicity is closely related to their adhesion to inanimate surface and phagocytic cells [59, 60], escape from macrophages [61], pathogenicity [62], and germination [63]. Thus, the characterization and understanding of *Bacillus cereus* spore surface hydrophobicity has great fundamental and applied importance.

To date, surface hydrophobicity of various species and strains of bacilli has been well studied using several methods including microbial adhesion to hydrocarbons (MATH) [67], hydrophobic interaction chromatography (HIC) [68], salt precipitation [69], and contact angle measurements [70]. The studied bacilli using these techniques involve *B. anthracis*, *B. cereus*, *B. thuringiensis*, *B. megaterium*, *B. subtilis*, *B. coagulans*, *E. coli*, *C. albicans* and so on. However, one of the primary disadvantages of these approaches is that they need large populations of spores for the bulk scale analysis. Considering the initial heterogeneous distribution and limited quantity of spores within a sample, as well as further analysis needs, they often require of increasing the spore concentration in a sample prior to analysis. This sample enrichment process itself often requires 8-72 hours [317, 318]. However, in the case of a bioterrorist attack, each hour of detection delay could increase infections and spread [319]. Prior reports have shown that the *bacilli* spore surface hydrophobicity differs widely among species and strains [64-66]. The composition of cultivation media such as amino acid content, or the type of complex additives could significantly affect the lipid composition of bacterial cultures. The lipid profile is itself useful in forensic investigations, e.g.: retracing culture condition and sample source [320]. This raises an intriguing question: does the culture medium affect *Bacillus cereus* spore surface hydrophobicity? Using MATH and HIC assays, Koshikawa et al. [321] and Wiencek et al. [65] studied the surface hydrophobicity of *B. megaterium* and *B. subtilis* spores in different culture media and concluded that culture media did not affect bacilli spore surface hydrophobicity. However, the *B. megaterium* and *B. subtilis* are genetically distant from *Bacillus ACT* group [169]. Also, considering their different structures (*megaterium, thuringiensis, cereus,* and *anthracis* with *exosporium versus subtilis* without exosporium), the previous conclusion that culture media did not have effect on bacilli spore surface hydrophobicity may not be able to apply to the ACT group. The effect of the culture medium on the hydrophobicity of the spore surface of the ACT group is still unclear. Thus, this emphasizes the real need to develop a facile, rapid and sensitive technique to characterize the surface hydrophobicity of the ACT group spores using minimal amount of samples.

Atomic force microscopy (AFM) based chemical force microscopy (CFM) has rapidly emerged as an important tool in microbiology [71, 72]. Specifically, using functional AFM tips as probes, adhesion forces between tip-bound groups and surface hydrophobic groups on bacteria can be measured. This technique enables researchers to map out spatial distributions of hydrophobic groups [9, 73]. The unique advantage of CFM is the ability to investigate single spore under near physiological environments in a non-destructive fashion. Previously, the hydrophobicity profiles of *Aspergillus fumigatus* spores and *Mycobacterium bovis* were reported [322, 323]. Previous chapter also has shown the versatility of this technique for detecting specific biomarkers on *B. cereus* vegetative cells and spores at the nanoscale [58]. However, to date, there have been no reports on surface hydrophobicity of *B. cereus* (or ACT group) single spores and the effect of the culture medium on their surface hydrophobicity.

In this chapter, the surface hydrophobicity profiles of bacterial spores at the single cell level and their variation as a function of the culture condition are studied. First, the CFM method for profiling *B. cereus* strain T spore hydrophobicity is developed. In contrast to earlier CFM studies which only observed localized areas on spore surfaces (typically less than 1×1 μm), the entire spore surface and its peripheral area are studied. The adhesion force value (as an index of nanoscale surface hydrophobicity) and its spatial distribution enable to distinguish highly hydrophobic exosporium and moderate hydrophobic spore coat. Second, the effect of different culture media on spore surface hydrophobicity is investigated by CFM and compared with a bulk scale HIC assay. Both methods indicate that culture media did not affect spore surface hydrophobicity significantly owing to the similar highly hydrophobic exosporium, while CFM shows an interesting hydrophobicity difference on spore coat in different culture media. Overall, CFM as a chemically sensitive imaging method offers a new way for studying the nanoscale surface hydrophobicity of single spore. The evaluation of culture medium effect on single spore surface hydrophobicity will provide more useful information for forensic investigation purpose such as retracing spore culture processes and sources.

8.2 Experimental section

8.2.1 Materials and instrumentation

1-undecanethiol, 3 aminopropyltriethoxysilane (APTES) and glutaraldehyde were purchased from Sigma-Aldrich (St. Louis, MO). Phosphate-buffered saline (PBS pH 7.4) (11.9 mM phosphates, 137 mM sodium chloride and 2.7 mM potassium chloride) and ethanol (200-proof) were purchased from Fisher Scientific. Mica was purchased from Ted Pella (Redding, CA). Ultrapure water (resistivity 18.2 MΩ•cm) was obtained from a MilliQ water purification system (Millipore Scientific, MA). Gold coated TR800PB cantilevers (Olympus) were used for chemical force mapping.

8.2.2 Cell culture and sporulation conditions

Cultures of vegetative *B. cereus* (T-strain) were maintained at 30°C on Trypticase Soy Agar

(TSA) (30 g Trypticase soy broth, (211768, Becton Dickinson, Franklin Lakes, NJ) and 15 g agar (AB1185, American BioAnalytical, Natick, MA)). Starter cultures were grown by inoculating single colonies of *B. cereus* into 125 mL of Trypticase soy broth and incubating for 24 hours at 30°C and 225 rpm. G Medium was used as the base sporulation formulation [183], and supplemented with peptone (BP9725, Fisher Scientific, Pittsburgh, PA) and tryptone (61184, Acros Organics, Waltham, MA)) (both at 8 g/L). Sporulation was performed by adding 1 mL of starter culture into 250 mL of sporulation medium and incubating at 30°C and 275 rpm in an orbital shaker. Sporulation media include G medium (G), G medium with peptone and tryptone (G+P, G+T).

8.2.3 Sample preparation for atomic force microscopy (AFM) imaging

Aminopropyl-mica (AP-mica) coupled with glutaraldehyde was used to immobilize spore samples. Freshly cleaved mica was incubated in APTES vapor in a vacuum desiccator for 12 hours. The AP-mica was immersed in 1 mL 2% (v/v) glutaraldehyde water solution for 1 hour and rinsed with ultrapure water. A 10 µL spore suspension was spotted and incubated for 30 minutes. Finally, the mica was rinsed with PBS to remove the loosely-immobilized spores. For making spore suspension, 1 mL spore suspension was taken from the culture medium and placed into a sterile 2 mL centrifuge tube. Spores were collected by low speed centrifugation (1 minute, 4°C, 4000 rpm). Each pellet was re-suspended and washed two times with 2 mL sterile ultrapure water. Finally, the pellet was resuspended in 2 mL PBS buffer and kept in refrigerator (4°C) before use.

8.2.4 AFM probe functionalization and chemical force mapping

Gold coated cantilevers were cleaned in UV/ozone for 15 minutes. Cantilevers were functionalized via immersion in1-undecanethiol solution in ethanol for 16 hours to obtain CH_3 terminated group on probe surface. Then the cantilevers were rinsed with ethanol to remove unbinding 1-undecanethiol. Subsequently, CH_3-functionalized cantilevers (spring constant ~0.16 N/m, resonance frequency 22 kHz) were used to obtain force data on spores in PBS buffer. Each experiment was repeated on at least 3 different *B.cereus* spore surfaces. Force-distance curves were obtained by collecting a series of sequential force curves in an $m \times n$ grid. Each force curve was obtained at the same loading rate (135 nN/s, at a ramp velocity of 900 nm/s) by pressing the cantilever to a low trigger point (200 pN), allowing binding to occur (contact time 0.1 second), and then retracting. All force maps were obtained by collecting ~80×80 force curves over a defined area (~2μm×2μm), estimating the adhesion force values, and displaying these values by scale of color. The height maps of the same area were generated simultaneously as the force mapping occurred. All images including height and force maps were performed using custom routines in Igor Pro 6.32 A (Wavemetrics Inc, OR) for fast processing of data.

8.3 Results and discussion

8.3.1 Single spore profiling of hydrophobicity using CFM.

Owing to the ability to measure adhesion forces with piconewton sensitivity and characterize biological surfaces with nanoscale resolution under near physiological conditions, CFM has been a fascinating technique to visualize the spatial hydrophobicity distribution on microorganism surfaces at the single cell level. For instance, Dague et al. used CFM to track the hydrophobicity change during *Aspergillus fumigates* spore germination and *Mycobacterium bovis* treated by isoniazid [323]. However, these studies only focused on small areas of the cell surface (700×700 nm^2 on *Aspergillus fumigates* spore and 400×400 nm^2 on *Mycobacterium bovis*). The primary reason for this was that the microorganisms were immobilized by mechanical trapping into polycarbonate membranes, and thus only the middle area of the microorganisms could be accessed by AFM probe. Here, the chemical immobilization method is able to expose the entire spore surface and its peripheral area without affecting spore surface biochemical properties [58]. This is important and useful for ACT group spore analysis because the loose balloon-like outer layer called exosporium can collapse at the peripheral area of the spore during sample preparation and dehydration. It is the exosporium that plays an important role in surface hydrophobicity of ACT group spores [321, 324].

To spatially map the hydrophobicity of *B. cereus* surface, CFM was conducted in a liquid microenvironment using $-CH_3$ functionalized AFM probe. The quantitative force value at each spot enables to visualize the nanoscale variations of hydrophobicity on single spores. Figure 8.1 shows the height and adhesion force maps of the spores grown in different media. An excellent correspondence can be observed between the spore profiles in the height map and a simultaneous increase of the adhesion events (increase of surface hydrophobicity) at the same areas. However, it can be observed that the hydrophobicity distribution on each force map is not homogeneous. There are three typical areas on each force map: I. Highly hydrophobic area with high adhesion force (larger than ~1.8 nN shown as blue area on force map — peripheral area of the spore in Figure 8.1b and 8.1f, and partial area on the spore surface in Figure 8.1d). II. Less hydrophobic area with adhesion force between 0.2 nN and ~ 1.8 nN (shown as light red, light blue and white areas on force map — as marked, the entire spore surface area on Figure 8.1b and 8.1f, and partial area on the spore surface in Figure 8.1d); III. Hydrophilic area with minimal adhesion force (smaller than ~0.2 nN shown as red area on force map).The highly hydrophobic area (I) is associated with the exosporium, which has sufficient amount of hydrophobic protein and lipid contents and plays a major role in spore surface hydrophobicity [321]. Interestingly, the combination of height and force map indicates that the exosporium has different states (locations and orientations) on each spore because of its loose binding and fragility [325], vividly depicting the exosporium movements during sample preparation. For instance, in Figure 8.1b and 8.1f, the exosporium collapsed at the peripheral area of spores and the underneath spore coat was then exposed. In Figure 8.1d, half of the exosporium fell off and half of it was still on spore surface. As shown on force maps, the less hydrophobic area (II) represents the moderate hydrophobic spore coat after the exosporium collapsed and fell off. Here, the force value as an index of surface hydrophobicity offer a new way to distinct the highly hydrophobic exosporium and moderate hydrophobic spore coat at the single spore level. This analysis is based on previous studies showing that both exosporium and spore coat contributes to spore surface hydrophobicty wherein exosporium is more hydrophobic than spore coat. For example, the removal of exosporium significantly reduced the spore surface hydrophobicity [324] and conversely, the hydrophobicity can be used as a marker for exosporium removal [326]. However, the spore coat still has hydrophobic sites due to the presence of spore coat hydrophobic proteins [68]. In addition, the red areas (III) without interaction on force maps are due to the hydrophilic substrate background and hydrophilic content on spore surface.

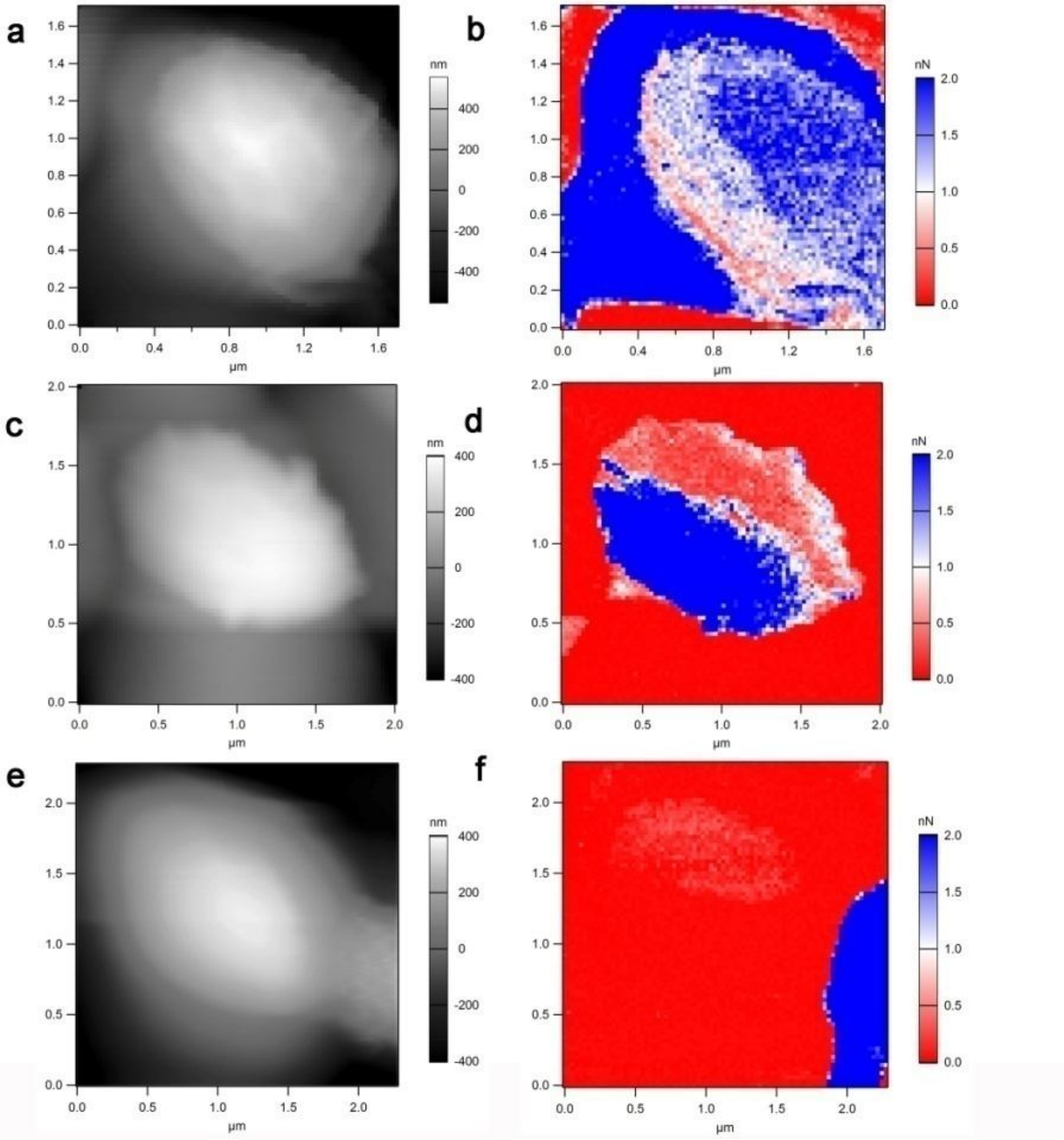

Figure 8.1. The height (left) and adhesion force (right) maps of the spores grown in different media. (a) and (b): G+T medium. (c) and (d): G+P medium. (e) and (f): G medium.

It should be noted that the different locations and orientations of exosporium in Figure 8.1 do not represent its typical states in different culture media. In other words, the culture media do not affect the exosporium states on spore surfaces. For example, Figure 8.2 a-d shows two different exosporium states of spores grown in the same culture medium (G+P). Figure 8.2b shows the exosporium was covering the entire spore coat, whereas Figure 8.2d reveals that half of the exosporium lost probably during the mechanical force during sample preparation. Interesting, the height difference along the breakage area on height map (Figure 8.2c) is ~30 nm, consistent with the reported thickness of *B. cereus* exosporium [194]. Also, the height map and force map show the identical boundary along the broken exosporium on spore surface. This further verifies our assumption (the high adhesion area I is exosporium and weak adhesion area II is spore coat) is correct. To further confirm the specificity of hydrophobic interaction between -CH_3 functionalized AFM probe and hydrophobic contents on spore surface, a control experiment was conducted using acetone washing prior to force mapping of single spores since the acetone washing is expected to remove the hydrophobic contents on spore surface [327]. Figure 8.2f shows the force map of spore after acetone treatment probing by -CH_3 functionalized AFM probe. As expected, minimal adhesion events can be observed on the spore surface, implying that the observed interaction between the -CH_3 functionalized probe and the spore surfaces are due to the spore surface hydrophobicity in nature.

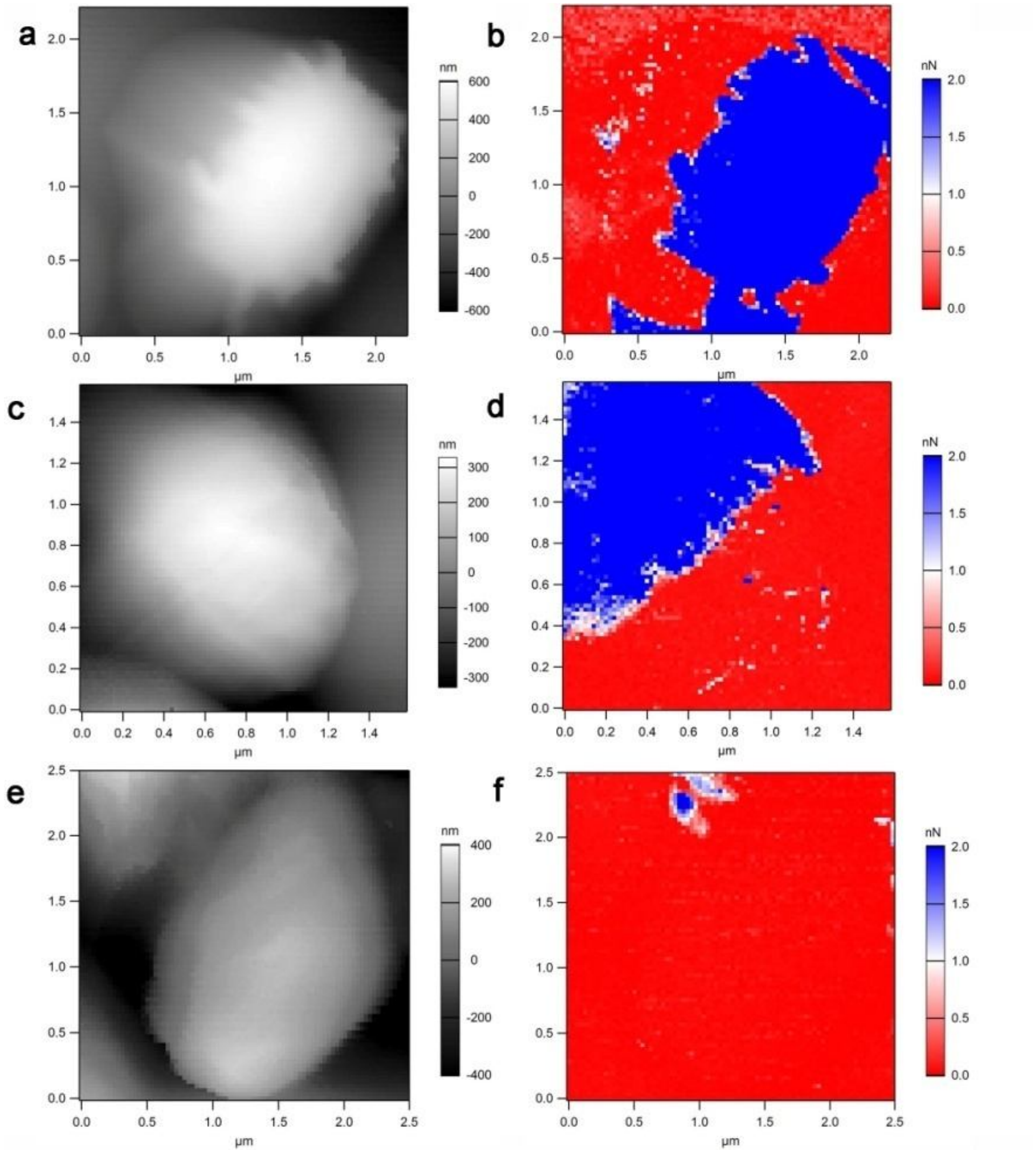

Figure 8.2. (a-d) Two different exosporium states of spores grown in the same culture medium (G+P). (e, f) Control experiment: the spore after acetone treatment probing by $-CH_3$ functionalized AFM probe.

8.3.2 The effect of culturing conditions on the spore surface hydrophobicity.

The second goal of this study was to determine whether culture media could affect *B. cereus* spore surface hydrophobicity. If so, the spore surface hydrophobicity profiling may provide useful information about the production processes of *Bacillus* organisms in a forensic investigation. Figure 8.3 shows the bulk scale analysis (HIC) of *B. cereus* hydrophobicity grown in different culture media. The percentage of retention can be used to estimate the spore surface hydrophobicity. The spores grown in all three different culture media show high retention in hydrophobic columns (~80%), consistent with the HIC retention value of the same strain(~85%, *B. cereus* T) in a previous study [321]. Also, from the close retention values (~84% in G+P, ~82% in G and ~79% in G+T), it seems that culture media did not affect the *B. cereus* spore surface hydrophobicity significantly, which is similar with *B. megaterium* and *B. subtilis* spores grown in different culture media [65, 321].

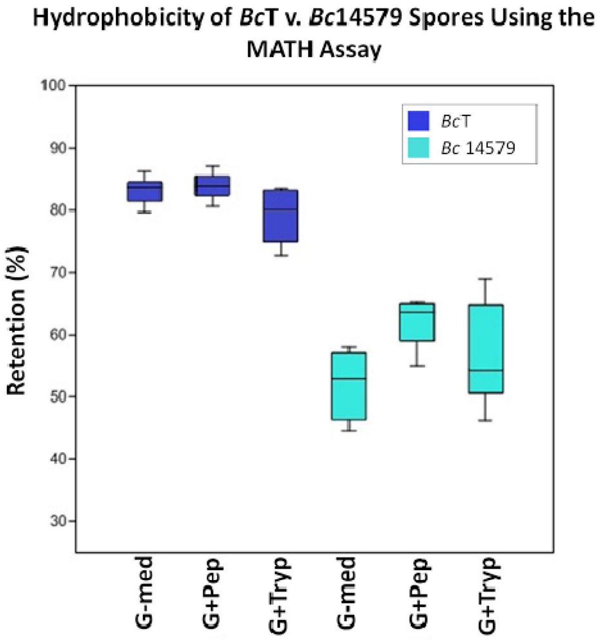

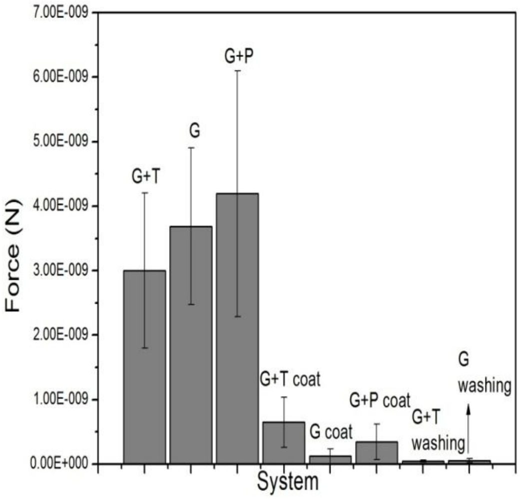

Figure 8.3. The bulk scale analysis (HIC) of *B. cereus* hydrophobicity grown in different culture media. (left)

Figure 8.4. Average force values on spore surfaces (exosporium and spore coat). (right)

This conclusion is also reasonable after incorporation with the CFM results. By quantitative analysis at least five single spores in each culture medium, we found that average adhesion force values on spore exosporium (area I: blue areas on force map) are close in different culture media (Figure 8.4). This provides a biophysical evidence to explain the similar retention % in HIC from a nanoscale perspective. Specifically, because the adhesion force values acquired at each single point (unit area around 20×20 nm) on exosporium are close, the bulk scale hydrophobicity of spore is similar in different culture media, assuming the exosporium covered the entire surface of all the spores or these spores are the mixture of many spores with different extent of exosporium losing in HIC. Also, the high average adhesion force values on exosporium further demonstrate the primary role of exosporium in spore surface hydrophobicity. Interestingly, the adhesion force values on exosporium shows similar trend with HIC retention values (~4.2 nN in G+P, ~3.7 nN in G and ~3 nN in G+T). However, due to the different methodology and sensitivity of the two techniques, we cannot over-interpret the data here.

As discussed before, CFM, as a nanoscale and chemically sensitive imaging technique, offers a unique advantage over bulk scale methods- nanoscale distribution of hydrophobicity are presented on single spores. The force maps have shown different exosporium states after spore immobilization: a. collapsed on peripheral areas of spores; b. part of it fell off. These two situations provide us opportunities to deconvolute the highly hydrophobic exosporium (area I) and weakly hydrophobic spore coat moderate (area II). Unlike the close adhesion force values on exosporium, the quantitative analysis shows that average adhesion force values on spore coat (area II) are different in different culture media (~0.34 nN in G+P, ~0.12 nN in G and ~0.65 nN in G+T Figure 8.4). One speculation is that peptone and tryptone as protein source supplements in culture media have direct biosynthetic relationship with spore coat hydrophobic protein and other hydrophobic contents such as fatty acid [328], and thus increase the spore coat hydrophobicity. This speculation is based on previous studies which reported the amount of nutrient in growth media affected protein expressions and relevant spore properties [329]. For instance, Hornstra et al. [183] found that the average transcription level of the *ger* operons (encoding germination receptors) per *B. cereus* spore was higher in a nutrient-rich medium (Y1 medium) and lower in a nutrient-poor medium (modified G medium). As a result, the number of germination receptors was higher in spores prepared in Y1 medium, leading to higher germination rates and efficiencies. Another study on *B. subtilis* spore [330] also showed similar result, in which spores grown in a nutrient-rich medium germinated faster than spores in a nutrient-poor medium due to the different expression level of germination receptors. Therefore, in this study, the G medium with peptone/tryptone (G+P and G+T) can be classified as a nutrient-rich medium, whereas G medium (G) can be grouped into a nutrient-poor medium. The higher hydrophobicity of spore coat in nutrient-rich media may be related to the higher expression of hydrophobic protein on spore coat. Further work is needed to clarify the biosynthesis route of spore coat protein and fatty acid, as well as their specific correlation with spore surface hydrophobicity. However, the use of CFM here helps us to re-evaluate the result of HIC since the high hydrophobic exosporium may hide the culture media effect on spore surface hydrophobicity such as the moderate hydrophobic spore coat beneath the exosporium. Overall, CFM provides a nanoscale angle to resolve surface properties of single spore and this may be an important complementary technique for retracing the production methods (e.g. culture medium fomula) of *Bacillus* organisms in a forensic investigation.

8.4 Conclusions

In this chapter, the CFM method is developed for profiling *B. cereus* strain T spore hydrophobicity at the single spore level. Both the entire spore surface and its peripheral area are mapped by hydrophobic AFM probe. The adhesion force value and its spatial distribution enable to distinguish highly hydrophobic exosporium and moderate hydrophobic spore coat. As a control experiment, acetone washing is used to remove hydrophobic contents on spore surface which is confirmed by CFM images. Then both CFM and HIC methods indicate that culture media did not affect spore surface hydrophobicity significantly owing to the presence of similar highly hydrophobic exosporium. Interestingly, CFM shows the hydrophobicity difference on spore coat in different culture media, which enables to distinct nutrient rich or nutrient poor culture medium. Taken together, CFM as a chemically sensitive imaging method offers a new way for studying the nanoscale surface hydrophobicity of single spore. The evaluation of culture medium effect on single spore surface hydrophobicity at the nanoscale will provide more useful information for forensic investigation purpose such as retracing spore culture processes and sources.

CHAPTER 9

DNA MAPPING ON HUMAN EPITHELIAL CELL SURFACES

9.1 Introduction

At the scene of a crime, suspects may usually leave behind few epithelial cells (such as palm and buccal cells) due to their body or body fluids touching a surface. Owing to the limited quantity of such cell samples, it is often difficult to conduct bulk scale analysis. Therefore, tools for the analysis of epithelial cell at the level of a single or few cells are useful for forensic identification. While most DNA is localized to the cell nucleus, evidence has been presented for the existence of other forms of DNA associated with the outer leaflet of the plasma membrane [331]. These cell membrane-associated DNAs (mDNAs), also called extracellular DNA (eDNA), originate at the cell nucleus and are expressed at the cell membrane. The function of mDNAs is still unclear. Previous study has shown that mDNAs can serve as specific targets for IgG autoantibodies in systemic lupus erythematosus (SLE) patients [332]. In addition, cell surfaces may loosely bind DNA that originates from body fluid or other sources. For example, buccal cell surface DNA comes partially from broken white blood cells in saliva. Palm cell surface may have DNA after touching some public surfaces or body fluid. Therefore, detecting and mapping the cell surface

DNA on single epithelial cells including mDNA and loosely binding DNA could be a novel means to identify suspects at the single cell level.

In a previous report, lactoferrin has been demonstrated to be a cell membrane-DNA binding protein [333]. In this chapter, AFM force mapping coupled with lactoferrin as the bioprobe were used to detect cell surface DNA on single epithelial surfaces. Buccal cells and palm cells from three different donors are studied. By calculating the binding percentages, it is interesting to see that cell surface DNA contents tend to be different on different donors. As a control, the same cells (same areas on mica) were imaged before and after (1 hour) the addition of DNase. The significant decrease of binding % further confirms the specificity of lactoferrin and cell surface DNA interactions. Thus cell surface DNA profiling could be a potential tool for forensic identification at the single cell level.

9.2 Experimental Section

9.2.1 Materials

(1-Mercaptoundec-11-yl) hexaethylene glycol (Oligoethylene glycol (OEG) terminated thiol), $HS\text{-}C_{11}\text{-}(EG)_6\text{-}OH$, and (1-mercaptohexadecanoic acid)-N-succinimidyl ester (NHS terminated thiol), $HS\text{-}C_{15}COO\text{-}NHS$, were purchased from NanocsInc. (Boston, MA). Lactoferrin and DNase II were purchased from Sigma-Aldrich (St. Louis, MO). Phosphate-buffered saline (PBS pH 7.4) (11.9 mM phosphates, 137 mM sodium chloride and 2.7 mM potassium chloride) and ethanol (200-proof) were purchased from Fisher Scientific (Waltham, MA). Mica was purchased from Ted Pella (Redding, CA). Ultrapure water (resistivity 18.2 MΩ.cm) was obtained from a MilliQ water purification system (Millipore Scientific, MA). AC240TS cantilevers (Olympus) were used for non-contact mode imaging in air, while gold coated TR800PB cantilevers (Olympus) were used for force measurements.

5.2.2 Cell collection

Buccal cells were collected using cotton swab. Palm cells were collected by rubbing palms on centrifuge tube. For washed cells, the collected cells were washed three times in water by high speed centrifugation.

5.2.3 Sample preparation for AFM

Cells were immobilized using the poly-L-lysine fixation method described earlier. Mica was coated with poly-L-lysine to increase the adherence of the cells. Freshly cleaved mica was immersed for 10 minutes in a solution of 0.05 mg/ml poly-L-lysine hydrobromide and 10 mM Tris (pH 8.0). The surface was then covered and dried vertically overnight at room temperature. The coated mica was stored at room temperature and was used within one week. Concentrated cells suspended in PBS were deposited on the coated mica and incubated for 30 minutes. The cells were kept hydrated at all times. Excess cells were rinsed off with three washes of 1 ml water. Images were taken in PBS using non-contact mode imaging. To observe the cells *in situ* and in real time, the same cells (same areas on mica) were imaged before and after (1 hour) addition of DNase (control experiment).

5.2.4 AFM probe functionalization and force recognition mapping

AC240TS cantilever (spring constant ~2 N/m, resonance frequency 70 kHz) were cleaned using high-intensity UV light to remove organic contamination and used for imaging in air and characterization of the surfaces in non contact mode. Gold coated cantilevers were cleaned in UV/ozone for 15 minutes. The gold cantilevers were then functionalized by immersion in mixed thiol solution ($HS-C_{11}-(EG)_6-OH$ and $HS-C_{15}COO-NHS$) in ethanol for 16 hours [87]. Cantilevers were rinsed with ethanol, and incubated in a 100 nM lactoferrin in PBS buffer for 1 hour at ambient temperature. Our group has earlier shown that this functionalization strategy limits the number of proteins on the tip surface to 1-3 [102]. Lactoferrin-functionalized cantilevers (spring constant ~0.15 Newton/meter (N/m), resonance frequency 15 kHz) were then used to obtain force data on cells in PBS. Each experiment was repeated on at least 3 different cells. Force curves were obtained by collecting a series of sequential force curves in an $m \times n$ grid (an array with m lines and n points per line). Each force curve was obtained at the same loading rate (135 nN/s, at a ramp velocity of 900 nm/s), allowing binding to occur (contact time 0.1 second), and then retracting. 50×50 force curves were collected over a defined area and unbinding forces were displayed on a scale of color. The height maps of the same area were generated simultaneously. As a control, DNase experiments were performed by a buffer exchange of PBS containing 100μg/ml DNase in the fluid cell. All images including height and force maps were analyzed using custom routines in Igor Pro 6.32 A (Wavemetrics Inc, OR).

9.3 Results and discussion

Initially, AFM imaging was used to image the nanoscale morphology of human epithelial cells. Figure 9.1 shows the different morphology of single buccal and palm cells. Buccal cells are flat, thin, and have a nucleus in the center, whereas palm cells are thicker and have no nucleus. Interestingly, the cell morphology did not change after being exposed for two or three weeks in air. Here, although AFM imaging can distinguish between buccal and palm cells from their morphology, it is not possible to identify specific donors.

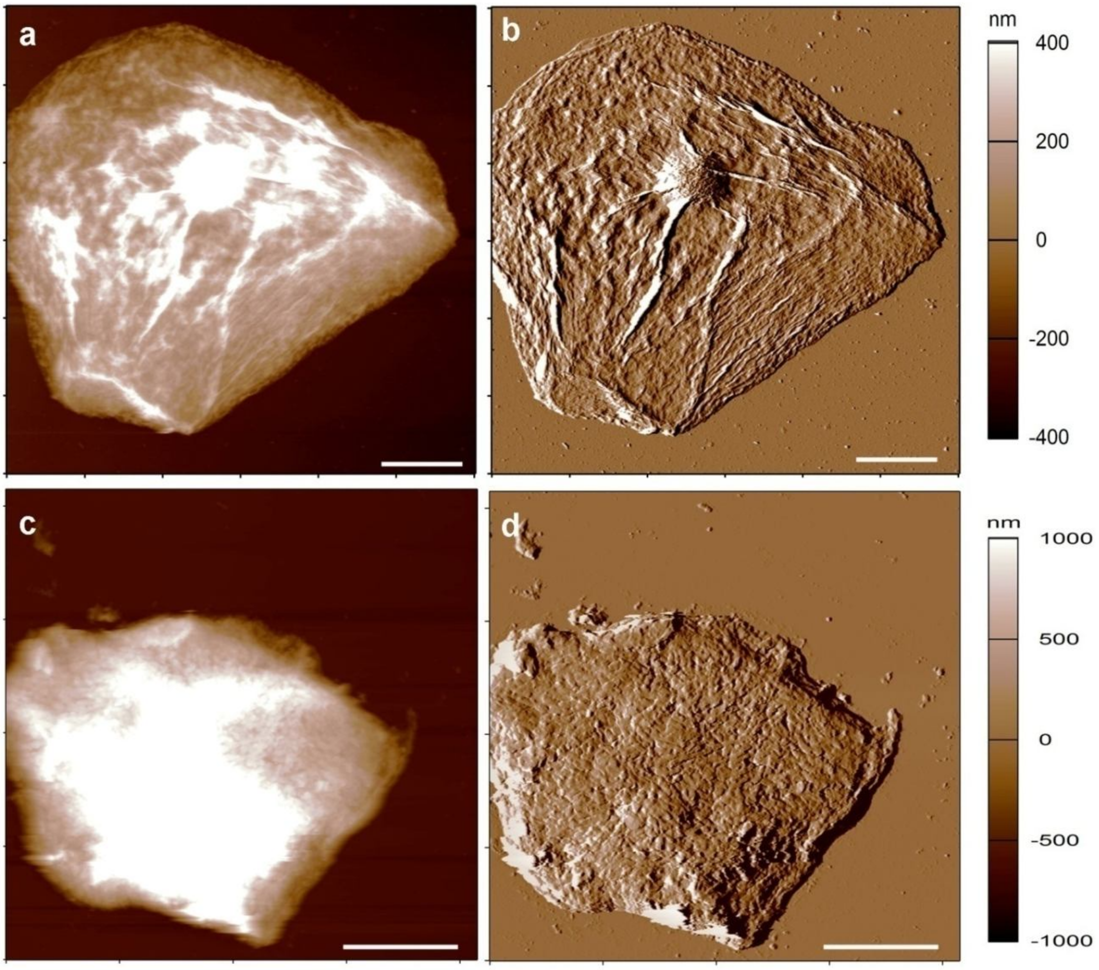

Figure 9.1. AFM imaging of morphology of single buccal (a, b) and palm cell (c, d). Scale bars: 10 µm.

According to the binding % calculation, the DNA content is the same, whether calculated on the entire cell surface or a smaller area of the cell. Both unwashed and washed cells were studied (Table 9.1-9.4). The hypothesis is that unwashed cell surfaces contain both mDNA and loosely binding DNA, whereas washed cell surfaces only contain mDNA, which is tightly binding. After washing three times, the DNA content is close across different donors for both buccal and palm cells (Table 9.2 and 9.4). It can be seen that buccal cells have more mDNA than palm cells, which implies that most of the DNA on palm cells originated from "touch" DNA, which is loosely binding. In contrast, unwashed cells show different DNA contents across different donors (Table 9.1 and 9.3). Therefore, unwashed cells can potentially be more useful for differentiating the donors. However, in buccal unwashed cells, "H73" and "D11" have similar DNA content. In palm unwashed cells, "CES and H73" have close DNA content. One solution could be the use of a combination of buccal and palm cell; each donor will have characteristic values in terms of cell surface DNA content. For instance, "H73 and D11" have similar DNA contents on buccal cells, but the DNA contents are different on palm cells.

To confirm the specificity of lactoferrin to cell surface DNA, a control experiment was conducted by adding DNase solution into the force mapping micro-environment. The same area was monitored in real time on unwashed palm cells before and after incubation with DNase. Table 9.5 shows that cell surface DNAs decreased after DNase incubation, implying the detection of DNAs on untreated cell is from DNA- lactoferrin interactions.

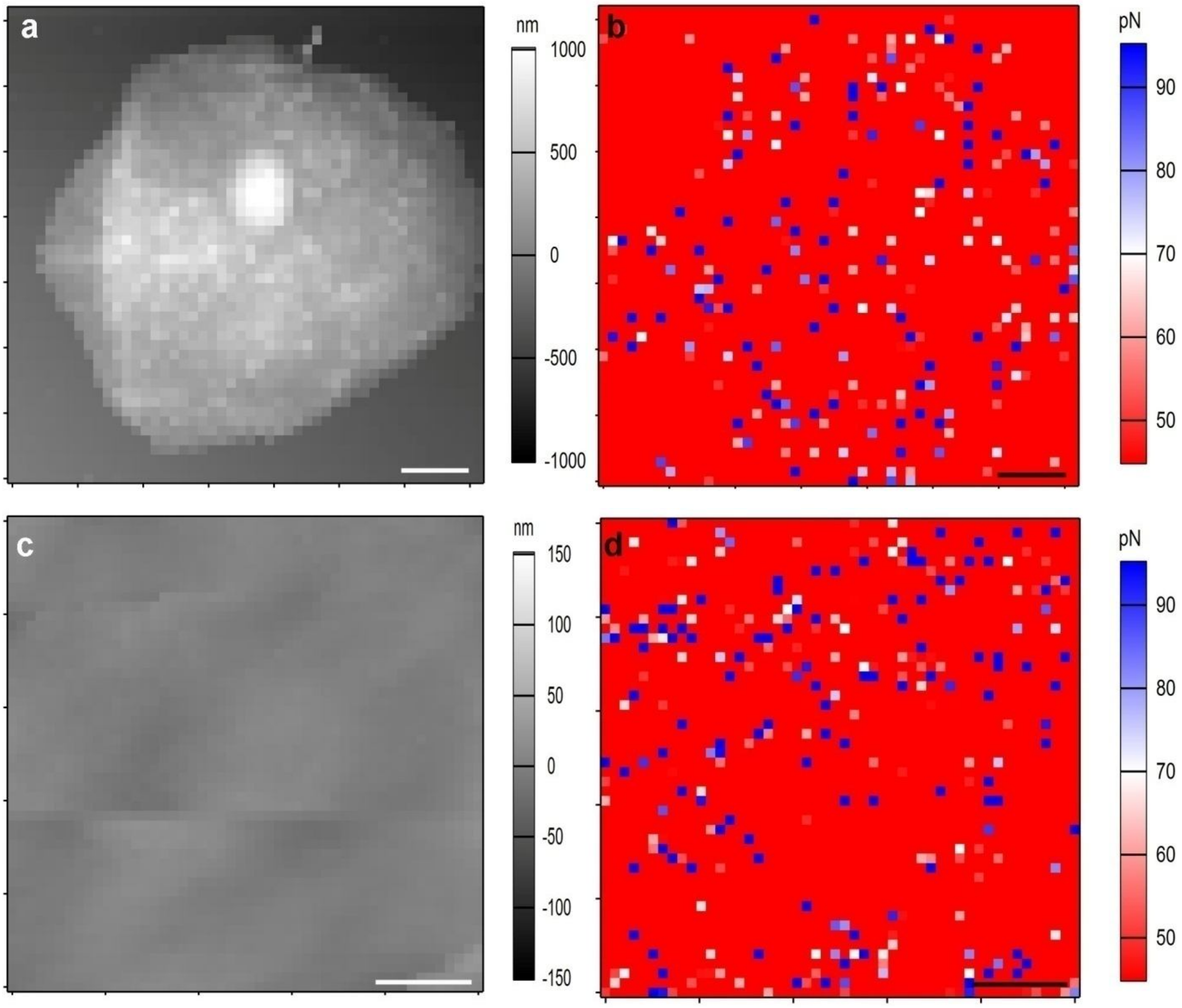

Figure 9.7. DNA force mapping of an entire single buccal cell (a, height map. b, force map. Scale bars: 10 µm) and a smaller area (a, height map. b, force map. Scale bars: 0.5 µm) of the same buccal cell.

Table 9.1.-9.4. DNA mapping on buccal and palm cells using lactoferrin.

Table 9.1. Unwashed buccal cells from three donors. Three individual cells were analyzed for each donor.

Donor name	Unwashed I	II	III	Mean and SD
CES	9.37%	10.05%	9.99%	9.71±0.48%
H73	16.2%	14.88%	16.64%	15.91±0.92%
D11	15.12%	12.84%	14.36%	14.11±1.16%

Table 9.2. Washed buccal cells from three donors. Three individual cells were analyzed for each donor.

Donor name	Washed I	II	III	Mean and SD
CES	6.46%	5.44%	6.45%	6.09±0.63%
H73	5.08%	5.2%	7.8%	6.02±1.55%
D11	4.32%	6.44%	4.92%	5.23±1.09%

Table 9.3. Unwashed palm cells from three donors. Three individual cells were analyzed for each donor.

Donor name	Unwashed I	Unwashed II	Unwashed III	Mean and SD
CES	8.56%	9%	9.64%	9.07±0.54%
H73	10.2%	9.6%	8.2%	9.33±1.02%
D11	5.7%	3.8%	3.3%	4.27±1.27%

Table 9.4. Washed palm cells from three donors. Three individual cells were analyzed for each donor.

Donor name	washed I	washed II	washed III	Mean and SD
CES	3.84%	2.64%	2.04%	2.84±0.92%
H73	2.4%	2.24%	3.16%	2.60±0.49%
D11	1.6%	2.12%	1.56%	1.76±0.31%

Table 9.5. Control experiment: real time detecting DNA on unwashed palm cells before and after DNase incubation.

Donor name	Before adding DNase	After adding DNase
CES	8.76%	1.64%
H73	11.8%	2.28%
D11	6.69%	0.8%

9.4 Conclusions and future work

Our preliminary results have shown cell surface DNA force mapping has the potential to differentiate different donors. However, the interaction of lactoferrin and cell surface DNA is primarily from electrostatic interactions. This increases the uncertainty of the detection since lactoferrin might interact with other negatively charged biopolymers on cell surfaces. Also, it is not possible to determine the specific sequence of DNA using this technique. Therefore, this nanoscale technique needs to be combined and compared with bulk scale analysis techniques such as DNA amplification for more conclusive results.

CHAPTER 10

CONCLUSIONS, CHALLENGES AND FUTURE WORK

10.1 Conclusions

In summary, the research described in this dissertation is focused on the development and enhancement of integrated nanoscale imaging, and biophysical recognition of single cell surface biomolecules and further the understanding of fundamental biological processes at the nanoscale. This could lead to novel robust methods for the analysis of individual cells, via detection and assessment of changes in cell behavior and function over time either as a result of natural state changes or when perturbed. This research followed sequential steps leading to the goal of studying complex cellular surfaces:

1. Fundamental investigation of the nature of the heparin-thrombin interaction was performed by AFM-based force spectroscopy. A protein-resistant and GAG-functionalized surface for measuring interactions in different liquid environments was developed. The insights into the heparin-thrombin interaction from a force and energy viewpoint at the single molecule scale can provide better understanding of the mechanisms of blood (anti)coagulation under applied force or flow conditions. Furthermore, this chapter builds an AFM platform to study the single-pair molecular

interactions and facilitates subsequent AFM-based single molecules detection and mapping on various surfaces.

2. Based on AFM-based force spectroscopy at the single molecular level, the location and distribution of single proteins were mapped using AFM-based force recognition mapping. Aptamers were highly stable and versatile against different targets such as human α-thrombin and $VEGF_{165}$ on mixed SAM surfaces. The overlay of height and force data on the same areas showed strong adhesion forces on high features at a resolution down to 10 nm. The specificity of DNA aptamers to their targets was confirmed by heparin blocking and control experiments. These results demonstrate that DNA aptamers as bioprobes coupled with the force recognition mapping have the capability to localize specific proteins at a single molecule level, as well as detect changes in binding due to environmental changes. This chapter also enables the development of broader techniques to study living cell surface combining force recognition with spatial localization.
3. *B. cereus* was selected as a model system to study the spatial distribution of cell surface carbohydrates and quantitatively assess the changes during a specific cellular process (sporulation) and under different micro-environments. By calculating the binding using different lectin probes, WGA and ConA, it was shown that surface molar ratios of Glu/Man:GlcNAc range ~1:4 on a vegetative cell but switch to ~3:1 on a spore. This leads to visualization of targets of interest and their changes on cell surfaces and the development of robust strategies for addressing specific cellular questions from nanoscale and single cell level. In addition, time-lapsed AFM imaging and elasticity mapping demonstrate the power of AFM applied in microbiology for multi-parametrically probing important biological processes at the single cell scale.

4. The spatial distribution and changes of the cell surface biomolecules were used for broader practical applications in single cell study:
    - Evaluating effect of inactivation methods and growth temperatures on *Y. pestis* using nanoscale imaging and carbohydrate mapping: the results provide insight into the tools for studying virulent pathogens with equipment that may not have elevated biocontainment capabilities - inactivation followed by nanoscale evaluation of the effects on cell morphology and surface bioactivity. Understanding how external microenvironments (temperature, irradiation), including those designed to inactivate the *Y. pestis*, affect the structure and biochemical behavior of the cell surface, can help us not only design better inactivation protocols, but also shed light on the in situ characteristics of pathogens.
    - Evaluating effect of antimicrobials on *E. coli* using real time nanoscale imaging and hydrophobicity mapping: unlike conventional methods, the same living cell was tracked over time to obtain a better picture of the mechanisms of copolyoxetane and copper microparticles behavior. The characteristic cell morphological and hydrophobicity change confirmed that the copolyoxetane molecules initially bind with cell membrane in a carpet-like fashion and further disturb the cell membrane. In contrast, the ROS generation caused by copper ions affected the biochemical nature of membrane lipid and protein, leading to the membrane damage and cytoplasm leakage. Taken together, the real time AFM approach clearly elucidates the antimicrobial mechanisms of copolyoxetane and copper microparticles at the single cell level and this will provide important

insights into mechanism of action of other similar antimicrobials.

- Evaluating effect of culture media on *B. cereus* spore using hydrophobicity mapping: the CFM showed that the adhesion force value and its spatial distribution enabled to distinguish highly hydrophobic exosporium and moderate hydrophobic spore coat. The hydrophobicity difference on spore coat in different culture media potentially enabled to distinct nutrient rich or nutrient poor culture medium. The evaluation of culture medium effect on single spore surface hydrophobicity at the nanoscale provides more useful information for forensic investigation purpose such as retracing spore culture processes and sources.

Overall, the localization of specific cell surface biomolecules offers a new avenue to classify various cell types/strains, monitor diverse cellular processes, study mechanisms of drug action, and reconstruct different growth conditions and cell states from a nanoscale and single cell perspective. Such nanoscale tools will further our understanding of fundamental biological processes, and lead to novel, robust methods for the analysis of individual cells.

10.2 Challenges and Future Work

10.2.1 Cells sample preparation for AFM imaging

Challenge and solution:

To image cell samples in liquid using AFM, a primary challenge is to immobilize the cells on substrates firmly otherwise AFM tips may drag or move the cells during scanning. Initially, we tried different methods in literatures including gelatin and glutaraldehyde immobilization methods. Unfortunately, the gelatin method did not work well as none of the cells were immobilized (Figure 10.1). We demonstrated that glutaraldehyde functionalized substrate was able to immobilize the bacteria in liquid firmly. This method used the aldehyde group to crosslink the amine group on substrate and one side of the cell surface covalently. Thus, the other side of the cell surface was untouched by glutaraldehyde and then specific targets on this side such as carbohydrates could be detected by force mapping. This glutaraldehyde method is suitable for nanoscale imaging and force mapping of biomolecules on cell surfaces in liquid.

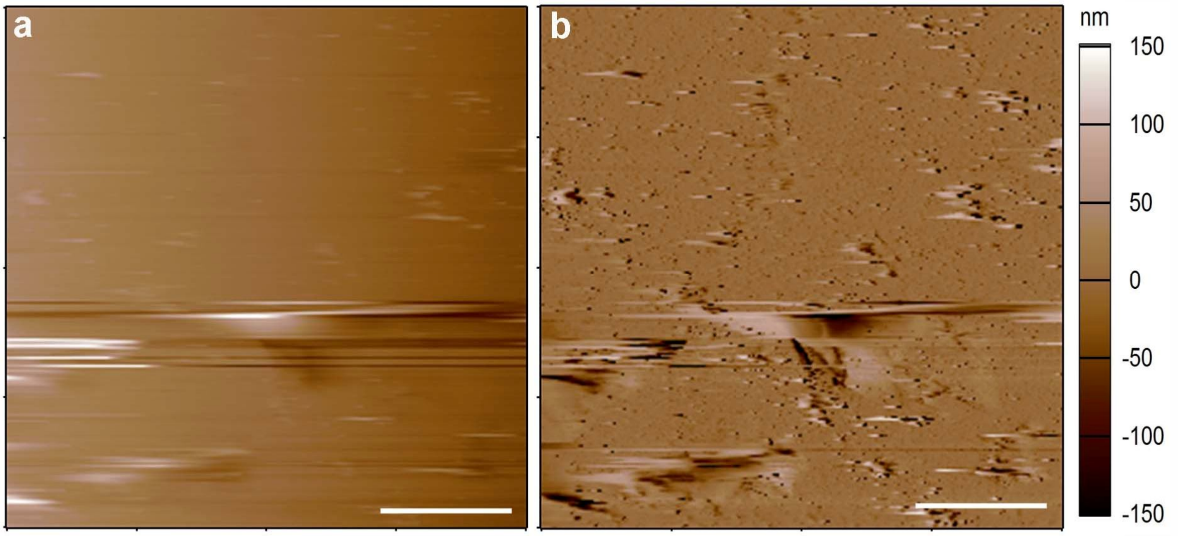

Figure 10.1. AFM imaging *E. coli* cells on gelatin coated mica (a: height image. b: amplitude image). No cells can be observed. Scale bars: 10 µm.

For real time study, a second challenge is in keeping the cells alive during and after immobilization. If the cells die, it is not possible to observe the cell response to external effectors such as antimicrobial treatments in real time. Initially, glutaraldehyde immobilization was attempted for the real time study. Unfortunately, the cell did not change during the antimicrobial treatment, presumably because the cell had already died prior to the addition of the antimicrobial (Figure 10.2). A second immobilization method – poly-L-lysine was demonstrated to be a nice method to immobilize the cells and meanwhile, keep the cells alive. The results described in Chapter 6 and 7, using this method, show that the cell morphology change and surface hydrophobicity change could be observed in real time using AFM imaging and force mapping, implying that the cells are alive and active. It should be noted that because poly-L-lysine method uses electrostatic interaction rather than covalent bonding, the immobilization is not as firm as glutaraldehyde fixation. This results in movement of some cells during imaging (Figure 10.3). A good solution for this is to use a soft AFM tip, NT-MDT tip (spring constant, 0.6 N/m).

Overall, depending on the goals, different methods can be used. The glutaraldehyde method can immobilize cells firmly and is proper for cell imaging and force mapping. Poly-L-lysine method can immobilize cells gently and keep cells alive, which is suitable for real time observation.

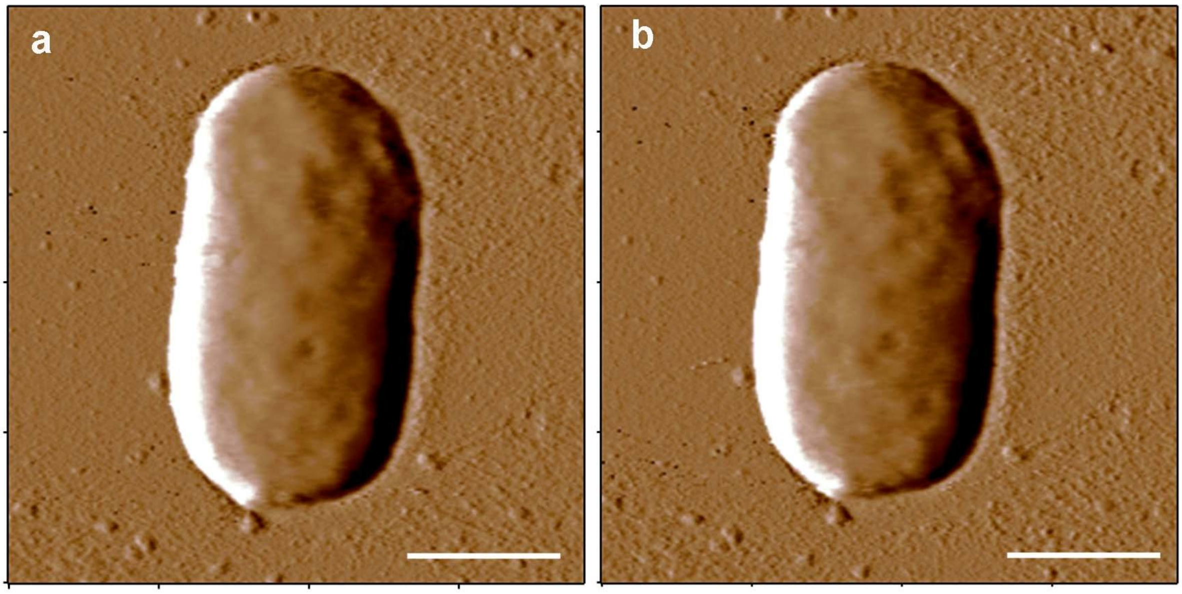

Figure 10.2. AFM amplitude images of *E. coli* cell on glutaraldehyde functionalized surface before (a, 0 h) and after (b, 3 h) adding antimicrobial polymer. There is no change can be observed, implying the cell death at 0 h. Scale bars: 1 µm.

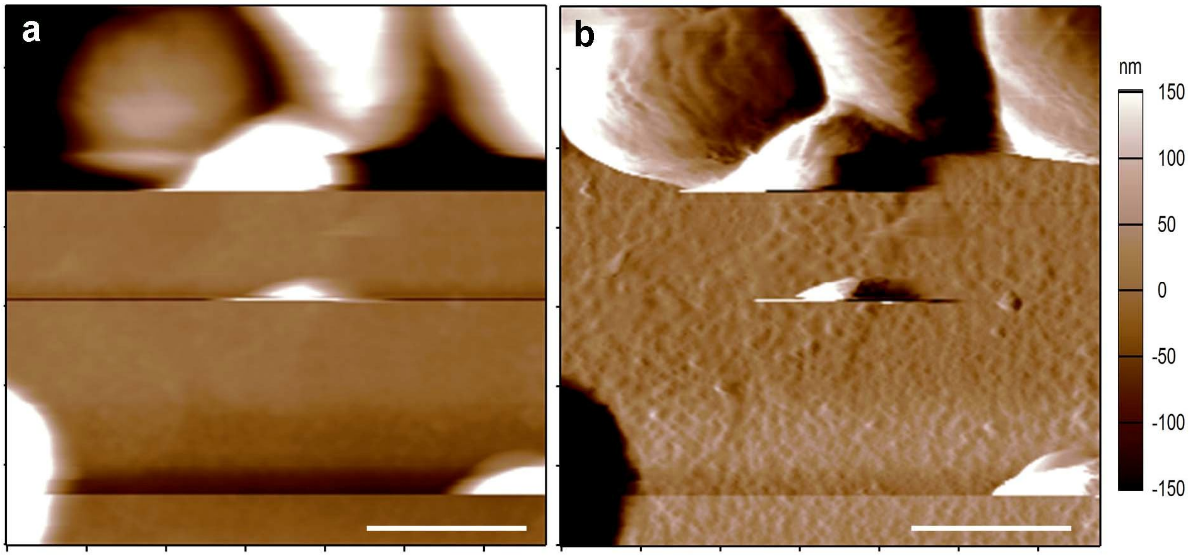

Figure 10.3. AFM imaging *E. coli* cells on poly-L-lysine coated mica (a: height image. b: amplitude image) scanned using stiff AFM tip. Scale bars: 1 µm.

Future work: The further development of the technique - temperature control

In this work, real time AFM has been demonstrated to be a powerful technique to study antimicrobial mechanisms at the single cell level. The prerequisite of these real time experiments is that the cells need to be alive during the monitoring process. In order to observe the living cells and their active responses to different drugs or external effectors, the monitoring process usually could not exceed 5 hours since the cells can die due to the lack of temperature control. Therefore, controlling of the temperature of the AFM stage to provide a favorable cell growth condition will extend the capability of this technique to study long-term dynamic biological processes at the single cell level. More importantly, the cell immobilization step can be skipped, and the cells can be analyzed in culture media and container directly.

10.2.2 AFM force mapping data collection and analysis

Challenge and solution:

A challenge in AFM force mapping is to collect reliable force curves. This is more difficult in a liquid environment or for a real time study, since thermal non-equilibrium in the system creates noise on force curves. Figure 10.4 shows significant vibration on both height and force map images of the cell, affecting the quality and accuracy of the force mapping. A good solution for this may be obtained by the following: a, leave the system at least 30 minutes for thermal equilibrium, after immersing the tip in liquid and changing buffer during real time study. b, put the buffer or drug solution in the AFM containment to make sure they have similar temperature as the buffer in fluid cell. To obtain reliable force curves, especially for detecting specific biomolecules on cell surfaces, it is important to decrease the non-specific interactions between AFM tips and cell surfaces. The use of mixed SAMs of OEG is efficient to control the bioprobe density on AFM tip and more importantly, decrease the non-specific protein absorption on AFM tip.

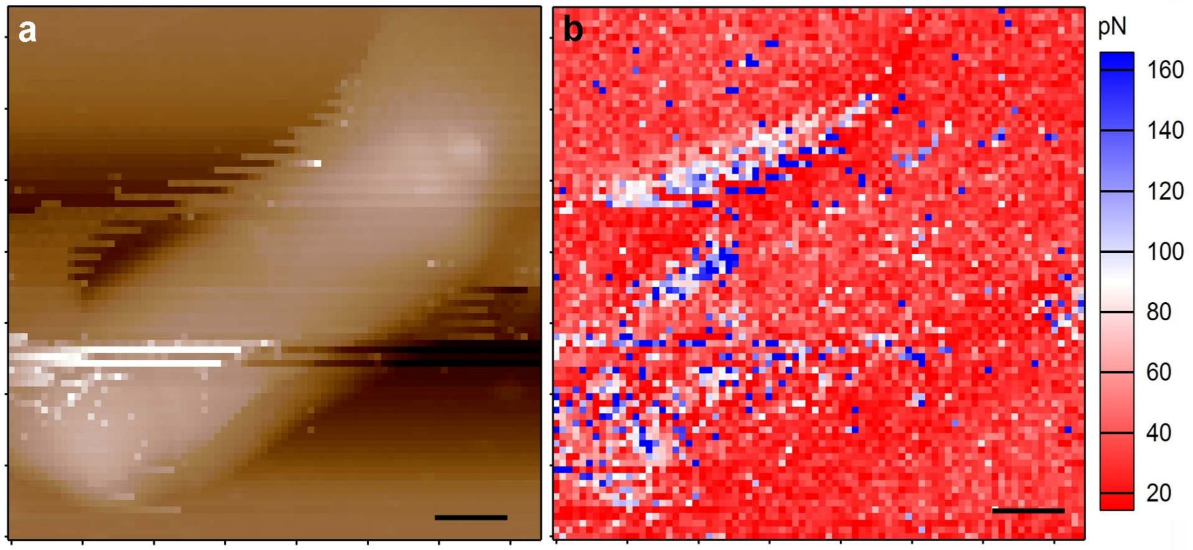

Figure 10.4. Vibration observed in both height (a) and force (b) map images of the cell because of thermal non- equilibrium. Scale bars: 0.5 μm.

After data collection, a challenge is to accurately process the large number of force curves, and differentiate specific and nonspecific interactions, even though PEG-OH SAM can decrease the non-specific interactions. Here, two important points are needed to be considered when differentiating specific and nonspecific interactions: a, for specific interactions, there is an obvious slope change at the retraction curves. b, noting the *expected* interaction force and rupture length values of the studied molecular interactions. (Typically, these values can be estimated from the literature). Based on the slope change, interaction force and rupture length, our lab developed software to analyze a large number of force curves and exclude non-specific force curves. Figure 10.5 shows the original and processed force map of carbohydrate on *B. cereus* cells. There is a rough consistency between the height map and original force map. However, there are still some non-specific interactions on the background (white area), comprising the quality and accuracy of the force map. By setting specific threshold values of interaction force and rupture length, most of non-specific interactions can be excluded.

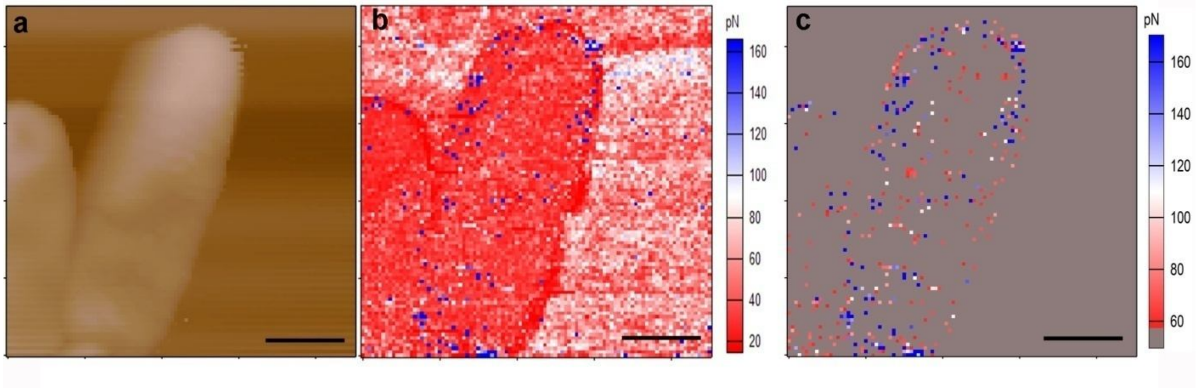

Figure 10.5. The height (a), original (b) and processed (c) force map of carbohydrate on *B. cereus* cells.

Future work:

AFM force mapping allows us to spatially detect specific biomolecules. The collection, differentiation and analysis of specific interactions have been discussed in last section. In future, in order to detect biomolecules accurately and study cell surfaces extensively, new nanoscale techniques can be applied.

I: Electrostatic force microscopy (EFM) for surface charge distribution:

In this work, antimicrobial polymers and copper particles have been demonstrated to disturb the cell membrane and thus lead to the cell death. The hydrophobicity mapping provides an indirect evidence to show the damage of the cell membrane integrity. Cell membrane charge and its distribution provide a direct and important parameter relevant to cell health and state [284]. EFM has emerged as a powerful tool for imaging charge propagation at the nanoscale because it is very sensitive to local charges and can image charge distribution within a single molecule like proteins [334]. Therefore, the study of cell membrane charge distribution and its change induced by external effectors will be a strong enhancement to the AFM technique for single cell analysis.

II: The combination of AFM with other ultra-sensitive surface techniques:

In this work, AFM-based techniques were used to detect cell surface biomolecules. Surface-enhanced Raman spectroscopy (SERS) can realize ultrasensitive levels of detection and non-invasive tagging of specific bioanalytes in living cells and animals [335]. With the single-molecule sensitivity and specificity, super-resolution fluorescence microscopy can localize single bio-molecules in 3D space and track their motion over time [336]. The cooperation of AFM with these ultra-sensitive surface techniques will expand the application of single cell analysis and address some more complicated cellular questions.

10.2.3 Single bacterial cell identification: building cell surface biomolecule database

Challenge:

In this work, the cell surface carbohydrates were detected using specific lection probes. It has been demonstrated that cell surface carbohydrate composition could be a potential tool for identification of *Bacillus* types and strains. However, carbohydrates are not necessarily stand-alone biomarkers for all cell types. Suppose we have a single or few unknown cell(s), or a mixture of different types of cells,   analyzing carbohydrates is not sufficient for cell type identification. An interesting method will be the detection of more specific biomarker and figure out its presence and absence. For instance, F1 antigen is the biomarker which can only found on *Y. pestis* cell surface. And the F1 antigen antibody is commercially available bioprobe. However, the ability of this technique is limited to targets that can be directly probed by specific binding ligands.

Future work:

For each type of bacterium, various cell surface biomolecules (a subset of 3 or 4 for instance) can be characterized to form a cell surface biomolecule database. Each type of cell will have a characteristic "fingerprint" in this database. These cell surface biomolecules can include two kinds of carbohydrates (which have been well established in this work) and one or two kind(s) of cell type specific target(s). The two carbohydrates molar ratio can narrow down the range of cell types, and then the detection of specific target will be the additional step to determine the cell type. This database will facilitate the single cell identification.

10.2.4 Evaluating and screening antimicrobial polycation using antimicrobial polycation functionalized probe

Challenge:

In this work, the antimicrobial polymer has been demonstrated to kill the cell via electrostatic absorption on the cell membrane, leading to the damage of the cell membrane. The cell surface hydrophobicity change provides an indirect evidence to show the damage of the cell membrane integrity. However, if we have several polycation candidates with similar chemical structure, it is difficult to evaluate or pick the best (or most efficient) polycation using cell morphology and hydrophobicity change.

Future work:

Follow-up work can focus on the use antimicrobial polycations as the probe directly. By functionalizing the AFM tip with different antimicrobial polycations, the interaction parameters of polycations with cell membrane can be obtained and compared. The hypothesis is that the polycation with the high affinity will have better antimicrobial effect on cells. This method can provide direct biophysical evidence for drug screen. In addition, the other interaction parameter, rupture length, will give a clear idea of specific target of antimicrobial polycation on cell surface.

10.2.5 Single mammalian cell analysis platform

Most of work in this dissertation focused on single cell analysis of bacterial system. The next stage of the research can be the single mammalian cell analysis. Various physiological and pathological processes in mammalian system are related to cell surface biomolecules. For example, cancer cell migration is along with the cell surface carbohydrates change [337]. Also, in tissue engineering, the early stage of cell adhesion is depending on the integrin density and distribution on cell surface [338]. Therefore, the application and development of the single cell analysis platform in mammalian system will illuminate more fundamental biological processes.

10.2.6 Single cell biosensor

In this work, force mapping on single cell could be conducted in real time and controllable micro-environments. This implies another potential application of this technique: single cell biosensor. The cell surface biomolecules provide the bio-active substrate and thus can detect specific targets in injected fluid using microfluidic exchanging systems. For instance, the antigen on cell surface can be mapped out by antibody functionalized AFM tip. The force signal will be quenched when antibody-contained fluid flushes into the micro-environment. The force map change can provide quantitative calculation of antibody concentration in fluid. Since this technique is based on single cell and molecular interaction, the detection limit will be low.

References

1. Hinterdorfer, P. and Y.F. Dufrene, *Detection and localization of single molecular recognition events using atomic force microscopy*. Nature Methods, 2006. **3**(5): p. 347-355.
2. Kim, J.S., et al., *AFM studies of inhibition effect in binding of antimicrobial peptide and immune proteins*. Langmuir, 2007. **23**(21): p. 10438-10440.
3. Yu, J.P., J. Warnke, and Y.L. Lyubchenko, *Nanoprobing of alpha-synuclein misfolding and aggregation with atomic force microscopy*. Nanomedicine, 2011. **7**(2): p. 146-152.
4. Fox, A., et al., *Carbohydrates and glycoproteins of Bacillus anthracis and related bacilli: targets for biodetection*. Journal of Microbiological Methods, 2003. **54**(2): p. 143-152.
5. Matz, L.L., T.C. Beaman, and P. Gerhardt, *Chemical composition of exosporium from spores of Bacillus cereus*. Journal of Bacteriology, 1970. **101**(1): p. 196-201.
6. Amano, K., et al., *Isolation and characterization of structural components of Bacillus cereus AHU 1356 cell-walls*. European Journal of Biochemistry, 1977. **75**(2): p. 513-522.
7. Florin, E.L., V.T. Moy, and H.E. Gaub, *Adhesion forces between individual ligand-receptor pairs*. Science, 1994. **264**(5157): p. 415-417.
8. Jalili, N. and K. Laxminarayana, *A review of atomic force microscopy imaging systems: application to molecular metrology and biological sciences*. Mechatronics, 2004. **14**(8): p. 907-945.

9. Wang, C.Z. and V.K. Yadavalli, *Investigating biomolecular recognition at the cell surface using atomic force microscopy*. Micron, 2014. **60**: p. 5-17.
10. Clausen-Schaumann, H., et al., *Force spectroscopy with single bio-molecules.* Current Opinion in Chemical Biology, 2000. **4**(5): p. 524-530.
11. De Pablo, P.J., et al., *Adhesion maps using scanning force microscopy techniques.* Journal of Adhesion, 1999. **71**(4): p. 339-356.
12. Kienberger, F., et al., *Molecular recognition imaging and force spectroscopy of single biomolecules.* Accounts of Chemical Research, 2006. **39**(1): p. 29-36.
13. Almqvist, N., et al., *Elasticity and adhesion force mapping reveals real-time clustering of growth factor receptors and associated changes in local cellular rheological properties.* Biophysical Journal, 2004. **86**(3): p. 1753-1762.
14. Wang, C.Z., et al., *Morphological and mechanical imaging of Bacillus cereus spore formation at the nanoscale*. Journal of Microscopy, 2015. **258**(1): p. 49-58.
15. Seo, Y. and W. Jhe, *Atomic force microscopy and spectroscopy*. Reports on Progress in Physics, 2008. **71**(1): p. 1-23.
16. Giessibl, F.J. and C.F. Quate, *Exploring the nanoworld with atomic force microscopy.* Physics Today, 2006. **59**(12): p. 44-50.
17. Evans, E.A. and D.A. Calderwood, *Forces and bond dynamics in cell adhesion.* Science, 2007. **316**(5828): p. 1148-1153.
18. Friddle, R.W., A. Noy, and J.J. De Yoreo, *Interpreting the widespread nonlinear force spectra of intermolecular bonds.* Proceedings of the National Academy of Sciences of the United States of America, 2012. **109**(34): p. 13573-13578.

19. Evans, E., *Probing the relation between force - Lifetime - and chemistry in single molecular bonds*. Annual Review of Biophysics and Biomolecular Structure, 2001. **30**: p. 105-128.

20. Hyeon, C. and D. Thirumalai, *Multiple barriers in forced rupture of protein complexes*. Journal of Chemical Physics, 2012. **137**(5).

21. Bustamante, C., et al., *Mechanical processes in biochemistry*. Annual Review of Biochemistry, 2004. **73**: p. 705-748.

22. Bertozzi, C.R. and L.L. Kiessling, *Chemical glycobiology*. Science, 2001. **291**(5512): p. 2357-2364.

23. Sheetz, M.P., *Cell control by membrane-cytoskeleton adhesion*. Nature Reviews Molecular Cell Biology, 2001. **2**(5): p. 392-396.

24. Lis, H. and N. Sharon, *Lectins: Carbohydrate-specific proteins that mediate cellular recognition*. Chemical reviews, 1998. **98**(2): p. 637-674.

25. Bjork, I. and U. Lindahl, *Mechanism of the anticoagulant action of heparin*. Molecular and Cellular Biochemistry, 1982. **48**(3): p. 161-182.

26. Jelinek, R. and S. Kolusheva, *Carbohydrate biosensors*. Chemical reviews, 2004. **104**(12): p. 5987-6015.

27. Ray, C., et al., *Kinetic parameters from detection probability in single molecule force spectroscopy*. Langmuir, 2010. **26**(14): p. 11951-11957.

28. Weitz, J.I., *Low-molecular-weight heparins*. New England Journal of Medicine, 1997. **337**(10): p. 688-698.

29. Maaroufi, R.M., et al., *Mechanism of thrombin inhibition by antithrombin and heparin cofactor II in the presence of heparin*. Biomaterials, 1997. **18**(3): p. 203-211.

30. Streusand, V.J., et al., *Mechanism of acceleration of antithrombin-proteinase reactions by low-affinity heparin*. Journal of Biological Chemistry, 1995. **270**(16): p. 9043-9051.

31. Li, W., et al., *Structure of the antithrombin-thrombin-heparin ternary complex reveals the antithrombotic mechanism of heparin*. Nature Structural & Molecular Biology, 2004. **11**(9): p. 857-862.

32. Danielsson, A., et al., *Role of ternary complexes, in which heparin binds both antithrombin and proteinase, in the acceleration of the reactions between antithrombin and thrombin or factor Xa*. Journal of Biological Chemistry, 1986. **261**(33): p. 5467-5473.

33. Desai, U.R., *New antithrombin based anticoagulants*. Medicinal Research Reviews, 2004. **24**(2): p. 151-181.

34. Sotres, J., et al., *Unbinding molecular recognition force maps of localized single receptor molecules by atomic force microscopy*. Chemphyschem, 2008. **9**(4): p. 590-599.

35. Almqvist, N., et al., *Elasticity and adhesion force mapping reveals real-time clustering of growth factor receptors and associated changes in local cellular rheological properties.* Biophysical Journal, 2004. **86**(3): p. 1753-1762.

36. Ulman, A., *Formation and structure of self-assembled monolayers*. Chemical Reviews, 1996. **96**(4): p. 1533-1554.

37. Hinterdorfer, P., et al., *Detection and localization of individual antibody-antigen recognition events by atomic force microscopy*. Proceedings of the National Academy of Sciences of the United States of America, 1996. **93**(8): p. 3477-3481.

38. Allison, D.P., P. Hinterdorfer, and W.H. Han, *Biomolecular force measurements and the atomic force microscope*. Current Opinion in Biotechnology, 2002. **13**(1): p. 47-51.

39. Lower, B.H., et al., *Antibody recognition force microscopy shows that outer membrane cytochromes OmcA and MtrC are expressed on the exterior surface of Shewanella oneidensis MR-1*. Applied and Environmental Microbiology, 2009. **75**(9): p. 2931-2935.

40. Lee, S., J. Mandic, and K.J. Van Vliet, *Chemomechanical mapping of ligand-receptor binding kinetics on cells*. Proceedings of the National Academy of Sciences of the United States of America, 2007. **104**(23): p. 9609-9614.

41. Tombelli, S., A. Minunni, and A. Mascini, *Analytical applications of aptamers*. Biosensors & Bioelectronics, 2005. **20**(12): p. 2424-2434.

42. Jayasena, S.D., *Aptamers: An emerging class of molecules that rival antibodies in diagnostics*. Clinical Chemistry, 1999. **45**(9): p. 1628-1650.

43. Andersson, S., et al., *Minimal-surfaces and structures - from inorganic and metal crystals to cell-membranes and bio-polymers*. Chemical Reviews, 1988. **88**(1): p. 221-242.

44. Korn, E.D., *Cell membranes - structure and synthesis*. Annual Review of Biochemistry, 1969. **38**: p. 263-288.

45. Aronson, A.I. and P. Fitzjames, *Structure and morphogenesis of the bacterial spore coat*. Bacteriological Reviews, 1976. **40**(2): p. 360-402.

46. Kuznetsova, T.G., et al., *Atomic force microscopy probing of cell elasticity*. Micron, 2007. **38**(8): p. 824-833.

47. Alsteens, D., et al., *Multiparametric atomic force microscopy imaging of single bacteriophages extruding from living bacteria*. Nature Communications, 2013. **4**.

48. Ebenstein, D.M. and L.A. Pruitt, *Nanoindentation of biological materials*. Nano Today, 2006. **1**(3): p. 26-33.

49. Parkhill, J., et al., *Genome sequence of Yersinia pestis, the causative agent of plague.* Nature, 2001. **413**(6855): p. 523-527.

50. Perry, R.D. and J.D. Fetherston, *Yersinia pestis - Etiologic agent of plague*. Clinical Microbiology Reviews, 1997. **10**(1): p. 35-66.

51. Galimand, M., et al., *Multidrug resistance in Yersinia pestis mediated by a transferable plasmid*. New England Journal of Medicine, 1997. **337**(10): p. 677-680.

52. Losada, L., et al., *Genome sequencing and analysis of Yersina pestis KIM D27, an avirulent strain exempt from select agent regulation*. Plos One, 2011. **6**(4).

53. Knirel, Y.A., et al., *Cold temperature-induced modifications to the composition and structure of the lipopolysaccharide of Yersinia pestis*. Carbohydrate Research, 2005. **340**(9): p. 1625-1630.

54. Suomalainen, M., et al., *Temperature-induced changes in the lipopolysaccharide of Yersinia pestis affect plasminogen activation by the Pla surface protease*. Infection and Immunity, 2010. **78**(6): p. 2644-2652.

55. Kolodziejek, A.M., et al., *Physiological levels of glucose induce membrane vesicle secretion and affect the lipid and protein composition of Yersinia pestis cell surfaces*. Applied and Environmental Microbiology, 2013. **79**(14): p. 4509-4514.

56. Yoong, P., C. Cywes-Bentley, and G.B. Pier, *Poly-N-acetylglucosamine expression by wild-type Yersinia pestis is maximal at mammalian, not flea, temperatures*. MBio, 2012. **3**(4): p. e00217-12.

57. Dufrene, Y.F., et al., *Multiparametric imaging of biological systems by force-distance curve-based AFM*. Nature Methods, 2013. **10**(9): p. 847-854.

58. Wang, C.Z., C.J. Ehrhardt, and V.K. Yadavalli, *Single cell profiling of surface carbohydrates on Bacillus cereus.* Journal of the Royal Society Interface, 2015. **12**(103).

59. Peng, J.S., W.C. Tsai, and C.C. Chou, *Surface characteristics of Bacillus cereus and its adhesion to stainless steel.* International Journal of Food Microbiology, 2001. **65**(1-2): p. 105-111.

60. Oliva, C.R., et al., *The integrin Mac-1 (CR3) mediates internalization and directs Bacillus anthracis spores into professional phagocytes.* Proceedings of the National Academy of Sciences of the United States of America, 2008. **105**(4): p. 1261-1266.

61. Ramarao, N. and D. Lereclus, *The InhA1 metalloprotease allows spores of the B-cereus group to escape macrophages.* Cellular Microbiology, 2005. **7**(9): p. 1357-1364.

62. Leggett, M.J., et al., *Bacterial spore structures and their protective role in biocide resistance.* Journal of Applied Microbiology, 2012. **113**(3): p. 485-498.

63. Giorno, R., et al., *Morphogenesis of the Bacillus anthracis spore.* Journal of Bacteriology, 2007. **189**(3): p. 691-705.

64. Ankolekar, C. and R.G. Labbe, *Physical characteristics of spores of food-associated isolates of the Bacillus cereus group.* Applied and Environmental Microbiology, 2010. **76**(3): p. 982-984.

65. Wiencek, K.M., N.A. Klapes, and P.M. Foegeding, *Hydrophobicity of Bacillus and Clostridium spores.* Applied and Environmental Microbiology, 1990. **56**(9): p. 2600-2605.

66. Faille, C., et al., *Morphology and physico-chemical properties of Bacillus spores surrounded or not with an exosporium Consequences on their ability to adhere to stainless steel.* International Journal of Food Microbiology, 2010. **143**(3): p. 125-135.

67. Rosenberg, M., *Bacterial adherence to hydrocarbons - a useful technique for studying cell-surface hydrophobicity*. Fems Microbiology Letters, 1984. **22**(3): p. 289-295.

68. Doyle, R.J., F. Nedjathaiem, and J.S. Singh, *hydrophobic characteristics of Bacillus spores*. Current Microbiology, 1984. **10**(6): p. 329-332.

69. Lindahl, M., et al., *A new test based on salting out to measure relative surface hydrophobicity of bacterial-cells*. Biochimica Et Biophysica Acta, 1981. **677**(3-4): p. 471-476.

70. Minagi, S., et al., *Cell-surface hydrophobicity of Candida species as determined by the contact-angle and hydrocarbon-adherence methods*. Journal of General Microbiology, 1986. **132**: p. 1111-1115.

71. Dufrene, Y.F., *Towards nanomicrobiology using atomic force microscopy*. Nature Reviews Microbiology, 2008. **6**(9): p. 674-680.

72. Dupres, V., et al., *Microbial nanoscopy: a closer look at microbial cell surfaces*. Trends in Microbiology, 2010. **18**(9): p. 397-405.

73. Frisbie, C.D., et al., *Functional-group imaging by chemical force microscopy*. Science, 1994. **265**(5181): p. 2071-2074.

74. Lai, X.Z., et al., *Ceragenins: cholic acid-based mimics of antimicrobial peptides*. Accounts of Chemical Research, 2008. **41**(10): p. 1233-1240.

75. Tew, G.N., et al., *De novo design of biomimetic antimicrobial polymers*. Proceedings of the National Academy of Sciences of the United States of America, 2002. **99**(8): p. 5110-5114.

76. Zasloff, M., *Magainins, a class of antimicrobial peptides from Xenopus skin - isolation, characterization of 2 active forms, and partial cdna sequence of a precursor*. Proceedings

of the National Academy of Sciences of the United States of America, 1987. **84**(15): p. 5449-5453.

77. Yeaman, M.R. and N.Y. Yount, *Mechanisms of antimicrobial peptide action and resistance*. Pharmacological Reviews, 2003. **55**(1): p. 27-55.
78. Brogden, K.A., *Antimicrobial peptides: Pore formers or metabolic inhibitors in bacteria?* Nature Reviews Microbiology, 2005. **3**(3): p. 238-250.
79. Fang, M., et al., *Antibacterial activities of inorganic agents on six bacteria associated with oral infections by two susceptibility tests.* International Journal of Antimicrobial Agents, 2006. **27**(6): p. 513-517.
80. Santo, C.E., et al., *Bacterial killing by dry metallic copper surfaces.* Applied and Environmental Microbiology, 2011. **77**(3): p. 794-802.
81. Olson, S.T., H.R. Halvorson, and I. Bjork, *Quantitative characterization of the thrombin-heparin interaction. Discrimination between specific and nonspecific binding models.* Journal of Biological Chemistry, 1991. **266**(10): p. 6342-6352.
82. Oshima, G., H. Uchiyama, and K. Nagasawa, *Effect of NaCl on the association of thrombin with heparin*. Biopolymers, 1986. **25**(4): p. 527-537.
83. vanDelden, C.J., et al., *Heparinization of gas plasma-modified polystyrene surfaces and the interactions of these surfaces with proteins studied with surface plasmon resonance.* Biomaterials, 1997. **18**(12): p. 845-852.
84. Zhang, X.J. and V.K. Yadavalli, *Molecular interaction studies of vascular endothelial growth factor with RNA aptamers*. Analyst, 2010. **135**(8): p. 2014-2021.
85. Giessibl, F.J. and C.F. Quate, *Exploring the nanoworld with atomic force microscopy.* Physics Today, 2006. **59**(12): p. 44-50.

86. Francis, L.W., et al., *Atomic force microscopy comes of age*. Biology of the Cell, 2010. **102**(2): p. 133-143.

87. Yadavalli, V.K., J.G. Forbes, and K. Wang, *Functionalized self-assembled monolayers on ultraflat gold as platforms for single molecule force spectroscopy and imaging*. Langmuir, 2006. **22**(16): p. 6969-6976.

88. Hutter, J.L. and J. Bechhoefer, *Calibration of atomic force microscope tips*. Review of Scientific Instruments, 1993. **64**(7): p. 1868-1873.

89. Neuman, K.C. and A. Nagy, *Single-molecule force spectroscopy: optical tweezers, magnetic tweezers and atomic force microscopy*. Nature Methods, 2008. **5**(6): p. 491-505.

90. Rusmini, F., Z.Y. Zhong, and J. Feijen, *Protein immobilization strategies for protein biochips*. Biomacromolecules, 2007. **8**(6): p. 1775-1789.

91. Wagner, P., *Immobilization strategies for biological scanning probe microscopy*. Febs Letters, 1998. **430**(1-2): p. 112-115.

92. Yu, H.N., et al., *Kinetic studies on the interactions of heparin and complement proteins using surface plasmon resonance*. Biochim. Biophys. Acta, 2005. **1726**(2): p. 168-176.

93. Pasche, B., et al., *Thrombin inactivation on surfaces with covalently bonded heparin*. Thrombosis Research, 1986. **44**(6): p. 739-748.

94. Chen, H., et al., *Immobilization of heparin on a silicone surface through a heterobifunctional PEG spacer*. Biomaterials, 2005. **26**(35): p. 7418-7424.

95. Nadkarni, V.D., A. Pervin, and R.J. Linhardt, *Directional immobilization of heparin onto beaded supports*. Analytical Biochemistry, 1994. **222**(1): p. 59-67.

96. Chao, Y.Q. and T. Zhang, *Optimization of fixation methods for observation of bacterial cell morphology and surface ultrastructures by atomic force microscopy*. Applied Microbiology and Biotechnology, 2011. **92**(2): p. 381-392.

97. Pavlov, G., et al., *Conformation of heparin studied with macromolecular hydrodynamic methods and X-ray scattering*. European Biophysics Journal with Biophysics Letters, 2003. **32**(5): p. 437-449.

98. Mulloy, B., et al., *NMR and molecular-modeling studies of the solution conformation of heparin*. Biochemical Journal, 1993. **293**: p. 849-858.

99. Khan, S., et al., *Semi-rigid solution structures of heparin by constrained X-ray scattering modelling: new insight into heparin-protein complexes*. Journal of Molecular Biology, 2010. **395**(3): p. 504-521.

100. Spinelli, F.J., K.L. Kiick, and E.M. Furst, *The role of heparin self-association in the gelation of heparin-functionalized polymers*. Biomaterials, 2008. **29**(10): p. 1299-1306.

101. Lee, C.K., et al., *Atomic force microscopy: Determination of unbinding force, off rate and energy barrier for protein-ligand interaction*. Micron, 2007. **38**(5): p. 446-461.

102. Zhang, X.J. and V.K. Yadavalli, *Functionalized self-assembled monolayers for measuring single molecule lectin carbohydrate interactions*. Analytica Chimica Acta, 2009. **649**(1): p. 1-7.

103. Carter, W.J., E. Cama, and J.A. Huntington, *Crystal structure of thrombin bound to heparin*. Journal of Biological Chemistry, 2005. **280**(4): p. 2745-2749.

104. Noy, A. and R.W. Friddle, *Practical single molecule force spectroscopy: How to determine fundamental thermodynamic parameters of intermolecular bonds with an atomic force microscope*. Methods, 2013. **60**(2): p. 142-150.

105. Friddle, R.W., A. Noy, and J.J. De Yoreo, *Interpreting the widespread nonlinear force spectra of intermolecular bonds*. Proceedings of the National Academy of Sciences of the United States of America, 2012. **109**(34): p. 13573-13578.

106. Allon, M. and M.L. Robbin, *Increasing arteriovenous fistulas in hemodialysis patients: Problems and solutions*. Kidney International, 2002. **62**(4): p. 1109-1124.

107. Evans, E. and K. Ritchie, *Dynamic strength of molecular adhesion bonds*. Biophysical Journal, 1997. **72**(4): p. 1541-1555.

108. Alon, R., et al., *The kinetics of L-selectin tethers and the mechanics of selectin-mediated rolling*. Journal of Cell Biology, 1997. **138**(5): p. 1169-1180.

109. Strunz, T., et al., *Model energy landscapes and the force-induced dissociation of ligand-receptor bonds*. Biophysical Journal, 2000. **79**(3): p. 1206-1212.

110. Lv, Z.J., J.H. Wang, and G.P. Chen, *Exploring the Energy Profile of Human IgG/Rat Anti-human IgG Interactions by Dynamic Force Spectroscopy*. Protein Journal, 2012. **31**(5): p. 425-431.

111. Capila, I. and R.J. Linhardt, *Heparin - protein interactions*. Angewandte Chemie International Edition, 2002. **41**(3): p. 391-412.

112. Li, F.Y., et al., *Force measurements of the alpha(5)beta(1) integrin-fibronectin interaction*. Biophysical Journal, 2003. **84**(2): p. 1252-1262.

113. Mosier, P.D., et al., *On the specificity of heparin/heparan sulfate binding to proteins. Anion-binding sites on antithrombin and thrombin are fundamentally different*. Plos One, 2012. **7**(11).

114. Seyrek, E., et al., *Ionic strength dependence of protein-polyelectrolyte interactions*. Biomacromolecules, 2003. **4**(2): p. 273-282.

115. Manning, G.S., *Molecular theory of polyelectrolyte solutions with applications to electrostatic properties of polynucleotides*. Quarterly Reviews of Biophysics, 1978. **11**(2): p. 179-246.

116. Guo, C.L., et al., *Structural basis of single molecular heparin-FX06 interaction revealed by SPM measurements and molecular simulations*. Chemical Communications, 2012. **48**(100): p. 12222-12224.

117. Odrljin, T.M., et al., *Heparin-binding domain of fibrin mediates its binding to endothelial cells*. Arteriosclerosis Thrombosis and Vascular Biology, 1996. **16**(12): p. 1544-1551.

118. Dammer, U., et al., *Specific antigen/antibody interactions measured by force microscopy*. Biophysical Journal, 1996. **70**(5): p. 2437-2441.

119. Ratto, T.V., et al., *Force spectroscopy of the double-tethered concanavalin-A mannose bond*. Biophysical Journal, 2004. **86**(4): p. 2430-2437.

120. Li, F.Y., et al., *Force measurements of the alpha(5)beta(1) integrin-fibronectin interaction*. Biophysical Journal, 2003. **84**(2): p. 1252-1262.

121. Sewald, N., et al., *Probing DNA-peptide interaction forces at the single-molecule level*. Journal of Peptide Science, 2006. **12**(12): p. 836-842.

122. Turner, A.P.F., *Biochemistry - Biosensors sense and sensitivity*. Science, 2000. **290**(5495): p. 1315-1317.

123. Wright, C.J. and I. Armstrong, *The application of atomic force microscopy force measurements to the characterisation of microbial surfaces*. Surface and Interface Analysis, 2006. **38**(11): p. 1419-1428.

124. Favre, M., et al., *Parallel AFM imaging and force spectroscopy using two-dimensional probe arrays for applications in cell biology*. Journal of Molecular Recognition, 2011. **24**(3): p. 446-452.

125. Willemsen, O.H., et al., *Simultaneous height and adhesion imaging of antibody-antigen interactions by atomic force microscopy*. Biophysical Journal, 1998. **75**(5): p. 2220-2228.

126. Muller, D.J., et al., *Force probing surfaces of living cells to molecular resolution*. Nature Chemical Biology, 2009. **5**(6): p. 383-390.

127. Heinz, W.F. and J.H. Hoh, *Spatially resolved force spectroscopy of biological surfaces using the atomic force microscope*. Trends Biotechnology, 1999. **17**(4): p. 143-150.

128. Dupres, V., C. Verbelen, and Y.F. Dufrene, *Probing molecular recognition sites on biosurfaces using AFM*. Biomaterials, 2007. **28**(15): p. 2393-2402.

129. Rao, S.V., K.W. Anderson, and L.G. Bachas, *Oriented immobilization of proteins*. Mikrochimica Acta, 1998. **128**(3-4): p. 127-143.

130. Zhang, X.J. and V.K. Yadavalli, *Surface immobilization of DNA aptamers for biosensing and protein interaction analysis*. Biosensors & Bioelectronics, 2011. **26**(7): p. 3142-3147.

131. Basnar, B., R. Elnathan, and I. Willner, *Following aptamer-thrombin binding by force measurements*. Analytical Chemistry, 2006. **78**(11): p. 3638-42.

132. Yu, J.P., et al., *Energy landscape of aptamer/protein complexes studied by single-molecule force spectroscopy*. Chemistry-an Asian Journal, 2007. **2**(2): p. 284-289.

133. Lin, L., et al., *Recognition imaging with a DNA aptamer*. Biophysical Journal, 2006. **90**(11): p. 4236-4238.

134. Boyd, R.D., et al., *Mapping the placement of oligonucleotide molecules using scanning probe microscopy*. Colloids Surf., B, 2011. **83**(1): p. 10-15.

135. Paborsky, L.R., et al., *The single-stranded DNA aptamer binding site of human thrombin*. Journal of Biological Chemistry, 1993. **268**(28): p. 20808-20811.

136. Sheehan, J.P. and J.E. Sadler, *Molecular mapping of the heparin-binding exosite of thrombin*. Proceedings of the National Academy of Sciences of the United States of America, 1994. **91**(12): p. 5518-5522.

137. Jellinek, D., et al., *Inhibition of receptor-binding by high-affinity RNA ligands to vascular endothelial growth-factor*. Biochemistry, 1994. **33**(34): p. 10450-10456.

138. Huizenga, D.E. and J.W. Szostak, *A DNA aptamer that binds adenosine and ATP*. Biochemistry, 1995. **34**(2): p. 656-665.

139. Taylor, J.N., et al., *Dynamics of an anti-VEGF DNA aptamer: A single-molecule study*. Biochem. Biophys. Res. Commun., 2008. **373**(2): p. 213-218.

140. Clarizia, L.J., et al., *Antibody orientation enhanced by selective polymer-protein noncovalent interactions*. Analytical and Bioanalytical Chemistry, 2009. **393**(5): p. 1531-1538.

141. Giessibl, F.J., *Advances in atomic force microscopy*. Reviews of Modern Physics, 2003. **75**(3): p. 949-983.

142. Lin, L.Y., et al., *Development of aptamers for recognition imaging*. Biochemistry and Cell Biology, 2007. **85**(4): p. 532-532.

143. Houck, K.A., et al., *The vascular endothelial growth factor family: Identification of a fourth molecular species and characterization of alternative splicing of RNA*. Molecular Endocrinology, 1991. **5**(12): p. 1806-1814.

144. Muller, Y.A., et al., *The crystal structure of vascular endothelial growth factor (VEGF) refined to 1.93 angstrom resolution: multiple copy flexibility and receptor binding.* Structure, 1997. **5**(10): p. 1325-1338.

145. Weisel, J.W., et al., *The shape of thrombomodulin and interactions with thrombin as determined by electron microscopy*. Journal of Biological Chemistry, 1996. **271**(49): p. 31485-31490.

146. Nasongkla, N., et al., *cRGD-functionalized polymer micelles for targeted doxorubicin delivery*. Angewandte Chemie-International Edition, 2004. **43**(46): p. 6323-6327.

147. Yu, J.P., J. Warnke, and Y.L. Lyubchenko, *Nanoprobing of alpha-synuclein misfolding and aggregation with atomic force microscopy*. Nanomedicine-Nanotechnology Biology and Medicine, 2011. **7**(2): p. 146-152.

148. Andre, G., et al., *Imaging the nanoscale organization of peptidoglycan in living Lactococcus lactis cells*. Nature Communications, 2010. **1**.

149. Cho, E.J., J.-W. Lee, and A.D. Ellington, *Applications of aptamers as sensors*. Annual Review of Analytical Chemistry, 2009. **2**(12): p. 12.1-12.24.

150. Jiang, Y.X., et al., *Specific aptamer-protein interaction studied by atomic force microscopy*. Analytical Chemistry, 2003. **75**(9): p. 2112-2116.

151. O'Donoghue, M.B., et al., *Single-molecule atomic force microscopy on live cells compares aptamer and antibody rupture forces*. Analytical and Bioanalytical Chemistry, 2012. **402**(10): p. 3205-3209.

152. Han, W.H., S.M. Lindsay, and T.W. Jing, *A magnetically driven oscillating probe microscope for operation in liquids*. Applied Physics Letters, 1996. **69**(26): p. 4111-4113.

153. Stroh, C., et al., *Single-molecule recognition imaging microscopy*. Proceedings of the National Academy of Sciences of the United States of America, 2004. **101**(34): p. 12503-12507.

154. Zhang, M.M., et al., *Imaging and measuring single-molecule interaction between a carbohydrate-binding module and natural plant cell wall cellulose*. The Journal of Physical Chemistry B, 2012. **116**(33): p. 9949-9956.

155. Yu, J.P., et al., *Single-molecule force spectroscopy study of interaction between transforming growth factor beta 1 and its receptor in living cells*. The Journal of Physical Chemistry B, 2007. **111**(48): p. 13619-13625.

156. Sasuga, S., et al., *Interaction between pheromone and its receptor of the fission yeast Schizosaccharomyces pombe examined by a force spectroscopy study*. Journal of Biomedicine and Biotechnology, 2012.

157. Quiles, F., et al., *Production of extracellular glycogen by Pseudomonas fluorescens: spectroscopic evidence and conformational analysis by biomolecular recognition*. Biomacromolecules, 2012. **13**(7): p. 2118-2127.

158. Kim, I.H., et al., *Nanoscale mapping and affinity constant measurement of signal-transducing proteins by atomic force microscopy*. Analytical Chemistry, 2011. **83**(5): p. 1500-1503.

159. Francius, G., et al., *Detection, localization, and conformational analysis of single polysaccharide molecules on live bacteria*. Acs Nano, 2008. **2**(9): p. 1921-1929.

160. Alsteens, D., et al., *Force-induced formation and propagation of adhesion nanodomains in living fungal cells*. Proceedings of the National Academy of Sciences of the United States of America, 2010. **107**(48): p. 20744-20749.

161. Li, M., et al., *Atomic force microscopy study of the antigen-antibody binding force on patient cancer cells based on ROR1 fluorescence recognition*. Journal of Molecular Recognition, 2013. **26**(9): p. 432-438.

162. Fox, A., et al., *Carbohydrates and glycoproteins of Bacillus anthracis and related bacilli: targets for biodetection*. Journal of Microbiological Methods, 2003. **54**(2): p. 143-52.

163. Kolter, R. and E.P. Greenberg, *Microbial sciences - The superficial life of microbes*. Nature, 2006. **441**(7091): p. 300-302.

164. Ofek, I. and N. Sharon, *Lectinophagocytosis: a molecular mechanism of recognition between cell surface sugars and lectins in the phagocytosis of bacteria*. Infection and Immunity, 1988. **56**(3): p. 539-547.

165. Weintraub, A., *Immunology of bacterial polysaccharide antigens*. Carbohydrate Research, 2003. **338**(23): p. 2539-2547.

166. Choudhury, B., et al., *The structure of the major cell wall polysaccharide of Bacillus anthracis is species-specific*. Journal of Biological Chemistry, 2006. **281**(38): p. 27932-27941.

167. Rao, S.S., K.V.K. Mohan, and C.D. Atreya, *Detection technologies for Bacillus anthracis: Prospects and challenges*. Journal of Microbiological Methods, 2010. **82**(1): p. 1-10.

168. Colburn, H.A., et al., *The effect of growth medium on B. anthracis Sterne spore carbohydrate content*. Journal of Microbiological Methods, 2011. **85**(3): p. 183-189.

169. Helgason, E., et al., *Bacillus anthracis, Bacillus cereus, and Bacillus thuringiensis - One species on the basis of genetic evidence*. Applied and Environmental Microbiology, 2000. **66**(6): p. 2627-2630.

170. Liu, Y.L., et al., *Confirmative electric DNA array-based test for food poisoning Bacillus cereus*. Journal of Microbiological Methods, 2007. **70**(1): p. 55-64.

171. Ivanova, N., et al., *Genome sequence of Bacillus cereus and comparative analysis with Bacillus anthracis.* Nature, 2003. **423**(6935): p. 87-91.

172. Leoff, C., et al., *Cell wall carbohydrate compositions of strains from the bacillus cereus group of species correlate with phylogenetic relatedness.* Journal of Bacteriology, 2008. **190**(1): p. 112-121.

173. Fox, A., et al., *Determination of carbohydrate profiles of Bacillus anthracis and Bacillus cereus including identification of O-methyl methylpentoses by using gas chromatography-mass spectrometry*. J Clin Microbiol, 1993. **31**(4): p. 887-94.

174. Matz, L.L., T.C. Beaman, and P. Gerhardt, *Chemical Composition of Exosporium from Spores of Bacillus-Cereus.* Journal of Bacteriology, 1970. **101**(1): p. 196-201.

175. Amano, K., et al., *Isolation and characterization of structural components of Bacillus-cereus AHU 1356 cell-walls*. European Journal of Biochemistry, 1977. **75**(2): p. 513-522.

176. Brown, W.C., *Rapid methods for extracting autolysins from Bacillus-subtilis.* Applied Microbiology, 1973. **25**(2): p. 295-300.

177. Fox, A., et al., *Chemotaxonomic differentiation of legionellae by detection and characterization of aminodideoxyhexoses and other unique sugars using gas-chromatography mass-spectrometry*. Journal of Clinical Microbiology, 1990. **28**(3): p. 546-552.

178. Bruggink, C., et al., *Analysis of carbohydrates by anion exchange chromatography and mass spectrometry*. Journal of Chromatography A, 2005. **1085**(1): p. 104-109.

179. Guignard, C., et al., *Analysis of carbohydrates in plants chromatography coupled with by high-performance anion-exchange electrospray mass spectrometry*. Journal of Chromatography A, 2005. **1085**(1): p. 137-142.

180. Muller, D.J. and Y.F. Dufrene, *Atomic force microscopy: a nanoscopic window on the cell surface*. Trends in Cell Biology, 2011. **21**(8): p. 461-469.

181. Alsteens, D., et al., *Unraveling the nanoscale surface properties of chitin synthase mutants of Aspergillus fumigatus and their biological implications*. Biophysical Journal, 2013. **105**(2): p. 320-327.

182. Beaussart, A., et al., *Single-molecule imaging and functional analysis of als adhesins and mannans during Candida albicans morphogenesis*. ACS Nano, 2012. **6**(12): p. 10950-10964.

183. Hornstra, L.M., et al., *Influence of sporulation medium composition on transcription of ger Operons and the germination response of spores of Bacillus cereus ATCC 14579*. Applied and Environmental Microbiology, 2006. **72**(5): p. 3746-3749.

184. Fernandes, J.C., et al., *Study of the antibacterial effects of chitosans on Bacillus cereus (and its spores) by atomic force microscopy imaging and nanoindentation*. Ultramicroscopy, 2009. **109**(8): p. 854-860.

185. Lin, D.C. and F. Horkay, *Nanomechanics of polymer gels and biological tissues: A critical review of analytical approaches in the Hertzian regime and beyond*. Soft Matter, 2008. **4**(4): p. 669-682.

186. Touhami, A., B. Nysten, and Y.F. Dufrene, *Nanoscale mapping of the elasticity of microbial cells by atomic force microscopy*. Langmuir, 2003. **19**(11): p. 4539-4543.

187. Dufrene, Y.F., *Using nanotechniques to explore microbial surfaces*. Nature Reviews Microbiology, 2004. **2**(6): p. 451-460.

188. Gillis, A., et al., *Nanoscale imaging of Bacillus thuringiensis flagella using atomic force microscopy*. Nanoscale, 2012. **4**(5): p. 1585-1591.

189. Pan, J.H., et al., *Characteristic features of Bacillus cereus cell surfaces with biosorption of Pb(II) ions by AFM and FT-IR*. Colloids and Surfaces B-Biointerfaces, 2006. **52**(1): p. 89-95.

190. Plomp, M., et al., *Architecture and high-resolution structure of Bacillus thuringiensis and Bacillus cereus spore coat surfaces*. Langmuir, 2005. **21**(17): p. 7892-7898.

191. Chen, X., et al., *Bacillus spores as building blocks for stimuli-responsive materials and nanogenerators*. Nature Nanotechnology, 2014. **9**(2): p. 137-141.

192. El-Kirat-Chatel, S., et al., *Single-molecule analysis of the major glycopolymers of pathogenic and non-pathogenic yeast cells*. Nanoscale, 2013. **5**(11): p. 4855-4863.

193. Murazumi, N., Y. Araki, and E. Ito, *Biosynthesis of the wall neutral polysaccharide in Bacillus-cereus AHU-1356*. European Journal of Biochemistry, 1986. **161**(1): p. 51-59.

194. Plomp, M., et al., *The high-resolution architecture and structural dynamics of Bacillus spores*. Biophysical Journal, 2005. **88**(1): p. 603-608.

195. Wunschel, D., et al., *Discrimination among the Bacillus-cereus group, in comparison to Bacillus-subtilis, by structural carbohydrate profiles and ribosomal-RNA spacer region PCR*. Systematic and Applied Microbiology, 1995. **17**(4): p. 625-635.

196. Boylen, C.W. and J.C. Ensign, *Ratio of teichoic acid and peptidoglycan in cell walls of Bacillus subtilis following spire germination and during vegetative growth*. Journal of Bacteriology, 1968. **96**(2): p. 421-7.

197. Lequette, Y., et al., *Role Played by Exosporium Glycoproteins in the Surface Properties of Bacillus cereus Spores and in Their Adhesion to Stainless Steel.* Applied and Environmental Microbiology, 2011. **77**(14): p. 4905-4911.

198. Sylvestre, P., E. Couture-Tosi, and M. Mock, *A collagen-like surface glycoprotein is a structural component of the Bacillus anthracis exosporium.* Molecular Microbiology, 2002. **45**(1): p. 169-178.

199. Daubenspeck, J.M., et al., *Novel oligosaccharide side chains of the collagen-like region of BclA, the major glycoprotein of the Bacillus anthracis exosporium.* Journal of Biological Chemistry, 2004. **279**(30): p. 30945-30953.

200. Alsteens, D., et al., *High-resolution imaging of chemical and biological sites on living cells using peak force tapping atomic force microscopy*. Langmuir, 2012. **28**(49): p. 16738-16744.

201. Pfreundschuh, M., et al., *Localizing chemical groups while imaging single native proteins by high-resolution atomic force microscopy*. Nano Letters, 2014. **14**(5): p. 2957-2964.

202. Ando, T., T. Uchihashi, and S. Scheuring, *Filming biomolecular processes by high-speed atomic force microscopy*. Chemical Reviews, 2014. **114**(6): p. 3120-3188.

203. Cappella, B. and G. Dietler, *Force-distance curves by atomic force microscopy*. Surface Science Reports, 1999. **34**(1-3): p. 1-104.

204. Lo, Y.S., Y.J. Zhu, and T.P. Beebe, *Loading-rate dependence of individual ligand-receptor bond-rupture forces studied by atomic force microscopy*. Langmuir, 2001. **17**(12): p. 3741-3748.

205. Piggot, P.J. and D.W. Hilbert, *Sporulation of Bacillus subtilis.* Current Opinion in Microbiology, 2004. **7**(6): p. 579-586.

206. Chada, V.G.R., et al., *Morphogenesis of Bacillus spore surfaces*. Journal of Bacteriology, 2003. **185**(21): p. 6255-6261.

207. Tocheva, E.I., et al., *Peptidoglycan transformations during Bacillus subtilis sporulation*. Molecular Microbiology, 2013. **88**(4): p. 673-686.

208. Errington, J., *Bacillus-subtilis sporulation - regulation of gene-expression and control of morphogenesis*. Microbiological Reviews, 1993. **57**(1): p. 1-33.

209. Hosoya, S., et al., *Cytological analysis of the mother cell death process during sporulation in Bacillus subtilis*. Journal of Bacteriology, 2007. **189**(6): p. 2561-2565.

210. Dufrene, Y.F. and A.E. Pelling, *Force nanoscopy of cell mechanics and cell adhesion*. Nanoscale, 2013. **5**(10): p. 4094-4104.

211. Suresh, S., *Biomechanics and biophysics of cancer cells*. Acta Biomaterialia, 2007. **3**(4): p. 413-438.

212. Cerf, A., et al., *Nanomechanical properties of dead or alive single-patterned bacteria*. Langmuir, 2009. **25**(10): p. 5731-5736.

213. Spedden, E., et al., *Elasticity maps of living neurons measured by combined fluorescence and atomic force microscopy*. Biophysical Journal, 2012. **103**(5): p. 868-877.

214. Formosa, C., et al., *Nanoscale analysis of the effects of antibiotics and CX1 on a Pseudomonas aeruginosa multidrug- resistant strain*. Scientific Reports, 2012. **2**.

215. Akhremitchev, B.B. and G.C. Walker, *Finite sample thickness effects on elasticity determination using atomic force microscopy*. Langmuir, 1999. **15**(17): p. 5630-5634.

216. McKenney, P.T., A. Driks, and P. Eichenberger, *The Bacillus subtilis endospore: assembly and functions of the multilayered coat*. Nature Reviews Microbiology, 2013. **11**(1): p. 33-44.

217. Plomp, M. and A.J. Malkin, *Mapping of proteomic composition on the surfaces of Bacillus spores by atomic force microscopy-based immunolabeling*. Langmuir, 2009. **25**(1): p. 403-409.

218. Zhao, L.M., D. Schaefer, and M.R. Marten, *Assessment of elasticity and topography of Aspergillus nidulans spores via atomic force microscopy*. Applied and Environmental Microbiology, 2005. **71**(2): p. 955-960.

219. Kiljunen, S., et al., *Identification of the lipopolysaccharide core of Yersinia pestis and Yersinia pseudotuberculosis as the receptor for Bacteriophage phi A1122*. Journal of Bacteriology, 2011. **193**(18): p. 4963-4972.

220. Blisnick, T., et al., *Oral vaccination against bubonic plague using a live avirulent Yersinia pseudotuberculosis strain*. Infection and Immunity, 2008. **76**(8): p. 3808-16.

221. Paoli, G.C., et al., *Inactivation of avirulent pgm(+) and Delta pgm Yersinia pestis by ultraviolet light (UV-C)*. Food Microbiology, 2014. **44**: p. 168-172.

222. Clery-Barraud, C., et al., *Combined effects of high hydrostatic pressure and temperature for inactivation of Bacillus anthracis spores*. Applied and Environmental Microbiology, 2004. **70**(1): p. 635-637.

223. Spotts Whitney, E.A., et al., *Inactivation of Bacillus anthracis spores*. Emerging Infectious Diseases journal, 2003. **9**(6): p. 623-7.

224. Sagripanti, J.L., et al., *Microbial inactivation for safe and rapid diagnostics of infectious samples*. Applied and Environmental Microbiology, 2011. **77**(20): p. 7289-7295.

225. Goldman, E. and L.H. Green, *Practical handbook of microbiology*. 2nd ed. 2009, Boca Raton: CRC Press. xx, 853 p.

226. St-Laurent, J., et al., *Comparison of cell fixation methods of induced sputum specimens: An immunocytochemical analysis.* Journal of Immunological Methods, 2006. **308**(1-2): p. 36-42.

227. Kniggendorf, A.K., T.W. Gaul, and M. Meinhardt-Wollweber, *Effects of ethanol, formaldehyde, and gentle heat fixation in confocal resonance Raman microscopy of purple nonsulfur bacteria*. Microscopy Research and Technique, 2011. **74**(2): p. 177-183.

228. Rose, L.J. and H. O'Connell, *UV Light Inactivation of bacterial biothreat agents.* Applied and Environmental Microbiology, 2009. **75**(9): p. 2987-2990.

229. Talbot, S.R., et al., *Effects of inactivation methods on the analysis of Bacillus atrophaeus endospores using real-time PCR and MALDI-TOF-MS.* Engineering in Life Sciences, 2010. **10**(2): p. 109-120.

230. Lin, A., et al., *Effects of bacterial inactivation methods on downstream proteomic analysis*. Journal of Microbiological Methods, 2015. **112**: p. 3-10.

231. Bos, K.I., et al., *A draft genome of Yersinia pestis from victims of the Black Death.* Nature, 2011. **478**(7370): p. 506-510.

232. Swietnicki, W., et al., *Identification of small-molecule inhibitors of Yersinia pestis type III secretion system YscN ATPase.* Plos One, 2011. **6**(5).

233. Prior, J.L., et al., *Characterization of the lipopolysaccharide of Yersinia pestis*. Microbial Pathogenesis, 2001. **30**(2): p. 49-57.

234. McEwen, G.D., Y.Z. Wu, and A.H. Zhou, *Probing Nanostructures of bacterial extracellular polymeric substances versus culture time by raman microspectroscopy and atomic force microscopy*. Biopolymers, 2010. **93**(2): p. 171-177.

235. Prior, J.L., et al., *The failure of different strains of Yersinia pestis to produce lipopolysaccharide O-antigen under different growth conditions is due to mutations in the O-antigen gene cluster*. FEMS Microbiology Letters, 2001. **197**(2): p. 229-233.

236. Kawahara, K., et al., *Modification of the structure and activity of lipid A in Yersinia pestis lipopolysaccharide by growth temperature*. Infection and Immunity, 2002. **70**(8): p. 4092-4098.

237. Knirel, Y.A., et al., *Temperature-dependent variations and intraspecies diversity of the structure of the lipopolysaccharide of Yersinia pestis*. Biochemistry, 2005. **44**(5): p. 1731-43.

238. Vinogradov, E.V., et al., *The core structure of the lipopolysaccharide from the causative agent of plague, Yersinia pestis*. Carbohydrate Research, 2002. **337**(9): p. 775-777.

239. Ayyadurai, S., et al., *Long-term persistence of virulent Yersinia pestis in soil*. Microbiology-Sgm, 2008. **154**: p. 2865-2871.

240. Bi, Y.J., et al., *Yersinia pestis and host macrophages: immunodeficiency of mouse macrophages induced by YscW*. Immunology, 2009. **128**(1): p. e406-e417.

241. Chen, T.H. and S.S. Elberg, *Scanning electron-microscopic study of virulent Yersinia-pestis and Yersinia-pseudotuberculosis type-I*. Infection and Immunity, 1977. **15**(3): p. 972-977.

242. Jarrett, C.O., et al., *Transmission of Yersinia pestis from an infectious biofilm in the flea vector*. Journal of Infectious Diseases, 2004. **190**(4): p. 783-792.

243. Xing, Y., et al., *Nanoscale structural and mechanical analysis of Bacillus anthracis spores inactivated with rapid dry heating*. Applied and Environmental Microbiology, 2014. **80**(5): p. 1739-1749.

244. Fox, C.H., et al., *Formaldehyde fixation*. Journal of Histochemistry & Cytochemistry, 1985. **33**(8): p. 845-853.

245. Clowers, B.H., et al., *Characterization of residual medium peptides from Yersinia pestis cultures*. Analytical Chemistry, 2013. **85**(8): p. 3933-3939.

246. Qian, J., et al., *MALDI-TOF mass signatures for differentiation of yeast species, strain grouping and monitoring of morphogenesis markers*. Analytical and Bioanalytical Chemistry, 2008. **392**(3): p. 439-449.

247. van Essen, H.F., et al., *Alcohol based tissue fixation as an alternative for formaldehyde: influence on immunohistochemistry*. Journal of Clinical Pathology, 2010. **63**(12): p. 1090-1094.

248. Dapson, R.W., *Macromolecular changes caused by formalin fixation and antigen retrieval*. Biotechnic & Histochemistry, 2007. **82**(3): p. 133-140.

249. Sjostedt, J., A. Hagstrom, and U.L. Zweifel, *Variation in cell volume and community composition of bacteria in response to temperature*. Aquatic Microbial Ecology, 2012. **66**(3): p. 237-246.

250. Sommers, C.H. and S. Sheen, *Inactivation of avirulent Yersinia pestis on food and food contact surfaces by ultraviolet light and freezing*. Food Microbiology, 2015. **50**(0): p. 1-4.

251. Koivunen, J. and H. Heinonen-Tanski, *Inactivation of enteric microorganisms with chemical disinfectants, UV irradiation and combined chemical/UV treatments*. Water Research, 2005. **39**(8): p. 1519-1526.

252. Salgot, M., et al., *Comparison of different advanced disinfection systems for wastewater reclamation*, in *2nd World Water Congress: Water and Health-Microbiology, Monitoring and Disinfection*, P. Wilderer, Editor. 2002, I W a Publishing: London. p. 213-218.

253. Price, P.B. and T. Sowers, *Temperature dependence of metabolic rates for microbial growth, maintenance, and survival.* Proceedings of the National Academy of Sciences of the United States of America, 2004. **101**(13): p. 4631-4636.

254. Pawlowski, D.R., et al., *Entry of Yersinia pestis into the Viable but Nonculturable State in a Low-Temperature Tap Water Microcosm.* Plos One, 2011. **6**(3).

255. Matsuura, M., *Structural Modifications of Bacterial Lipopolysaccharide that Facilitate Gram-Negative Bacteria Evasion of Host Innate Immunity.* Frontiers in immunology, 2013. **4**: p. 109.

256. Laxminarayan, R., et al., *Antibiotic resistance-the need for global solutions.* Lancet Infectious Diseases, 2013. **13**(12): p. 1057-1098.

257. Davies, J. and D. Davies, *Origins and evolution of antibiotic resistance.* Microbiology and Molecular Biology Reviews, 2010. **74**(3): p. 417-433.

258. Alanis, A.J., *Resistance to antibiotics: Are we in the post-antibiotic era?* Archives of Medical Research, 2005. **36**(6): p. 697-705.

259. Mularski, A., et al., *Atomic force microscopy reveals the mechanobiology of lytic peptide action on bacteria.* Langmuir, 2015. **31**(22): p. 6164-6171.

260. Chakrabarty, S., et al., *Highly effective, water-soluble, hemocompatible 1,3-propylene oxide-based antimicrobials: poly (3,3-quaternary/PEG)-copolyoxetanes.* Biomacromolecules, 2011. **12**(3): p. 757-769.

261. King, A., et al., *High Antimicrobial effectiveness with low hemolytic and cytotoxic activity for PEG/quaternary copolyoxetanes*. Biomacromolecules, 2014. **15**(2): p. 456-467.

262. Kurt, P., et al., *Highly effective contact antimicrobial surfaces via polymer surface modifiers*. Langmuir, 2007. **23**(9): p. 4719-4723.

263. Mor, A., *Peptide-based antibiotics: A potential answer to raging antimicrobial resistance*. Drug Development Research, 2000. **50**(3-4): p. 440-447.

264. Tashiro, T., *Antibacterial and bacterium adsorbing macromolecules*. Macromolecular Materials and Engineering, 2001. **286**(2): p. 63-87.

265. Huang, H.W., *Action of antimicrobial peptides: Two-state model*. Biochemistry, 2000. **39**(29): p. 8347-8352.

266. Yang, L., et al., *Barrel-stave model or toroidal model? A case study on melittin pores*. Biophysical Journal, 2001. **81**(3): p. 1475-1485.

267. Melo, M.N., Ferre R., and Castanho M., *Antimicrobial peptides: linking partition, activity and high membrane-bound concentrations*. Nature Reviews Microbiology, 2009. **7**(3): p. 245-250.

268. Matsuzaki, K., et al., *An antimicrobial peptide, magainin 2, induced rapid flip-flop of phospholipids coupled with pore formation and peptide translocation*. Biochemistry, 1996. **35**(35): p. 11361-11368.

269. Ladokhin, A.S. and S.H. White, *'Detergent-like' permeabilization of anionic lipid vesicles by melittin*. Biochimica Et Biophysica Acta-Biomembranes, 2001. **1514**(2): p. 253-260.

270. Pouny, Y., et al., *Interaction of antimicrobial dermaseptin and its fluorescently labeled analogs with phospholipid-membranes*. Biochemistry, 1992. **31**(49): p. 12416-12423.

271. Shai, Y. and Z. Oren, *From "carpet" mechanism to de-novo designed diastereomeric cell-selective antimicrobial peptides*. Peptides, 2001. **22**(10): p. 1629-1641.

272. Longo, G., et al., *Rapid detection of bacterial resistance to antibiotics using AFM cantilevers as nanomechanical sensors*. Nature Nanotechnology, 2013. **8**(7): p. 522-526.

273. Zhang, L., et al., *In-situ detection of resveratrol inhibition effect on epidermal growth factor receptor of living MCF-7 cells by Atomic Force Microscopy*. Biosensors & Bioelectronics, 2014. **56**: p. 271-277.

274. El-Kirat-Chatel, S., et al., *Force Nanoscopy of Hydrophobic Interactions in the Fungal Pathogen Candida glabrata*. Acs Nano, 2015. **9**(2): p. 1648-1655.

275. Alves, C.S., et al., *Escherichia coli cell surface perturbation and disruption induced by antimicrobial peptides BP100 and pepR*. Journal of Biological Chemistry, 2010. **285**(36): p. 27536-27544.

276. da Silva, A. and O. Teschke, *Effects of the antimicrobial peptide PGLa on live Escherichia coli*. Biochimica Et Biophysica Acta-Molecular Cell Research, 2003. **1643**(1-3): p. 95-103.

277. Meincken, A., D.L. Holroyd, and M. Rautenbach, *Atomic force microscopy study of the effect of antimicrobial peptides on the cell envelope of Escherichia coli*. Antimicrobial Agents and Chemotherapy, 2005. **49**(10): p. 4085-4092.

278. Su, H.N., et al., *Antimicrobial peptide trichokonin VI-induced alterations in the morphological and nanomechanical properties of Bacillus subtilis*. Plos One, 2012. **7**(9).

279. Li, A., et al., *Atomic force microscopy study of the antimicrobial action of Sushi peptides on Gram negative bacteria*. Biochimica Et Biophysica Acta-Biomembranes, 2007. **1768**(3): p. 411-418.

280. Eaton, P., et al., *Atomic force microscopy study of the antibacterial effects of chitosans on Escherichia coli and Staphylococcus aureus*. Ultramicroscopy, 2008. **108**(10): p. 1128-1134.

281. Formosa, C., et al., *Unravelling of a mechanism of resistance to colistin in Klebsiella pneumoniae using atomic force microscopy*. Journal of Antimicrobial Chemotherapy, 2015. **70**(8): p. 2261-2270.

282. Fantner, G.E., et al., *Kinetics of antimicrobial peptide activity measured on individual bacterial cells using high-speed atomic force microscopy*. Nature Nanotechnology, 2010. **5**(4): p. 280-285.

283. Wu, Y.Z., R.C. Sims, and A.H. Zhou, *AFM resolves effects of ethambutol on nanomechanics and nanostructures of single dividing mycobacteria in real-time*. Physical Chemistry Chemical Physics, 2014. **16**(36): p. 19156-19164.

284. Hyldgaard, M., et al., *The antimicrobial mechanism of action of epsilon- poly-l-lysine*. Applied and Environmental Microbiology, 2014. **80**(24): p. 7758-7770.

285. Vaara, M. and T. Vaara, *Polycations as outer membrane-disorganizing agents*. Antimicrobial Agents and Chemotherapy, 1983. **24**(1): p. 114-122.

286. Mileykovskaya, E. and W. Dowhan, *Visualization of phospholipid domains in Escherichia coli by using the cardiolipin-specific fluorescent dye 10-N-nonyl acridine orange*. Journal of Bacteriology, 2000. **182**(4): p. 1172-1175.

287. Som, A., et al., *Synthetic mimics of antimicrobial peptides*. Biopolymers, 2008. **90**(2): p. 83-93.

288. Strauss, J., et al., *Binding, inactivation, and adhesion forces between antimicrobial peptide cecropin P1 and pathogenic E. coli*. Colloids and Surfaces B-Biointerfaces, 2010. **75**(1): p. 156-164.

289. Ong, Y.L., et al., *Adhesion forces between E-coli bacteria and biomaterial surfaces.* Langmuir, 1999. **15**(8): p. 2719-2725.

290. Smyth, C.J., et al., *Differences in hydrophobic surface characteristics of porcine enteropathogenic Escherichia-coli with or without k88 antigen as revealed by hydrophobic interaction chromatography*. Infection and Immunity, 1978. **22**(2): p. 462-472.

291. Grass, G., C. Rensing, and M. Solioz, *Metallic copper as an antimicrobial surface.* Applied and Environmental Microbiology, 2011. **77**(5): p. 1541-1547.

292. Zhao, G.J. and S.E. Stevens, *Multiple parameters for the comprehensive evaluation of the susceptibility of Escherichia coli to the silver ion*. Biometals, 1998. **11**(1): p. 27-32.

293. Stoimenov, P.K., et al., *Metal oxide nanoparticles as bactericidal agents*. Langmuir, 2002. **18**(17): p. 6679-6686.

294. Ruparelia, J.P., et al., *Strain specificity in antimicrobial activity of silver and copper nanoparticles*. Acta Biomaterialia, 2008. **4**(3): p. 707-716.

295. Zhou, Y., et al., *Antibacterial activities of gold and silver nanoparticles against Escherichia coli and bacillus Calmette-Guerin*. Journal of Nanobiotechnology, 2012. **10**.

296. Xie, Y.P., et al., *Antibacterial activity and mechanism of action of zinc oxide nanoparticles against Campylobacter jejuni*. Applied and Environmental Microbiology, 2011. **77**(7): p. 2325-2331.

297. Tran, N., et al., *Bactericidal effect of iron oxide nanoparticles on Staphylococcus aureus.* International Journal of Nanomedicine, 2010. **5**: p. 277-283.

298. Santo, C.E., D. Quaranta, and G. Grass, *Antimicrobial metallic copper surfaces kill Staphylococcus haemolyticus via membrane damage.* Microbiologyopen, 2012. **1**(1): p. 46-52.

299. Palza, H., R. Quijada, and K. Delgado, *Antimicrobial polymer composites with copper micro- and nanoparticles: Effect of particle size and polymer matrix.* Journal of Bioactive and Compatible Polymers, 2015. **30**(4): p. 366-380.

300. Thomas, S.F., et al., *The bactericidal effect of dendritic copper microparticles, contained in an alginate matrix, on Escherichia coli.* Plos One, 2014. **9**(5).

301. Eser, O.K., A. Ergin, and G. Hascelik, *Antimicrobial activity of copper alloys against invasive multidrug-resistant nosocomial pathogens.* Current Microbiology, 2015. **71**(2): p. 291-295.

302. Monk, A.B., et al., *Potent bactericidal efficacy of copper oxide impregnated non-porous solid surfaces.* Bmc Microbiology, 2014. **14**.

303. Lemire, J.A., J.J. Harrison, and R.J. Turner, *Antimicrobial activity of metals: mechanisms, molecular targets and applications.* Nature Reviews Microbiology, 2013. **11**(6): p. 371-384.

304. Morones, J.R., et al., *The bactericidal effect of silver nanoparticles.* Nanotechnology, 2005. **16**(10): p. 2346-2353.

305. Brayner, R., et al., *Toxicological impact studies based on Escherichia coli bacteria in ultrafine ZnO nanoparticles colloidal medium.* Nano Letters, 2006. **6**(4): p. 866-870.

306. Chatterjee, A.K., R. Chakraborty, and T. Basu, *Mechanism of antibacterial activity of copper nanoparticles*. Nanotechnology, 2014. **25**(13).

307. Hong, R., et al., *Membrane Lipid Peroxidation in Copper Alloy-Mediated Contact Killing of Escherichia coli.* Applied and Environmental Microbiology, 2012. **78**(6): p. 1776-1784.

308. Pramanik, A., et al., *A novel study of antibacterial activity of copper iodide nanoparticle mediated by DNA and membrane damage.* Colloids and Surfaces B-Biointerfaces, 2012. **96**: p. 50-55.

309. Dimkpa, C.O., et al., *Interaction of silver nanoparticles with an environmentally beneficial bacterium, Pseudomonas chlororaphis.* Journal of Hazardous Materials, 2011. **188**(1-3): p. 428-435.

310. Melo, M.N., Ferre R., and Castanho M., *Antimicrobial peptides: linking partition, activity and high membrane-bound concentrations.* Nature Reviews Microbiology, 2009. **7**(3): p. 245-250.

311. Wang, C., et al., *Real time observation of antimicrobial polycation effects on Escherichia coli: adapting the carpet model for membrane disruption to quaternary copolyoxetanes.* submitted, 2015.

312. Valko, M., H. Morris, and M.T.D. Cronin, *Metals, toxicity and oxidative stress*. Current Medicinal Chemistry, 2005. **12**(10): p. 1161-1208.

313. Tong, G., et al., *Antibacterial effects of the Cu(II)-exchanged montmorillonite on Escherichia coli K88 and Salmonella choleraesuis.* Veterinary Microbiology, 2005. **105**(2): p. 113-122.

314. Letelier, M.E., et al., *Possible mechanisms underlying copper-induced damage in biological membranes leading to cellular toxicity*. Chemico-Biological Interactions, 2005. **151**(2): p. 71-82.

315. Schoeni, J.L. and A.C.L. Wong, *Bacillus cereus food poisoning and its toxins*. Journal of Food Protection, 2005. **68**(3): p. 636-648.

316. Jernigan, J.A., et al., *Bioterrorism-related inhalational anthrax: The first 10 cases reported in the United States*. Emerging Infectious Diseases, 2001. **7**(6): p. 933-944.

317. Benoit, P.W. and D.W. Donahue, *Methods for rapid separation and concentration of bacteria in food that bypass time-consuming cultural enrichment*. Journal of Food Protection, 2003. **66**(10): p. 1935-1948.

318. Stevens, K.A. and L.A. Jaykus, *Bacterial separation and concentration from complex sample matrices: A review*. Critical Reviews in Microbiology, 2004. **30**(1): p. 7-24.

319. Leishman, O.N., T.P. Labuza, and F. Diez-Gonzalez, *Hydrophobic properties and extraction of Bacillus anthracis spores from liquid foods*. Food Microbiology, 2010. **27**(5): p. 661-666.

320. Ehrhardt, C.J., et al., *Use of fatty acid methyl ester profiles for discrimination of Bacillus cereus T-strain spores grown on different media*. Applied and Environmental Microbiology, 2010. **76**(6): p. 1902-1912.

321. Koshikawa, T., et al., *Surface hydrophobicity of spores of Bacillus spp*. Journal of General Microbiology, 1989. **135**: p. 2717-2722.

322. Dague, E., et al., *High-resolution cell surface dynamics of germinating Aspergillus fumigatus conidia*. Biophysical Journal, 2008. **94**(2): p. 656-660.

323. Dague, E., et al., *Chemical force microscopy of single live cells*. Nano Letters, 2007. **7**(10): p. 3026-3030.

324. Williams, G., et al., *The role of the exosporium in the environmental distribution of anthrax*. Journal of Applied Microbiology, 2013. **114**(2): p. 396-403.

325. Tauveron, G., et al., *Variability among Bacillus cereus strains in spore surface properties and influence on their ability to contaminate food surface equipment*. International Journal of Food Microbiology, 2006. **110**(3): p. 254-262.

326. Escobar-Cortes, K., J. Barra-Carrasco, and D. Paredes-Sabja, *Proteases and sonication specifically remove the exosporium layer of spores of Clostridium difficile strain 630*. Journal of Microbiological Methods, 2013. **93**(1): p. 25-31.

327. Esfahani, M., et al., *Lipid-protein interactions in membranes - interaction of phospholipids with respiratory enzymes of Escherichia-coli membrane*. Journal of Biological Chemistry, 1977. **252**(10): p. 3194-3198.

328. Kaneda, T., *Factors affecting relative ratio of fatty acids in Bacillus-cereus*. Canadian Journal of Microbiology, 1971. **17**(2): p. 269-275.

329. de Vries, Y.P., et al., *Influence of glutamate on growth, sporulation, and spore properties of Bacillus cereus ATCC 14579 in defined medium*. Applied and Environmental Microbiology, 2005. **71**(6): p. 3248-3254.

330. Ramirez-Peralta, A., et al., *Effects of sporulation conditions on the germination and germination protein levels of Bacillus subtilis spores*. Applied and Environmental Microbiology, 2012. **78**(8): p. 2689-2697.

331. Chen, H.Y., J.L. Guo, and Z.G. Li, *Significance of anti-cell membrane-associated DNA (mDNA) antibodies in systemic lupus erythematosus*. Clinical Rheumatology, 2008. **27**(2): p. 183-187.

332. Servais, G., et al., *Evidence of autoantibodies to cell membrane associated DNA (cultured lymphocytes): a new specific marker for rapid identification of systemic lupus erythematosus*. Annals of the Rheumatic Diseases, 1998. **57**(10): p. 606-613.

333. Bennett, R.M., et al., *Lactoferrin binds to cell-membrane DNA - association of surface DNA with an enriched population of B-cells and monocytes*. Journal of Clinical Investigation, 1983. **71**(3): p. 611-618.

334. Malvankar, N.S., et al., *Visualization of charge propagation along individual pili proteins using ambient electrostatic force microscopy*. Nature Nanotechnology, 2014. **9**(12): p. 1012-1017.

335. Xiao, L., et al., *Imaging of epidermal growth factor receptor on single breast cancer cells using surface-enhanced Raman spectroscopy*. Analytica Chimica Acta, 2014. **843**: p. 73-82.

336. Gahlmann, A. and W.E. Moerner, *Exploring bacterial cell biology with single-molecule tracking and super-resolution imaging*. Nature reviews. Microbiology, 2014. **12**(1): p. 9-22.

337. Zhao, W.D., et al., *Detection of carbohydrates on the surface of cancer and normal cells by topography and recognition imaging*. Chemical Communications, 2013. **49**(29): p. 2980-2982.

338. Pierres, A., A.M. Benoliel, and P. Bongrand, *Studying receptor-mediated cell adhesion at the single molecule level*. Cell Adhesion and Communication, 1998. **5**(5): p. 375-395

Vita

Congzhou Wang was born on 22 December 1986 in Luan, Anhui, China and is a Chinese Citizen. He grew up in Anhui, China and graduated from Huaibei First High School in 2005. He received a Bachelor of Engineering in 2009 from Huaqiao University (Fujian, China), with a major in Pharmaceutical Engineering. In 2012, he earned a Master of Medicine in Pharmacy from Chongqing University (Chongqing, China). Doctoral work was concurrently carried out under the supervision of Dr. Vamsi Yadavalli at Virginia Commonwealth University. During his PhD, he has published 7 peer-reviewed papers and currently has 5 papers submitted/in preparation.